

Reservoir Performance and Architecture of a Fluvial Meanderbelt System, Joggins Formation, Nova Scotia



Trevor B. Kelly

Supervisors: Dr. Grant Wach & Dr. Michael Pegg
Submitted in Partial Fulfillment of the Requirements
For the degree of Master of Engineering, Petroleum Engineering

The Department of Chemical/Petroleum Engineering
and the Department of Earth Sciences
Dalhousie University, Halifax, Nova Scotia

September 2013



Abstract

The fundamental elements of reservoir engineering include data collection, analysis, the preparation of a reservoir model and the subsequent simulation of said model. The determination as to whether or not a reservoir proceeds into the front end engineering and design (FEED) phase is ultimately reliant upon the preliminary results of the aforementioned elements. During the initial stages of reservoir engineering, there is typically a lack of available information regarding the geological complexities and architecture of a reservoir; thus, there is a need to make reasonable assumptions and apply various analogous reservoir parameters. Throughout the development and production phases of the reservoir, new data will be gathered, which can be fed into the reservoir model. Additionally, it greatly aids the reservoir engineer when they are aware of the depositional environment in which the reservoir was formed as well as information regarding the remaining petroleum system elements.

The Joggins Formation represents a fluvial meanderbelt system that spectacularly outcrops along the shoreline of Chignecto Bay of the Bay of Fundy, Nova Scotia. The preservation of this outcrop is likely due to several factors such as its diagenetic history and tectonic history, in addition to many others; all of which have had profound effects on the quality of this fluvial meandering system.

The objectives of this project are two-fold; the first being to define the stratal geometry and architecture of fluvial meanderbelt depositional systems and secondly; to develop a 3-D model of this geometry and architecture of the fluvial meanderbelt system that developed during the Carboniferous Period and relate this to reservoir performance.

The two primary methods of data collection are light detection and ranging (LIDAR) and ground penetrating radar (GPR); both of which have incorporated the use of a differential global positioning system (DGPS). To further create a reservoir model that is of somewhat suitable accuracy, outcrop descriptions, scintillometer readings, permeameter readings, hand sample analysis and thin section analysis will be used. Furthermore, geological and petrophysical data from the analogous Sable Offshore Mega-Merge reservoir will be utilized. All necessary data for reservoir modelling will be inputted into the modelling software known as Petrel and will be simulated using the nested software known as ECLIPSE.

Table of Contents

Abstract.....	Error! Bookmark not defined.
Table of Contents	iii
List of Figures.....	vi
List of Tables	xv
List of Abbreviations	xviii
List of Symbols	xviii
Acknowledgements.....	xix
1.0 Introduction.....	1
1.1 Problem Statement.....	1
1.2 Purpose.....	2
1.3 Outcomes and Significance	3
1.4 Thesis Organization.....	3
1.5 Geographical Setting and Access.....	4
1.6 Bay of Fundy Tides	7
1.7 Field Work Safety	8
2.0 Geological Background	9
2.1 Tectono-Stratigraphic Framework for the Cumberland Basin.....	9
2.1.1 Late Devonian through to Early Namurian	9
2.1.2 Late Namurian through to Westphalian A	10
2.1.3 Late Westphalian A through to Lower Permian.....	11
2.2 Tectonic Setting.....	12
2.3 Stratigraphy.....	13
3.0 Meandering Fluvial System	16
3.1 Meandering Fluvial Channel Deposits and Facies.....	16
3.2 Geometry and Structural Elements	23
4.0 Research Methods	25
4.1 Light Detection and Ranging (LIDAR).....	25
4.1.1 Data Collection.....	25

4.1.2	<i>Background</i>	25
4.1.3	<i>Data Processing</i>	30
4.2	Ground Penetrating RADAR (GPR)	32
4.2.1	<i>Data Collection</i>	32
4.2.2	<i>Background</i>	32
4.2.2.1	<i>Theoretical Background</i>	34
4.2.2.2	<i>Unprocessed GPR Data Limitations</i>	36
4.2.3	<i>Data Processing</i>	42
4.3	Differential Global Positioning System (DGPS)	46
4.4	Handheld Gamma-Ray Spectrometer	49
4.5	Handheld Air Permeameter	50
4.6	Rock Sampling	52
4.7	Thin Section Image Analysis	52
5.0	Results	54
5.1	Light Detection and Ranging (LIDAR)	54
5.2	Ground Penetrating Radar (GPR)	57
5.3	Handheld Gamma-Ray Spectrometer	58
5.4	Handheld Air Permeameter	59
5.5	Hand Sample / Thin Section Analysis	60
6.0	Petroleum System	61
6.1	Elements	61
6.1.1	<i>Source Rock</i>	61
6.1.2	<i>Reservoir Rock</i>	62
6.1.3	<i>Trap</i>	62
6.1.4	<i>Seal</i>	63
6.1.5	<i>Maturation</i>	63
6.1.6	<i>Migration</i>	64
7.0	Discussion	65
7.1	Fieldwork and Related Data Collection	65
7.2	Model Analysis	65
7.3	Problems and Limitations	66

8.0 Future Work.....69

9.0 References71

10.0 Appendix A: LIDAR Technical Information76

11.0 Appendix B: GPR Technical Information.....94

12.0 Appendix C: Scintillometer, Permeameter and Measured Section Log 107

13.0 Appendix D: Hand Sample Descriptions121

14.0 Appendix E: Thin Section Descriptions (Mineralogy)130

15.0 Appendix F: Thin Section Descriptions (Porosity)147

List of Figures

Figure 1-1: Satellite image showing the location of the community of Joggins (point 1), the town of Amherst (point 2) and the city of Halifax (point 3). The scale is 1cm = 45 km (Google Earth, 2013). 4

Figure 1-2: Satellite image showing a closer view of the community of Joggins (point 1), Nova Scotia in addition to Chignecto Bay (point 2). The scale is 1cm = 0.4 km (Google Earth, 2013). 5

Figure 1-3: Aerial image of the Joggins area showing the three entry/exit points that were used during the two day field trip. The scale is 1 cm = 0.1 km (Google Earth, 2013). 6

Figure 1-4: Tidal variation chart for the Joggins Wharf from the time period Wednesday, May 29th up to and including June 5th, 2013 (Fisheries and Ocean Canada, 2013). The red box shows the tidal variations during the two field days in which data was collected at Joggins. 7

Figure 1-5: Warning sign posted at Joggins near the outlet of Little River showing the three major safety hazards (Wach, 2013). 8

Figure 2-1: Diagrammatic sketch of Devonian through to Namurian sedimentation, where the sedimentation represents the Fountain Lake, Horton, Windsor and Mabou groups of the Cumberland Basin (Ryan and Boehner, 1994). 10

Figure 2-2: Diagrammatic sketch of Devonian to Westphalian A sedimentation, where the sedimentation represents the Boss Point and Little River formations of the Cumberland Basin (Ryan and Boehner, 1994). 11

Figure 2-3: Diagrammatic sketch of Devonian to middle Westphalian sedimentation, where the sedimentation includes the Polly Brook, Joggins and Springhill Mines formations of the Cumberland Basin (Ryan and Boehner, 1994). 12

Figure 2-4: (A); Geological map of the western Cumberland Basin showing major basinal structures within the basin as well as the location of the Joggins Formation (Rygel, 2005). (B); The accompanying legend and stratigraphic column (Rygel, 2005). 15

Figure 3-1: (A); Illustration showing the deposits and physiography of a meandering channel complex (Selley, 2000). Inset (B); Aerial photograph showing a present-day meandering channel system (Charlton, 2008). 17

Figure 3-2: Width versus thickness plot for the Joggins Formation meandering channel system (black outlined area). The average width to thickness value plots at the black point. The blue outlined area represents where other meandering channel systems in the geological record would plot (modified from Gibling, 2006). 24

Figure 3-3: Meandering channel body type as applied to the meander channels at Joggins (Rygel, 2005). 24

Figure 4-1: Left (A); image of the LIDAR system setup showing the batteries and holder (1), the tripod (2) and the laptop computer (3). Right (B); closer view of the LIDAR system showing the

LIDAR unit (1), the pan/tilt base (2), a USB flash drive for saving the data (3), the pan/tilt cable (4), the Ethernet network cable (5) and the power cable going to the battery holder (6). 26

Figure 4-2: Image demonstrating the placement limitations of the LIDAR unit. The positioning of the LIDAR unit is similar to that of the third scan at Coal Mine Point/Hardscrabble Point. With this configuration, the beams (red lines) from the unit (yellow square) are unable to capture points behind the small protruding headland, resulting in an un-imaged zone (shown in grey). Scale is 1 cm = 35.5 m (Google Earth, 2013). 28

Figure 4-3: Left (A); image of the LIDAR georeferencing targets that are placed at varying X, Y, and Z coordinates in front of the cliff face portion to be scanned (Rafuse, 2011). Right (B); image showing the placement of one of the georeferencing targets with the cliff and the Joggins Fossil Centre in the background (Rafuse, 2011). 29

Figure 4-4: The top (A) image is similar to the image captured by the ILRIS unit during its 360° panoramic scan of the Hardscrabble Point area. The bottom (B) image is the same as that above, but the user-defined blue box shows that area that the ILRIS unit will scan. The unit will not scan outside of the user-defined area; thereby minimizing the amount of erroneous data points (e.g. intertidal zone and sky) collected (Wach, 2013). 30

Figure 4-5: Simplified processing workflow that was applied to the raw LIDAR data. 31

Figure 4-6: Image of the Sensors and Software, Inc. GPR SmartCart. The various parts of the SmartCart are highlighted (Sensors and Software, Inc., 2013). 33

Figure 4-7: Geometry of the common offset survey where R = receiver and T = transmitter (Daniels, 1996). 34

Figure 4-8: Raw, unprocessed GPR profile of Line 46. 41

Figure 4-9: Processed GPR profile of Line 46. 42

Figure 4-10: Lines 12-14 are examples of the raw data, while lines 09-11 have the applied DGPS fixes, elevations, and re-computed step-sizes. 43

Figure 4-11: Processing window showing the processes, the order in which they were applied and their respective properties. 43

Figure 4-12: Processing workflow that was applied to the raw GPR data in EKKO_View Deluxe. The process evolved via trial and error. 45

Figure 4-13: Left; image of the Leica base station on the right side and the radio transmitter and antenna on the left side. Right; close-up view of the Leica base station. 46

Figure 4-14: Left; photograph of a Leica GNSS rover/receiver similar to the one used at Joggins for measuring the LIDAR system setup locations and LIDAR target locations (Leica Geosystems, n.d.). Right; photograph of the GPR cart showing the mobile rover/receiver. 48

Figure 4-15: Photograph of the Exploranium GR-130 handheld gamma-ray spectrometer (miniSPEC). 49

Figure 4-16: Front view of the Exploranium GR-130 handheld gamma-ray spectrometer showing the portion that is held against the surface for takings measurements..... 50

Figure 4-17: Photograph showing the TinyPerm II portable permeameter and its associated parts (NER, 2013)..... 50

Figure 4-18: Permeability calibration chart which is used to correlate a TinyPerm II value to a corresponding permeability (Modified from NER, 2013). 51

Figure 5-1: Image showing the four separate scan tasks that make up the full scan to the north of Hardscrabble/Coal Mine Point. The white lines indicate the limits of the tasks and these four tasks are also assigned an identification number automatically by the LIDAR unit. 54

Figure 5-2: Image showing the six separate scan tasks that make up the full scan to the south of Hardscrabble/Coal Mine Point. The white lines indicate the limits of the tasks and these six tasks are also assigned an identification number automatically by the LIDAR unit. 55

Figure 5-3: Screen capture of the third scan located on the northern side of Hardscrabble/Coal Mine Point as viewed in Petrel 2011. All data points in the point cloud are activated and a colour ramp was applied based on intensity. The colours correlate to the various lithologies. The white box shows the area that was zoomed in and is displayed in the following figure. 56

Figure 5-4: Screen capture of a portion of the third scan located on the northern side of Hardscrabble Point/Coal Mine Point as viewed in Petrel 2011. All data points in the point cloud are activated and a colour ramp was applied based on intensity. The reds, oranges, yellows and to a lesser extent, the greens, represent the sand bodies while the blues and purples represent the finer-grained lithologies in the outcrop or vegetation at the top of the cliff..... 56

Figure 5-5: Two examples of concave downwards reflectors representing old mine workings or culverts..... 57

Figure 6-1: Sketch showing the three migration phases. The figure shows primary migration from the source rock into a trapped reservoir (reservoir 2) or into a carrier bed (reservoir 1); secondary migration in carrier reservoir 2 and up faults into reservoir 3; and tertiary migration from reservoir 3 into the surface (Gluyas and Swarbrick, 2004)..... 64

Figure 10-1: Aerial photograph showing the approximate location of the base station near the Joggins Fossil Centre (Google Earth, 2013). Scale is 1cm = 20 m. 77

Figure 10-2: Aerial photograph showing the approximate location of LIDAR Setup # 1 near the location of the Fundy Forest (Google Earth, 2013). Scale is 1cm = 27 m. 78

Figure 10-3: Aerial photograph showing the approximate location of the LIDAR Setup # 1 georeferencing targets (Google Earth, 2013). Scale is 1cm = 27 m. 80

Figure 10-4: Aerial photograph showing the approximate location of LIDAR Setup # 2. (Google Earth, 2013). Scale is 1cm = 27 m. 81

Figure 10-5: Aerial photograph showing the approximate location of the LIDAR Setup # 2 georeferencing targets (Google Earth, 2013). Scale is 1cm = 27 m. 83

Figure 10-6: Aerial photograph showing the approximate location of LIDAR Setup # 3 near Hardscrabble Point/Coal Mine Point (Google Earth, 2013). Scale is 1cm = 30 m. 84

Figure 10-7: Aerial photograph showing the approximate location of the LIDAR Setup # 3 georeferencing targets near Hardscrabble Point/Coal Mine Point (Google Earth, 2013). Scale is 1cm = 30 m. 86

Figure 10-8: Aerial photograph showing the setup locations of the LIDAR unit, targets and base station. Scale is 1 cm = 13 m. 87

Figure 11-1: North is towards the top left-hand corner. Scale is 1cm = 39 m. 98

Figure 11-2: Ground penetrating radar profiles for line 09 to 14 inclusive. 99

Figure 11-3: Ground penetrating radar profiles for line 15 to 20 inclusive. 100

Figure 11-4: Ground penetrating radar profiles for line 21 to 26 inclusive. 101

Figure 11-5: Ground penetrating radar profiles for line 27 to 32 inclusive. 102

Figure 11-6: Ground penetrating radar profiles for line 33 to 38 inclusive. 103

Figure 11-7: Ground penetrating radar profiles for line 39 to 44 inclusive. 104

Figure 11-8: Ground penetrating radar profiles for line 45 to 51 inclusive. 105

Figure 11-9: Ground penetrating radar profiles for line 52 to 57 inclusive. 106

Figure 12-1: Gamma-ray curve for a measured section. Curve is based on average readings from Table 12-2. 110

Figure 12-2: Scintillometer readings from each sample displayed as a trace for each of the eight samples collected. 113

Figure 12-3: Scintillometer readings for the coal sample, limestone samples and the average of the six sandstones samples displayed together. 114

Figure 12-4: Measured section along the Fundy Coal Seam and Fundy Forest at Joggins. Gamma-ray readings were recorded at various points along this portion of the section and the corresponding plot is to the right of the section. 116

Figure 12-5: Measured section at Hardscrabble Point/Coal Mine Point at Joggins. 119

Figure 13-1: Photograph of hand sample GW101-2013TK. 122

Figure 13-2: Photograph of hand sample GW102-2013TK. 123

Figure 13-3: Photograph of hand sample GW103-2013TK. 124

Figure 13-4: Photograph of hand sample GW104-2013TK. 125

Figure 13-5: Photograph of hand sample GW105-2013TK. 126

Figure 13-6: Photograph of hand sample GW106-2013TK. 127

Figure 13-7: Photograph of hand sample GW107-2013TK. 128

Figure 13-8: Photograph of hand sample GW108-2013TK. 129

Figure 14-1: Left; photograph of thin section from hand sample GW101-2013TK. Right; corresponding photograph of rock sample that thin section was made from. 131

Figure 14-2: Top; sample GW101-2013TK in plane polarized light at 2X magnification. Bottom; sample in crossed Nicols at 2X magnification..... 131

Figure 14-3: Top; sample GW101-2013TK in plane polarized light at 10X magnification. Bottom; sample in crossed Nicols at 10X magnification..... 132

Figure 14-4: Left; photograph of thin section from hand sample GW101-2013TK. Right; corresponding photograph of rock sample that thin section was made from. 133

Figure 14-5: Top; sample GW102-2013TK in plane polarized light at 2X magnification. Bottom; sample in crossed Nicols at 2X magnification..... 133

Figure 14-6: Top; sample GW102-2013TK in plane polarized light at 10X magnification. Bottom; sample in crossed Nicols at 10X magnification..... 134

Figure 14-7: Left; photograph of thin section from hand sample GW103-2013TK. Right; corresponding photograph of rock sample that thin section was made from. 135

Figure 14-8: Top; sample GW103-2013TK in plane polarized light at 2X magnification. Bottom; sample in crossed Nicols at 2X magnification..... 135

Figure 14-9: Top; sample GW103-2013TK in plane polarized light at 10X magnification. Bottom; sample in crossed Nicols at 10X magnification..... 136

Figure 14-10: Left; photograph of thin section from hand sample GW104-2013TK. Right; corresponding photograph of rock sample that thin section was made from. 137

Figure 14-11: Top; sample GW104-2013TK in plane polarized light at 2X magnification. Bottom; another image of the sample in plane polarized light at 2X magnification. 137

Figure 14-12: Top; sample GW104-2013TK in plane polarized light at 10X magnification. Bottom; another image of the sample in plane polarized light at 10X magnification. 138

Figure 14-13: Left; photograph of thin section from hand sample GW105-2013TK. Right; corresponding photograph of rock sample that thin section was made from. 139

Figure 14-14: Top; sample GW105-2013TK in plane polarized light at 2X magnification. Bottom; sample in crossed Nicols at 2X magnification..... 139

Figure 14-15: Top; sample GW105-2013TK in plane polarized light at 10X magnification. Bottom; sample in crossed Nicols at 10X magnification..... 140

Figure 14-16: Left; photograph of thin section from hand sample GW106-2013TK. Right; corresponding photograph of rock sample that thin section was made from. 141

Figure 14-17: Top; sample GW106-2013TK in plane polarized light at 2X magnification. Bottom; sample in crossed Nicols at 2X magnification..... 141

Figure 14-18: Top; sample GW106-2013TK in plane polarized light at 10X magnification. Bottom; sample in crossed Nicols at 10X magnification..... 142

Figure 14-19: Left; photograph of thin section from hand sample GW107-2013TK. Right; corresponding photograph of rock sample that thin section was made from. 143

Figure 14-20: Top; sample GW107-2013TK in plane polarized light at 2X magnification. Bottom; sample in crossed Nicols at 2X magnification..... 143

Figure 14-21: Top; sample GW107-2013TK in plane polarized light at 10X magnification. Bottom; sample in crossed Nicols at 10X magnification..... 144

Figure 14-22: Left; photograph of thin section from hand sample GW108-2013TK. Right; corresponding photograph of rock sample that thin section was made from. 145

Figure 14-23: Top; sample GW108-2013TK in plane polarized light at 2X magnification. Bottom; sample in crossed Nicols at 2X magnification..... 145

Figure 14-24: Top; sample GW108-2013TK in plane polarized light at 10X magnification. Bottom; sample in crossed Nicols at 10X magnification..... 146

Figure 15-1: Left; thin section image GW101-2013TK-1 (@ 10X) in normal light with porosity shown in blue (dye). Right; same image, but with porosity shown in yellow, grains as blue and cement as brown. 148

Figure 15-2: Left; thin section image GW101-2013TK-2 (@ 10X) in normal light with porosity shown in blue (dye). Right; same image, but with porosity shown in yellow, grains as blue and cement as brown. 148

Figure 15-3: Left; thin section image GW101-2013TK-3 (@ 10X) in normal light with porosity shown in blue (dye). Right; same image, but with porosity shown in yellow, grains as blue and cement as brown. 149

Figure 15-4: Left; thin section image GW101-2013TK-4 (@ 10X) in normal light with porosity shown in blue (dye). Right; same image, but with porosity shown in yellow, grains as blue and cement as brown. 149

Figure 15-5: Left; thin section image GW101-2013TK-5 (@ 10X) in normal light with porosity shown in blue (dye). Right; same image, but with porosity shown in yellow, grains as blue and cement as brown. 150

Figure 15-6: Left; thin section image GW101-2013TK-6 (@ 10X) in normal light with porosity shown in blue (dye). Right; same image, but with porosity shown in yellow, grains as blue and cement as brown. 150

Figure 15-7: Left; thin section image GW102-2013TK-1 (@ 10X) in normal light with porosity shown in blue (dye). Right; same image, but with porosity shown in yellow, grains as blue and cement as brown. 152

Figure 15-8: Left; thin section image GW102-2013TK-2 (@ 10X) in normal light with porosity shown in blue (dye). Right; same image, but with porosity shown in yellow, grains as blue and cement as brown. 152

Figure 15-9: Left; thin section image GW102-2013TK-3 (@ 10X) in normal light with porosity shown in blue (dye). Right; same image, but with porosity shown in yellow, grains as blue and cement as brown. 153

Figure 15-10: Left; thin section image GW102-2013TK-4 (@ 10X) in normal light with porosity shown in blue (dye). Right; same image, but with porosity shown in yellow, grains as blue and cement as brown. 153

Figure 15-11: Left; thin section image GW102-2013TK-5 (@ 10X) in normal light with porosity shown in blue (dye). Right; same image, but with porosity shown in yellow, grains as blue and cement as brown. 154

Figure 15-12: Left; thin section image GW102-2013TK-6 (@ 10X) in normal light with porosity shown in blue (dye). Right; same image, but with porosity shown in yellow, grains as blue and cement as brown. 154

Figure 15-13: Left; thin section image GW102-2013TK-7 (@ 10X) in normal light with porosity shown in blue (dye). Right; same image, but with porosity shown in yellow, grains as blue and cement as brown. 155

Figure 15-14: Left; thin section image GW102-2013TK-8 (@ 10X) in normal light with porosity shown in blue (dye). Right; same image, but with porosity shown in yellow, grains as blue and cement as brown. 155

Figure 15-15: Left; thin section image GW102-2013TK-9 (@ 10X) in normal light with porosity shown in blue (dye). Right; same image, but with porosity shown in yellow, grains as blue and cement as brown. 156

Figure 15-16: Left; thin section image GW102-2013TK-10 (@ 10X) in normal light with porosity shown in blue (dye). Right; same image, but with porosity shown in yellow, grains as blue and cement as brown. 156

Figure 15-17: Left; thin section image GW103-2013TK-1 (@ 10X) in normal light with porosity shown in blue (dye). Right; same image, but with porosity shown in yellow, grains as blue and cement as brown. 158

Figure 15-18: Left; thin section image GW103-2013TK-2 (@ 10X) in normal light with porosity shown in blue (dye). Right; same image, but with porosity shown in yellow, grains as blue and cement as brown. 158

Figure 15-19: Left; thin section image GW103-2013TK-3 (@ 10X) in normal light with porosity shown in blue (dye). Right; same image, but with porosity shown in yellow, grains as blue and cement as brown. 159

Figure 15-20: Left; thin section image GW103-2013TK-4 (@ 10X) in normal light with porosity shown in blue (dye). Right; same image, but with porosity shown in yellow, grains as blue and cement as brown. 159

Figure 15-21: Left; thin section image GW103-2013TK-5 (@ 10X) in normal light with porosity shown in blue (dye). Right; same image, but with porosity shown in yellow, grains as blue and cement as brown. 160

Figure 15-22: Left; thin section image GW103-2013TK-6 (@ 10X) in normal light with porosity shown in blue (dye). Right; same image, but with porosity shown in yellow, grains as blue and cement as brown. 160

Figure 15-23: Left; thin section image GW106-2013TK-1 (@ 10X) in normal light with porosity shown in blue (dye). Right; same image, but with porosity shown in yellow, grains as blue and cement as brown. 162

Figure 15-24: Left; thin section image GW106-2013TK-2 (@ 10X) in normal light with porosity shown in blue (dye). Right; same image, but with porosity shown in yellow, grains as blue and cement as brown. 162

Figure 15-25: Left; thin section image GW106-2013TK-3 (@ 10X) in normal light with porosity shown in blue (dye). Right; same image, but with porosity shown in yellow, grains as blue and cement as brown. 163

Figure 15-26: Left; thin section image GW106-2013TK-4 (@ 10X) in normal light with porosity shown in blue (dye). Right; same image, but with porosity shown in yellow, grains as blue and cement as brown. 163

Figure 15-27: Left; thin section image GW106-2013TK-5 (@ 10X) in normal light with porosity shown in blue (dye). Right; same image, but with porosity shown in yellow, grains as blue and cement as brown. 164

Figure 15-28: Left; thin section image GW106-2013TK-6 (@ 10X) in normal light with porosity shown in blue (dye). Right; same image, but with porosity shown in yellow, grains as blue and cement as brown. 164

Figure 15-29: Left; thin section image GW106-2013TK-7 (@ 10X) in normal light with porosity shown in blue (dye). Right; same image, but with porosity shown in yellow, grains as blue and cement as brown. 165

Figure 15-30: Left; thin section image GW106-2013TK-8 (@ 10X) in normal light with porosity shown in blue (dye). Right; same image, but with porosity shown in yellow, grains as blue and cement as brown. 165

Figure 15-31: Left; thin section image GW106-2013TK-9 (@ 10X) in normal light with porosity shown in blue (dye). Right; same image, but with porosity shown in yellow, grains as blue and cement as brown. 166

Figure 15-32: Left; thin section image GW106-2013TK-10 (@ 10X) in normal light with porosity shown in blue (dye). Right; same image, but with porosity shown in yellow, grains as blue and cement as brown. 166

Figure 15-33: Left; thin section image GW107-2013TK-1 (@ 5X) in normal light with porosity shown in blue (dye). Right; same image, but with porosity shown in yellow, grains as blue and cement as brown. 168

Figure 15-34: Left; thin section image GW107-2013TK-2 (@ 5X) in normal light with porosity shown in blue (dye). Right; same image, but with porosity shown in yellow, grains as blue and cement as brown. 168

Figure 15-35: Left; thin section image GW107-2013TK-3 (@ 5X) in normal light with porosity shown in blue (dye). Right; same image, but with porosity shown in yellow, grains as blue and cement as brown. 169

Figure 15-36: Left; thin section image GW107-2013TK-4 (@ 5X) in normal light with porosity shown in blue (dye). Right; same image, but with porosity shown in yellow, grains as blue and cement as brown. 169

Figure 15-37: Left; thin section image GW107-2013TK-5 (@ 5X) in normal light with porosity shown in blue (dye). Right; same image, but with porosity shown in yellow, grains as blue and cement as brown. 170

Figure 15-38: Left; thin section image GW107-2013TK-6 (@ 5X) in normal light with porosity shown in blue (dye). Right; same image, but with porosity shown in yellow, grains as blue and cement as brown. 170

Figure 15-39: Left; thin section image GW107-2013TK-7 (@ 5X) in normal light with porosity shown in blue (dye). Right; same image, but with porosity shown in yellow, grains as blue and cement as brown. 171

Figure 15-40: Left; thin section image GW107-2013TK-8 (@ 5X) in normal light with porosity shown in blue (dye). Right; same image, but with porosity shown in yellow, grains as blue and cement as brown. 171

Figure 15-41: Left; thin section image GW108-2013TK-1 (@ 5X) in normal light with porosity shown in blue (dye). Right; same image, but with porosity shown in yellow, grains as blue and cement as brown. 173

Figure 15-42: Left; thin section image GW108-2013TK-2 (@ 5X) in normal light with porosity shown in blue (dye). Right; same image, but with porosity shown in yellow, grains as blue and cement as brown. 173

Figure 15-43: Left; thin section image GW108-2013TK-3 (@ 5X) in normal light with porosity shown in blue (dye). Right; same image, but with porosity shown in yellow, grains as blue and cement as brown. 174

Figure 15-44: Left; thin section image GW108-2013TK-4 (@ 5X) in normal light with porosity shown in blue (dye). Right; same image, but with porosity shown in yellow, grains as blue and cement as brown. 174

Figure 15-45: Left; thin section image GW108-2013TK-5 (@ 5X) in normal light with porosity shown in blue (dye). Right; same image, but with porosity shown in yellow, grains as blue and cement as brown. 175

Figure 15-46: Left; thin section image GW108-2013TK-6 (@ 5X) in normal light with porosity shown in blue (dye). Right; same image, but with porosity shown in yellow, grains as blue and cement as brown. 175

List of Tables

Table 3-1: Possible meander channel facies that occur or could occur at Joggins. 18

Table 3-2: Facies that can be expected in the floodplain of a meander channel system. 20

Table 3-3: Oxbow lake facies that can be expected in a meander channel system. 22

Table 4-1: Permeability ranking (Nabaway *et al.*, 2009). 52

Table 4-2: Porosity Ranking (Nabaway *et al.*, 2009). 53

Table 5-1: Calculated average porosity, cement and grain area values based on image analysis of a representative thin section for each of the hand samples collected at Joggins. 61

Table 6-1: Examples of the two trap types that are part of a petroleum system (Allen and Allen, 1990). 63

Table 8-1: Work tasks completed and possible ideas for future work regarding the Joggins Formation fluvial meanderbelt system. 69

Table 10-1: Base station setup technical information. 77

Table 10-2: LIDAR unit setup # 1 technical information. 78

Table 10-3: First scan; left target (if viewing from the water) technical information. 79

Table 10-4: First scan; middle target (if viewing from the water) technical information. 79

Table 10-5: First scan; right target (if viewing from the water) technical information. 80

Table 10-6: LIDAR unit setup # 2 technical information. 81

Table 10-7: Second scan; left target (if viewing from the water) technical information. 82

Table 10-8: Second scan; middle target (if viewing from the water) technical information. 82

Table 10-9: Second scan; right target (if viewing from the water) technical information. 83

Table 10-10: LIDAR unit setup # 3 technical information. 84

Table 10-11: Third scan; left target (if viewing from the water) technical information. 85

Table 10-12: Third scan; middle target (if viewing from the water) technical information. 85

Table 10-13: Third scan; right target (if viewing from the water) technical information. 86

Table 10-14: Various distances from the LIDAR unit to cliff face, targets and base station. 87

Table 10-15: Scan to the north of Hardscrabble/Coal Mine Point technical information. 88

Table 10-16: Hardscrabble/Coal Mine Point – scan to the north – scan task ID 107 technical information. 88

Table 10-17: Hardscrabble/Coal Mine Point – scan to the north – scan task ID 108 technical information. 89

Table 10-18: Hardscrabble/Coal Mine Point – scan to the north – scan task ID 109 technical information..... 89

Table 10-19: Hardscrabble/Coal Mine Point – scan to the north – scan task ID 110 technical information..... 90

Table 10-20: Scan to the south of Hardscrabble/Coal Mine Point technical information. 90

Table 10-21: Hardscrabble/Coal Mine Point – scan to the south – scan task ID 105 technical information..... 91

Table 10-22: Hardscrabble/Coal Mine Point – scan to the south – scan task ID 106 technical information..... 91

Table 10-23: Hardscrabble/Coal Mine Point – scan to the south – scan task ID 107 technical information..... 92

Table 10-24: Hardscrabble/Coal Mine Point – scan to the south – scan task ID 137 technical information..... 92

Table 10-25: Hardscrabble/Coal Mine Point – scan to the south – scan task ID 138 technical information..... 93

Table 10-26: Hardscrabble/Coal Mine Point – scan to the south – scan task ID 139 technical information..... 93

Table 11-1: Ground penetrating radar system setup summary 95

Table 11-2: GPR survey data pertaining to each survey line..... 96

Table 12-1: Scintillometer readings on various fallen sandstone blocks located near the Strat. Class outcrop..... 108

Table 12-2: Scintillometer readings on various lithologies within the cliff face..... 110

Table 12-3: Scintillometer readings for each of the collected rock samples over a 66 second time period. 111

Table 12-4: Permeameter values collected on various fallen blocks. 115

Table 12-5: Permeameter measurements taken at the Strat. Class outcrop. 115

Table 15-1: Summary table for sample GW101-2013TK listing the area percentage for voids, grains and cement in each image captured of the thin section. The average area for each of the three parameters is also calculated..... 151

Table 15-2: Summary table for sample GW102-2013TK listing the area percentage for voids, grains and cement in each image captured of the thin section. The average area for each of the three parameters is also calculated..... 157

Table 15-3: Summary table for sample GW103-2013TK listing the area percentage for voids, grains and cement in each image captured of the thin section. The average area for each of the three parameters is also calculated..... 161

Table 15-4: Summary table for sample GW106-2013TK listing the area percentage for voids, grains and cement in each image captured of the thin section. The average area for each of the three parameters is also calculated..... 167

Table 15-5: Summary table for sample GW107-2013TK listing the area percentage for voids, grains and cement in each image captured of the thin section. The average area for each of the three parameters is also calculated..... 172

Table 15-6: Summary table for sample GW108-2013TK listing the area percentage for voids, grains and cement in each image captured of the thin section. The average area for each of the three parameters is also calculated..... 176

List of Abbreviations

2-D:	Two-Dimensional
3-D:	Three-Dimensional
ASC:	Adaptive Shade Correction
D:	Darcy's
DGPS:	Differential Global Positioning System
Ell:	Ellipsoid
GNSS:	Global Navigation Satellite System
GPS:	Global Positioning System
GPR:	Ground Penetrating RADAR
Hz:	Hertz
ILRIS:	Intelligent Laser Ranging and Imaging System
LIDAR:	Light Detection and Ranging
M.A.	Millions of years ago
mD:	milli-Darcy's
RADAR:	Radio Detection and Ranging
ROI:	Region of Interest
SA:	Selective Availability
TWT:	Two-way Travel Time
UHF:	Ultra-High Frequency
UNESCO:	United Nations Educational, Scientific and Cultural Organization

List of Symbols

λ :	Wavelength
f :	Wave Frequency
v :	Wave Velocity
μ_r :	Magnetic Permeability
ϵ_r :	Dielectric Permittivity
σ :	Electrical Conductivity
ω :	Angular Frequency
α :	Attenuation Coefficient
C_o :	Electromagnetic Wave Velocity (in Vacuum)
A :	Wave Amplitude
A_o :	Initial Wave Amplitude
Z :	Distance
R :	Reflection Coefficient
ϕ :	Porosity
K :	Permeability

Acknowledgements

The completion of this thesis was made possible by numerous individuals, who at this time I would like to acknowledge. First of all, I would like to express my great appreciation to my supervisor Dr. Grant Wach for accepting me as one of his graduate students, suggesting the topic, for providing me with the tools necessary to make this thesis possible and for his support and assistance throughout the duration of this thesis compilation. I would also like to thank my co-supervisor, Dr. Michael Pegg for providing support and assistance throughout the completion of this thesis. I am particularly grateful for the field assistance provided to me by Darragh O'Connor, Allison Grant, Dawn Tobey, Naomi Plummer and Jillian Haynes. Without their help in performing various fieldwork-related tasks, data collection would have been extremely difficult. I would like to offer my special thanks to Laurie Melanson of the Joggins Volunteer Fire Department for making an all-terrain vehicle available for the transportation of various pieces of equipment to the beach. Without this, the field work would have taken much longer. Thanks must also be given to Kristie McVicar for the various logistical work done prior to performing the field work at Joggins and to John Thibodeau for providing technical support regarding computer related and LIDAR related issues. I am also appreciative to Dr. Yawooz Kettanah for training me on the proper use of the microscope and software necessary to perform the digital image porosity analysis. Many thanks go out to Dr. Lawrence Plug for allowing me the use of his differential global positioning system equipment and to Gordon Brown for preparing thin sections. My special thanks are extended to the fine folks at the Joggins Fossil Center for accommodating us during a busy time of year.



Photograph of five members of the Joggins field trip team. Pictured from left to right are Allison Grant, Darragh O'Connor, Trevor Kelly, Jillian Haynes and Grant Wach.

1.0 Introduction

1.1 Problem Statement

Petroleum system reservoir modelling and engineering are ever-evolving, since they are never truly complete. Reservoir models must be continuously updated as a result of changes in performance and the fact that new architectural features may be discovered that were previously unknown. In the real world, petroleum reservoirs are never perfectly shaped, homogenous structures; but rather, they are a complex, interwoven system of macroscopic to microscopic elements. As a reservoir engineer or reservoir geologist, the modelling of a reservoir often conjures up questions that are open-ended and rarely have one single best answer. While these questions may not have a best answer, different companies do have protocols, philosophies and methodologies that they follow as a way of progressing.

Petrel software is a Schlumberger owned suite of software that allows the user to, in this case, construct a reservoir model. The reservoir model allows for the aggregation of various types of data (e.g. seismic data, well test data, etc.) into a model that can range from the simple to the complex, depending on the amount and type of data that has been acquired. It is important to note that should a reservoir of high complexity be the goal, a vast amount of data must be collected from teams of interacting geophysicists, geologists, engineers, petrophysicists and the like.

To be a successful reservoir engineer, it is essential to know and understand the architecture of the reservoir and the geological features that result in its compartmentalization. According to Mulcahy (2006), the primary causes of reservoir compartmentalization are “depositional setting, facies stacking patterns, lateral and vertical lithology and grain size changes, continuity of sandstone units, effect of bounding surfaces and petrophysical properties”. Since a great majority of the key features that comprise a reservoir are below the limits of seismic detection and resolution, other methods such as outcrop studies and core studies must be used in conjunction.

This study will use Petrel to create a model of the fluvial meanderbelt system at Joggins, Nova Scotia and apply Eclipse in order to simulate the reservoir.

1.2 Purpose

The Joggins Fossil Cliffs are known the world over for their exceptionally well preserved Carboniferous-aged in-situ standing fossilized forest in addition to a myriad of other vertebrate and invertebrate fauna from terrestrial and aquatic environments. The site is of such importance because it influenced concepts in early geological and evolutionary science thought and was even mentioned in Sir Charles Darwin's "The Origin of Species".

Past research on the Joggins Formation, at Joggins, Nova Scotia (Figure 1-1 and Figure 1-2) has studied sedimentology and stratigraphy (e.g. Davies and Gibling, 2005; Rygel, 2005), paleo-biology (e.g. Falcon-Lang *et al.*, 2006; Calder *et al.*, 2006; Dolby, 2003; Utting *et al.*, 2010) and paleo-ecology (e.g. DiMichele *et al.*, 2010; Falcon-Lang *et al.*, 2000). With the advent of new technology, such as ground penetrating radar (GPR) and light detection and ranging (LIDAR), it is now possible to integrate different methods of data acquisition and analyze the collected data sets using visualization techniques to develop 2-D and 3-D models of the outcrop for interpretation and modelling.

While the meanderbelt system at Joggins has been studied based on the visible cliff face, no work has been done with respect to using LIDAR in conjunction with GPR as a means of attempting to extend the 2-D cliff face surface into the subsurface beyond the outcrop. It is possible to use this technology to analyse the Joggins Formation meanderbelt system in a 2-D and 3-D manner. The outcrop provides the 2-D requirements for study. The 3-D representation arises from the merging of both the GPR and LIDAR data to then model the meanderbelt system using software, such as Petrel. This will allow for fluid simulation modelling to show how fluids flow within a fluvial meanderbelt reservoir. The goal will also be to create a 3-D surface within the overall 3-D model that may be tested as an analog to reservoirs within the Sable Offshore Mega-Merge.

1.3 Outcomes and Significance

There are a number of results that this study hopes to offer. One is that at the completion of this study a 3-D model of the Joggins Formation fluvial meanderbelt system will have been built that incorporates various geobodies and architectural elements in the lateral and vertical extent and then show how these elements can affect fluid flow. The study will portray the importance of using detailed geological models to characterize a reservoir. As an analogue, the Sable Offshore Mega-Merge will be tested against the 3-D model. Additionally, the project aims to collect quality data to allow for further research on the Joggins Formation to be done or further investigations into a fluvial meanderbelt system can be performed. As an indirect outcome, the project will provide valuable background as to the proper process a petroleum engineer must go through when tasked with developing a reservoir model from the initial data collection phase all the way through to the construction of a computerized reservoir model and subsequent simulation.

1.4 Thesis Organization

This report will first outline the necessary geology of the Fundy Basin and Cumberland Basin and then will discuss the fundamentals of a meander channel system by means of their morphological and sedimentological characteristics. The methods section to follow will introduce the numerous research methods deployed (e.g. permeameter, DGPS, GPR, LIDAR etc.), by way of how the method was used, why it was used and the parameters that lead to its use in examining a fluvial meanderbelt system. The results section will discuss the data acquired by the methods used and also the 3-D model that was constructed and simulated. The discussion section will attempt to examine the results and explain what was found. In other words, it will discuss qualitatively and quantitatively the reservoir performance and architecture of the Joggins Formation fluvial meanderbelt system. Finally, the conclusion will attempt to summarize the findings and tie it all back to the research that was performed. A fairly extensive appendix is also included and serves to present and document all of the detailed work that was done in the field.

1.5 Geographical Setting and Access

The Joggins Formation is exposed along the southeastern shoreline of the Chignecto Basin, Bay of Fundy, Nova Scotia. The community of Joggins, Nova Scotia is located approximately 230 km north northwest of Dalhousie University in Halifax, Nova Scotia and approximately 33 km southwest from Amherst, Nova Scotia (Refer to Figure 1-1 and Figure 1-2). Arriving at the Joggins Fossil Cliffs involves driving northward to Truro on Highway 102. At Truro, take exit 15W and travel northwest along Highway 104. Take exit 4 and make a left hand turn onto Albion Street South. Turn right onto the Nappan Road and follow it all the way to the end, which will eventually turn into Main Street. Staying on Main Street; continue to the end, finally ending at the Joggins Fossil Cliffs Centre. The Joggins Formation outcrop section at the study area is approximately 3.0 km long and begins approximately 0.5 km south of Coal Mine Point / Hardscrabble Point and continues north along Lower Cove Beach for roughly 2.5 km (Refer to Figure 1-3).



Figure 1-1: Satellite image showing the location of the community of Joggins (point 1), the town of Amherst (point 2) and the city of Halifax (point 3). The scale is 1cm = 45 km (Google Earth, 2013).



Figure 1-2: Satellite image showing a closer view of the community of Joggins (point 1), Nova Scotia in addition to Chignecto Bay (point 2). The scale is 1cm = 0.4 km (Google Earth, 2013).

Access to the beach can be gained from three different locations along the cliff section. One of these entry routes is via a set of steps built as part of the Joggins Fossil Cliffs Centre infrastructure (See Figure 1-3; point 1). The steps are probably the safest of the three entry/exit options. Another entry/exit point is near the outlet of the Little River off the Lower Cover Road some 3.0 km from the Joggins Fossil Centre (See Figure 1-3; point 8). The last point of entry / exit lies just off of the Hearts Gravel Road where a creek empties onto the intertidal zone (See Figure 1-3; point 2). This path is rocky and steep in some areas and where the water flows over the rocks, slipping hazards can occur. This is the least safe entry/exit point of the three.

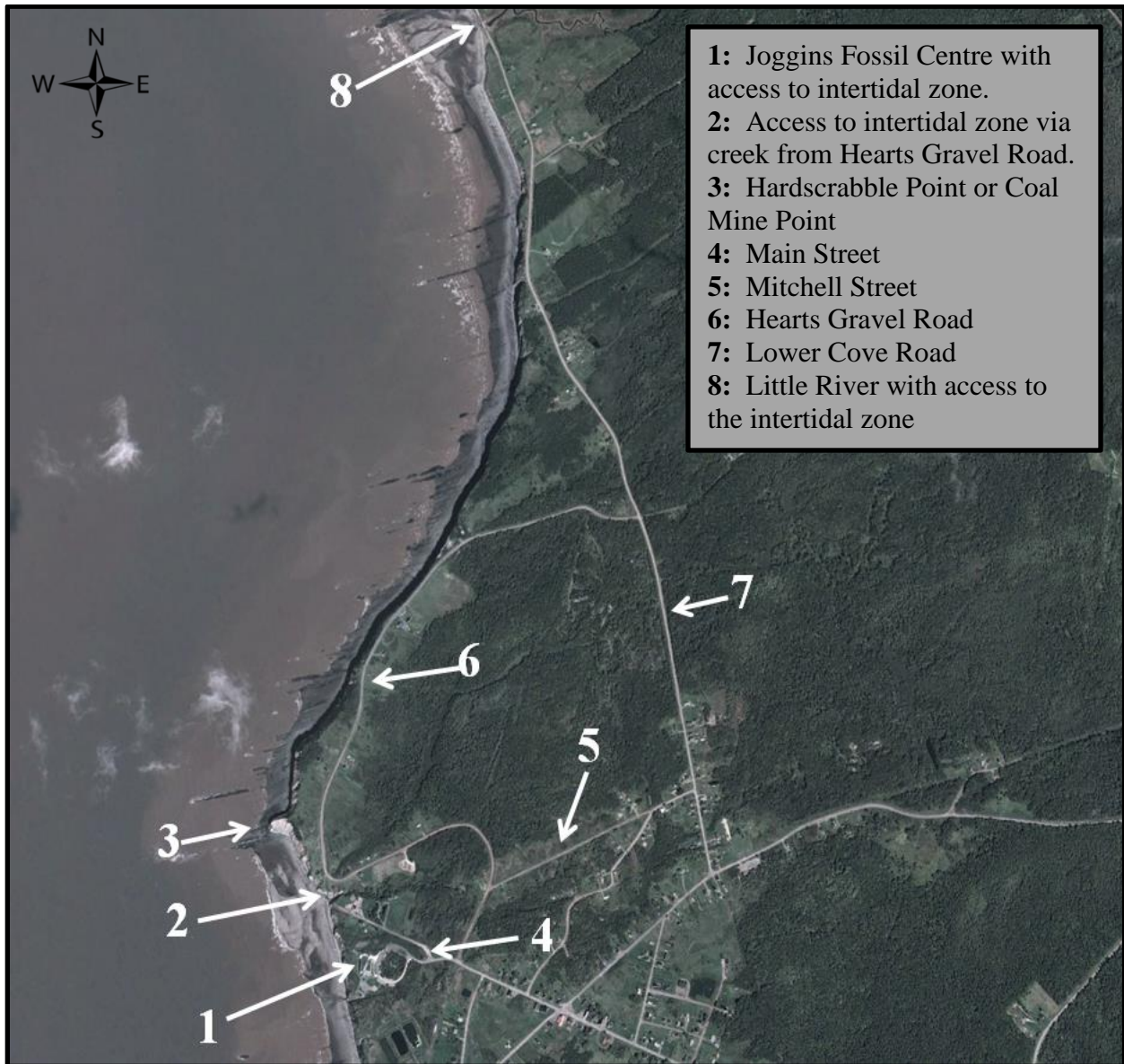


Figure 1-3: Aerial image of the Joggins area showing the three entry/exit points that were used during the two day field trip. The scale is 1 cm = 0.1 km (Google Earth, 2013).

1.6 Bay of Fundy Tides

Since Chignecto Bay is an inlet of the Bay of Fundy, it is subjected to some of the highest tidal variations in the world, which at Joggins can fluctuate approximately 12 m. The lower couple of meters of the Joggins outcrop section may be covered during an unusually high tide. As a result of these tides, it is not possible to perform any field work at the base of the cliff. At low tide however; the waters of Chignecto Bay recede far from the cliff face, allowing field work to be carried out for approximately 6 hours at the most. If coordinated properly, it is possible to work with the falling tide and gain a few more hours of possible field work time. It is very important to check the water location regularly such that sufficient time is available to remove all personnel and equipment from the beach. Some of the equipment, especially the LIDAR, is rather bulky and heavy, so it takes a fair amount of time to pack and remove this equipment from the beach. Fisheries and Oceans Canada provides tidal information that allows for proper planning of field work to be carried out in the area. Field work was carried out on Thursday, May 30th and Friday, May 31st. The high and low tide times can be estimated from Figure 1-4 which shows high and low tide times against height.

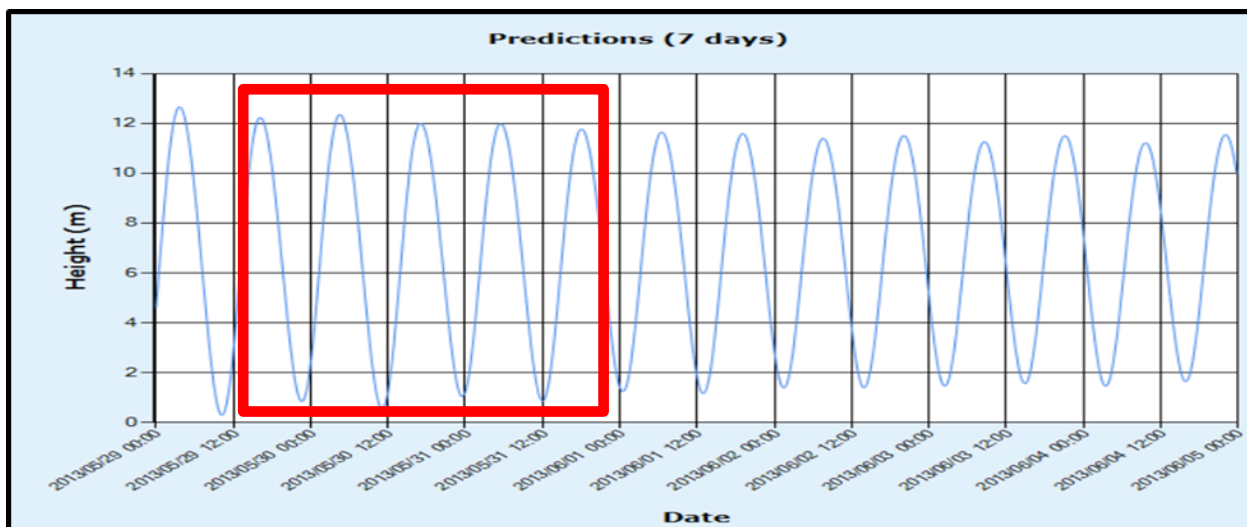


Figure 1-4: Tidal variation chart for the Joggins Wharf from the time period Wednesday, May 29th up to and including June 5th, 2013 (Fisheries and Ocean Canada, 2013). The red box shows the tidal variations during the two field days in which data was collected at Joggins.

1.7 Field Work Safety

During the two days spent in the field at Joggins, the safety of the crew was first and foremost, followed by that of the equipment. The field work that was performed was done so in the intertidal zone and was either performed next to the cliff face or a ways from it. Additionally, field work was carried out above the cliff face. This work entailed a GPR survey. The work that was carried out at the base of the cliff (e.g. permeameter measurements, scintillometer measurements and rock sampling) was the most dangerous due to the instability of the cliff face and the other geo-hazards that existed (Refer to Figure 1-5). It was determined that this work should be done using steel-toed safety footwear, safety glasses and hard hats in the event that rock fragments should fall. It is also suggested that perhaps someone maintain a watchful eye from a distance and inform the cliff base crew of any developments. It is easy to lose track of time while conducting various studies along the cliff section. As a result, the tide can “sneak” up on you fairly quickly. For that reason, it is important to be aware of the water level, especially when a large amount of equipment is being used that must be hiked off the beach. The work to be done on atop the cliff involved a GPR survey. The GPR survey was conducted on various paved and gravel roads that lie atop of the Joggins Formation. As such, it was particularly important to maintain a visual for automobiles. Safety vests were also worn during the GPR survey to increase the likelihood of being spotted by an approaching motorist. Since the community of Joggins is a quiet place, there were only a couple instances where the GPR cart had to be pushed to the shoulder of the road; otherwise, the GPR work was unimpeded. Additionally, first aid kits were brought along and were readily available.



Figure 1-5: Warning sign posted at Joggins near the outlet of Little River showing the three major safety hazards (Wach, 2013).

2.0 Geological Background

2.1 Tectono-Stratigraphic Framework for the Cumberland Basin

The Cumberland Basin is a fairly complex basin which has been tectonically disturbed over geologic time and represents the “welded” zone between the Avalon Terrane in northern Nova Scotia and the Meguma Terrane in Southern Nova Scotia (Ryan and Boehner, 1994). The basin was formed to the north of the east-west trending Cobequid-Chedabucto Fault System and more or less parallels it (Ryan and Boehner, 1994). At the height of sediment deposition in the basin, Ryan and Boehner (1994) believe that sediment thicknesses in excess of 7 km could have existed; however, with the constant erosion over the course of time, the basin is now represented by its structural remnants.

According to Ryan *et al.* (1987), the development of the Cumberland Basin can be divided into three major time spans. The time spans are Late Devonian through to Early Namurian, Late Namurian through to Middle Westphalian and Late Westphalian A to Lower Permian.

2.1.1 Late Devonian through to Early Namurian

The earliest sediment deposition during the initial basin development stages after the Middle Devonian Acadian Orogeny was the placement of the Fountain Lake strata and the Horton Group Strata to a thickness exceeding 4 km (Ryan and Boehner, 1994). According to Boehner *et al.* (1986), a marine incursion during the Visean concluded Horton Group sedimentation, which along with an arid climate, resulted in what Giles (1981) states as being a 1 km thick, cyclical “sequence of saline marine evaporates, fine to coarse red beds, and thin but laterally extensive marine carbonates of the Windsor Group.” Following the Windsor Group deposition was an up to 1.5 km thick package of continentally derived deposits known as the Mabou or Canso Group, which is a composition of red to grey, fine-grained fluvial and lacustrine sediments (Ryan and Boehner, 1994). Therefore, the Late Devonian through to the Early Namurian most likely represents a rapidly subsiding basin with fluvial-lacustrine and continental alluvial sediment deposition; followed secondly by a period of marine carbonate and evaporate

deposition with redbeds and lastly; a period of decreased subsidence with fluvial-lacustrine sediment deposition (Ryan *et al.*, 1987). A diagrammatic sketch of this period of sedimentation is shown in Figure 2-1.

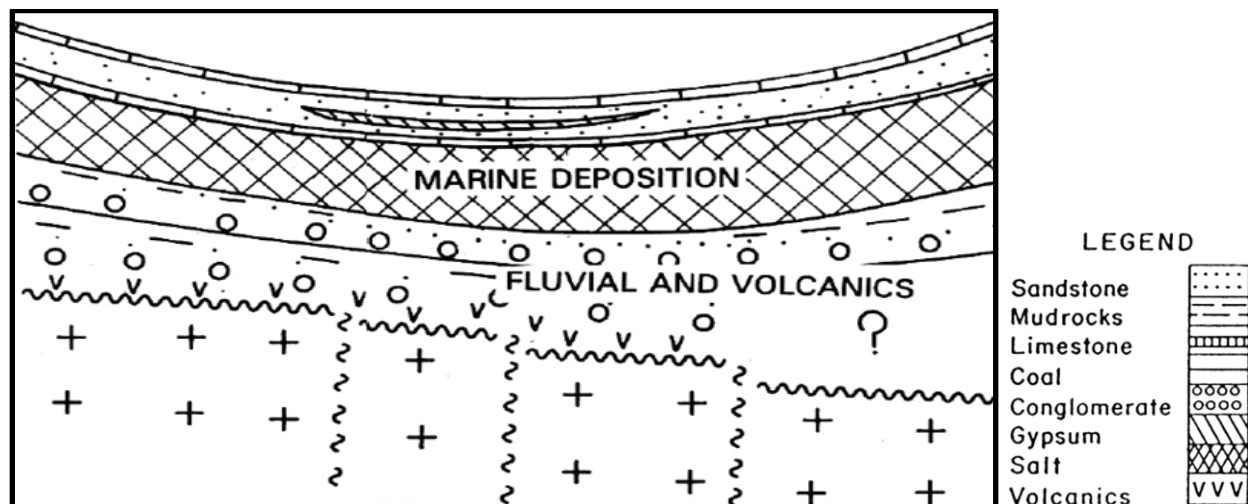


Figure 2-1: Diagrammatic sketch of Devonian through to Namurian sedimentation, where the sedimentation represents the Fountain Lake, Horton, Windsor and Mabou groups of the Cumberland Basin (Ryan and Boehner, 1994).

2.1.2 Late Namurian through to Westphalian A

During this timeframe, the basal portions of the Cumberland Basin were deposited diachronously on top of the Mabou Group, while also containing, in some instances, widespread and thick extraformational conglomerates representing the Claremont Formation (Ryan and Boehner, 1994). Following this deposition, is the deposition of the Boss Point Formation sediments, which are widespread, have a thickness in excess of 1 km and are comprised of grey sandstones and fine-grained red beds (Ryan and Boehner, 1994). Therefore, the Late Namurian through to Westphalian A time period represents uplift and rapid subsidence with respect to the Claremont Formation and a period of much slower, regional subsidence as represented by the mudstone and sandstone lithologies of the Boss Point Formation (Ryan and Boehner, 1994). A diagrammatic sketch of this period of sedimentation is shown in Figure 2-2.

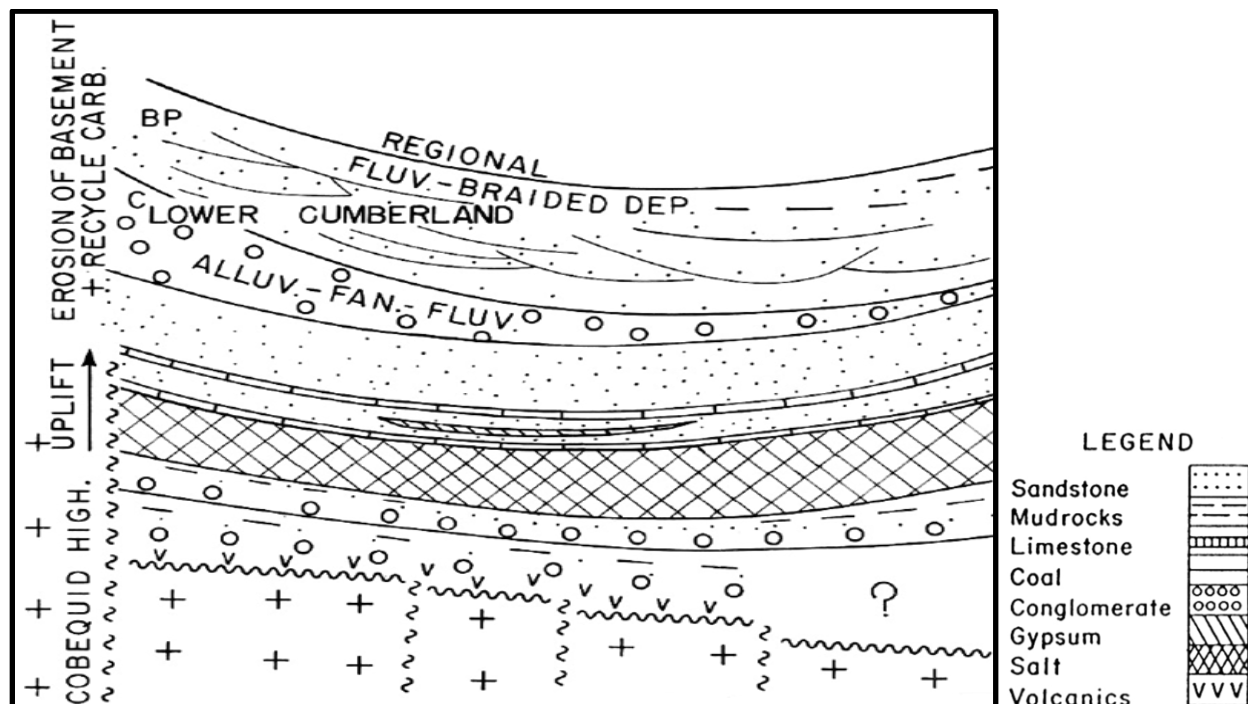


Figure 2-2: Diagrammatic sketch of Devonian to Westphalian A sedimentation, where the sedimentation represents the Boss Point and Little River formations of the Cumberland Basin (Ryan and Boehner, 1994).

2.1.3 Late Westphalian A through to Lower Permian

During this period of time, the Boss Point Formation strata became overlain, both conformably and disconformably by younger Cumberland Group strata (Ryan and Boehner, 1994). The younger, upper portions of the Cumberland Group are generally restricted to the deeper downward trending portions of the western Cumberland Basin or are absent altogether (Copeland, 1959; Ryan *et al.*, 1987). Ryan and Boehner (1994) state that during this timeframe, alluvial fan deposition occurred at least three times, representing uplift of the highland areas and subsidence of the basinal area with the development of widespread drainage systems within the highlands. With the development of these drainage systems, the various fluvial channel systems developed along with some minor lacustrine facies. The Joggins Formation represents the meandering fluvial channel system that developed as a result of the extensive highland drainage systems that developed during this time interval. A diagrammatic sketch of this period of sedimentation is shown in Figure 2-3.

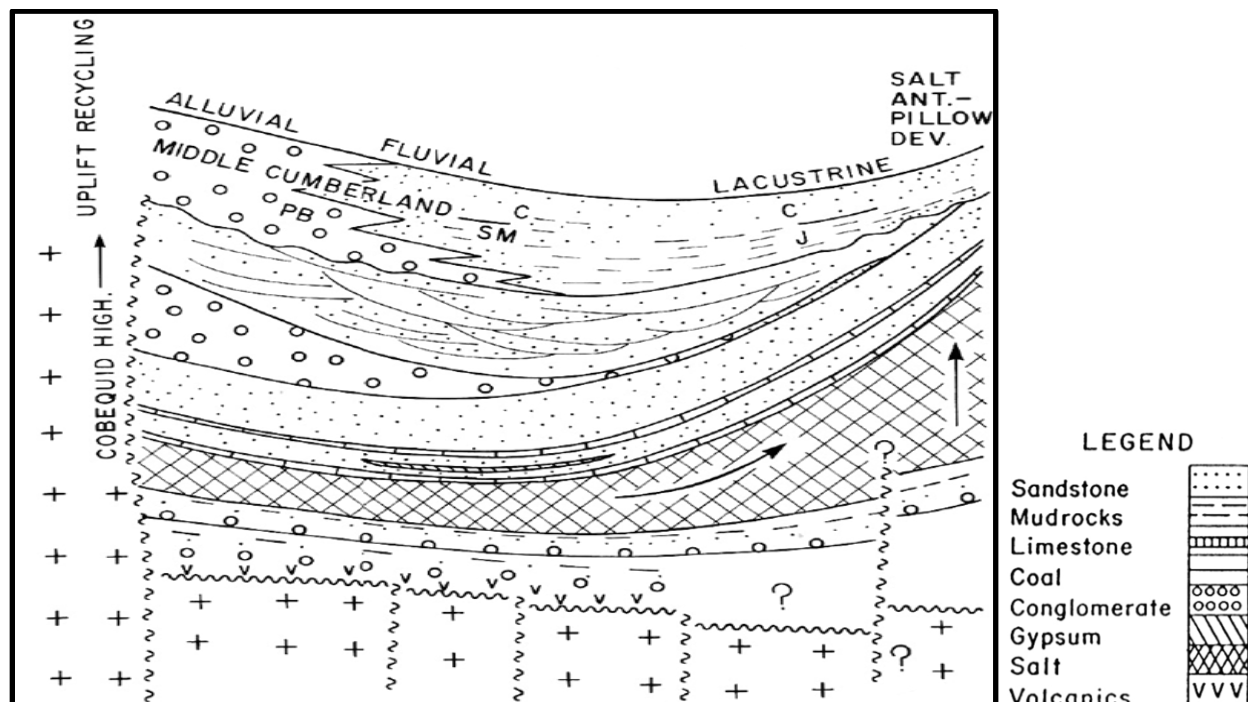


Figure 2-3: Diagrammatic sketch of Devonian to middle Westphalian sedimentation, where the sedimentation includes the Polly Brook, Joggins and Springhill Mines formations of the Cumberland Basin (Ryan and Boehner, 1994).

2.2 Tectonic Setting

The Cumberland Basin is an approximately 3,600 km² area of deposited sediments that is bounded by faults (Ryan *et al.*, 1987). Covering large tracts of northwestern Nova Scotia and to a much lesser extent, areas of southern New Brunswick, the Cumberland Basin is situated between the Caledonia Highlands to the north and the Cobequid Highlands to the south (Ryan and Boehner, 1994). Browne and Plint (1994) have stated that the margins of the Cumberland Basin are defined by the North Fault to the south, the Caledonia-Dorchester Faults to the north and the Harvey-Hopewell Fault to the west; while Martel (1987) suggests the northwestern extents may be delineated by a basement horst along the Hastings Fault.

Internally, the basin is a compositional series of synclines, namely the Athol, Tatamagouche, Scotsburn, Amherst and Wallace synclines, along with two diapiric anticlines known as the Claremont/Malagash and Minudie anticlines (Ryan and Boehner, 1994). According to Ryan and Boehner (1994), the structural features contained within the Cumberland

Basin are related to basin development and growth features such as growth faults, strike-slip faults and major synclines that are either not related or are indirectly related to evaporate tectonics, in addition to salt structures such as diapirs, domes, diapiric anticlines and salt movement-related folds and faults. In addition, joint and thrust faults pertaining to buried uplift blocks can also occur as structural features within the basin.

The Joggins Formation, which is the formation of interest within the Cumberland Basin, occurs along the northern limb of the Athol Syncline, which also happens to be the dominant structural feature to occur in the basin and has been approximated to be some 25 km wide by 75 km long (Rygel, 2005). The Athol Syncline, as stated by Calder (1994), can be found occurring between the Minudie Anticline to the north, the Athol-Sand Cove Fault zone to the south and the Back River Diapir to the east. Evidence seems to suggest that salt body movement was syndepositionally-related and aided in the creation of the accommodation space that was necessary in the basin (Waldron and Rygel, 2005). Perhaps the best evidence for this is that the stratal units thin and pinch against the diapiric structures.

2.3 Stratigraphy

The Cumberland Group is a compilation of nine formations that are late Carboniferous Period (358.9 – 298.9 M.A.) in age (Rygel, 2005). These nine formations, youngest to oldest, as per Rygel (2005) are as follows;

1. Ragged Reef Formation
 2. Malagash Formation
 3. Salisbury Formation
 4. Springhill Mines Formation
 5. Polly Brook Formation
 6. Joggins Formation
 7. Grand Anse Formation
 8. Little River Formation
 9. Boss Point Formation
- } Undivided; grouped together and called the upper Cumberland Group.

According to Ryan and Boehner (1994), the type area for the Cumberland Group is located in the Joggins and Springhill coalfields on the western margins of the Cumberland Basin, Cumberland County, Nova Scotia. Figure 2-4 shows the geological map of the western Cumberland Basin showing the relationships between the nine Cumberland Group formations. The type section is a lengthy outcropping that occurs along the southeastern shores of Chignecto Bay, stretching from Downing Cove some 6.5 km north of Joggins to Squally Point, some 51 km to the southwest of Joggins with the most complete and continuous section occurring between Sand Cove and Lower Cove (Ryan and Boehner, 1994).

The Joggins Formation has been estimated to be 2.8 km thick at Joggins; though it may be thicker in the interior of the Cumberland Basin or more specifically, the central portion of the Athol Syncline (Davies *et al.*, 2005; Ryan and Boehner, 1994). In the eastern and southern extents of the Cumberland Basin, however; it is assumed that the Joggins Formation thins out due to its absence from the Tatamagouche Syncline area (Refer to Figure 2-4).

At the type section locality, the Joggins Formation is conformable with the underlying Boss Point Formation, whereas in the eastern and southern portions of the Cumberland Basin, it is conformable with the underlying Polly Brook Formation (Ryan and Boehner, 1994). The Springhill Mines Formation conformably overlays the Joggins Formation.

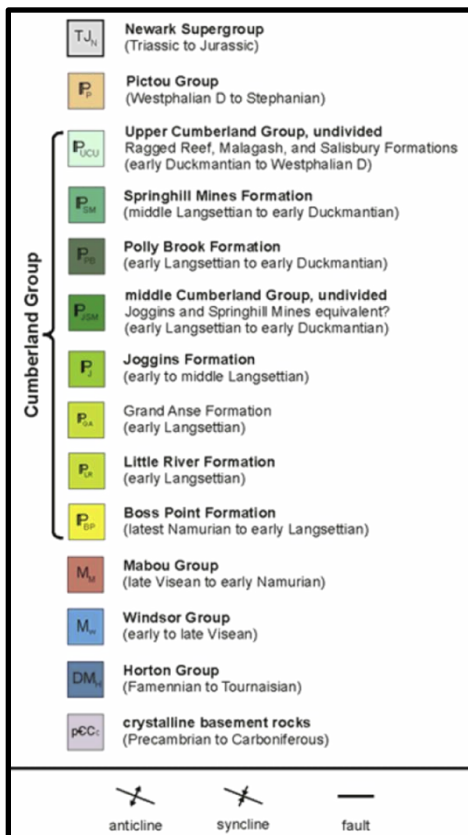
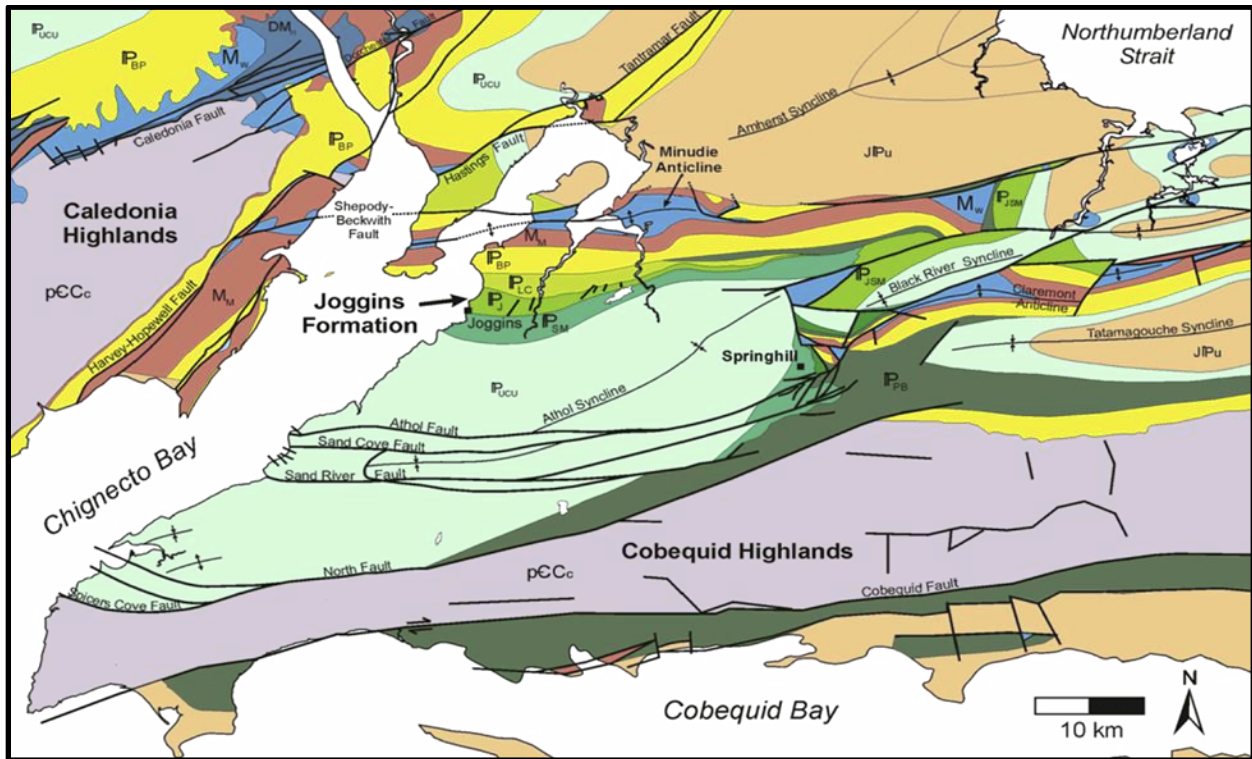


Figure 2-4: (A); Geological map of the western Cumberland Basin showing major basinal structures within the basin as well as the location of the Joggins Formation (Rygel, 2005). (B); The accompanying legend and stratigraphic column (Rygel, 2005).

3.0 Meandering Fluvial System

To allow for logical deductions and interpretations to be made with respect to the Joggins Formation depositional environment during the Carboniferous Period, the sedimentary processes by which it was formed must be understood. In determining the most likely depositional environment for the Joggins Formation, a vast amount of literature was reviewed. The consensus is that the Joggins Formation represents a fluvial meanderbelt system, which is proven by applying the knowledge of rock lithologies and sedimentary structures that can be seen in modern systems to ancient systems. This is further reinforced by the examination of the cliff face at Joggins as well as the other research that was conducted in the area. There are some 14 meandering channel bodies in the Joggins Formation outcrop, with the most prevalent and of particular interest for this project being the channel body represented by Coal Mine Point / Hardscrabble Point (Rygel, 2005).

3.1 Meandering Fluvial Channel Deposits and Facies

A meandering fluvial system is generally characterized as having a sandy bedload in which the migrating channel is narrow and deep with relatively thick sand bodies occurring in the channel (Miall, 2010; Davies *et al.*, 1992). The meandering channel is a result of the lateral migration of the system (Refer to Figure 3-1; B) and is caused by the erosion of the outer bank sediments and the subsequent deposition of said material on the inner bends of the channel (Deschamps *et al.*, 2011). The continual erosion and deposition of sediments gives the meandering channel a profile that is steepest on the outside bend and shallows to a gradual slope on the inside bend. According to Trenhaile (2010), meandering fluvial systems are low in gradient, have a very well-formed and distinct floodplain and have their primary sediment load transported in suspension, with lesser amounts transported as bed load. Meandering channel deposits, as a direct result of their hydrodynamic characteristics, are heterogeneous and can vary in their morphology over relatively short distances (Davies *et al.*, 1992).

Meandering fluvial systems are typically contained within the lower margins of the craton, which is the older and more stabilized section of the continental lithosphere and are

generally preserved as a result of aggradational coastal sequences or as a result of basinal subsidence (Prothero & Schwab, 2004). Meandering fluvial systems are known to grade upstream into a braided fluvial system and to grade downstream into a deltaic system (Prothero & Schwab, 2004). In addition, meandering channel systems are associated with floodplain muds and lake deposits.

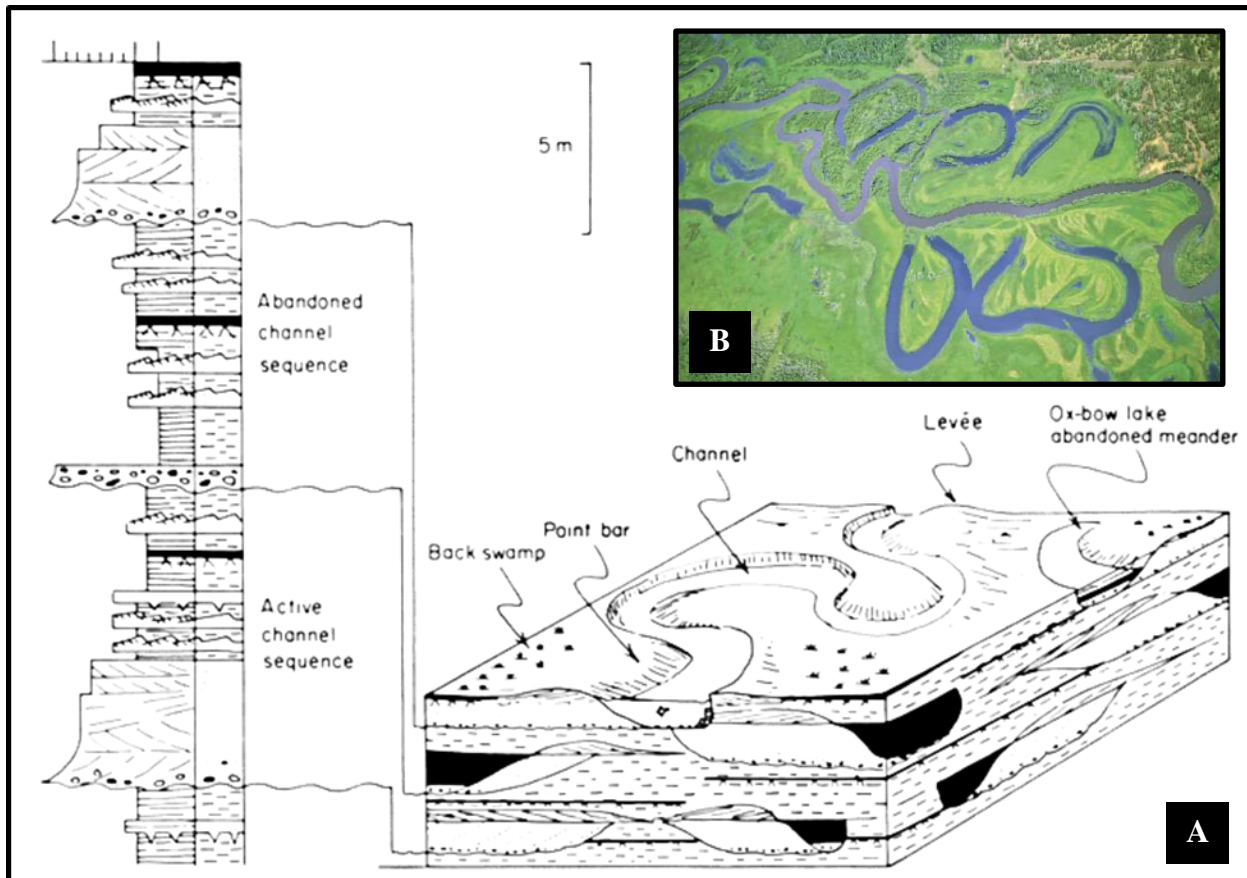


Figure 3-1: (A); Illustration showing the deposits and physiography of a meandering channel complex (Selley, 2000). Inset (B); Aerial photograph showing a present-day meandering channel system (Charlton, 2008).

The sedimentology of a meanderbelt system can range from coarse channel-lag gravels down to very fine grained muds associated with the adjacent floodplain (Refer to Figure 3-1; A). Point-bar sands that have been laterally accreted show sedimentary structures that are reminiscent of a decreasing flow velocity; these structures being trough cross beds, ripple cross-lamination and plane beds (Prothero and Schwab, 2004). The floodplain muds on the other hand

are vertically accreted and finely laminated and typically show climbing ripple patterns, mudcracks, raindrop impacts, fossils, soil horizons and organic matter. The meander channel bodies at Joggins have a specific grain size of fine- to medium-grained sandstone along with mudstone and intra-formational conglomerate (Rygel, 2005).

There are numerous facies that are associated with a meandering fluvial system, and thus; can be used as diagnostic indicators when determining a depositional environment. These meandering channel facies, including those that are the result of meandering-river systems are listed by Sumner (2008);

- (1) scoured base,
- (2) lag deposits with mud rip-up clasts,
- (3) fining upward sequence of sands containing trough cross-stratification,
- (4) ripple marks in sand, and;
- (5) sigmoidally-shaped cross stratification as a result of migrating point bars.

Table 3-1: Possible meander channel facies that occur or could occur at Joggins.

<p>(1) Scoured base</p>	 A photograph of a rock outcrop showing a scoured base contact. A white curved line is drawn across the base of the outcrop, highlighting the irregular, eroded surface where the upper sandstone layers meet the lower, darker layers.	<p>Photograph showing an example of a scoured base contact at Joggins, Nova Scotia (Plummer, 2013).</p>
-----------------------------	---	---

Table 3-1: Continued...

<p>(2) Lag deposits with mud rip-up clasts</p>		<p>Photograph showing examples of mud rip-up clasts in a fluvial formation (Ranney, 2009). This photograph was not taken at Joggins.</p>
<p>(3) Fining upwards sequence of sands containing trough cross-stratification</p>		<p>Photograph showing examples of trough cross-stratification (Sumner, n.d.). This photograph was not taken at Joggins.</p>
<p>(4) Ripple marks in sand</p>		<p>Photograph showing examples of ripple marks in sandstone at Joggins (Duff, 2013).</p>

Table 3-1: Continued...

<p>(5) Sigmoidally-shaped cross stratification as a result of migrating point bars</p>		<p>Photograph showing an example of cross stratification in sandstone at Joggins, Nova Scotia (Wach, 2013).</p>
--	--	---

The related flood plain facies include:

- (6) fine sand with climbing ripple marks,
- (7) mudstones and shales with mud cracks, and;
- (8) soils
- (9) root casts

Table 3-2: Facies that can be expected in the floodplain of a meander channel system.

<p>(6) Fine sand with climbing ripple marks</p>		<p>Photograph showing examples of climbing ripples (Cope, n.d.). This photograph was not taken at Joggins.</p>
---	--	--

Table 3-2: Continued...

<p>(7) Mudstones and shales with mud cracks</p>		<p>Photograph showing mud cracks in a mudstone sample at Joggins, Nova Scotia (Plummer, 2013).</p>
<p>(8) Soils</p>		<p>Photograph showing an example of floodplain soils (Lorz and Makeschin, 2012). This photograph was not taken at Joggins.</p>
<p>(9) Root casts</p>		<p>Photograph showing an example of numerous root casts in a fallen block of sandstone at Joggins (Dennar, 2012).</p>

The related oxbow lake facies include:

- (10) mudstones and/or shales without mud cracks
- (11) organic-rich deposits, such as coal, and;

- (12) anoxic related water indicators.

Table 3-3: Oxbow lake facies that can be expected in a meander channel system.

<p>(10) Mudstones and/or shales without mud cracks</p>		<p>Photograph showing shale layers (Lapoix <i>et al.</i>, 2011). This photograph was not taken at Joggins.</p>
<p>(11) Organic-rich deposits, such as coal</p>		<p>Photograph showing a relatively thick coal seam at Joggins, Nova Scotia (Haynes, 2013).</p>
<p>(12) Anoxic-related water indicators</p>		<p>Photograph showing an example of anoxic conditions (grey/green colour) in mudstone at Joggins, Nova Scotia (Wach, 2013).</p>

Within individual meander channel bodies, there are various lithofacies that occur. According to Rygel (2005), these lithofacies are ripple cross-laminated sandstone, trough cross-bedded sandstone, low angled laminated sandstone, horizontally laminated sandstone, laminated mudrock and massive mudrock.

3.2 Geometry and Structural Elements

As fluvial processes continually alter the fluvial channel bodies and associated facies over time, distinct 3-D forms are generated. The characteristics of meandering fluvial channel bodies in the geological record have been compiled by Gibling (2006) and show distinct features. The thickness of meandering fluvial channels within the geological record ranges from thin to thick (1 – 38 m) with an average range between 4 – 20 m; whereas their width can range from narrow to very wide (30 m – 15 km) with the majority being less than 3 km with an average range between 0.3 – 3 km (Gibling, 2006). The width to thickness ratio (W/T), according to Gibling (2006) ranges from between broad ribbons to broad sheets (7 – 940) with the majority being less than 250 and the average range being between 30 – 250. A width versus thickness plot showing where the Joggins Formation meander channel bodies would plot in relation to other in the geological record is shown in Figure 3-2. Dealing specifically with the meander channel bodies at Joggins, the 14 bodies have a thickness that ranges from 1.8 m to 10.5 m for Coal Mine Point / Hardscrabble Point with width to thickness ratios between 11.8 and 63.9 (Rygel, 2005).

A meandering channel can have either single story bodies or multi-story bodies in which lateral-accretion sets are prominent, specifically as point-bar deposits and the tops of these single or multi-story bodies typically display scroll bar forms, accretionary ridges and chute channels; while the base can contain bedform sheets (Gibling, 2006). The meander channel bodies at Joggins are almost exclusively single storied bodies with flat bases and laterally accreted fills as portrayed in Figure 3-3 (Rygel, 2005). Abandoned channels typically contain sand with lesser amounts of gravel than in storied channels, occur as a sequence of fining upwards sediments (Gibling, 2006). There also exists the possibility of these channel bodies containing tidally influenced structures as well.

The Coal Mine Point / Hardscrabble Point meandering channel body, due to its increased size when compared to the other meander channels at Joggins, probably represents a river channel that was an acceptor of numerous other smaller channels (Rygel, 2005). Thus, Coal Mine Point / Hardscrabble Point was most likely a major drainage channel for the surrounding area.

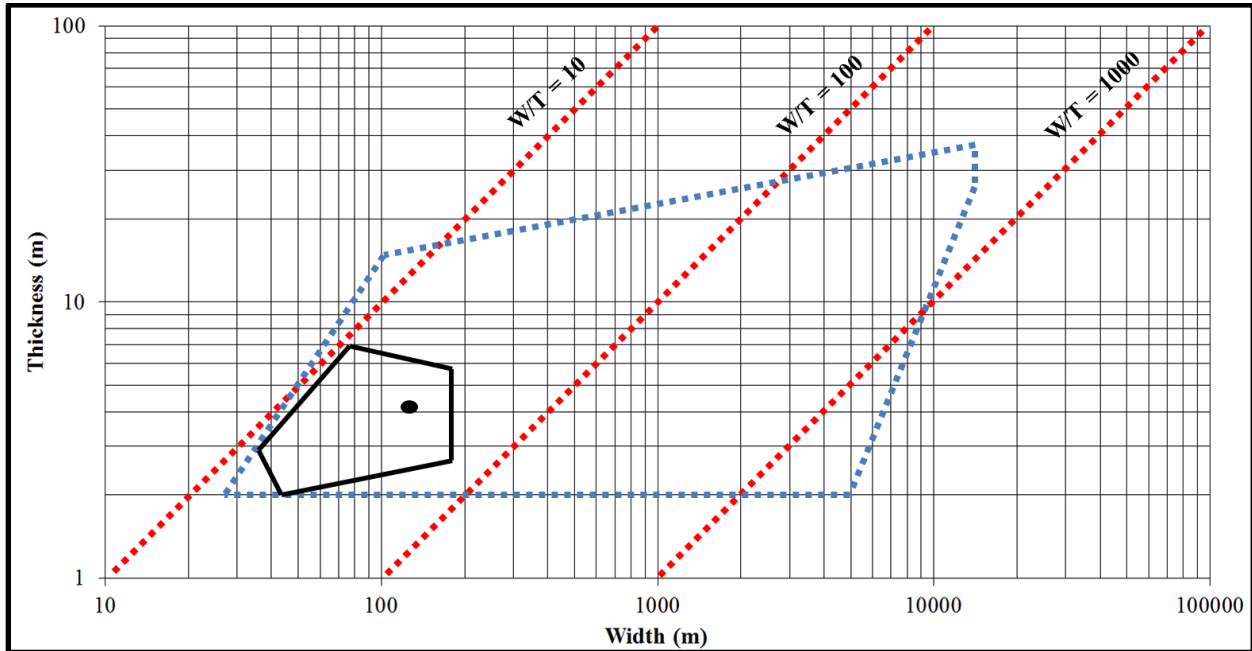


Figure 3-2: Width versus thickness plot for the Joggins Formation meandering channel system (black outlined area). The average width to thickness value plots at the black point. The blue outlined area represents where other meandering channel systems in the geological record would plot (modified from Gibling, 2006).

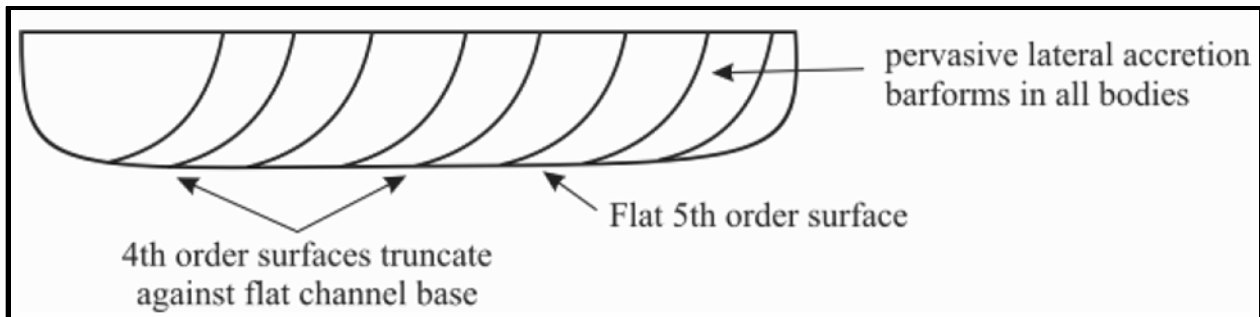


Figure 3-3: Meandering channel body type as applied to the meander channels at Joggins (Rygel, 2005).

4.0 Research Methods

Numerous research and data collection methods were applied during the course of this project in order to generate and provide the relevant and necessary data to allow for the progression of this project. The research methods that were used were a handheld permeameter, handheld gamma-ray spectrometer, ground penetrating radar (GPR), light detection and ranging (LIDAR), rock sampling and thin sections. The GPR and LIDAR surveys both utilized a differential global positioning system. The goal is that by integrating all of this data together, a fairly comprehensive understanding of the performance and architecture will be gained.

4.1 Light Detection and Ranging (LIDAR)

4.1.1 Data Collection

The LIDAR data was collected over the period of two days, May 30th and May 31st of 2013. On May 30th, an all-terrain vehicle was used to transport the LIDAR equipment from the outlet of the Little River along the intertidal zone to the location of the Fundy Forest. On May 31st, two scans were performed. The first was the area from Hardscrabble Point to the steps leading from the Joggins Fossil Centre to the intertidal zone. The second scan was performed on the Lower Cove side of Hardscrabble Point. The scans on May 31st required that the equipment be carried to its location by hand from Hearts Gravel Road, down the creek and onto the intertidal zone. Scan 1 on May 30th used a 20 mm resolution and scanned approximately 650 m of the cliff face. Scans 2 and 3 on May 31st used 10 mm and 15 mm resolutions respectively and scanned approximately 650 m and 235 m of the cliff face respectively.

4.1.2 Background

The LIDAR survey used an Optech Incorporated ILRIS HD LIDAR unit with a scan speed of 2.5 kHz as pictured in Figure 4-1. A highly versatile tool for the remote collection of data, LIDAR shares a multitude of similarities, including its data collection procedure, to that of Radio Detection and Ranging or RADAR for short (Rafuse, 2011). The major difference

between the two is that RADAR operates within the microwave and radio frequency bands; whereas LIDAR on the other hand, operates within the ultraviolet, visible, and near infrared spectrum (Rafuse, 2011). LIDAR imaging is performed by bombarding a surface with a laser pulse and measuring the subsequent gap in time between the emission of the initial pulse and the detection of the returning signal. In the case of the survey performed at Joggins, the laser pulse is emitted from the stationary LIDAR unit millions of times in order to gather the data required for the predetermined scan area.

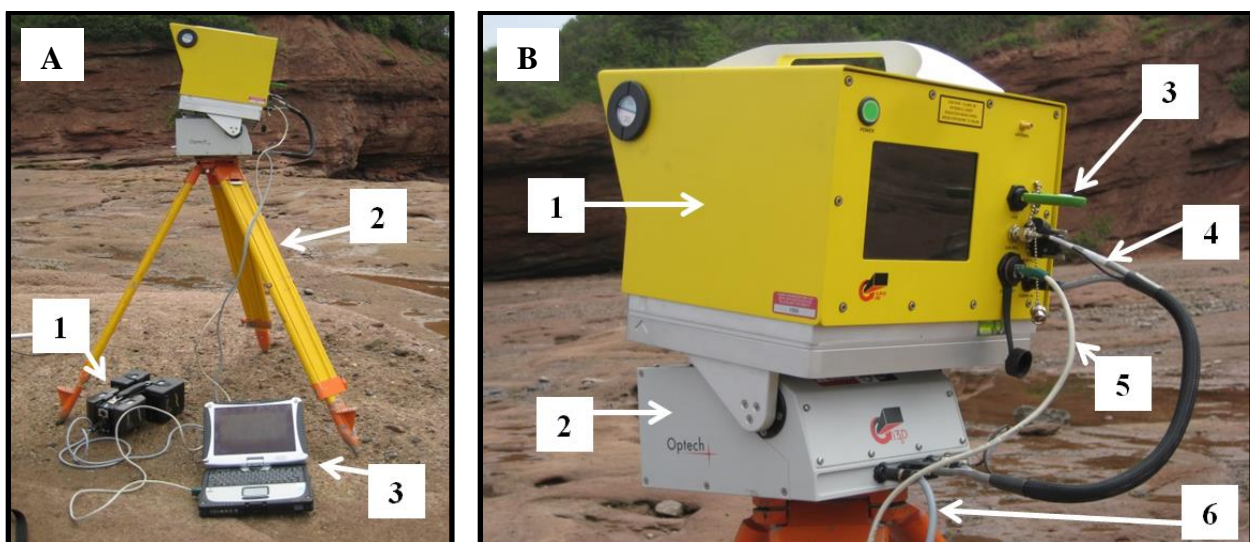


Figure 4-1: Left (A); image of the LIDAR system setup showing the batteries and holder (1), the tripod (2) and the laptop computer (3). Right (B); closer view of the LIDAR system showing the LIDAR unit (1), the pan/tilt base (2), a USB flash drive for saving the data (3), the pan/tilt cable (4), the Ethernet network cable (5) and the power cable going to the battery holder (6).

According to Rafuse (2011), for a reflection to be obtained, the rock being bombarded by the laser pulses must be of the type which produces a dielectric discontinuity, thereby allowing the original wave to be reflected back to the source. This property is what makes LIDAR the clear choice over RADAR for this particular application. If you consider that when a metallic object of significant dielectric discontinuity contrast compared to the surrounding environment is bombarded by RADAR wavelengths, the resulting reflections will be of very high quality (Rafuse, 2011). As a result, RADAR is used for various applications such as aircraft tracking and a multitude of other civilian- and military-related applications. A rock surface on the other

hand will typically not exhibit a significant dielectric discontinuity contrast over its surface, which is why LIDAR wavelengths must be used (Rafuse, 2011). The range of LIDAR wavelengths can vary from 10 micrometer to 250 nanometers range and are of sufficient resolution to strike surfaces grouped together by RADAR; thereby creating backscatter. Backscatter is defined as the diffuse reflection of waves back towards the transmitter/receiver such that when processed, can generate a highly detailed image (Optech ILRIS User Manual, 2009).

The collection of data via LIDAR is advantageous in many ways; with perhaps the most significant being that the data points are represented spatially and with respect to all other data points; meaning that a point cloud can be generated in which millions of points can be displayed, all with their own unique X, Y and Z coordinates (Rafuse, 2011; English Heritage, 2010). This feature is what makes LIDAR more appealing than high resolution photography; the LIDAR unit performs time corrections on the incoming data to ensure that distance offsets are taken into account, thereby eliminating the distortions that are the norm for digital photographs (Rafuse, 2011). According to Rafuse (2011), “a digital photograph operates on theoretically similar principles of reflectance values representing a physical image”; the limitation being that the sensor in a digital camera only collects data without the ranging capability of LIDAR. However, since LIDAR does have ranging capabilities, reflectance values that are used to produce an image are spatially allocated with reference to a base station.

Prior to the commencement of a scan, there are numerous unit positioning conditions that must be accounted for. Since LIDAR does not have the ability to wrap around or penetrate objects, LIDAR placement becomes a critical task to the success of a scan. For simplicity, the LIDAR scanner is analogous to a flashlight in that protrusions will prevent the beams of light, or in the case of the LIDAR, the laser pulses from seeing the details behind them. At Joggins, the cliff section contains large boulders, coves, old mine workings, points and large intertidal zone features. These features, along with the length of the Joggins section prevent it from being imaged in one scan. Figure 4-2 depicts how the placement of the LIDAR system can result in un-imaged zones. In reality, 10 scans (?) or more may be required to completely image the Joggins section.

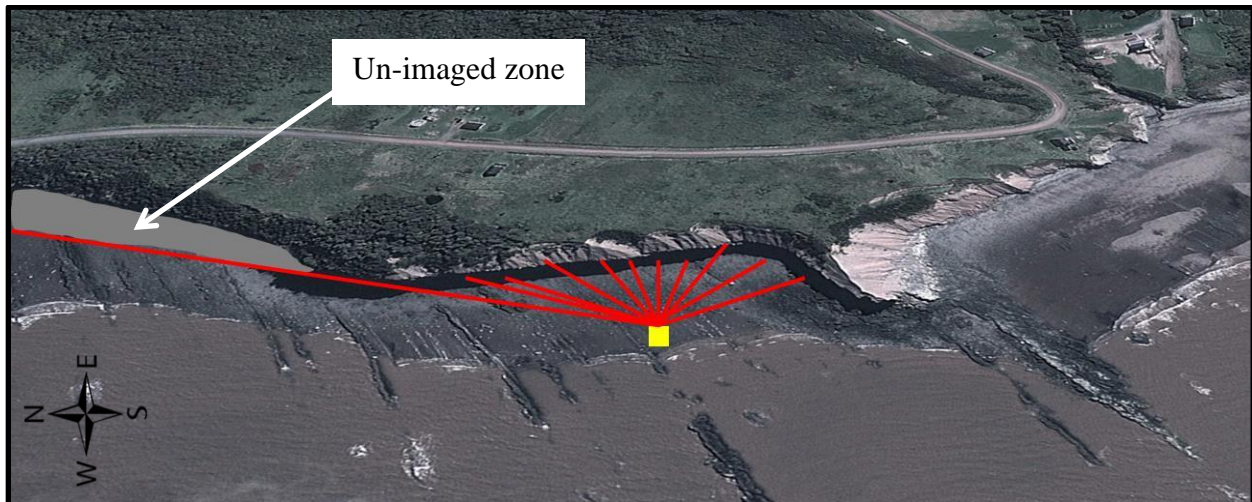


Figure 4-2: Image demonstrating the placement limitations of the LIDAR unit. The positioning of the LIDAR unit is similar to that of the third scan at Coal Mine Point/Hardscrabble Point. With this configuration, the beams (red lines) from the unit (yellow square) are unable to capture points behind the small protruding headland, resulting in an un-imaged zone (shown in grey). Scale is 1 cm = 35.5 m (Google Earth, 2013).

These un-imaged areas can be imaged by simply repositioning the entire LIDAR unit in such a way so as to capture the area of interest. In order to properly merge all of the scans together as one cohesive image, georeferencing targets must be used. A successful LIDAR scan must incorporate at least three targets and they must be placed at varying X, Y and Z locations such that triangulation can be performed and accuracy is maximized. Ideally, when using three targets, one would be placed at the top of the section and the remaining two would be placed a distance on either side of the LIDAR unit. The targets are “homemade” and consist of a piece of plywood cut into a square with an outer area covered in black, retro-reflective paint and an inner circle that is white and non-reflective. The targets are placed in such a way that the black outer area and white inner circle face the LIDAR unit. When these targets are imaged by the LIDAR unit, they return a distinct signature that when combined with the differential GPS readings of the centers of the white inner circles allows for the scans to be georeferenced (Rafuse, 2011). It is estimated that the use of the three targets allows for accuracies in the range of +/- 3 cm.

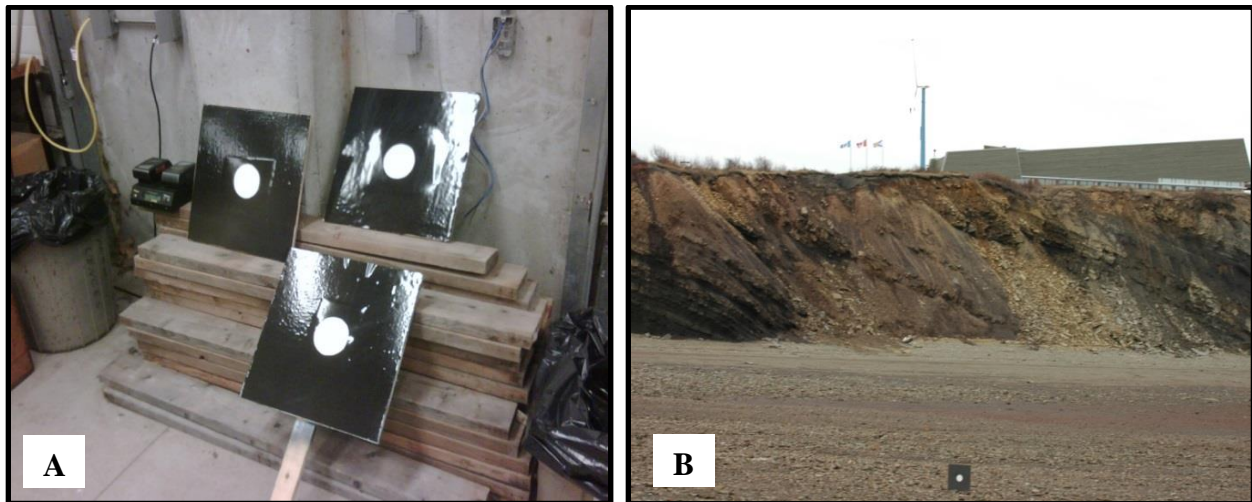


Figure 4-3: Left (A); image of the LIDAR georeferencing targets that are placed at varying X, Y, and Z coordinates in front of the cliff face portion to be scanned (Rafuse, 2011). Right (B); image showing the placement of one of the georeferencing targets with the cliff and the Joggins Fossil Centre in the background (Rafuse, 2011).

With the LIDAR unit fully assembled, as shown in Figure 4-1, the first task is to acquire a 360° panoramic image at that setup location, which it performs in 10, 36° intervals. This initial photograph is essential prior to the commencement of the scan because it allows for the user to determine if the targets are visible as well as if the area of interest is within the scan area. The first 360° photograph revealed that the top portion of the cliff section was not within the scan window. As a result, the unit had to be tilted upwards slightly in order to image the section from top to bottom and the 360° panoramic image had to be recaptured. This initial photograph also allows the user to determine whether the brightness settings for the built-in camera are sufficient to allow the user to be able to see the image. Camera settings can be adjusted to acquire photographs in full sunlight all the way to completely overcast skies. It may still be required that an umbrella be used to shelter the laptop and the LIDAR unit screen to allow the user to be able to see the images presented.

Assuming the preliminary photograph is satisfactory, the blue box that appears on the screen can then be manipulated to constrain the scan area (Figure 4-4). This step is important because it allows the user to include certain areas, while excluding other areas; thereby eliminating irrelevant or excessive points and reducing the overall scan time. The final step before the scan can be started is to set the resolution of the scan. While millimeter resolution is

certainly possible, the tides must be considered and if an all-terrain vehicle is made available, then the amount of time the operator is willing to stay must also be taken into account. As a result, the Joggins scans had different resolution as mentioned in the previous section. While a millimeter scan may be the desired resolution, it is probably not feasible, safe nor required.

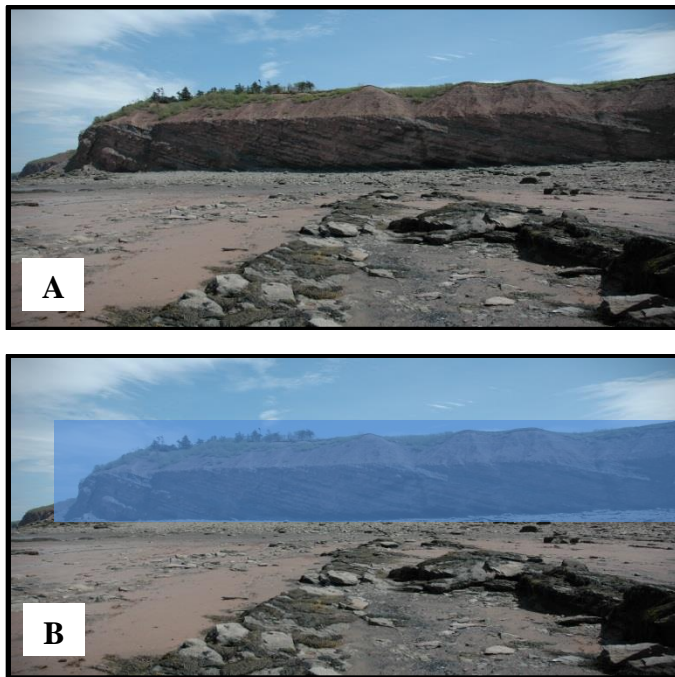


Figure 4-4: The top (A) image is similar to the image captured by the ILRIS unit during its 360° panoramic scan of the Hardscrabble Point area. The bottom (B) image is the same as that above, but the user-defined blue box shows that area that the ILRIS unit will scan. The unit will not scan outside of the user-defined area; thereby minimizing the amount of erroneous data points (e.g. intertidal zone and sky) collected (Wach, 2013).

4.1.3 Data Processing

Originally, parsing was done such that every point was included in the point cloud; however, trying to work with the large volume of points in ArcGIS proved extremely problematic. The purpose for using ArcGIS software was to georeference the LIDAR data to ensure that the point clouds were not simply “floating in space”. In some cases, the point clouds would display satisfactory; in other cases, the program would crash and in some instances, only part of a task was completed. Wait times, as much as 45 minutes, were also a major inconvenience as they restricted working time. To overcome the problems related to the voluminous data, it was decided the best option would be to re-parse the data; except this time a shot reduction factor of 50 % would be applied, meaning half of the points collected would be removed. This, along with deleting the irrelevant points, such as the intertidal zone, vegetation

and structures, allowed for georeferencing to finally be completed. A detailed document regarding the steps taken to parse and georeference the LIDAR data can be seen in Appendix X. The workflow shown in Figure 4-5 documents the major steps involved in obtaining a fully georeferenced suite of data.

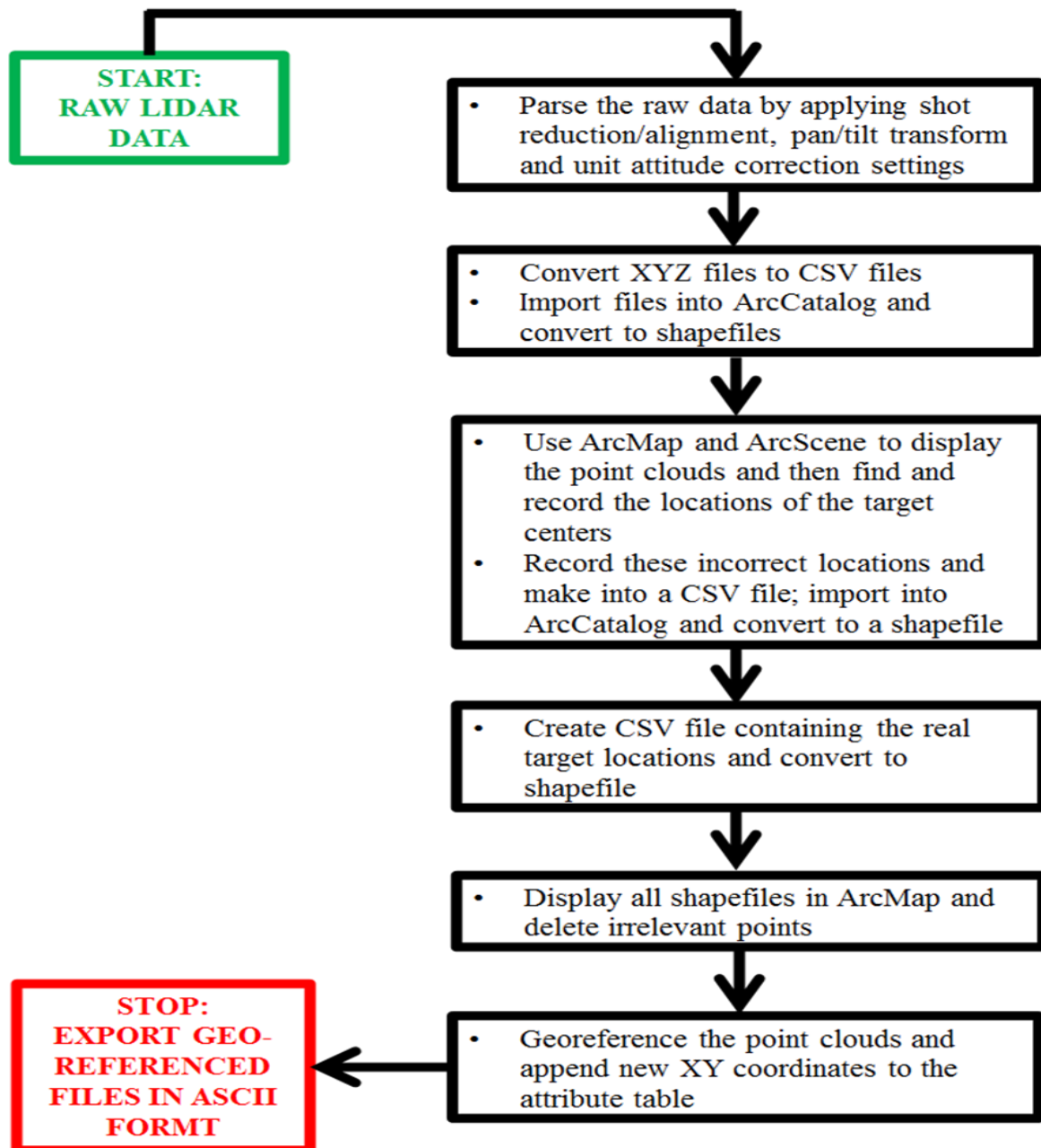


Figure 4-5: Simplified processing workflow that was applied to the raw LIDAR data.

4.2 Ground Penetrating RADAR (GPR)

4.2.1 Data Collection

The GPR data was collected on May 31st, 2013. GPR surveys were conducted at the end of the day on May 30th, but these surveys were short and were done so as a test to determine what the reflectors would look like. GPR data was gathered using a Sensors and Software Incorporated pulseEKKO PRO SmartCart as pictured in Figure 4-6. The survey conducted on May 31st consisted of 48 lines for a total distance of 3.7 kilometers over the Joggins Formation. Over that distance, a total of 8,800 traces were recorded between elevations of 16.97 and 47.47 meters above sea level. The majority of the survey lines were conducted on road surfaces, namely Hearts Gravel Road, Mitchell Street and Main Street. A handful of survey lines were performed on fields and grassy areas as well. A total of 44 GPR lines were done using the 50 MHz antennae and their associated parameters with the remaining 4 lines done using the 200 MHz antennae and their associated parameters.

4.2.2 Background

The GPR survey at Joggins will use the electromagnetic energy reflection profiling technique known as the common offset survey method (refer to Figure 4-7), also known as the optimum offset method (Burger *et al.*, 2006). The common offset method is one of the most popular reflection profiling techniques used for GPR studies with the equipment consisting of a single transmitting antenna and receiving antenna at a predetermined fixed spacing (Neal, 2004). In addition, the two antennas have the same directional orientation and are perpendicular to the survey lines (Neal, 2004). According to Neal (2004), the antenna configuration previously described is known as co-polarized, perpendicular broadside survey geometry. For the survey to occur, the antennas are secured to the cart and are dragged along the ground surface. The horizontal distances travelled by the cart are measured using the on-board odometer, which functions as the triggering device (Vaughan, 2011).



Figure 4-6: Image of the Sensors and Software, Inc. GPR SmartCart. The various parts of the SmartCart are highlighted (Sensors and Software, Inc., 2013).

As the equipment is pushed and the subsequent data points are recorded during the survey, sequential reflection traces are gathered and staked side by side to build a RADAR reflection profile. Each trace results from the system emitting a very short pulse of high frequency electromagnetic energy that is transmitted into the subsurface. As the pulse propagates and encounters materials of differing electrical properties, its velocity is altered. If these changes are abrupt with respect to the dominant wavelength of the pulse, some of the pulse energy is reflected back to the surface. The signal is detected by the receiving antenna. The time between transmission and detection, referred to as the two-way travel time (TWT), is measured in nano-seconds, much faster than the typical milliseconds or seconds used with reflection seismology, and is a function of depth, the antenna spacing, and the average RADAR wave velocity in the overlying material.

Unfortunately, subsurface reflections are not the only signals that are generated and received by the GPR equipment and must be recognized and accounted for during the data processing stage. Neal (2004) states that the first of these unwanted pulses to reach the receiving antenna is that of the air wave, which travels between the transmitting antenna and the receiving antenna at the speed of light ($\sim 3.0 \times 10^8$ m/s). The second pulse to arrive is known as the ground wave, which travels through the interface between the ground and air from the transmitting antenna to the receiving antenna (Neal, 2004). These two pulses can therefore result in any primary reflectors towards the top of the reflection profile to become disguised as noise. Lastly, the reason for performing this type of survey is to detect the reflected arrivals, which hopefully will show the subsurface elements of interest.

During this study, the GPR data acquisition was conducted on May 31st of 2013. The weather for this study was sunny and clear. No modifications to the GPR cart were necessary (e.g. modifications for snow cover, rain, etc.).

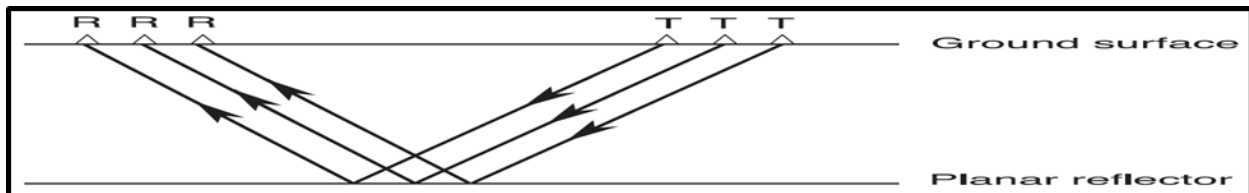


Figure 4-7: Geometry of the common offset survey where R = receiver and T = transmitter (Daniels, 1996).

4.2.2.1 Theoretical Background

There are three material properties that determine how electromagnetic energy in the material will behave (Neal, 2004). The three properties are dielectric permittivity (ϵ_r), electrical conductivity (σ), and magnetic permeability (μ_r). The electromagnetic wave velocity (v) is a function of the wave's frequency (f), the free space speed of light, and the characteristics of the material (dielectric permittivity, electrical conductivity, and magnetic permeability). In mathematical terms, this velocity is defined by Equation 1.

$$v = \frac{c_0}{\sqrt{\epsilon_r \mu_r \frac{1 + \sqrt{1 + \left(\frac{\sigma}{\omega \epsilon}\right)^2}}{2}}}$$

Equation 1: Electromagnetic wave velocity

In Equation 1, C_0 is the velocity of the electromagnetic wave velocity in a vacuum (3.0×10^8 m/s) and $\sigma/\omega\epsilon$ is a loss factor with $\omega = 2\pi f$ being the angular frequency (Neal, 2004). If we assume that the material being tested is a low-loss material (e.g. clean sand and gravel), which is to say a material that has a limited signal loss during propagation as compared to less homogenous material; the influence of magnetic permeability and electrical conductivity are assumed to be negligible, so $\sigma/\omega\epsilon \approx 0$ (Davis and Annan, 1989; Reynolds, 1997). It can also be assumed that the influence of μ_r is negligible and is thus given the value of 1 (Neal, 2004). The resulting relationship as defined by Neal (2004) is given in Equation 2.

$$v = \frac{c_0}{\sqrt{\epsilon_r}}$$

Equation 2: Electromagnetic wave velocity

As the propagation of the electromagnetic wave occurs within the material, the wave amplitude (A) deteriorates exponentially from an initial value of A_0 as it travels a distance, z (Neal, 2004). The resulting relationship as defined by Neal (2004) is shown in Equation 3. The symbol σ stands for the attenuation constant.

$$A = A_0 e^{-\alpha z}$$

Equation 3: Electromagnetic wave amplitude

The attenuation constant can be calculated directly for low-loss materials and is independent of the frequency (Neal, 2004). The mathematical relationship describing the attenuation constant as per Neal (2004) is given in Equation 4.

$$\alpha = \frac{\sigma}{2} \sqrt{\frac{\mu}{\epsilon}}$$

Equation 4: Attenuation constant

Based on the assumptions that are used to derive the above equations, a number of assumptions about the behaviour of electromagnetic fields in earth materials can be made. Since water exhibits a high value of ϵ compared to air and typical rock-forming minerals, water

saturation will exert the primary control over the dielectric properties of common sedimentary materials. This has significant implications when considering the regime in which a survey is staged, since water-saturated sediments will yield bright water table reflections on the profiles. However, the assumptions above break down when highly conductive substances such as sea water or significant amounts of magnetics material such as magnetite or hematite-rich clays are present.

When propagating magnetic fields encounter a significant subsurface electrical discontinuity, some of the incident energy is reflected. The amount of energy reflected is defined by the reflection coefficient (R). Assuming that the contrasts between the electrical resistivity and magnetic permeability are negligible; Equation 5 will result.

$$R = \frac{\sqrt{v_2} - \sqrt{v_1}}{\sqrt{v_2} + \sqrt{v_1}}$$

Equation 5: Reflection coefficient

In Equation 5, v_1 and v_2 are the adjacent layers 1 and 2 velocities. In all cases, the value of R lies between +1 and -1. Reflection coefficient modelling for subsurface discontinuities in various unconsolidated sediments suggest that RADAR is sensitive to changes in the sediment/air/fresh water ratio (Baker, 1991).

4.2.2.2 Unprocessed GPR Data Limitations

After the collection of GPR data and prior to its interpretation, the raw GPR data must be processed in a similar manner to that of raw seismic data to help with the elimination of errors and noise; thereby making it possible to successfully evaluate and infer valuable sedimentological information. According to Neal (2004), there are numerous inherent limitations of unprocessed GPR data. A list of these is as follows;

1. Time-zero drift
2. Normal moveout
3. Signal saturation
4. Depth of penetration
5. Horizontal and vertical resolution

6. Distortions, diffractions and dip displacements
7. Ambient and systematic electromagnetic noise
8. Surface reflections
9. Horizontal and vertical subsurface RADAR wave velocity variations
10. Topographic variations along the survey line

1. *Time-zero drift*

Neal (2004) describes this as occurring when the airwave RADAR reflection profile changes its position from trace to trace during the collection of data and is responsible for creating the misalignment of the air and ground waves, in addition to the primary and secondary reflections. The drift typically occurs if the difference in temperature between the ambient air and the console electronics is great or it could be the result of damaged cables (Sensors and Software, Inc., 1999; Sensors and Software, Inc., 1998). According to Bano *et al.* (2000), this problem is eliminated by simply allowing the console temperature to equilibrate. Since the GPR work is being done in the summer months, this error should be negligible.

2. *Normal moveout*

Normal moveout is defined by Neal (2004) as being the difference between the zero offset travel time and the travel time at a particular offset. Since the transmitting antenna and the receiving antenna are non-coincident, the travel times of the reflections are unusually long as compared to the depth of the reflector that initiated them (Fisher *et al.*, 1992; Neal, 2004). **Add more later; how will bed dips of 20 degrees be corrected

3. *Signal saturation*

According to Fisher *et al.* (1996), there is a possibility for the receivers to undergo signal saturation; a direct result of the short time periods that occur between transmitter pulses during surveying and the fairly large ground wave, air wave and near-surface reflections

energy input. If signal saturation should happen, it will introduce a low-frequency, slowly decaying anomaly on the traces of the higher frequency reflections where its magnitude will be related to antenna separation and the surrounding ground conditions (Sensors and Software, Inc., 1999; Sensors and Software, Inc., 1998).

4. *Depth of penetration*

As a result of electromagnetic waves experiencing large energy losses as they propagate through the subsurface, the depth at which RADAR waves can successfully penetrate at a particular location or frequency is greatly limited (Neal, 2004). Since electromagnetic wave attenuation is a frequency-based function, then it follows that the greater the antenna's frequency, the shallower the depth of penetration will be (Davis and Annan, 1989; Neal, 2004). Therefore, the weakening of the energy levels to extinction will cause a decreased reflected wave amplitude such that they can become too low in energy to be detected and are thus not visible on the RADAR trace; this renders the deep reflecting arrivals indistinguishable (Vaughan, 2011).

5. *Horizontal and vertical resolution*

The horizontal resolution is greatly affected by the complex shape of the propagating RADAR wave front and is further complicated by the interaction this wave front has with the subsurface, which leads to production of an elliptical RADAR footprint that when surveying over dipping reflectors, becomes further complicated. All of these complications combined will cause the horizontal resolution with depth to decrease.

Knapp (1990) states that the vertical resolution of reflections is a function of the pulse width and the wavelet sharpness and is proportional to frequency. Therefore, it follows that if there is an increase in frequency, there should be an increase in the vertical resolution. The mathematical relationship between the wavelength (λ) and the wave velocity (v) and wave frequency (f) as per Neal (2004) is as follows.

$$\lambda = \frac{v}{f}$$

Equation 6: Wavelength

The receiving antenna will typically detect a frequency that is less than the centre frequency released from the transmitting antenna, which is caused by the weakening of higher frequencies during propagation in addition to the frequency composition of the pulse being transmitted. As a result, the accurate way of determining the vertical resolution is to use the return pulse. The wave theory states that $\lambda/4$ is the maximum vertical resolution that can be recorded, meaning that any subsurface layers thinner than $1/4$ of the incident pulse probably will not be detected.

6. Distortions, diffractions and dip displacements

Since RADAR antennae radiate and receive electromagnetic energy in a complex 3-D cone, reflections recorded on the profile do not necessarily come from immediately below the survey point. Reflected energy can radiate from anywhere on the wave RADAR front and from various points on undulating subsurface reflectors. This can lead to errors in apparent dips, bowtie anomalies and diffractions from point anomalies that obscure primary reflectors.

7. Ambient and systematic electromagnetic noise

The fact that the GPR system is basically a wide bandwidth receiver means that the potential exists for it to be affected by external, man-made sources of electromagnetic energy. These possible outside sources can include mobile cell phones and their related towers, FM radio transmitters, television transmitters and walkie-talkies, just to name a few (Conyers and Goodman, 1997; Olhoeft, 1999, 2000). In some cases, it may be possible to avoid these sources of EM energy, while in others, it may be impossible to avoid them; therefore, it is important to understand how these sources can affect the reflection profile. In general, the noise generated from these extraneous sources can result in ‘ringing’ multiples or ‘reflection’ events that can obscure primary reflectors (Neal, 2004). Ringing is common where wire cables are used to connect the transmitter and receiver to the console. The effect of this type of noise is effectively reduced in the survey through the use of fibre-optic cables instead. Ringing can also be caused when a signal bounces back and forth between a highly conductive reflector and the receiver a number of times (Sensors and Software, Inc., 2006).

This can sometimes indicate the presence of highly conductive saline ground water and limits the use of GPR where these saline waters are present.

8. Surface and subsurface reflections

Although GPR antennae direct most of their energy into the ground, some energy is also dissipated into the air. When airborne RADAR waves strike an object or planar surface with high electrical contrast, the resultant reflected signal is recognized by the receiver. Therefore, on some RADAR profiles, not all reflections are of the subsurface origin. This is a common issue with unshielded antennae, but shielding limits the size of antenna and therefore the frequency. Common examples of surface reflectors are power lines and poles, trees, metallic fences, large boulders, walls and highly irregular topography. These surface reflectors can sometimes be confused with, or obscure subsurface reflections. Common subsurface obstructions such as pipelines, metallic fence lines, irrigation systems, culverts and electrical cables can produce erroneous reflections from the subsurface. Unfortunately, the roads that were surveyed contained metallic fence lines, power lines, pipes and culverts. Therefore, the resulting subsurface images will likely suffer as a result.

9. Horizontal and vertical subsurface RADAR wave velocity variations

According to Neal (2004), since GPR data is recorded on a fixed time base; to estimate the depths on the reflection profile, the associated wave velocities must be known. In cases where a single, average velocity can be used for subsurface characterization, then the TWT can undergo a simple linear conversion to depth, resulting in an undistorted profile (Neal, 2004). Examples of materials that could produce an undistorted profile would be unsaturated sands and gravels. Should wide swings in wave velocities occur with depth; the RADAR profile will become distorted due to the depth scale expanding and contracting with the increased TWT (Neal, 2004). Distortion could be caused by the water table, changes in porosity, or changes in the clay and silt content.

10. Topographic variations along the survey line

Elevation changes along a survey line are not taken into account on raw RADAR sections. This can lead to significant distortions of the subsurface images if not corrected for. This problem is made worse because the radiated energy from the transmitter is no longer directed vertically downward on slopes, but instead has a horizontal component that increases with increasing slope. At slopes greater than approximately 6 degrees, the subsurface reflections will be miss-located. Topographic variations are therefore corrected using the DGPS Z-coordinates as shown in Figure 4-9; the raw image, Figure 4-8, has not been corrected for topography, whereas the processed image has been.

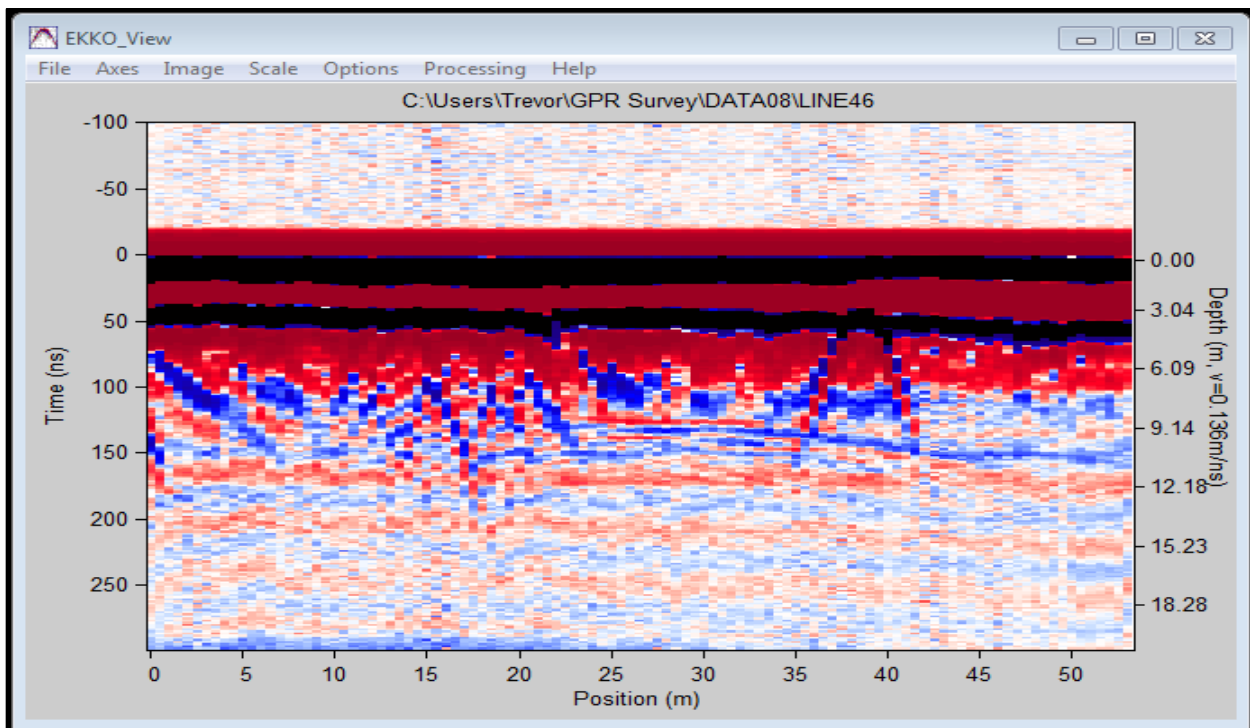


Figure 4-8: Raw, unprocessed GPR profile of Line 46.

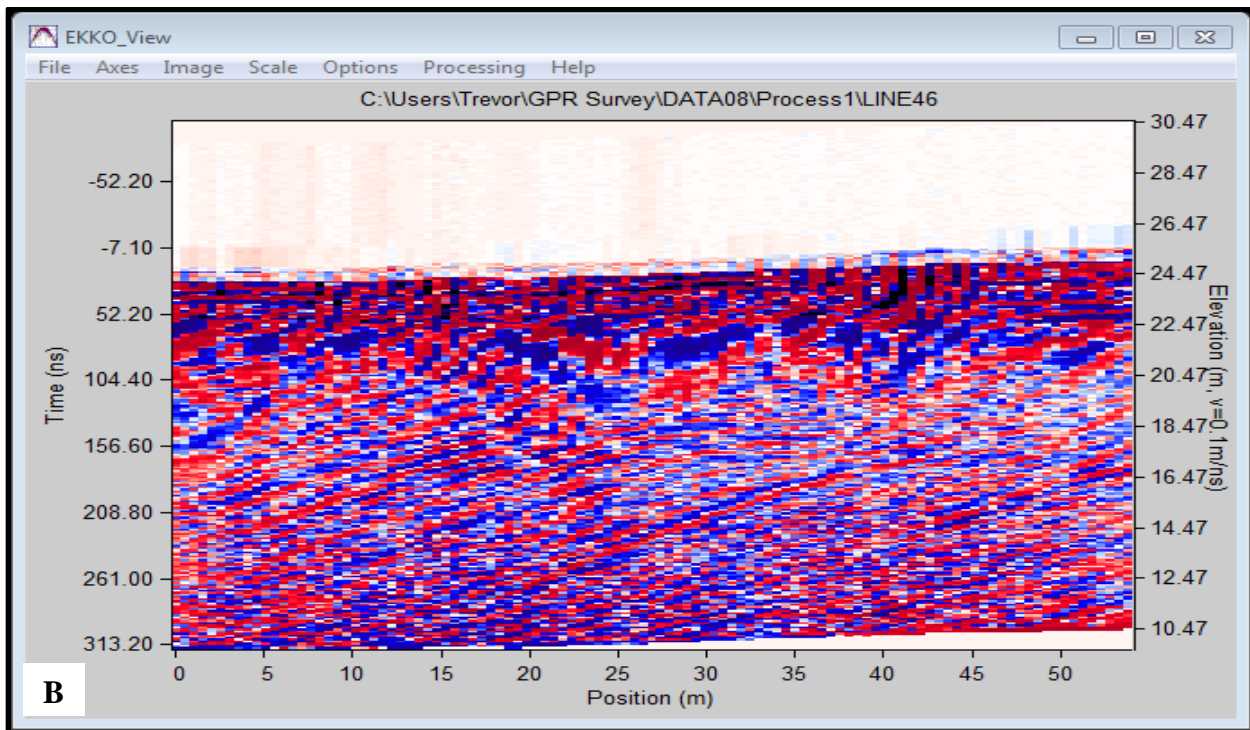


Figure 4-9: Processed GPR profile of Line 46.

4.2.3 Data Processing

With the GPR data successfully collected, the next task that must be carried out is the processing phase, which is required for any geophysically-related research. As previously mentioned, the initial GPR data contains many types of noise that must be removed and filtered out such that useful subsurface profiles can be used for meaningful interpretation. To perform the processing of the raw data, a software package known as EKKO_View Deluxe will be used. This software was developed by Sensors and Software Incorporated and its purpose is to allow for subsurface sections to be displayed and processed through the application of various filters, attributes, operations, etc. According to Sensors and Software Inc. (2003), EKKO_View Deluxe is a professional “software version that allows for data plotting, editing and full processing routines including spatial and temporal filters, migration, instantaneous attributes, amplitude spectra, CMP velocity analysis and more.”

The raw GPR data is first imported into EKKO_View Deluxe where the data and sections can be viewed. Any incomplete sections (line 48) and test sections (lines 00-08) were removed

and the remaining GPR lines had their associated differential GPS data assigned. The DGPS data was also converted to UTM coordinates and the step-sizes were re-computed, which did not change much. The topography data was imported as well based on the Z coordinate recorded by the DGPS. This was followed by applying the topography shift operation. The difference between the raw data and the data with a re-computed step size, topographic correction, DGPS fixes and line orientation corrections can be seen in Figure 4-10. Following these initial stages of data editing, various processing techniques can were applied, which can be seen in Figure 4-11.

File Name	Start Position	Stop Position	Stepsize	Antenna Separation	Units	Frequency (MHz)	# Traces	Min Elevation	Max Elevation	GPS Data
LINE09	0.0	70.952	0.496	1.0	m	50.0	144	45.547	47.471	Yes
LINE10	0.0	99.929	0.497	1.0	m	50.0	202	43.688	45.51	Yes
LINE11	0.0	106.825	0.497	1.0	m	50.0	216	41.006	43.679	Yes
LINE12	0.0	67.5	0.5	1.0	m	50.0	136	0.0	0.0	No
LINE13	0.0	145.5	0.5	1.0	m	50.0	292	0.0	0.0	No
LINE14	0.0	44.0	0.5	1.0	m	50.0	89	0.0	0.0	No

Figure 4-10: Lines 12-14 are examples of the raw data, while lines 09-11 have the applied DGPS fixes, elevations, and re-computed step-sizes.

These processes are added to form what is known as a recipe and upon applying the processes in series, results in higher quality subsurface images. The processes are determined by an inspection of the data, namely the Average Time-Amplitude Plot and the Average Amplitude Spectrum Plot.

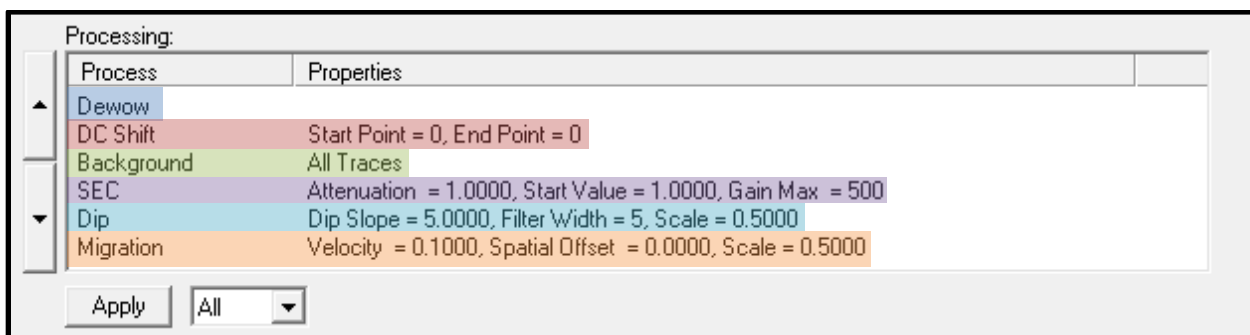


Figure 4-11: Processing window showing the processes, the order in which they were applied and their respective properties.

As a result of the Joggins Formation not being surveyed previously, the results of the survey were unknown. Therefore, the only real way of approaching the data from a processing

perspective was to perform a trial and error analysis, whereby certain processes were applied individually and in conjunction with other processes until the image quality became higher. With numerous process trials run, the flow chart that was ultimately used is shown in Figure 4-12.

The first process to be applied to the subsurface profiles is the dewow time filter. The dewow filter is typically almost always applied and is usually the first process applied because it corrects for signal saturation or “wow” within the dataset (Sensors and Software Inc., 2003). This low frequency, slowly decaying “wow” is related to the transmitting signal and becomes superimposed on the high frequency reflections (Sensors and Software Inc., 2003). As the name suggests, the dewow time filter is applied to remove these undesirable low frequencies, while maintaining the high frequencies.

The second process to be applied is the direct current (DC) shift time filter. The purpose of this filter is eliminate the DC level from every trace in the initial data set and is performed by subtracting an input DC level from every point in every trace of the data set (Sensors and Software Inc., 2003).

The third process that was utilized is known as the background subtraction spatial filter. The background subtraction filter applies a running-average background subtraction to the entire set of data with the effect of enhancing any dipping reflections whilst helping to suppress horizontal reflections (Sensors and Software Inc., 2003). Since the strata of the Joggins Formation have dips of between 15 and 20 degrees, this filter seems to work well in helping to further define them within the subsurface profiles.

The fourth process applied is known as the Spreading and Exponential Compensation (SEC) gain function. The SEC gain function can be thought of as an amalgamation of an exponential time gain and a linear time gain with the purpose being to help compensate for any exponential ohmic dissipation in energy or spherical spreading losses during the data collection process (Sensors and Software Inc., 2003).

The fifth process that was used is known as the dip 2-D filter and serves the purpose of enhancing reflections at certain dip angles (Sensors and Software Inc., 2003). Once again, the

dipping strata of the Joggins Formation can be further visualized in the subsurface profile by applying this type of filter.

The final process that was applied is known as the migration 2-D filter. This 2-D filter was applied because many of the subsurface profiles exhibited parabolic reflectors, which the migration filter aims to collapse or dissipate their magnitude (Sensors and Software Inc., 2003).

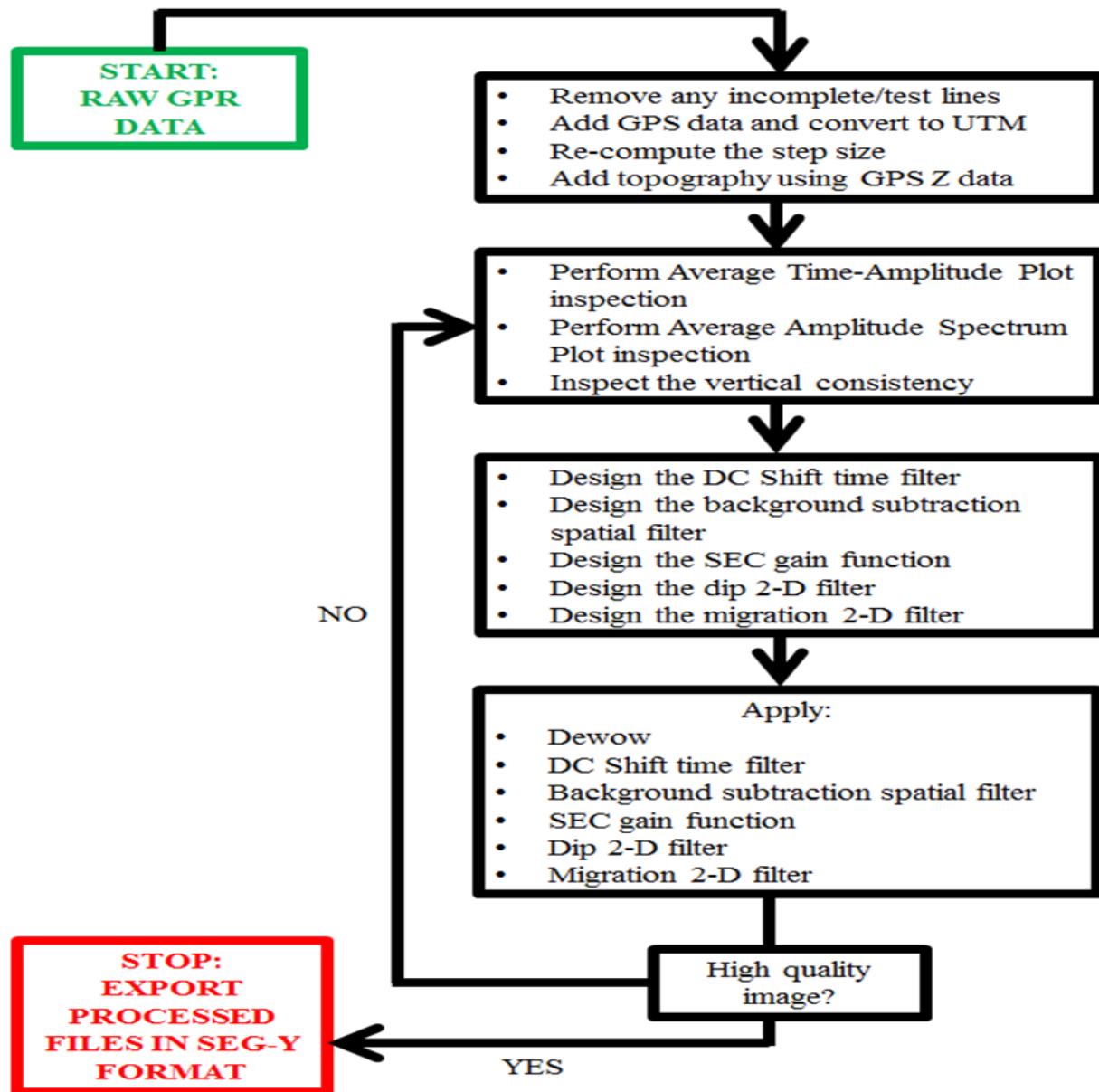


Figure 4-12: Processing workflow that was applied to the raw GPR data in EKKO_View Deluxe. The process evolved via trial and error.

4.3 Differential Global Positioning System (DGPS)

A differential GPS applies differential correction techniques in order to improve the accuracy of location data that is gathered using GPS receivers (Chivers, n.d.). The research that was carried out on the Joggins Formation, specifically the GPR survey and the LIDAR survey, both used DGPS to enhance the gathered data (Refer to Figure 4-13).



Figure 4-13: Left; image of the Leica base station on the right side and the radio transmitter and antenna on the left side. Right; close-up view of the Leica base station.

To carry out the GPR survey and LIDAR survey, a base station of known location in addition to a DGPS rover was used. For the LIDAR survey, the DGPS rover (refer to Figure 4-14, left) was mounted on a pole and was moved when necessary. The GPR survey is a slightly different setup in that the DGPS rover is mounted on the cart (refer to Figure 4-14, right). The correction calculations performed by the base station are done so in real-time and are transmitted to the rover as they become available. The Department of Natural Resources installed a high accuracy survey marker near the Joggins Fossil Cliffs Centre, which served as the base station setup position (Rafuse, 2011). The coordinates of that survey marker were recorded and inputted into the DGPS controller. It is estimated that an accuracy of +/- 3.0 cm was achieved.

Following the placement of the targets in the LIDAR survey area, the coordinates of the center of each target was recorded for georeferencing purposes that took place back at the Basin and Reservoir Lab. Georeferencing ensures that the LIDAR data is spatially anchored and has real-world coordinates associated with it.

There are numerous elements that are necessary for performing a successful GPR and LIDAR survey, in addition to producing high resolution and spatially correct data. Differential GPS allows for both accurate and precise location data so as to properly georeference the acquired data in 3-D space (Vaughan, 2011). A standard stand-alone GPS system, while useful for certain applications, is not the best when performing GPR and LIDAR surveys because of the built-in errors that accompany them; which in the horizontal X and Y planes can be as much as several meters and in the case of the vertical Z plane the error can be 10 meters or more. The random timing errors (known as Selective Availability or simply SA) in the standard GPS systems were introduced by the United States Department of Defense as a way of limiting the effectiveness of GPS and thus; make it more difficult for GPS to be used in an ill manner (Chivers, n.d.). The lack of accuracy, especially in the vertical plane, causes various problems such as attempting to correct a GPR subsurface profile for surface topography variations in an area of data collection (Vaughan, 2011). Substantial movements in the X, Y and Z directions of a subsurface profile can result due to the movements of the GPR cart, resulting in GPS coordinates being degraded or lost all together. As such, a typical GPS system could result in the production of subsurface anomalies that are false and when importing the profiles into other software for the purposes of 3-D modelling, could cause their true locations to be offset.

At Joggins, the DGPS was placed on the fixed base station of known location and the differences in position between the satellite systems and the surveyed base station are broadcasted. The DGPS base station was used to monitor and record the wander that occurs to a stationary point as a result of the orbiting satellites (Vaughan, 2011). When paired with the roving receiver, either cart mounted in the case of GPR or moved by an individual in the case of the LIDAR survey, the GPS position is acquired and is in constant communication with the surveyed base station by way of ultra-high frequency (UHF) radio transmitters. As the rover acquires GPS coordinates, the wander that is recorded by the base station is subtracted in real-

time from the coordinates and the corrected points are recorded into the GPR profile or into the LIDAR profile (Chivers, n.d.). The resulting data set therefore contains extremely accurate GPS data that results in very accurate grid survey line positions and topographic corrections.

Both the GPR and LIDAR surveys were conducted using a differential GPS system, which was integrated with the data acquisition. The surveys incorporated a Leica GPS1200+ Series High Performance Global Navigation Satellite System (GNSS) for obtaining the real-time GPS positions and were accurate to 2 cm or less in the X, Y and Z planes.

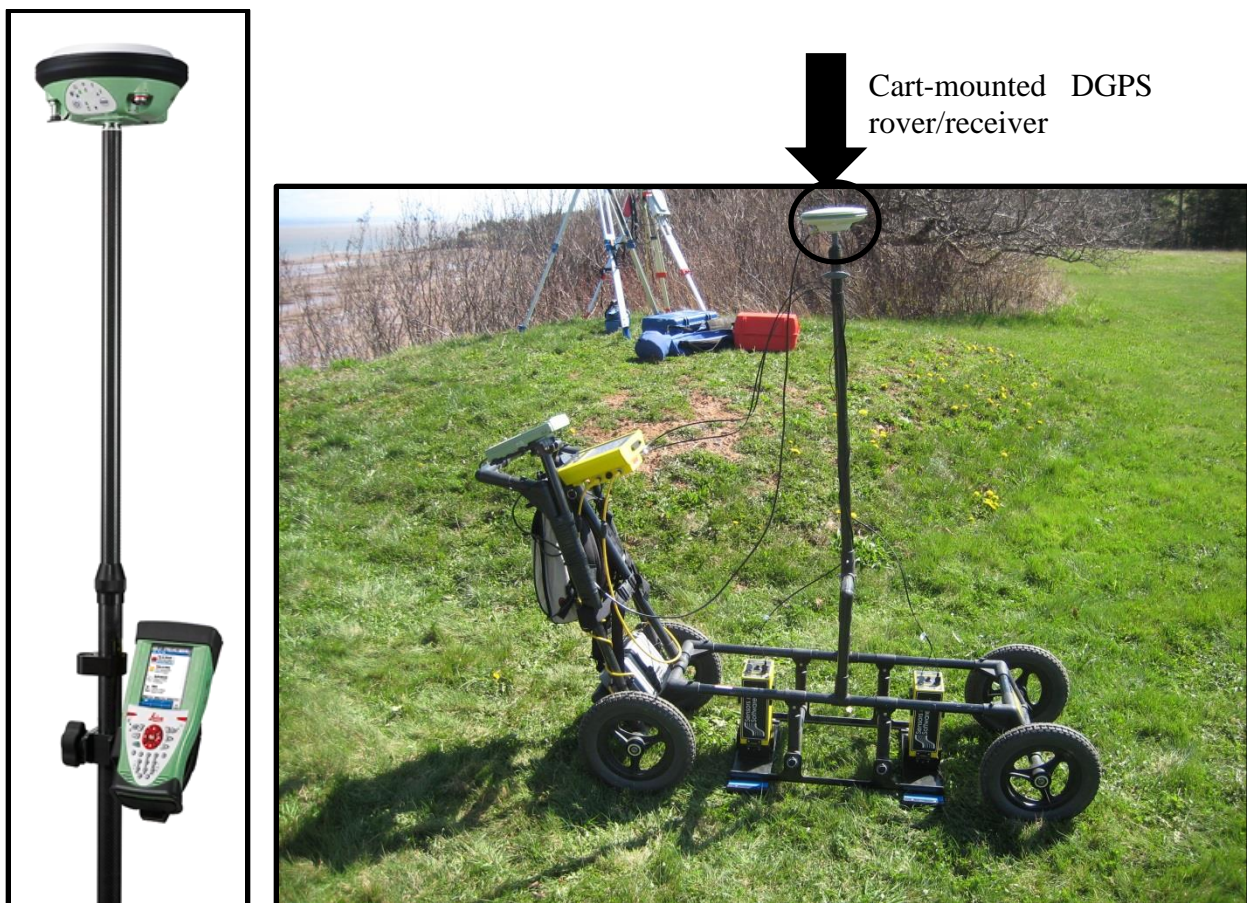


Figure 4-14: Left; photograph of a Leica GNSS rover/receiver similar to the one used at Joggins for measuring the LIDAR system setup locations and LIDAR target locations (Leica Geosystems, 2012). Right; photograph of the GPR cart showing the mobile rover/receiver.

4.4 Handheld Gamma-Ray Spectrometer

As part of the field work carried out at Joggins, a handheld/portable gamma-ray spectrometer was used to take measurements at a consistent interval along the Joggins outcrop. This study utilized a Science Applications International Corporation Exploranium GR-130 miniSPEC, which is pictured in Figure 4-15 and Figure 4-16. The spectrometer that was used at Joggins has numerous functions and can be used for multiple reasons. For this study, only the gamma-ray scintillometer survey function was required. This function is activated by turning the device on and selecting the survey mode from the main menu list. The device displays the current count rate in the format of counts per second. A gamma-ray scintillometer is a device that is used to measure the radioactive content of a rock sample or lithology through the measuring of the amount of uranium, thorium and potassium that the sample contains. Readings are taken at regular intervals by simply placing the device against the rock surface to be measured and recording the value that is displayed. The theory behind using a scintillometer lies in its ability to detect gamma radiation. Typically the finer-grained lithologies, such as siltstones, mudstones and shales will contain abundant concentrations of radioactive elements when compared to sands which are typically cleaner due to increased working and re-working during transport. On a gamma ray log trace, sand will kick to the left; shale will kick to the right. This allows for the variations within the sand bodies to be determined that otherwise would not have been discerned. The use of this data will provide a more accurate model in Petrel.

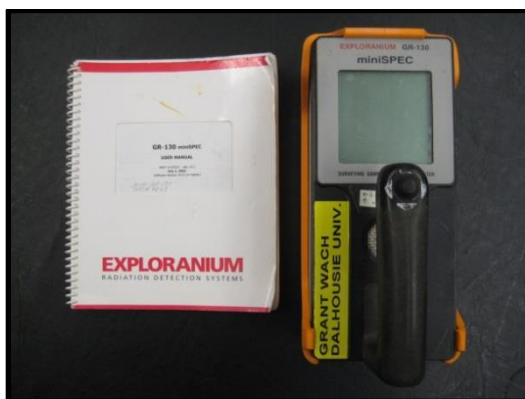


Figure 4-15: Photograph of the Exploranium GR-130 handheld gamma-ray spectrometer (miniSPEC).

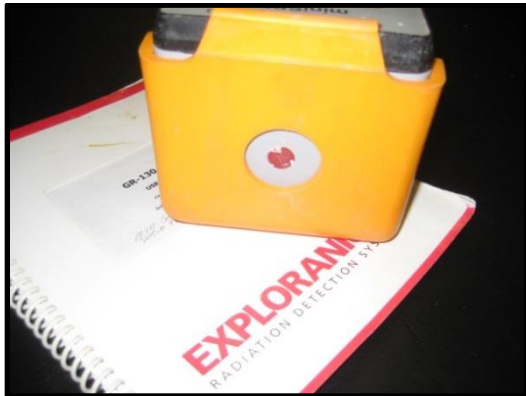
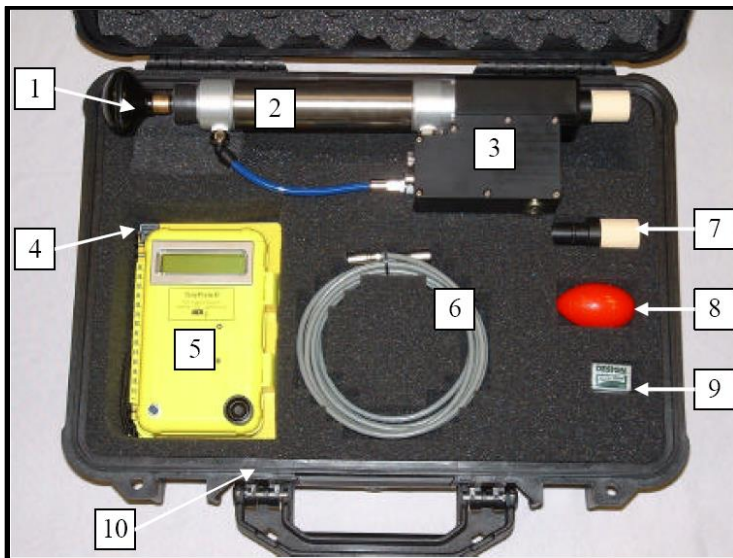


Figure 4-16: Front view of the Exploranium GR-130 handheld gamma-ray spectrometer showing the portion that is held against the surface for takings measurements.

4.5 Handheld Air Permeameter

Permeability is a vital measurement that must be taken into account when evaluating the performance of a petroleum reservoir. During the field trip to Joggins, permeability values were collected using a handheld air permeameter, which is known as the TinyPerm II (Figure 4-17) and it was developed by New England Research, Inc. It is important to note that the TinyPerm II measures the rock matrix permeability.



Components:

1. Handle and plunger
2. Vacuum cylinder
3. Pressure transducer enclosure
4. Documentation with field notebook and calibrations
5. Microprocessor and control unit
6. Electrical Cable
7. Spare nozzle
8. Silly putty
9. Eraser
10. Carrying case

Figure 4-17: Photograph showing the TinyPerm II portable permeameter and its associated parts (NER, 2013).

The procedure for taking measurements as described by NER (2013) is as follows;

1. Turn the TinyPerm II on. Pull the plunger all the way out and ensure that the screen on the control unit is displaying the “Push + Hold” reading. The current value of the vacuum status is displayed on the right-hand side of the screen and should be zero prior to a measurement being made.
2. Firmly press the nozzle against the intended rock surface to be measured.
3. Fully depress the plunger, which will display the current vacuum and a measurement status bar on the screen. Hold the plunger in while continuing to press the nozzle against the rock surface. Eventually, the vacuum will go to zero and the status bar will indicate that a successful measurement has been made.
4. The result will be displayed on the control unit screen. The value should be recorded in a field notebook.
5. Pull the plunger back out and continue to the next measurement location.

The resulting values that are displayed on the microcontroller can then be correlated to an actual permeability value in milli-Darcy’s using a calibration chart as seen in Figure 4-18. The correlation that exists between the TinyPerm II value as displayed on the microcontrollers screen and the resulting permeability is linear, with high TinyPerm II values corresponding to low permeabilities and vice versa.

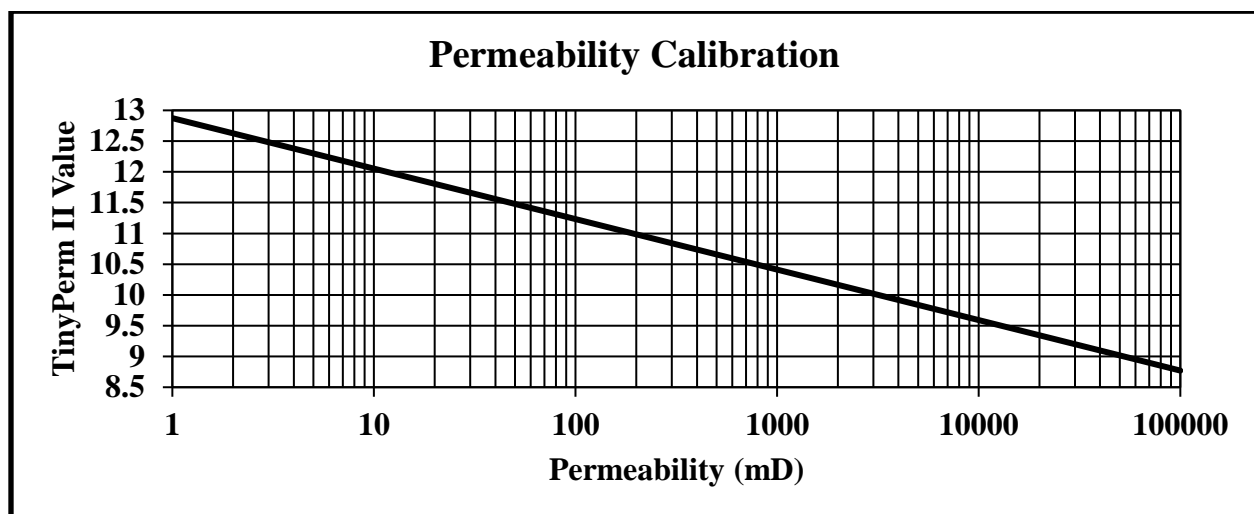


Figure 4-18: Permeability calibration chart which is used to correlate a TinyPerm II value to a corresponding permeability (Modified from NER, 2013).

The resulting permeability values can then be given a rank. The ranking that is applied to the numerical permeability values is provided by Nabaway *et al.* (2009) and is as follows in Table 4-1.

Table 4-1: Permeability ranking (Nabaway *et al.*, 2009).

Rank	Range
Fair	$1 < K \leq 10$ mD
Good	$10 < K \leq 100$ mD
Very Good	$100 < K \leq 1000$ mD
Excellent	$1000 < K$

4.6 Rock Sampling

Rock samples were collected along the beach traverse of the outcropping Joggins Formation with permission of the Joggins Fossil Institute. The samples that were collected represented the major lithologies that are representative of the Joggins Formation. In total, 8 rock samples were collected for later analysis and use. The samples ranged in size from X to X. The samples were labelled and their approximate locations were recorded. The samples will be useful for a variety of research techniques such as the creation of thin sections.

4.7 Thin Section Image Analysis

One of the reasons for collecting rock samples from the Joggins Formation was for the making of thin sections. The thin sections allowed for a detailed petrographic microscope study to be performed. Using the thin sections in conjunction with a petrographic microscope, the mineralogy, in addition to other valuable information related to the fabric, texture and other microscopic features of the rock can be gathered. Additionally, the thin sections can be imaged using specialized software that helps with the determination of porosity. The information gathered from these thin sections can be used as input for the Petrel model to allow for real data utilization instead of assumed values based on an analogous reservoir.

The thin sections were prepared by Gordon Brown, who is the resident Dalhousie University Thin Section Technologist. In total, 16 thin sections were made, two for each of the rock samples collected; of which one thin section was un-stained and one that was stained. Thin

sections that were un-stained allowed for a description of the mineralogy to be described. Thin sections that were stained allowed for porosity determinations.

4.7.1 Mineralogy

The eight thin sections were analyzed for mineralogy description purposes in the Mineralogy and Petrology Laboratory (room 2020) of the earth sciences wing of the Life Science Centre. A Nikon Eclipse 50iPOL microscope was used in conjunction with a Nikon Digital Sight camera for capturing thin section images.

4.7.2 Digital Image Porosity Analysis

The digital image porosity analysis was completed using an Olympus BX51 polarizing microscope. The microscope is fitted with a camera to allow for digital images to be captured on the connected desktop computer using the DP Controller software. The digital images were then imported, one by one, into Image Pro Plus. This software allows for the manual selection of porosity, which shows up in the thin section slides as areas of blue. Apart from the void space, the grain area percentage and cement area percentage were also selected. Therefore, for each thin section image, three area percentages were calculated; void area, grain area and cement area. Upon selecting these areas, which are each given a unique colour, the software scans the image and compiles the areas as either voids, grains or cement and returns a total percentage value based on the area that each colour occupies in the image. The resulting porosity values can then be given a rank. The ranking that is applied to the porosity values is provided by Nabaway *et al.* (2009) and is as follows in Table 4-2.

Table 4-2: Porosity Ranking (Nabaway *et al.*, 2009).

Rank	Range
Negligible	$0 < \phi \leq 5 \%$
Poor	$5 < \phi \leq 10 \%$
Fair	$10 < \phi \leq 15 \%$
Good	$15 < \phi \leq 20 \%$
Very Good	$20 < \phi \leq 25 \%$
Excellent	$25 < \phi$

5.0 Results

5.1 Light Detection and Ranging (LIDAR)

The two LIDAR scans that will be used for this project (the two on either side of Hardscrabble/Coal Mine Point) were divided automatically by the LIDAR unit into four scan tasks for the scan to the north of the point and six scan tasks for the scan to the south of the point. The scan task identification numbers as set by the LIDAR unit for the two scans are labelled in Figure 5-1 and Figure 5-2. The LIDAR unit also creates a log that lists the technical specifications for each scan as well as for each of the scan tasks. Refer to Appendix C for the detailed technical information regarding the base station setup, LIDAR Unit Setup #1 and its respective targets, LIDAR Unit Setup # 2 and its respective targets, LIDAR Unit Setup # 3 and its respective targets as well as information regarding the approximate distances of the three LIDAR unit setups from their associated targets, the cliff face and the base station. Additionally, the technical information regarding each of the scan tasks for each of the two scans used for this report are tabulated in this section as well.

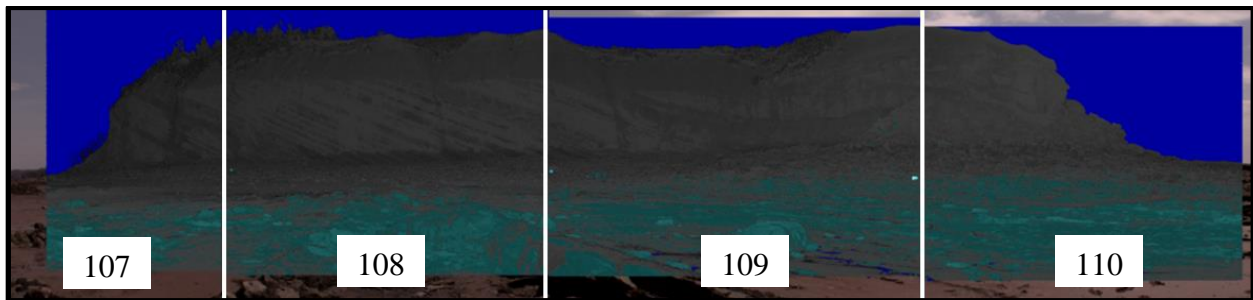


Figure 5-1: Image showing the four separate scan tasks that make up the full scan to the north of Hardscrabble/Coal Mine Point. The white lines indicate the limits of the tasks and these four tasks are also assigned an identification number automatically by the LIDAR unit.

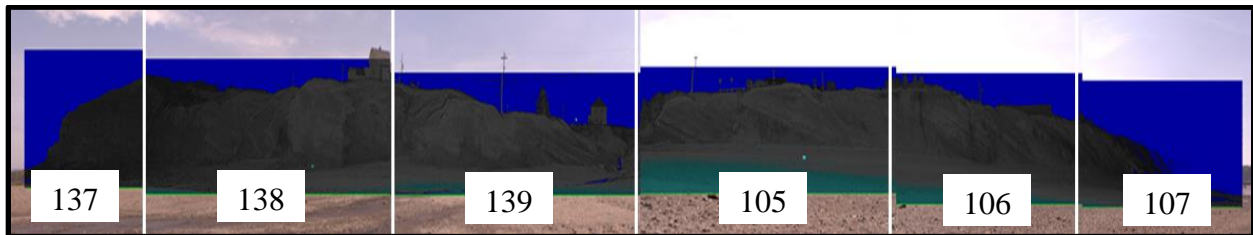


Figure 5-2: Image showing the six separate scan tasks that make up the full scan to the south of Hardscrabble/Coal Mine Point. The white lines indicate the limits of the tasks and these six tasks are also assigned an identification number automatically by the LIDAR unit.

Through the visual analysis of the LIDAR images along with the outcrop photographs and measured sections, it was possible to identify the numerous dipping strata within the dataset. By identifying these dipping strata in the LIDAR image, they can be correlated with the GPR data in an attempt to produce a 3-D rendering of the Joggins Formation fluvial meanderbelt system. The LIDAR images show the variations in sand body thickness, which are also observed in the outcrop. The pinch and swell nature of these sand bodies points to the complexities of understanding a reservoir and that over short distances (few meters), the characteristics of a good reservoir rock can change immensely. The different lithological beds can be discerned in the LIDAR images through correlation with the outcrop photographs. They show that sand layers of good permeability are sandwiched between poor permeability layers such as coals, siltstones and sandy siltstones. These layers vary widely in their thickness from a couple meters for some of the thicker sand bodies to a couple of centimetres for some of the coal strata. The important thing here is to realize the complexities in reservoir heterogeneity that exist here and the difficulties that would exist should production from a similar reservoir type be undertaken. By displaying the point cloud using a gradual, intensity based colour scheme in either ArcScene 10 or Petrel 2011, the various lithologies were discernible. The greens, reds, oranges and yellows, as seen in Figure 5-3 and Figure 5-4, represent the sand bodies, while the blues and purples represent the finer-grained lithologies, namely the siltstones.

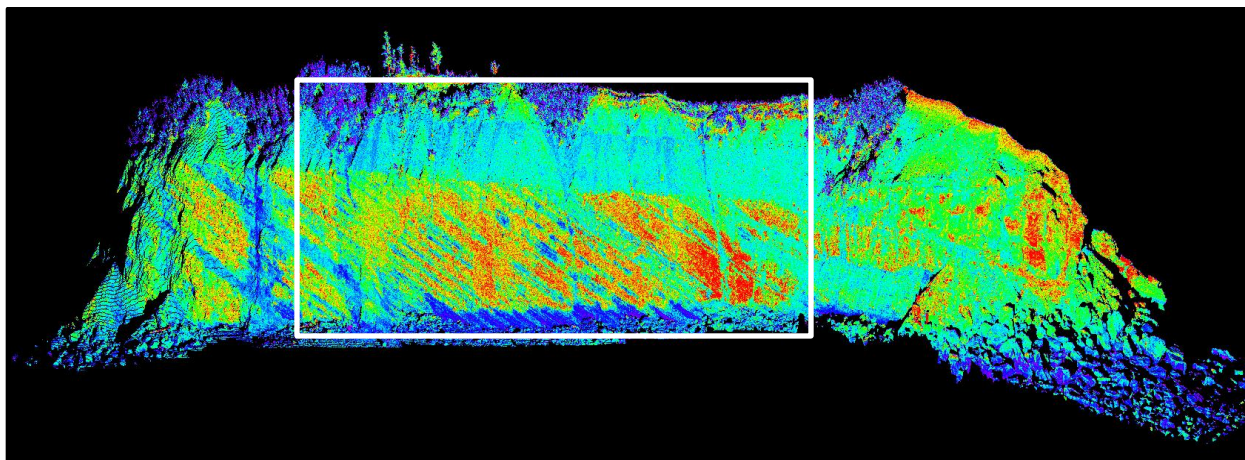


Figure 5-3: Screen capture of the third scan located on the northern side of Hardscrabble/Coal Mine Point as viewed in Petrel 2011. All data points in the point cloud are activated and a colour ramp was applied based on intensity. The colours correlate to the various lithologies. The white box shows the area that was zoomed in and is displayed in the following figure.

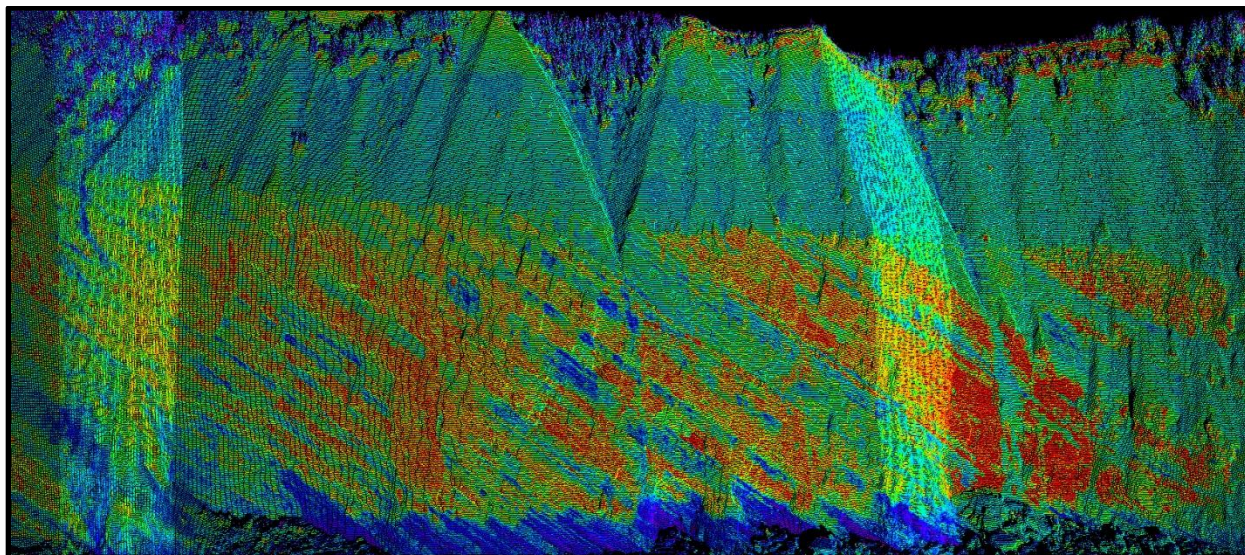


Figure 5-4: Screen capture of a portion of the third scan located on the northern side of Hardscrabble Point/Coal Mine Point as viewed in Petrel 2011. All data points in the point cloud are activated and a colour ramp was applied based on intensity. The reds, oranges, yellows and to a lesser extent, the greens, represent the sand bodies while the blues and purples represent the finer-grained lithologies in the outcrop or vegetation at the top of the cliff.

5.2 Ground Penetrating Radar (GPR)

The use of the 50 MHz antennae reduced the resolution of the subsurface profiles such that only large-scale features could be inferred, such as lithological contacts between thick units. However, compared with the 100 and 200 MHz antennae, the 50 MHz does provide the depth required in order to obtain any useful subsurface information. The 4 GPR lines that were taken over Coal Mine Point / Hardscrabble Point using the 200 MHz antennae appear to have not penetrated through the overburden, which is several meters thick. This conclusion was reached because the subsurface profiles exhibit highly chaotic reflectors, which is probably expected for overburden. In addition, the Joggins Formation strata are dipping in similar directions and at similar angles, so it is likely that these well-defined strata continue landward and would produce a subsurface image that was more ordered.

Through the examination of the GPR images, it was determined that a couple of distinct facies were identified. The first of these are the numerous examples of concave downwards reflectors, such as those highlighted in Figure 5-5.

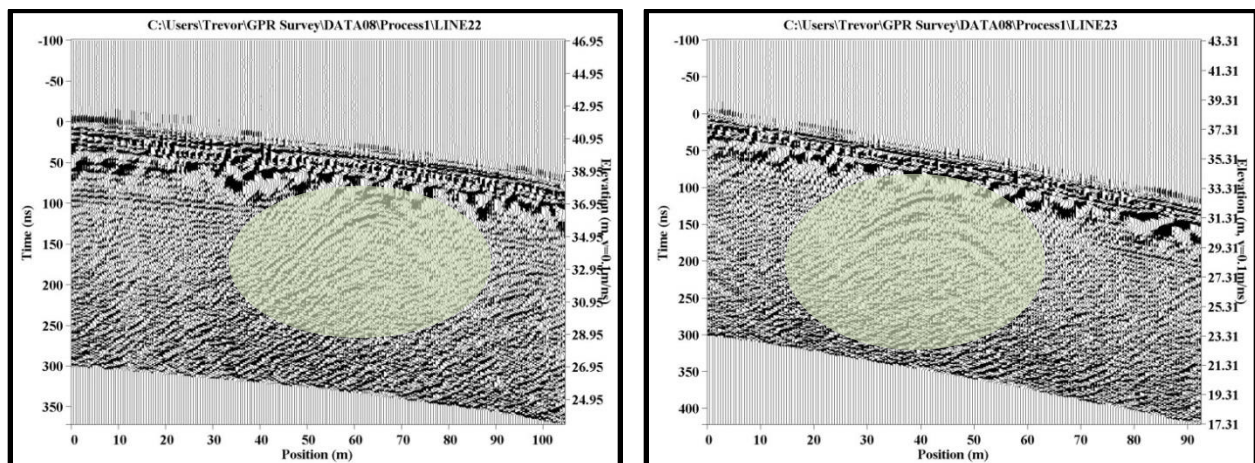


Figure 5-5: Two examples of concave downwards reflectors representing old mine workings or culverts.

Given the coal mining history in the area, these reflectors probably represent the old underground mine workings such as drifts and adits. These reflectors may also represent the locations of culverts or some other drainage pipe that led beneath the road. While these

reflectors have no usefulness in helping to decipher the fluvial meanderbelt system, they are a rather pronounced and common reflector that must be explained. These reflectors occur in lines 09, 10, 18, 21, 22, 23, 24, 25, 27, 31, 32, 33, 35, 36, 42, 44 and 46.

5.3 Handheld Gamma-Ray Spectrometer

Gamma-ray readings were conducted at various locations along the Joggins Formation outcrop. Along the Fundy Coal Seam / Fundy Forest portion of the outcrop, 51 samples were surveyed in which five readings were recorded for each sample. The samples chosen were simply fallen sandstone blocks that once resided in the cliff face strata. The range of values recorded was between 136 and 163 with an average value of 109. The sandstone blocks were chosen randomly and were surveyed in order to determine the variability in gamma-ray counts within the sandstone lithology. It was determined that the range of gamma-ray values amongst the fallen blocks was not significant; suggesting that for the most part, the sandstone units probably have similar characteristics. In addition, a twelve meter section of the Joggins Formation was surveyed at this same locale.

The gamma-ray counts are important for increasing the knowledge base of the subsurface because of their use in helping to determine baffles and barriers to flow in a reservoir. It is general knowledge that a typical gamma-ray trace will tend to trend towards the right when encountering a fine-grained unit. This is a result of a fine-grained unit containing an increased concentration of radioactive elements / ions since silt and clay particles acts in such a way as to readily accept these elements / ions. A left trending gamma-ray log will generally indicate a cleaner lithology such as a sandstone in which the reworking of the sediments it is comprised of have for the most part removed most of the clays and silts along with their associated radioactive elements.

Gamma-ray scintillometer readings were recorded on 51 sandstone blocks that had eroded from the cliff face. A total of five measurements were done at each sandstone block. The five measurements for each sandstone block are shown in Table 13-1 of Appendix C, along with the average value for each block. Readings from these sandstone blocks ranged from 97 to 195. The range of values indicates that the sandstone, in some cases, contains radioactive elements

and thus; contains finer-grained lithologies. In terms of a sandstone reservoir rock, having finer-grained material within causes more difficulties when trying to extract oil and gas as there now exists baffles and barriers to flow at the microscopic level.

A 12 meter section was measured with the scintillometer. Again, five readings were taken at each one meter interval and the average was computed. This data is shown in Table 13-2 of Appendix C. From this data, a gamma-ray curve was constructed based on the average values. This curve is shown in Figure 13-1 of Appendix C. The curve shows that the finer-grained lithologies have values of approximately 200, while the coarser-grained material has lower gamma-ray values.

The eight hand samples were also analyzed with the scintillometer for a total of 66 seconds. Values were displayed one every second for a total of 66 readings for each sample. These values are displayed in Table 13-3 of Appendix C along with the average of the values and the maximum and minimum values. Sample GW101-2013TK had a range of values from 115-155; sample GW102-2013TK displayed values from 116-151; sample GW103-2013TK had values between 118-149; sample GW104-2013TK ranged from 111-154; sample GW105-2013TK ranged from 113-143; sample GW106-2013TK displayed values ranging from 120-143; sample GW107-2013TK displayed values between 112-145 and sample GW108-2013TK displayed values between 112-142. The traces of each sample response over the 66 second sampling interval are shown in Figure 13-2 of Appendix C. In Figure 13-3 of Appendix C, the sandstone samples have been averaged into one trace and are plotted against the coal sample and limestone sample. In other words, the gamma trace has been displayed based on lithology. It was determined that the average gamma value for the sandstone, limestone and coal lithologies is approximately 130 for each with the sandstone lithology trace being much tighter to this average and the coal and limestone lithology displaying a much higher range of values.

5.4 Handheld Air Permeameter

Permeability values were collected during a traverse across the beach along the cliff face and were limited to the height of reach; however, due to the dipping nature of the strata, values recorded at low heights are assumed to be equivalent higher up the cliff face. Values were taken

at each bed change across the face. The values were collected using a handheld air permeameter, which is known as the TinyPerm II (Figure 4-17) and was developed by New England Research, Inc.

Permeameter values were collected on eight sandstone blocks that were eroded from the cliff face. These values are shown in Table 13-4 of Appendix C. Permeability values ranged from 66 mD, which is considered good to 1,917 mD, which is considered excellent. Permeameter measurements were also recorded at varying locations along the cliff face. These values are displayed in Table 13-5 of Appendix C. A total of 10 samples were tested. Values ranged from 7 mD to 410 mD, which is considered to fair to very good.

5.5 Thin Section Image Analysis

5.5.1 Mineralogy

The thin sections indicate that the dominant mineral for the six sandstone lithology samples is quartz, all of which contain considerable amounts of a carbonate mineral. The carbonate mineral occurs as a light to dark brown, seemingly fine-grained coalescence that judging from the colour is iron-rich and most likely that of ankerite. The fossiliferous limestone sample contains abundant bivalve fragments and once again appears to be rich in ankerite. The sample of coal collected is mainly carbon with some wood fragments.

5.5.2 Digital Image Porosity Analysis

Using the stained thin sections and image analysis software, the total porosity of the representative lithologies at Joggins revealed that the porosity of the six sandstone lithologies ranged from 0.9 (negligible) to 7.4 (poor), assuming the ranking scheme by Nabaway *et al.* (2009). The porosity calculated is total porosity because all void spaces within the thin sections were measured, regardless of whether or not the voids were isolated or connected. The porosity exhibited by the samples is intergranular because it occurs between the grains. The total porosity analysis also indicated that the percentage of cement is greater than first thought with the majority of the cement in the samples most likely being ankerite, a type of carbonate mineral. A

summary of the cement area, grain area and porosity of each of the six sandstone lithologies can be seen in Table 5-1. The original and enhanced thin section images can be seen in Appendix F, along with their respective summary tables.

Table 5-1: Calculated average porosity, cement and grain area values based on image analysis of a representative thin section for each of the hand samples collected at Joggins.

Sample #	Cement Area (%)	Grain Area (%)	Porosity (%) & Rank
GW101-2013TK	29.2	69.1	1.7 (Negligible)
GW102-2013TK	23.1	69.5	7.4 (Poor)
GW103-2013TK	37.8	59.5	2.8 (Negligible)
GW106-2013TK	25.5	70.4	4.1 (Negligible)
GW107-2013TK	39.6	59.6	0.9 (Negligible)
GW108-2013TK	41.6	56.4	2.0 (Negligible)

6.0 Petroleum System

In order for an area to contain hydrocarbon accumulations, there are several aspects that must be in place, which when combined together forms what is known as a petroleum system. The essential components of any petroleum system are a source rock, a reservoir rock, a trap, a seal, maturation and migration.

6.1 Elements

The following section will briefly introduce each of the necessary elements of a petroleum system.

6.1.1 Source Rock

The source rock is the origin of the hydrocarbons in a petroleum system and is typically organic-rich shale or limestone, that given a sufficient heating regime, will generate oil and gas (Schlumberger, 2013). A typical source rock contains in excess of 1.0 wt % organic carbon with rich source rocks containing greater than 5.0 wt % organic carbon with values as high as 20 wt % organic carbon possible (Gluyas and Swarbrick, 2004). The carbon is a result of terrestrial, lacustrine, or marine plants and animals that have been buried by fine-grained sediments in an

oxygen-deficient setting (Mulcahy, 2006). According to Dietrich *et al.* (2009), the upper Carboniferous coals of the Cumberland Basin do contain Type II (planktonic/sulfurous) and Type III (humic) organic matter. Type II kerogen is typically associated with the production of an oil and gas mixture; whereas Type III kerogen is generally prone to gas formation.

6.1.2 Reservoir Rock

The reservoir rock is the subsurface formation or rock body that provides the storage capacity (relates to porosity) and transmissivity (relates to permeability) necessary for oil and gas (Schlumberger, 2013; Mulcahy, 2006). According to Gluyas and Swarbrick (2004), a reservoir rock can have porosities from the average of 20 – 30 %, all the way up to 70 % and permeability values from 0.1 mD to greater than 10 D. It is generally considered that sandstones make the best reservoir rocks, although carbonate rock types are also important (Mulcahy, 2006). The sedimentary rock types are by far the most dominant hydrocarbon producing reservoirs and relates to their formation. The igneous and metamorphic rock types are generally not hydrocarbon prone, which again relates to their formation and in the case of metamorphic rocks, their deformational history. The best reservoir rocks in the Cumberland Basin would probably be those of the Joggins Formation and the Polly Brook Formation, since they are generally coarser, clastic-type material. However, upon examination of the Joggins Formation, it was determined that porosity values were low.

6.1.3 Trap

In order for a reservoir rock to contain hydrocarbons, there must not exist any pathways that would allow for hydrocarbons migration out of the reservoir rock. This is extremely important because oil and gas are less dense than water; and since water is always present with hydrocarbons, the hydrocarbons will rise towards the surface. Therefore, Schlumberger (2013) defines a trap as being a suitable configuration of rock that can contain hydrocarbons and is sealed by a relatively impermeable formation that prevents the migration of hydrocarbons. Traps can be classified as being either structurally related or stratigraphically related. Examples of these two types are provided in Table 6-1 as per Allen and Allen (1990).

Table 6-1: Examples of the two trap types that are part of a petroleum system (Allen and Allen, 1990).

Structural	Tectonic	- Extensional - Compressional
	Diapiric	- Salt movement - Mud movement
	Compactional	- Drape structures
	Gravitational	- Listric fault generation
Stratigraphic	Depositional	- Pinchouts (e.g. dunes, bars, reefs, channels, etc.) - Unconformities (e.g. erosional, subcrop, karst, etc.)
	Diagenetic	- Mineral precipitation - Mineral dissolution (e.g. thermal karst, dolomitization) - Tar mats - Permafrost - Gas hydrate crystallization

Analyzing the Cumberland Basin with respect to a petroleum system suggests that the trap preservation is likely to be a problem. At one time, perhaps the Cumberland Basin did have adequate trap formation. However, Dietrich *et al.* (2009) point out that since the window for peak hydrocarbon generation was in the late Carboniferous to early Permian time period, any hydrocarbon preservation would have been difficult since the Mesozoic uplift and erosion of the upper portion of the basin occurred post hydrocarbon generation.

6.1.4 Seal

A seal is an impermeable rock formation, such as shale, salt, anhydrite, or mudstone that is fine-grained and closely packed such that the grain tightness acts as a cap rock and prevents hydrocarbon escape both vertically and horizontally (Mulcahy, 2006; Schlumberger, 2013). The most likely sealing rock type that would have prevented the escape of hydrocarbons from the Cumberland Basin, should they exist would be the evaporitic lithologies associated with the Windsor Group.

6.1.5 Maturation

Maturation is the process by which a source rock becomes able to generate hydrocarbons when exposed to appropriate pressure and temperature regimes (Schlumberger, 2013). The

average temperature gradient for a sedimentary basin is typically between 20 °C/km and 40 °C/km with oil generation occurring somewhere between 50 – 130 °C and gas generation occurring between 150 – 250 °C (Gluyas and Swarbrick, 2004).

6.1.6 Migration

Migration can be defined as the movement of hydrocarbons from source rock to reservoir rock along connecting pathways between the two (Schlumberger, 2013). The migration process can be split into three stages. Primary migration is that which occurs as a result of hydrocarbon expulsion from the source rock (Gluyas and Swarbrick, 2004). Secondary migration deals with the migration of hydrocarbons from the source rock to the trap (Gluyas and Swarbrick, 2004). Lastly, tertiary migration occurs when hydrocarbons are leaked and dissipated at the surface of the earth (Gluyas and Swarbrick, 2004). These three types of migration are portrayed in Figure 6-1.

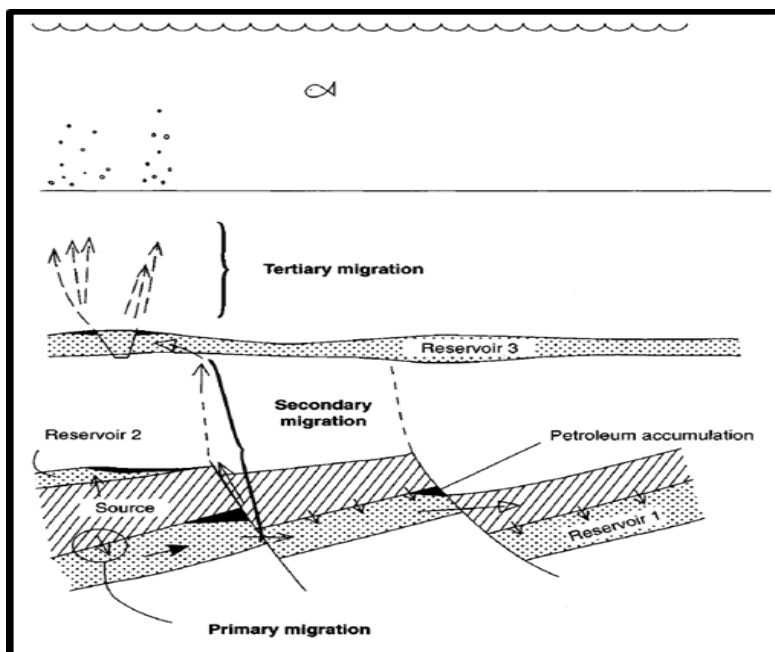


Figure 6-1: Sketch showing the three migration phases. The figure shows primary migration from the source rock into a trapped reservoir (reservoir 2) or into a carrier bed (reservoir 1); secondary migration in carrier reservoir 2 and up faults into reservoir 3; and tertiary migration from reservoir 3 into the surface (Gluyas and Swarbrick, 2004).

7.0 Discussion

7.1 Fieldwork and Related Data Collection

It is difficult to determine just how accurate the permeability values that were collected are. The large range in permeability values is likely the result of multiple factors and the values recorded from the outcrop probably differ greatly from those that would be obtained from deep within the subsurface. According to Rogiers *et al.* (2013), the variations in permeability can be the result of weathering, differential compaction, different paleo-environmental conditions, clay migration, etc. Perhaps the biggest unknown at Joggins is how the seawater affects the permeability values since twice a day the cliffs are covered by several meters of water. All permeability recordings were done on the cliff face or on fallen blocks; both of which are exposed to seawater.

Perhaps a better method of collecting permeability values would be to collect a representative sample or samples; dry them back in the laboratory; expose a fresh and flat surface using a rock saw and then apply the permeameter to the sample. Obviously, this may not be feasible with regards to time or the number of samples required, but would likely result in better permeability estimates. The best way of obtaining permeability values would be to test a core plug using a laboratory apparatus specially designed for such a test. However, diamond drill core may not always be available, as was the case with Joggins.

Like permeability, the determination of porosity may also result in highly variable values that may or may not be representative of a lithology. The porosity that is obtained using thin section image analysis gives a 2-D value. A more accurate porosity value would be obtained using core plugs in which the values obtained would be based on 3-D. Similar to permeability, the porosity also varies greatly, which is most likely the result of such processes as cementation, precipitation and other diagenetic changes.

7.2 Model Analysis

7.3 Problems and Limitations

Overall the progression of this project was unimpeded, although at various stages, there were some issues and concerns that emerged, which were subsequently dealt with and overcome. The two days of field work (May 30th and May 31st) that was done at Joggins to collect the necessary data were virtually flawless. All of the field equipment worked properly and every member of the team had a specific task to perform, which each member performed exceptionally.

During the first day when a LIDAR scan was being performed at the Fundy Forest location, a LIDAR target was blown over due to gusty conditions. This occurred part way through the scan and resulted in the scan being cancelled and re-started. Having to cancel and re-start a scan can cost a fair bit of time depending on how far along the scan was prior to cancelling it.

The use of ArcGIS for georeferencing the LIDAR data created some problems. Firstly, the LIDAR data was initially parsed such that all points were to be utilized. However, when attempts to open the point clouds in ArcGIS were done, the result was extremely long wait times followed by a typical freezing and crashing of the software prior to the task being completed. The task of displaying the point clouds and working with them in ArcGIS became too aggravating while attempting to work with all the points, so it was decided to re-parse the data by applying a 50 % reduction in points. This reduction in points significantly decreased wait times and allowed the software to perform a task to completion. Another problem that arose using ArcGIS to georeference was that a workflow had to be developed from scratch, since georeferencing this way was previously not attempted. Significant amounts of time were required to familiarize and become acquainted with the software to develop a proper workflow. This workflow was developed through trial and error.

7.4 Thin Section Image Analysis

The results of the porosity analysis indicate that the sandstone lithologies are generally poor quality when it comes to their porosity. It should be noted that the porosity measured was in fact the total porosity, which takes into account all of the voids space. A more realistic

indicator of the porosity ranking of reservoir rock would be to measure the effective porosity because it pertains to the porosity that is accessible to free fluids. Another issue with the determination of porosity as completed for this project is that the value is based on a 2-D image only. A more accurate porosity measurement would involve using core plugs in which the values obtained would be 3-D based and would therefore be more representative of the sample porosity.

Additionally, the measurement of porosity based on an image can also be greatly flawed when selecting the void space in the image. For this study, the thin sections had a blue dye applied to them such that when selecting the void spaces, any shade of blue from light to dark was selected. In reality, there may have been grains that exhibited a light blue colour as well, but these would have been selected as representing porous areas; thus, leading to an overestimated porosity value. Fractures and bubbles in the slides as a result of thin section preparation could have also added to inaccurate porosity values by way of the accumulation of blue dye; however, these areas of the slides were avoided wherever possible so as to not skew the results.

8.0 Conclusions

The characterization of a reservoir by way of its architecture and performance is a highly useful tool that not only the reservoir engineer will use and various other engineering and science-related professional will use, but organizations as well who bare the brunt of the financial risk associated with a project. As the role of a reservoir engineer is, in part, to predict the performance of the reservoir while also deducing a logical and lower risk production scenario during operation, they must be able to interact with and convey their ideas to a fully integrated and multi-disciplinary team. Regardless of whether or not a reservoir can sustain the production of oil and/or gas, it is nonetheless important to have a confidence in the data that exists as well as the model that represents it. A reservoir is a highly complex assemblage of lithologies that contain heterogeneities down to the microscopic level. As such, information about the reservoir in question might come from core samples, various well tests, reservoir and outcrop analogues and seismic, just to name a few. Despite all of these information sources, there will always be unknowns associated with a reservoir. For example, the porosity and permeability values that were obtained from the study of the outcrop indicate the permeability is highly variable and the porosity is fairly low. However, these properties might be extremely different if you could study the lithologies further inland and at depth. It is difficult to know exactly how an outcrop that is exposed to atmospheric conditions will differ from an equivalent lithological unit that is at some depth and not exposed to surface conditions.

9.0 Future Work

Since the scope of this M.Eng project was constrained by time and certain objectives, it was not necessary to make full use of the data collected. However, the data that was collected, whether used or not could be applied to a variety of future projects at the masters or doctorate level. The scope of the project as proposed by Dr. Grant Wach entailed phases I to III in Table 9-1. Possible ideas for future work follow from IV to VIII.

Table 9-1: Work tasks completed and possible ideas for future work pertaining to the Joggins Formation fluvial meanderbelt system.

Phase	Task
I	Collect field data using GPR, LIDAR, DGPS, scintillometer, permeameter in addition to hand samples.
II	Construct a geological model of the data using Petrel software.
III	Perform a reservoir simulation using ECLIPSE software in Petrel.
	End of M.Eng Project; Ideas for Future Work
IV	Attempt a GPR survey using 25 MHz antennae and compare with 50 MHz and 100 MHz.
V	Perform a fluid flow simulation using Petrel/ECLIPSE software.
VI	Obtain core plugs for a detailed petrographic study and fluid flow testing.
VII	Paleoclimate study/model.
VIII	Vegetation density/model of the Carboniferous forest.
IX	Performance and architecture of fixed or multi-story channel systems.

Phases I - III are complete and are included in this project report. All the data collected will be made available should further work be pursued. The appendices in this report provide much of the information collected.

Apart from the 50, 100 and 200 MHz antennae that can be used for collecting data, the department also has 25 MHz antennae available. These have not been utilized in any of the past research carried out using GPR; therefore, it might make a good project to re-run the GPR lines at Joggins with the 25 MHz antennae and compare those results with the images in this report.

A fluid flow simulation using Petrel/ECLIPSE software could be another potential project idea, especially if it was paired with a study of core plugs and fluid testing of the core plugs. The Department of Chemical Engineering has the specialized equipment that would be

necessary for carrying out fluid testing using different types of fluids. Various experiments could be performed using differ API gravity oil or various types of gases along with the application of enhanced recovery techniques, such as flooding the core plug with water in an attempt to increase recovery. By doing so, the data collected could be imported into Petrel/ECLIPSE and the designing of production/injection wells could be done.

Additionally, a paleoclimate study paired with a vegetation density study could result in a very interesting project as well. For a project of this type to be successful, there would have to be several more scans performed on the Fundy Forest area of the Joggins section taken over the next few years. There are some previous scans that were performed at Joggins; however, some of these scans were done so without the placement of the LIDAR targets; thus making the georeferencing of these scans nearly impossible. If a couple scans were done each year at Joggins, then within a few years, there would likely be sufficient data available to determine the vegetation density of the Carboniferous forest that existed at the time.

10.0 References

Allen, P.A., and Allen, J.R. (2005). *Basin Analysis: Principles and Applications*. Malden: Blackwell Publishing.

Bano, M., Marquis, G., Niviere, B., Maurin, J.C., & Cushing, M. (2000). Investigating alluvial and tectonic features with ground-penetrating RADAR and analyzing diffractions patterns. *Journal of Applied Geophysics*, 43, 33 – 41. Retrieved from <http://www.sciencedirect.com/science/article/pii/S0926985199000312>.

Boehner, R.C., Calder, J.H., Carter, D.C., Donohoe, H.V., Ferguson, L., Pickerall, R.K., & Ryan, R.J. (1986). Carboniferous-Jurassic Sedimentation and Tectonics: Minas, Cumberland and Moncton Basins, Nova Scotia and New Brunswick. *Atlantic Geoscience Society, Special Publication No. 4*, 122.

Browne, B & Plint, G. (1994). Alternating Braidplain and Lacustrine Deposition in a Strike-Slip Setting: The Pennsylvanian Boss Point Formation of the Cumberland Basin, Maritime Canada. *Journal of Sedimentary Research*, 64(1), 1073-1318.

Burger, R.H., Sheehan, A.F., and Jones, C.H. (2006). *Introduction to Applied Geophysics*. New York: W.W. Norton & Company, Inc.

Calder, J.H. (1994). The Impact of Climate Change, Tectonism and Hydrology on the Formation of Carboniferous Tropical Intermontane Mires: The Springhill Coalfield, Cumberland Basin, Nova Scotia. *Palaeogeography, Palaeoclimatology, Palaeoecology*, 106, 323-351.

Charlton, Ro. (2008). *Fundamentals of Fluvial Geomorphology*. New York: Routledge.

Chivers, M. (n.d.). *Differential GPS Explained*. Retrieved from <http://www.esri.com/news/arcuser/0103/differential1of2.html>.

Cope, D. (n.d.). *Climbing ripples*. [Digital photograph], Retrieved from: <http://acad.depauw.edu/tcope/SedStruct.html>.

Copeland, M.J. (1959). Coalfields of the west half of Cumberland Basin, Nova Scotia. *Geological Survey of Canada, Memoir 298*, 89.

Davies, D.K., Williams, B.P.J., & Vessell, R.K. (1992). Models for Meandering and Braided Fluvial Reservoirs With Examples from the Travis Peak Formation, East Texas. *Proceedings from the SPE Annual Technical Conference and Exhibition, USA*, 321-329. Retrieved from <http://www.onepetro.org/mslib/servlet/onepetropreview?id=00024692>.

Davies, S.J., Gibling, M.R. (2003). Architecture of Coastal and Alluvial Deposits in an Extensional Basin: The Carboniferous Joggins Formation of Eastern Canada. *Sedimentology*, 50, 415-439.

Davies, S.J., Gibling, M.R., Rygel, M.C., Calder, J.H., & Skilliter, D.M. (2005). The Pennsylvanian Joggins Formation of Nova Scotia: Sedimentological Log and Stratigraphic Framework of the Historic Fossil Cliffs. *Atlantic Geology*, 41, 115-142.

Dennar, C.I. (2012). *Vegetation Influence in Strengthening Channel Banks in the Pennsylvanian Joggins Formation, Nova Scotia*. (Undergraduate Honours Thesis). Department of Earth Sciences, Dalhousie University, Canada.

Deschamps, R., Guy, N., Preux, C., & Lerat, O. (2011). Impact of Upscaling on 3-D Modelling of SAGD in a Meander Belt. *Proceedings of the SPE Annual Technical Conference and Exhibition, USA*, 1-16. Retrieved from <http://www.onepetro.org/mslib/servlet/onepetropreview?id=SPE-147035-MS>.

Dietrich, J., Hannigan, P. & Hu, K. (2009). Petroleum Resource Potential of the Carboniferous Maritimes Basin, Eastern Canada. *Proceedings from the 2009 CSPG CSEG CWLS Convention, Canada*, 34-36. Retrieved from <http://www.cspg.org/documents/conventions/archives/annual/2009/164.pdf>.

Duff, J. (2013). *Ripple marks*. [Digital photograph], Retrieved August 1st, 2013 from: <http://thenaturalhistorian.com/2013/06/04/trip-to-joggins-fossil-cliffs-nova-scotia-polystrate-trees/>.

Jones, D. (Ed.). (2010). *The Light Fantastic: Using Airborne LIDAR in Archaeological Survey*. Swindon: English Heritage. Retrieved from <http://www.english-heritage.org.uk/publications/light-fantastic/light-fantastic.pdf>.

Fisheries and Oceans Canada. (2013). *Joggins (#215) – 7 Days Tidal Predictions*. Retrieved from <http://www.tides.gc.ca/eng/station?sid=215>.

Gibling, M. (2006). Width and Thickness of Fluvial Channel Bodies and Valley Fills in the Geological Record: A Literature Compilation and Classification. *Journal of Sedimentary Research*, 76, 731-770.

Giles, P.S. (1981). Major Transgressive-Regressive Cycles in Middle to Late Visean Rocks of Nova Scotia. *Nova Scotia Department of Mines and Energy, Paper 81-2*.

Gluyas, J., and Swarbrick, R. (2004). *Petroleum Geoscience*. Malden: Blackwell Publishing.

Google Earth. (2013). Google Earth Images. [Aerial and Satellite Images].

Lapoux, S., Noor, O. & Ropert, P. (2011). *Shale*. [Digital photograph], Retrieved July 30th, 2013 from: <http://owni.eu/2011/02/14/shale-gas-energy-revolution-or-ecological-threat/>.

Leica Geosystems. (2012). *News – Leica Geosystems News Overview*. Retrieved from http://www.leica-geosystems.com/en/News_360.htm?id=4208.

Lorz, C. & Makeschin, F. (2012). *Alluvial floodplain soil near R. Torto, North of Brasilia*. [Digital photograph], Retrieved July 30th, 2013 from: <http://www.ufz.de/iwas-sachsen/index.php?en=19650>.

Martel, A.T. (1987). Seismic Stratigraphy and Hydrocarbon Potential of the Strike-Slip Sackville Sub-basin, New Brunswick. *Atlantic Geoscience Society, Special Publication No. 5*, 319-334.

Miall, A. (2010). Alluvial Deposits. In N.P. James (Ed.) & R.W. Dalrymple (Ed.), *Facies Models 4* (pp. 105-137). St. John's: Geological Association of Canada.

Mulcahy, P. (2006). *Reservoir Modeling and Simulation of a Braided Channel Complex at Cambridge Cove, Nova Scotia*. (Master of Engineering Thesis). Department of Engineering, Dalhousie University, Canada.

Nabaway, B.S., Rochette, P. & Geraud, Yves. (2009). Petrophysical and magnetic pore network anisotropy of some cretaceous sandstone from Tushka Basin, Egypt. *Geophysics Journal International*, 177, 43-61.

National Oceanic and Atmospheric Administration (NOAA) Coastal Services Center. (2012). *LIDAR 101: An Introduction to LIDAR Technology, Data, and Applications*. Revised. Charleston, SC: NOAA Coastal Services Center.

New England Research, Inc. (2013). *TinyPerm II – Portable Permeameter*. [Brochure]. White River Junction, Vermont: Author. Retrieved from <http://ner.com/pdf/tinyperm.pdf>.

Nickerson, J. (2010). *Architecture and geometry of braided channel complex in the Triassic Wolfville Formation* (Undergraduate Honours Thesis). Department of Earth Sciences, Dalhousie University, Canada.

Plummer, N. (2013). *Mudcracks*. [Digital photograph].

Prothero, D.R., and Schwab, Fred. (2004). *Sedimentary Geology: An Introduction to Sedimentary Rocks and Stratigraphy*. New York: W.H. Freeman and Company.

Prothero, D.R. & Schwab, F. (2004). *Sedimentary Geology: An Introduction to Sedimentary Rocks and Stratigraphy*, 2nd Edition. New York: W.H. Freeman and Company.

Rafuse, C. & Wach, G. (2011). *Reservoir architecture of meanderbelt systems and vegetation density in Carboniferous using LIDAR imagery*. (Undergraduate directed studies project). Department of Earth Sciences, Dalhousie University, Canada.

Ranney, W. (2009). *Rip-up clasts in the fluvial Kayenta Formation*. [Digital photograph], Retrieved July 30th, 2013 from: http://earthly-musings.blogspot.ca/2009_05_01_archive.html.

Rogiers, B., Beerten, K., Smeekens, T., Mallants, D., Gedeon, M., Huysmans, M., Batelaan, O. & Dessargues, A. (2013). The usefulness of outcrop analogue air permeameter measurements for analysing aquifer heterogeneities: testing outcrop hydrogeological parameters with independent borehole data. *Hydrology and Earth System Sciences*, 10, 9689-9720. Retrieved August 26th, 2013 from: <http://www.hydrol-earth-syst-sci-discuss.net/10/9689/2013/hessd-10-9689-2013-print.pdf>.

Ryan, R.J. & Boehner, R.C. (1994). Geology of the Cumberland Basin, Cumberland, Colchester and Pictou Counties, Nova Scotia. *Nova Scotia Department of Natural Resources – Mines and Energy Branches, Memoir 10*.

Ryan, R.J., Calder, J.H., Donohoe, H.V., & Naylor, R. (1987). Late Paleozoic Sedimentation and Basin Development Adjacent to the Cobequid Highlands Massif, Eastern Canada. *Sedimentary Basins and Basin-Forming Mechanisms, Memoir 12*, 311-317.

Rygel, M.C. (2005). *Alluvial sedimentology and basin analysis of Carboniferous strata near Joggins, Nova Scotia, Atlantic Canada* (Doctoral dissertation). Department of Earth Sciences, Dalhousie University, Canada.

Rygel, M.C. & Gibling, M.R. (2006). Natural Geomorphic Variability Recorded in a High-Accommodation Setting: Fluvial Architecture of the Pennsylvanian Joggins Formation of Atlantic Canada. *Journal of Sedimentary Research*, v. 76, 1230-1251.

Schlumberger Limited. (2013). *Oilfield Glossary*. Retrieved from <http://www.glossary.oilfield.slb.com/>.

Selley, R.C. (2000). *Applied Sedimentology*, 2nd Edition. New York: Academic Press.

Sensors and Software Inc. (2003). *EKKO_View Enhanced and EKKO_View Deluxe*. [User Guide]. Mississauga, Ontario: Author.

Sumner, D. (n.d.). *Ancient trough cross-stratification*. [Digital photograph], Retrieved July 30th, 2013 from: <http://mygeologypage.ucdavis.edu/sumner/gel109/sedstructures/Dunes.html>.

Sumner, D. (2008). *Rivers – Meandering and Braided*. Personal collection of D. Sumner, University of California at Davis, Davis, California. Retrieved from <https://www.geology.ucdavis.edu/weblog/gel1109group/LectureNotes2010/2010/02/01/Rivers.html>.

Trenhaile, A.S. (2010). *Geomorphology: A Canadian Perspective*. Toronto: Oxford University Press.

Vaughan, M. (2011). *High resolution RADAR stratigraphy (GPR) of braided channel complexes in the Triassic Wolfville Formation – Controls on reservoir heterogeneity*. (Undergraduate Honours Thesis). Department of Earth Sciences, Dalhousie University, Canada.

Wach, Grant. (2013). *Joggins Photographs*. [Digital photographs].

Waldron, J., & Rygel, M. (2005). Role of evaporate withdrawal in the preservation of a unique coal-bearing succession: Pennsylvanian Joggins Formation, Nova Scotia. *Geological Society of America*, 33(5), 337-340.

11.0 Appendix A: LIDAR Technical Information

Table 11-1: Base station setup technical information.

Point ID:	Base Station		
Description:	Location of base station over well cap at the Joggins Fossil Center.		
Class:	REF		
Subclass:	Fixed (Pos & Ht)		
3D CQ:	0.000 m		
WGS84 Lat:	45°41'40.15186" N	Easting:	387,098.72 m
WGS84 Long:	64°27'00.38670" W	Northing:	5,061,126.31 m
WGS84 Ell Ht:	26.453 m		
Antenna:	AX1202 Pole		
Ref Stn Ht:	2.019 m		
Time:	11:23:03 AM		
Date:	30.05.13 (D.M.Y)		
Instrument:	GPS		
Source:	Survey (Static)		
Coords:	X = 1,924,749.698 m Y = - 4,026,295.004 m Z = 4,541,612.735 m		



Figure 11-1: Aerial photograph showing the approximate location of the base station near the Joggins Fossil Centre (Google Earth, 2013). Scale is 1cm = 20 m.

Table 11-2: LIDAR unit setup # 1 technical information.

Point ID:	LIDAR Setup # 1		
Description:	Location of the LIDAR unit setup on Day 1 @ Fundy Forest.		
Class:	MEAS		
Subclass:	GPS Fixed		
3D CQ:	0.015 m		
WGS84 Lat:	45°42'14.92280" N	Easting:	387,651.32 m
WGS84 Long:	64°26'35.72715" W	Northing:	5,062,189.74 m
WGS84 Ell Ht:	0.829 m		
Time:	11:24:04 AM		
Date:	30.05.13 (D.M.Y)		
Instrument:	GPS		
Source:	Survey (Static)		
Coords:	X = 1,924,891.873 m Y = - 4,025,355.596 m Z = 4,542,344.162 m		



Figure 11-2: Aerial photograph showing the approximate location of LIDAR Setup # 1 near the location of the Fundy Forest (Google Earth, 2013). Scale is 1cm = 27 m.

Table 11-3: First scan; left target (if viewing from the water) technical information.

Point ID:	Scan # 1 Left Target		
Description:	Location of the left target as viewing the cliff face from the water.		
Class:	MEAS		
Subclass:	GPS Fixed		
3D CQ:	0.025 m		
WGS84 Lat:	45°42'14.20119" N	Easting:	387,711.24 m
WGS84 Long:	64°26'32.94191" W	Northing:	5,062,166.38 m
WGS84 Ell Ht:	6.676 m		
Time:	11:28:57 AM		
Date:	30.05.13 (D.M.Y)		
Instrument:	GPS		
Source:	Survey (Static)		
Coords:	X = 1,924,954.869 m Y = - 4,025,347.673 m Z = 4,542,332.788 m		

Table 11-4: First scan; middle target (if viewing from the water) technical information.

Point ID:	Scan # 1 Middle Target		
Description:	Location of the middle target as viewing the cliff face from the water.		
Class:	MEAS		
Subclass:	GPS Fixed		
3D CQ:	0.061 m		
WGS84 Lat:	45°42'12.42506" N	Easting:	387,633.71 m
WGS84 Long:	64°26'36.48252" W	Northing:	5,062,112.95 m
WGS84 Ell Ht:	6.156 m		
Time:	12:03:03 PM		
Date:	30.05.13 (D.M.Y)		
Instrument:	GPS		
Source:	Survey (Static)		
Coords:	X = 1,924,902.547 m Y = - 4,025,415.796 m Z = 4,542,294.120 m		

Table 11-5: First scan; right target (if viewing from the water) technical information.

Point ID:	Scan # 1 Right Target		
Description:	Location of the right target as viewing the cliff face from the water.		
Class:	MEAS		
Subclass:	GPS Fixed		
3D CQ:	0.032 m		
WGS84 Lat:	45°42'09.95918" N	Easting:	387,475.35 m
WGS84 Long:	64°26'43.74114" W	Northing:	5,062,039.68 m
WGS84 Ell Ht:	6.427 m		
Time:	11:38:02 AM		
Date:	30.05.13 (D.M.Y)		
Instrument:	GPS		
Source:	Survey (Static)		
Coords:	X = 1,924,784.475 m Y = - 4,025,532.862 m Z = 4,542,241.146 m		



Figure 11-3: Aerial photograph showing the approximate location of the LIDAR Setup # 1 georeferencing targets (Google Earth, 2013). Scale is 1cm = 27 m.

Table 11-6: LIDAR unit setup # 2 technical information.

Point ID:	LIDAR Setup # 2		
Description:	Location of the LIDAR setup on Day 2 near the Joggins Fossil Centre.		
Class:	MEAS		
Subclass:	GPS Fixed		
3D CQ:	0.015 m		
WGS84 Lat:	45°41'46.46719" N	Easting:	386,989.29 m
WGS84 Long:	64°27'05.60951" W	Northing:	5,061,323.25 m
WGS84 Ell Ht:	2.258 m		
Time:	10:08:20 AM		
Date:	31.05.13 (D.M.Y)		
Instrument:	GPS		
Source:	Survey (Static)		
Coords:	X = 1,924,580.283 m Y = - 4,026,202.602 m Z = 4,541,731.607		



Figure 11-4: Aerial photograph showing the approximate location of LIDAR Setup # 2. (Google Earth, 2013). Scale is 1cm = 27 m.

Table 11-7: Second scan; left target (if viewing from the water) technical information.

Point ID:	Scan # 2 Left Target		
Description:	Location of the left target as viewing the cliff face from the water.		
Class:	MEAS		
Subclass:	GPS Fixed		
3D CQ:	0.021 m		
WGS84 Lat:	45°41'49.13292" N	Easting:	387,047.88 m
WGS84 Long:	64°27'02.97314" W	Northing:	5,061,404.49 m
WGS84 Ell Ht:	6.394 m		
Time:	09:55:28 AM		
Date:	31.05.13 (D.M.Y)		
Instrument:	GPS		
Source:	Survey (Static)		
Coords:	X = 1,924,607.587 m Y = - 4,026,127.470 m Z = 4,541,792.051 m		

Table 11-8: Second scan; middle target (if viewing from the water) technical information.

Point ID:	Scan # 2 Middle Target		
Description:	Location of the middle target as viewing the cliff face from the water.		
Class:	MEAS		
Subclass:	GPS Fixed		
3D CQ:	0.015 m		
WGS84 Lat:	45°41'45.89776" N	Easting:	387,051.04 m
WGS84 Long:	64°27'02.73665" W	Northing:	5,061,304.56 m
WGS84 Ell Ht:	5.461 m		
Time:	09:59:16 AM		
Date:	31.05.13 (D.M.Y)		
Instrument:	GPS		
Source:	Survey (Static)		
Coords:	X = 1,924,642.751 m Y = - 4,026,189.166 m Z = 4,541,721.620 m		

Table 11-9: Second scan; right target (if viewing from the water) technical information.

Point ID:	Scan # 2 Right Target		
Description:	Location of the right target as viewing the cliff face from the water.		
Class:	MEAS		
Subclass:	GPS Fixed		
3D CQ:	0.019 m		
WGS84 Lat:	45°41'41.38329" N	Easting:	387,057.38 m
WGS84 Long:	64°27'02.33456" W	Northing:	5,061,165.07 m
WGS84 Ell Ht:	6.737 m		
Time:	10:02:32 AM		
Date:	31.05.13 (D.M.Y)		
Instrument:	GPS		
Source:	Survey (Static)		
Coords:	X = 1,924,694.002 m Y = - 4,026,276.208 m Z = 4,541,625.181 m		



Figure 11-5: Aerial photograph showing the approximate location of the LIDAR Setup # 2 georeferencing targets (Google Earth, 2013). Scale is 1cm = 27 m.

Table 11-10: LIDAR unit setup # 3 technical information.

Point ID:	LIDAR Setup # 3		
Description:	Location of the LIDAR setup on Day 2 near Hardscrabble Point.		
Class:	MEAS		
Subclass:	GPS Fixed		
3D CQ:	0.023 m		
WGS84 Lat:	45°41'57.87993" N	Easting:	386,962.38 m
WGS84 Long:	64°27'07.14929" W	Northing:	5,061,676.07 m
WGS84 Ell Ht:	-1.240 m		
Time:	12:26:32 PM		
Date:	31.05.13 (D.M.Y)		
Instrument:	GPS		
Source:	Survey (Static)		
Coords:	X = 1,924,440.421 m Y = - 4,025,987.253 m Z = 4,541,975.203 m		



Figure 11-6: Aerial photograph showing the approximate location of LIDAR Setup # 3 near Hardscrabble Point / Coal Mine Point (Google Earth, 2013). Scale is 1cm = 30 m.

Table 11-11: Third scan; left target (if viewing from the water) technical information.

Point ID:	Scan # 3 Left Target		
Description:	Location of the left target as viewing the cliff face from the water.		
Class:	MEAS		
Subclass:	GPS Fixed		
3D CQ:	0.026 m		
WGS84 Lat:	45°41'58.86683" N	Easting:	387,069.97 m
WGS84 Long:	64°27'02.19604" W	Northing:	5,061,704.58 m
WGS84 Ell Ht:	3.875 m		
Time:	12:23:37 PM		
Date:	31.05.13 (D.M.Y)		
Instrument:	GPS		
Source:	Survey (Static)		
Coords:	X = 1,924,529.237 m Y = - 4,025,924.587 m Z = 4,542,000.144 m		

Table 11-12: Third scan; middle target (if viewing from the water) technical information.

Point ID:	Scan # 3 Middle Target		
Description:	Location of the middle target as viewing the cliff face from the water.		
Class:	MEAS		
Subclass:	GPS Fixed		
3D CQ:	0.023 m		
WGS84 Lat:	45°41'56.98459" N	Easting:	387,039.72 m
WGS84 Long:	64°27'03.55149" W	Northing:	5,061,647.03 m
WGS84 Ell Ht:	3.055 m		
Time:	12:22:05 PM		
Date:	31.05.13 (D.M.Y)		
Instrument:	GPS		
Source:	Survey (Static)		
Coords:	X = 1,924,520.471 m Y = - 4,025,974.240 m Z = 4,541,958.970 m		

Table 11-13: Third scan; right target (if viewing from the water) technical information.

Point ID:	Scan # 3 Right Target		
Description:	Location of the right target as viewing the cliff face from the water.		
Class:	MEAS		
Subclass:	GPS Fixed		
3D CQ:	0.016 m		
WGS84 Lat:	45°41'56.58706" N	Easting:	386,989.33 m
WGS84 Long:	64°27'05.86754" W	Northing:	5,061,635.67 m
WGS84 Ell Ht:	1.036 m		
Time:	12:20:40 PM		
Date:	31.05.13 (D.M.Y)		
Instrument:	GPS		
Source:	Survey (Static)		
Coords:	X = 1,924,478.445 m Y = - 4,026,002.502 m Z = 4,541,948.953 m		



Figure 11-7: Aerial photograph showing the approximate location of the LIDAR Setup # 3 georeferencing targets near Hardscrabble Point / Coal Mine Point (Google Earth, 2013). Scale is 1cm = 30 m.

LIDAR Scan Setup and Technical Information:

Table 11-14: Various distances from the LIDAR unit to cliff face, targets and base station.

Setup #	Parameter	Distance (m)
LIDAR Setup # 1	Distance to cliff face	~ 58
	Distance to left target	~ 64
	Distance to middle target	~ 79
	Distance to right target	~ 231
	Distance to base station	~ 1,198
LIDAR Setup # 2	Distance to cliff face	~ 80
	Distance to left target	~ 100
	Distance to middle target	~ 64
	Distance to right target	~ 173
	Distance to base station	~ 226
LIDAR Setup # 3	Distance to cliff face	~ 75
	Distance to left target	~ 112
	Distance to middle target	~ 83
	Distance to right target	~ 49
	Distance to base station	~ 567



Figure 11-8: Aerial photograph showing the setup locations of the LIDAR unit, targets and base station. Scale is 1 cm = 13 m.

Table 11-15: Scan to the north of Hardscrabble / Coal Mine Point technical information.

Parser version:	5.0.0.3
Name of scan project:	C:\Documents and settings\Grant Wach\Desktop\Joggins Parsing Modified\Hardscrabble Point\
Time stamp:	Fri May 31 12:50:23 2013 (UTC, 1370004623)
Horizontal angle resolution (uRad):	20
Vertical angle resolution (uRad):	20
Meta header version:	3
Unit title:	ILRIS-3D
Unit serial number:	SN010371
Unit software version:	5.0.10.10-FBCntrlWin
Controller ID:	CntrlWin
Controller version:	5.0.0.4
GRP point:	(386962.000531, 5061676.004664, -1.235210)
Applies ASC correction:	Yes
Trims shot data:	Yes
Applies ric correction:	Yes
Smooth's polar shot data:	No
Reduces shot data:	No

Table 11-16: Hardscrabble / Coal Mine Point – scan to the north – scan task ID 107 technical information.

Scan task ID:	107
Number of shots:	2483052
Number of scan lines:	1716
Points per line:	1447
Number of loops:	1
Scan task mode:	Scan
Pulse mode:	First pulse
Scan pattern:	Step stare
Shot type:	Shot I3D
Scan start position:	Lower left
Scan orientation:	Horizontal
Scan in ER mode:	No
ROI ID:	107
ROI start point:	(-3.212448, -9.426529)
ROI stop point:	(20.000000, 18.092724)
Average range:	97.32
X spot spacing (counts/mm):	14/27.2
Y shot spacing (counts/mm):	14/27.2

Table 11-17: Hardscrabble / Coal Mine Point – scan to the north – scan task ID 108 technical information.

Scan task ID:	108
Number of shots:	4279704
Number of scan lines:	1716
Points per line:	2494
Number of loops:	1
Scan task mode:	Scan
Pulse mode:	First pulse
Scan pattern:	Step stare
Shot type:	Shot I3D
Scan start position:	Lower left
Scan orientation:	Horizontal
Scan in ER mode:	No
ROI ID:	108
ROI start point:	(-20.000000, -9.426529)
ROI stop point:	(20.000000, 18.092724)
Average range:	86.47
X spot spacing (counts/mm):	14/24.2
Y shot spacing (counts/mm):	14/24.2

Table 11-18: Hardscrabble / Coal Mine Point – scan to the north – scan task ID 109 technical information.

Scan task ID:	109
Number of shots:	4279704
Number of scan lines:	1716
Points per line:	2494
Number of loops:	1
Scan task mode:	Scan
Pulse mode:	First pulse
Scan pattern:	Step stare
Shot type:	Shot I3D
Scan start position:	Lower left
Scan orientation:	Horizontal
Scan in ER mode:	No
ROI ID:	109
ROI start point:	(-20.000000, -9.426529)
ROI stop point:	(20.000000, 18.092724)
Average range:	68.91
X spot spacing (counts/mm):	14/19.3
Y shot spacing (counts/mm):	14/19.3

Table 11-19: Hardscrabble / Coal Mine Point – scan to the north – scan task ID 110 technical information.

Scan task ID:	110
Number of shots:	3505788
Number of scan lines:	1716
Points per line:	2043
Number of loops:	1
Scan task mode:	Scan
Pulse mode:	First pulse
Scan pattern:	Step stare
Shot type:	Shot I3D
Scan start position:	Lower left
Scan orientation:	Horizontal
Scan in ER mode:	No
ROI ID:	110
ROI start point:	(-20.000000, -9.426529)
ROI stop point:	(12.760422, 18.092724)
Average range:	47.74
X spot spacing (counts/mm):	14/13.4
Y shot spacing (counts/mm):	14/13.4

Table 11-20: Scan to the south of Hardscrabble / Coal Mine Point technical information.

Parser version:	5.0.0.3
Name of scan project:	C:\Documents and settings\Grant Wach\Desktop\Joggins Parsing – original\Scan at end of Main Street
Time stamp:	Fri May 31 11:29:22 2013 (UTC, 1369999762)
Horizontal angle resolution (uRad):	20
Vertical angle resolution (uRad):	20
Meta header version:	3
Unit title:	ILRIS-3D
Unit serial number:	SN010371
Unit software version:	5.0.10.10-FBCntrlWin
Controller ID:	CntrlWin
Controller version:	5.0.0.4
GRP point:	(386989.000531, 5061323.004664, 2.262789)
Applies ASC correction:	Yes
Trims shot data:	Yes
Applies ric correction:	Yes
Smooth's polar shot data:	No
Reduces shot data:	No

Table 11-21: Hardscrabble / Coal Mine Point – scan to the south – scan task ID 105 technical information.

Scan task ID:	105
Number of shots:	4039087
Number of scan lines:	1157
Points per line:	3491
Number of loops:	1
Scan task mode:	Scan
Pulse mode:	First pulse
Scan pattern:	Step stare
Shot type:	Shot I3D
Scan start position:	Lower left
Scan orientation:	Horizontal
Scan in ER mode:	No
ROI ID:	105
ROI start point:	(-20.000000, -2.494947)
ROI stop point:	(20.000000, 10.757889)
Average range:	79.96
X spot spacing (counts/mm):	10/16.0
Y shot spacing (counts/mm):	10/16.0

Table 11-22: Hardscrabble / Coal Mine Point – scan to the south – scan task ID 106 technical information.

Scan task ID:	106
Number of shots:	4039087
Number of scan lines:	1157
Points per line:	3491
Number of loops:	1
Scan task mode:	Scan
Pulse mode:	First pulse
Scan pattern:	Step stare
Shot type:	Shot I3D
Scan start position:	Lower left
Scan orientation:	Horizontal
Scan in ER mode:	No
ROI ID:	106
ROI start point:	(-20.000000, -2.494947)
ROI stop point:	(20.000000, 10.757889)
Average range:	115.02
X spot spacing (counts/mm):	10/23.0
Y shot spacing (counts/mm):	10/23.0

Table 11-23: Hardscrabble / Coal Mine Point – scan to the south – scan task ID 107 technical information.

Scan task ID:	107
Number of shots:	3664219
Number of scan lines:	1157
Points per line:	3167
Number of loops:	1
Scan task mode:	Scan
Pulse mode:	First pulse
Scan pattern:	Step stare
Shot type:	Shot I3D
Scan start position:	Lower left
Scan orientation:	Horizontal
Scan in ER mode:	No
ROI ID:	107
ROI start point:	(-20.000000, -2.494947)
ROI stop point:	(16.289635, 10.757889)
Average range:	188.04
X spot spacing (counts/mm)	10/37.6
Y shot spacing (counts/mm)	10/37.6

Table 11-24: Hardscrabble / Coal Mine Point – scan to the south – scan task ID 137 technical information.

Scan task ID:	137
Number of shots:	1433781
Number of scan lines:	837
Points per line:	1713
Number of loops:	1
Scan task mode:	Scan
Pulse mode:	First pulse
Scan pattern:	Step stare
Shot type:	Shot I3D
Scan start position:	Lower left
Scan orientation:	Horizontal
Scan in ER mode:	No
ROI ID:	137
ROI start point:	(0.380692, 0.120745)
ROI stop point:	(20.000000, 9.711613)
Average range:	225.80
X spot spacing (counts/mm):	10/45.2
Y shot spacing (counts/mm):	10/45.2

Table 11-25: Hardscrabble / Coal Mine Point – scan to the south – scan task ID 138 technical information.

Scan task ID:	138
Number of shots:	2921967
Number of scan lines:	837
Points per line:	3491
Number of loops:	1
Scan task mode:	Scan
Pulse mode:	First pulse
Scan pattern:	Step stare
Shot type:	Shot I3D
Scan start position:	Lower left
Scan orientation:	Horizontal
Scan in ER mode:	No
ROI ID:	138
ROI start point:	(-20.000000, 0.120745)
ROI stop point:	(20.000000, 9.711613)
Average range:	132.10
X spot spacing (counts/mm):	10/26.4
Y shot spacing (counts/mm):	10/26.4

Table 11-26: Hardscrabble / Coal Mine Point – scan to the south – scan task ID 139 technical information.

Scan task ID:	139
Number of shots:	2916945
Number of scan lines:	837
Points per line:	3485
Number of loops:	1
Scan task mode:	Scan
Pulse mode:	First pulse
Scan pattern:	Step stare
Shot type:	Shot I3D
Scan start position:	Lower left
Scan orientation:	Horizontal
Scan in ER mode:	No
ROI ID:	139
ROI start point:	(-20.000000, 0.120745)
ROI stop point:	(19.929901, 9.711613)
Average range:	96.61
X spot spacing (counts/mm):	10/19.3
Y shot spacing (counts/mm):	10/19.3

12.0 Appendix B: GPR Technical Information

System Setup Summary:

Table 12-1: Ground penetrating radar system setup summary

----GPR Parameters----	
Antenna Frequency	50.0 MHz
Antenna Separation	1.000 metres
Assumed Velocity	0.100 m/ns
	0.328 ft/ns
Time Window	400.00 ns
Number of Points	250
Sample Interval	1.60 ns
System Stacking	32
Pulser Settings	Auto PRO
----Acquisition Control----	
Triggering Method	Odometer
Trace Delay	0.0 sec
Odometer Calibration	1045.75 forward
Beeper Active	None
Data Storage	Removable
GPS Usage	Every Trace
GPS Baud Rate	19200
GPS Transfer Bits	1s 8d N
GPS End String	\$GPRMC
----Survey Parameters----	
Start Position	0.00 metres
Antenna Step Size	0.100 metres
Position Units	Metric
Data Directory #	8
Survey Type	Reflection
Grid Survey Type	X – Y
X Line Spacing	1.00 metres
Y Line Spacing	1.00 metres
----Display Parameters----	
Trace Type	Grey Scale
Trace Spacing	8 pixels
Gain Type Applied	SEC

Table 12-2: GPR survey data pertaining to each survey line.

Line #	Units	Line Length	Step Size	Antenna Separation	Frequency (MHz)	# Traces	Min Elev.	Max Elev.
Line09	m	71.5	0.5	1.0	50.0	144.0	45.55	47.47
Line10	m	100.5	0.5	1.0	50.0	202.0	43.69	45.51
Line11	m	107.5	0.5	1.0	50.0	216.0	41.01	43.68
Line12	m	67.5	0.5	1.0	50.0	136.0	39.02	40.98
Line13	m	145.5	0.5	1.0	50.0	292.0	36.79	38.99
Line14	m	44.0	0.5	1.0	50.0	89.0	36.73	36.96
Line15	m	120.5	0.5	1.0	50.0	242.0	36.69	37.01
Line16	m	87.0	0.5	1.0	50.0	175.0	37.03	38.22
Line17	m	95.0	0.5	1.0	50.0	191.0	38.22	41.56
Line18	m	156.5	0.5	1.0	50.0	314.0	41.57	44.49
Line19	m	65.0	0.5	1.0	50.0	131.0	44.49	44.85
Line20	m	102.0	0.5	1.0	50.0	205.0	42.95	44.74
Line21	m	79.0	0.5	1.0	50.0	159.0	41.93	42.97
Line22	m	105.0	0.5	1.0	50.0	211.0	38.33	41.92
Line23	m	93.0	0.5	1.0	50.0	187.0	32.20	38.31
Line24	m	100.5	0.5	1.0	50.0	202.0	24.23	32.18
Line25	m	92.0	0.5	1.0	50.0	185.0	17.93	24.18
Line26	m	34.0	0.5	1.0	50.0	69.0	16.97	17.90
Line27	m	77.0	0.5	1.0	50.0	155.0	17.20	23.45
Line28	m	64.5	0.5	1.0	50.0	130.0	23.47	25.48
Line29	m	65.5	0.5	1.0	50.0	132.0	24.38	25.48
Line30	m	33.0	0.5	1.0	50.0	67.0	24.12	24.40
Line31	m	93.0	0.5	1.0	50.0	187.0	24.09	25.93
Line32	m	84.0	0.5	1.0	50.0	169.0	25.94	28.48
Line33	m	49.5	0.5	1.0	50.0	100.0	28.45	29.62
Line34	m	56.5	0.5	1.0	50.0	114.0	29.61	30.85
Line35	m	66.5	0.5	1.0	50.0	134.0	30.79	31.19
Line36	m	54.5	0.5	1.0	50.0	110.0	30.52	31.31
Line37	m	43.5	0.5	1.0	50.0	88.0	29.14	30.53

Table 12-2: Continued...

Line #	Units	Line Length	Step Size	Antenna Separation	Frequency (MHz)	# Traces	Min Elev.	Max Elev.
Line38	m	57.0	0.5	1.0	50.0	115.0	29.06	30.85
Line39	m	73.5	0.5	1.0	50.0	148.0	30.88	33.00
Line40	m	34.5	0.5	1.0	50.0	70.0	30.94	31.18
Line41	m	31.0	0.5	1.0	50.0	63.0	30.20	30.97
Line42	m	98.0	0.5	1.0	50.0	197.0	26.11	30.20
Line43	m	62.0	0.5	1.0	50.0	125.0	24.27	26.17
Line44	m	81.0	0.5	1.0	50.0	163.0	19.32	24.02
Line45	m	72.5	0.5	1.0	50.0	146.0	23.76	26.09
Line46	m	53.0	0.5	1.0	50.0	107.0	24.52	25.43
Line47	m	33.5	0.5	1.0	50.0	68.0	25.14	26.51
Line49	m	46.5	0.5	1.0	50.0	94.0	25.51	26.57
Line50	m	30.5	0.5	1.0	50.0	62.0	24.50	25.60
Line51	m	433.5	0.5	1.0	50.0	868.0	30.90	43.04
Line52	m	33.5	0.5	1.0	50.0	68.0	31.70	35.11
Line53	m	36.5	0.5	1.0	50.0	74.0	31.22	35.09
Line54	m	41.2	0.1	0.5	200.0	413.0	31.27	35.47
Line55	m	41.5	0.1	0.5	200.0	416.0	31.26	35.42
Line56	m	59.4	0.1	0.5	200.0	595.0	27.04	31.41
Line57	m	27.0	0.1	0.5	200.0	271.0	27.22	27.73



Figure 12-1: North is towards the top left-hand corner. Scale is 1cm = 39 m.

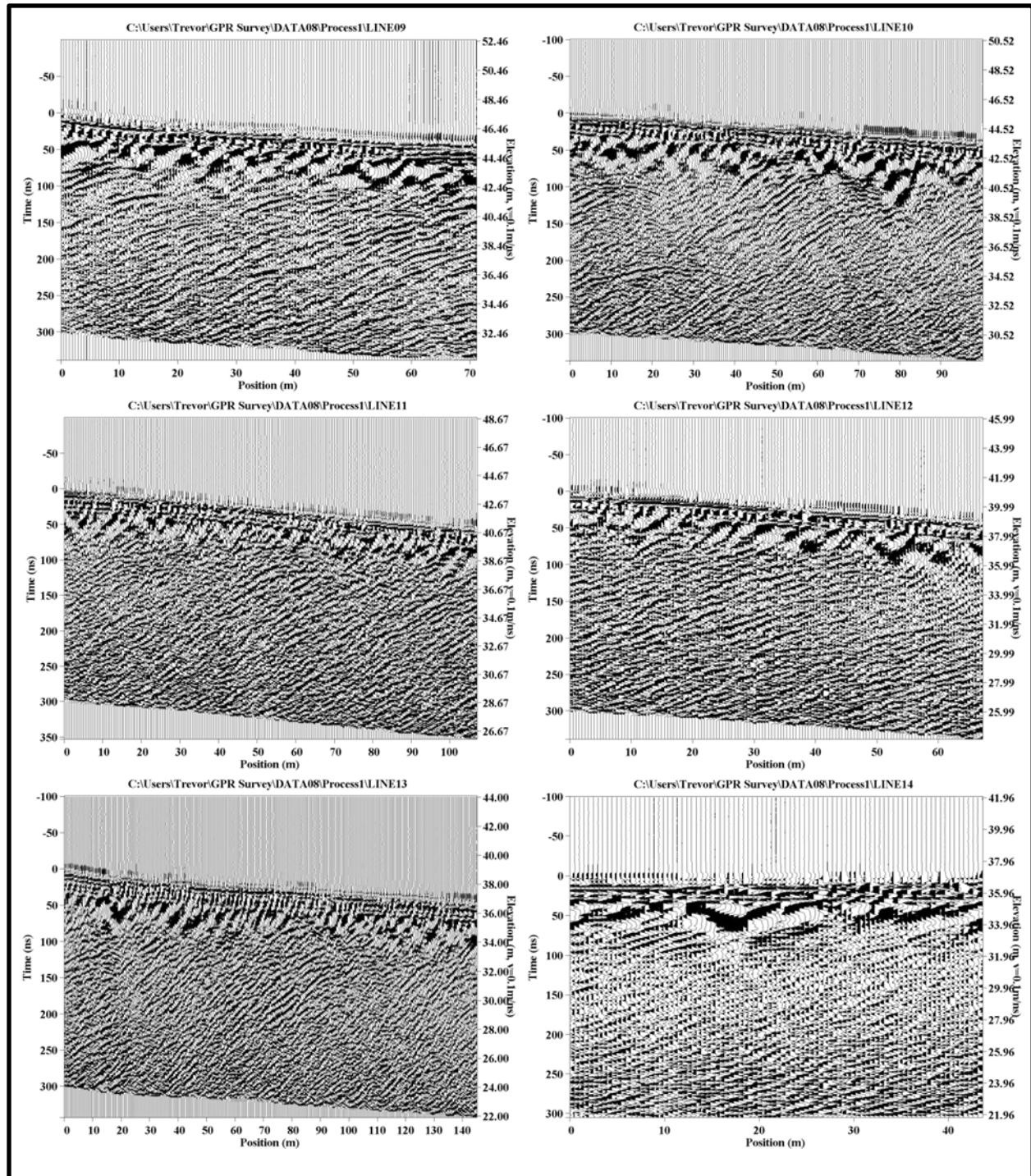


Figure 12-2: Ground penetrating radar profiles for line 09 to 14 inclusive.

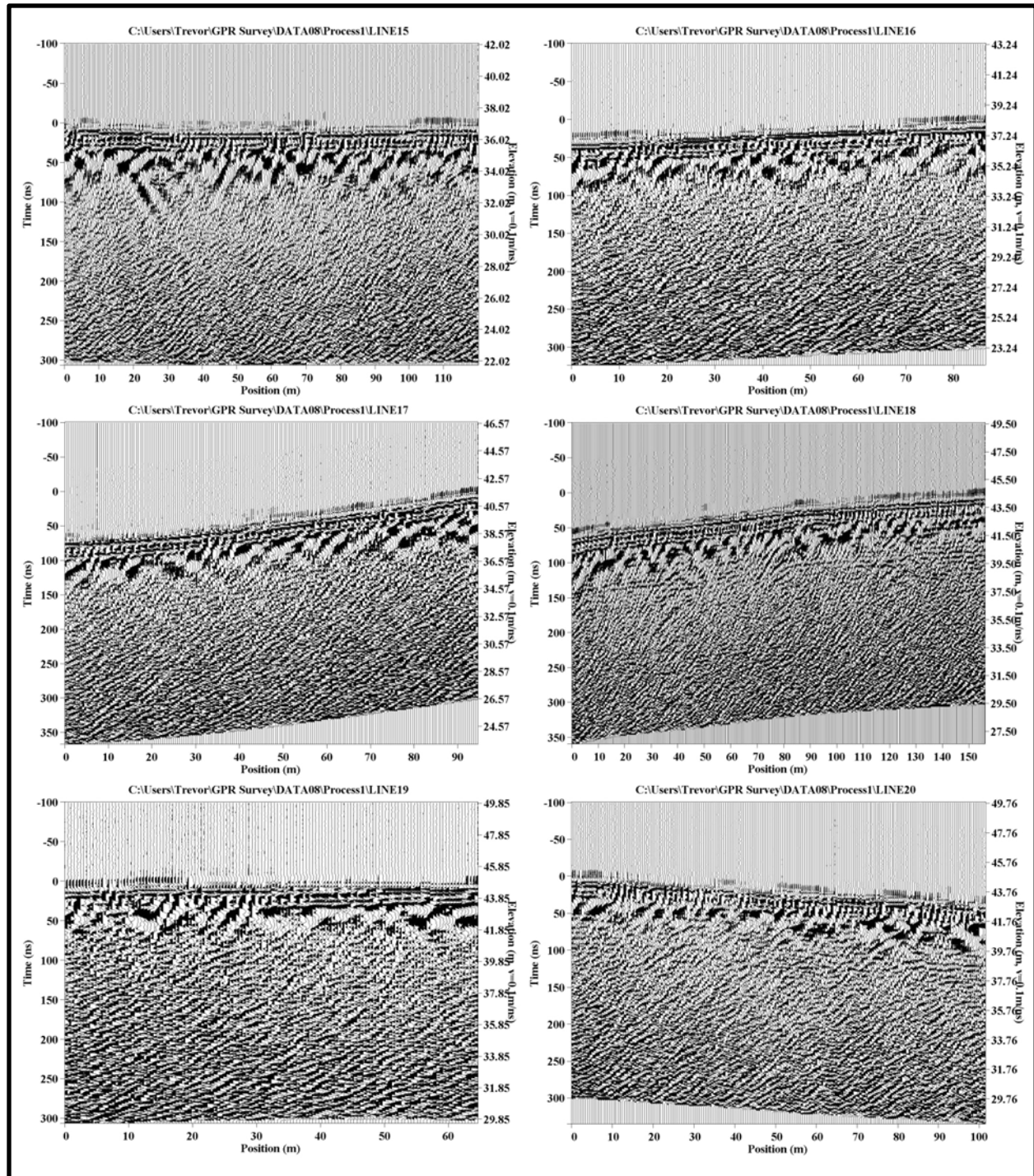


Figure 12-3: Ground penetrating radar profiles for line 15 to 20 inclusive.

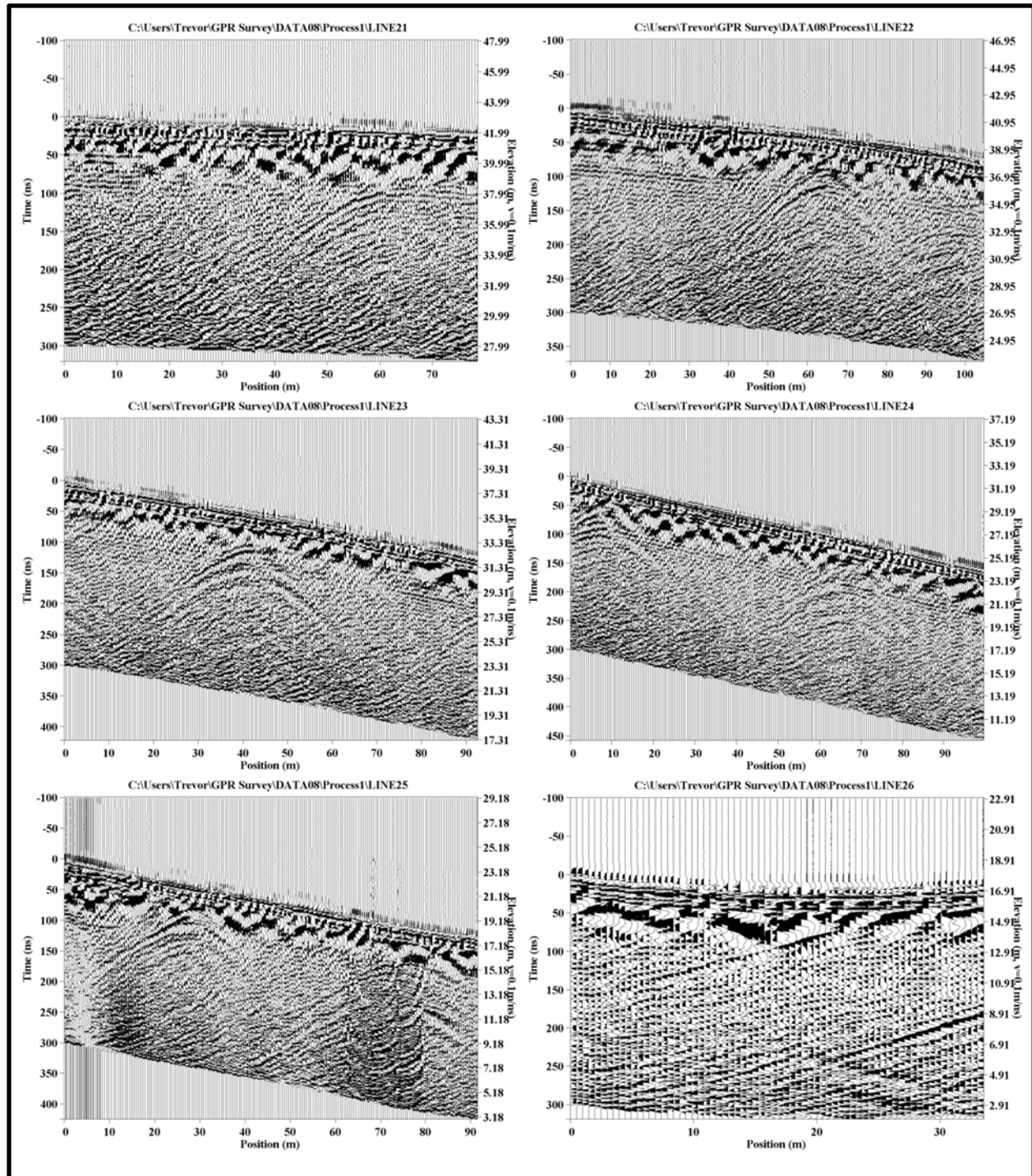


Figure 12-4: Ground penetrating radar profiles for line 21 to 26 inclusive.

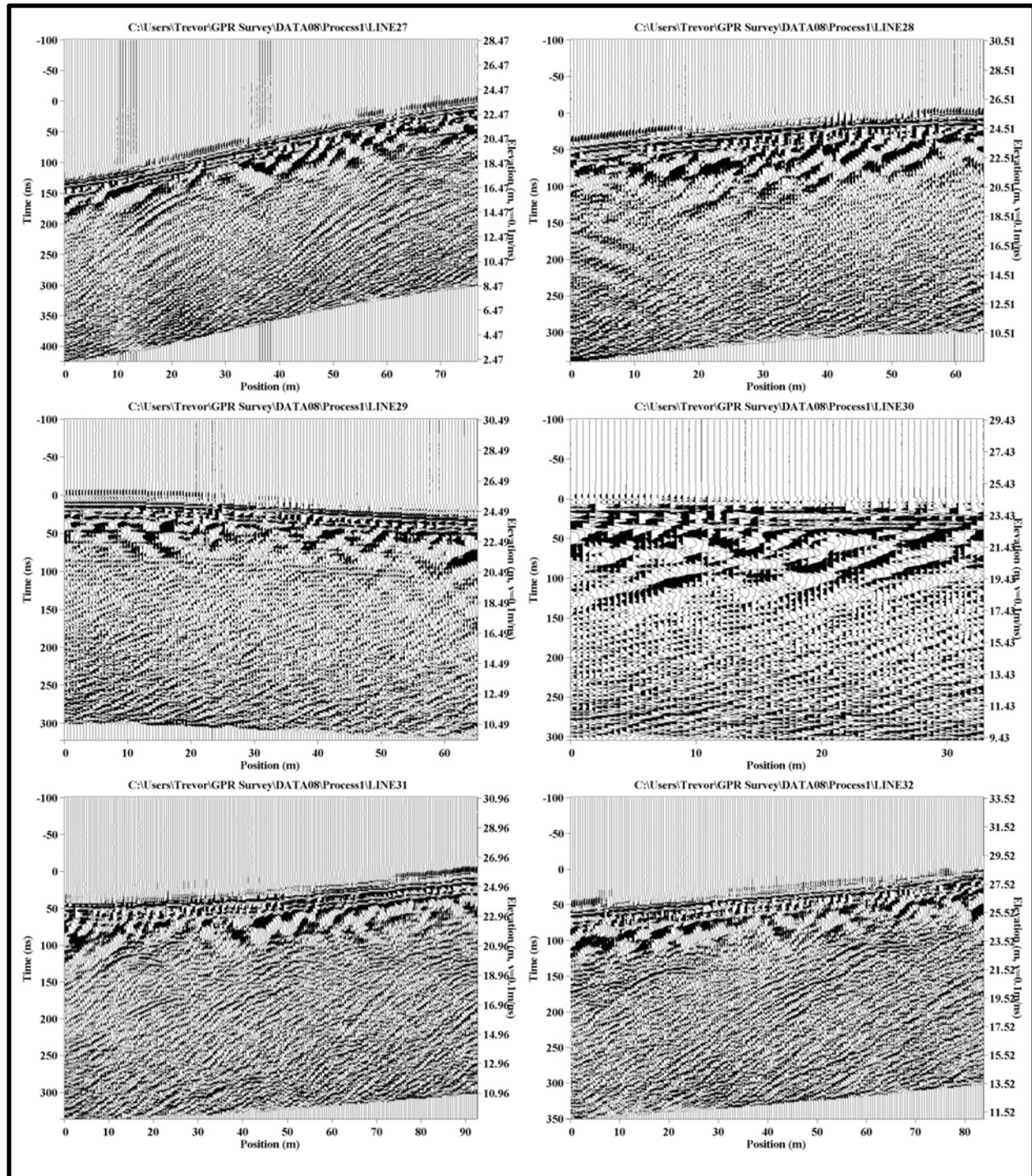


Figure 12-5: Ground penetrating radar profiles for line 27 to 32 inclusive.

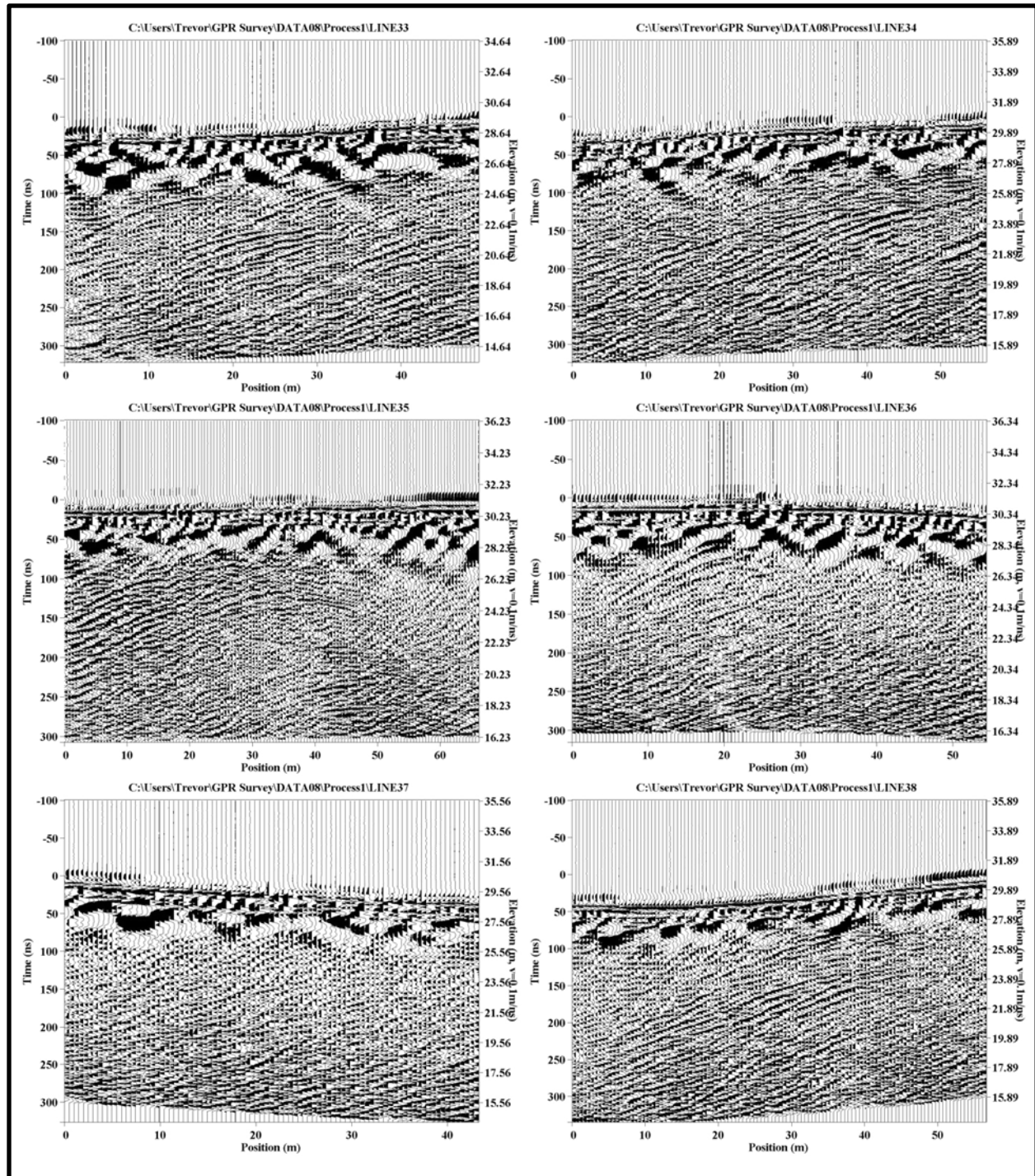


Figure 12-6: Ground penetrating radar profiles for line 33 to 38 inclusive.

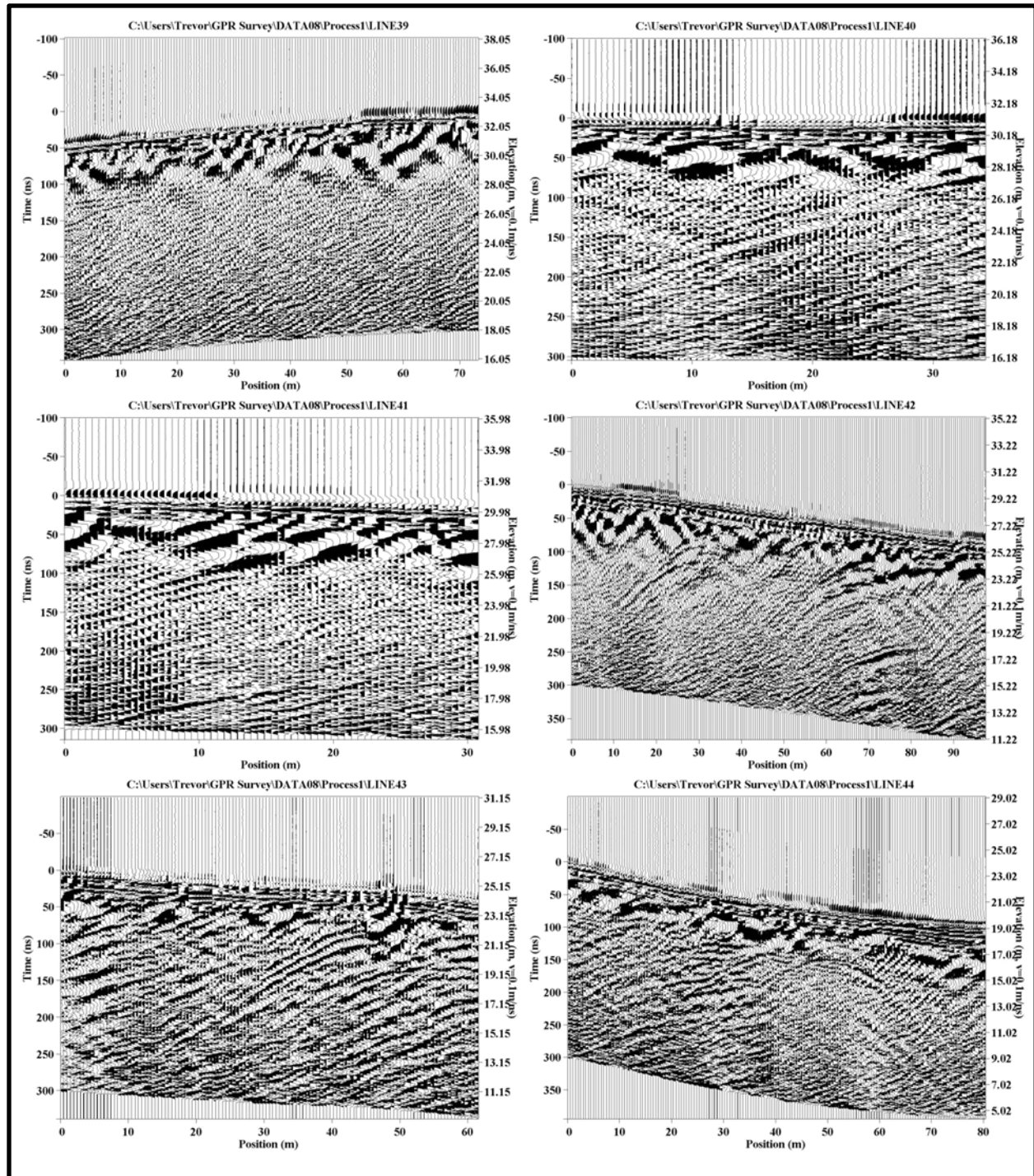


Figure 12-7: Ground penetrating radar profiles for line 39 to 44 inclusive.

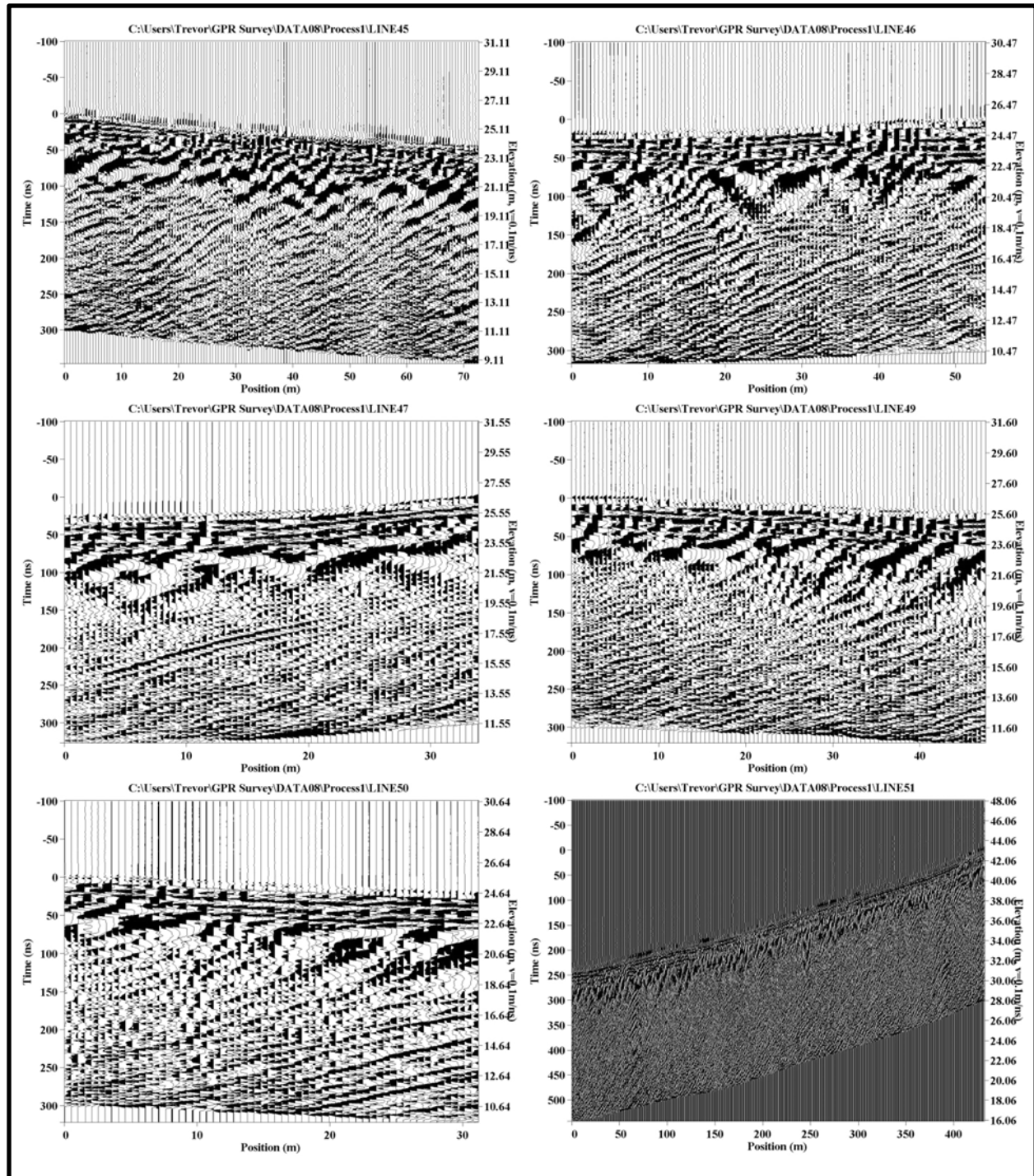


Figure 12-8: Ground penetrating radar profiles for line 45 to 51 inclusive.

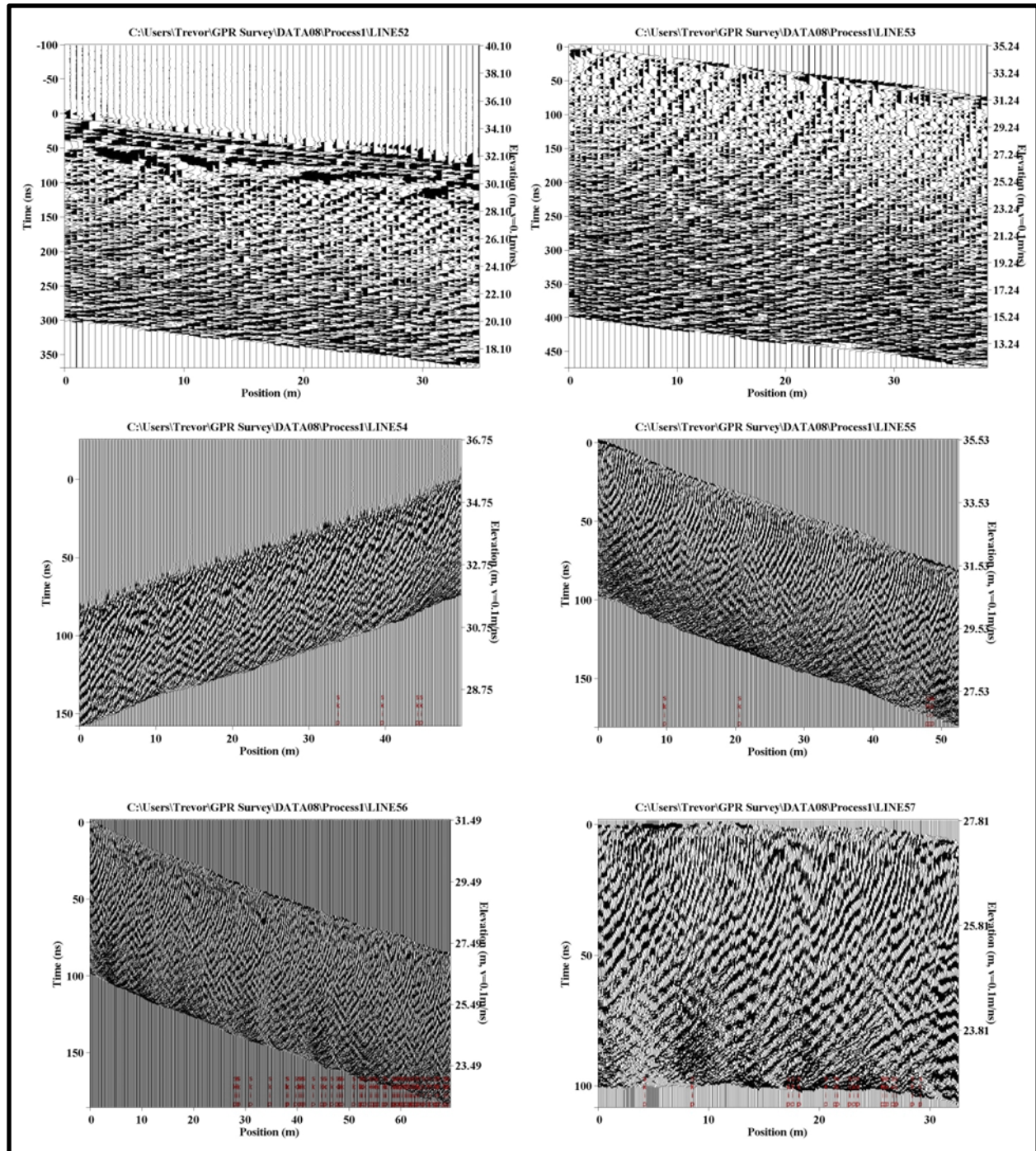


Figure 12-9: Ground penetrating radar profiles for line 52 to 57 inclusive.

13.0 Appendix C: Scintillometer, Permeameter and Measured Section Log

Table 13-1: Scintillometer readings on various fallen sandstone blocks located near the Strat. Class outcrop.

Sample	Lithology	Reading					Average	Min.	Max.
1	Sandstone	136	137	140	163	170	149	136	170
2	Sandstone	109	161	134	138	136	136	109	161
3	Sandstone	119	126	156	129	122	130	119	156
4	Sandstone	114	139	144	147	133	135	114	147
5	Sandstone	130	109	132	135	120	125	109	135
6	Sandstone	170	178	122	173	169	162	122	178
7	Sandstone	145	130	160	149	130	143	130	160
8	Sandstone	155	157	120	137	126	139	120	157
9	Sandstone	139	137	136	120	140	134	120	140
10	Sandstone	146	127	141	118	121	131	118	146
11	Sandstone	123	121	131	128	133	127	121	133
12	Sandstone	128	137	133	135	125	132	125	137
13	Sandstone	130	135	132	126	154	135	126	154
14	Sandstone	129	155	145	143	156	146	129	156
15	Sandstone	145	135	126	129	113	130	113	145
16	Sandstone	146	135	129	147	135	138	129	147
17	Sandstone	150	146	165	141	116	144	116	165
18	Sandstone	143	149	147	158	140	147	140	158
19	Sandstone	131	130	147	144	142	139	130	147
20	Sandstone	132	154	163	114	140	141	114	163
21	Sandstone	147	143	146	139	133	142	133	147
22	Sandstone	140	120	145	137	142	137	120	145
23	Sandstone	137	151	157	130	146	144	130	157
24	Sandstone	161	170	149	164	146	158	146	170
25	Sandstone	153	159	141	159	155	153	141	159
26	Sandstone	162	160	126	129	128	141	126	162
27	Sandstone	141	133	139	121	109	129	109	141
28	Sandstone	115	123	119	147	125	126	115	147
29	Sandstone	132	156	146	179	137	150	132	179
30	Sandstone	110	127	112	97	100	109	97	127
31	Sandstone	156	150	164	191	156	163	150	191
32	Sandstone	135	117	138	149	117	131	117	149
33	Sandstone	132	97	112	107	133	116	97	133
34	Sandstone	129	135	125	126	124	128	124	135

Table 13-1: Continued...

Sample	Lithology	Reading					Average	Min.	Max.
35	Sandstone	108	114	121	125	103	114	103	125
36	Sandstone	153	116	128	157	145	140	116	157
37	Sandstone	141	133	121	144	111	130	111	144
38	Sandstone	117	126	133	105	117	120	105	133
39	Sandstone	135	128	144	146	134	137	128	146
40	Sandstone	127	123	127	125	120	124	120	127
41	Sandstone	143	149	134	114	133	135	114	149
42	Sandstone	127	120	142	117	138	129	117	142
43	Sandstone	122	150	144	150	149	143	122	150
44	Sandstone	135	130	124	128	129	129	124	135
45	Sandstone	151	134	172	132	136	145	132	172
46	Sandstone	128	142	195	127	115	141	115	195
47	Sandstone	148	137	123	125	132	133	123	148
48	Sandstone	122	120	147	156	146	138	120	156
49	Sandstone	125	105	134	134	132	126	105	134
50	Sandstone	164	132	136	130	127	138	127	164
51	Sandstone	127	141	131	132	127	132	127	141

Table 13-2: Scintillometer readings on various lithologies within the cliff face.

Sample	Height (m)	Lithology	Readings					Average
1	0	coal	292	300	302	296	305	299
2	1	siltstone	197	225	240	204	214	216
3	2	siltstone	182	196	194	204	210	197
4	3	siltstone	193	218	213	298	221	229
5	4	siltstone	186	191	171	161	187	179
6	5	siltstone	212	210	211	197	204	207
7	6	siltstone	237	245	208	211	222	225
8	7	siltstone	210	211	240	197	218	215
9	8	siltstone	209	220	235	224	247	227
10	9	sandstone	132	146	141	121	137	135
11	10	sandstone	130	128	150	105	119	126
12	11	siltstone	172	180	170	185	164	174
13	12	sandstone	168	161	175	162	146	162

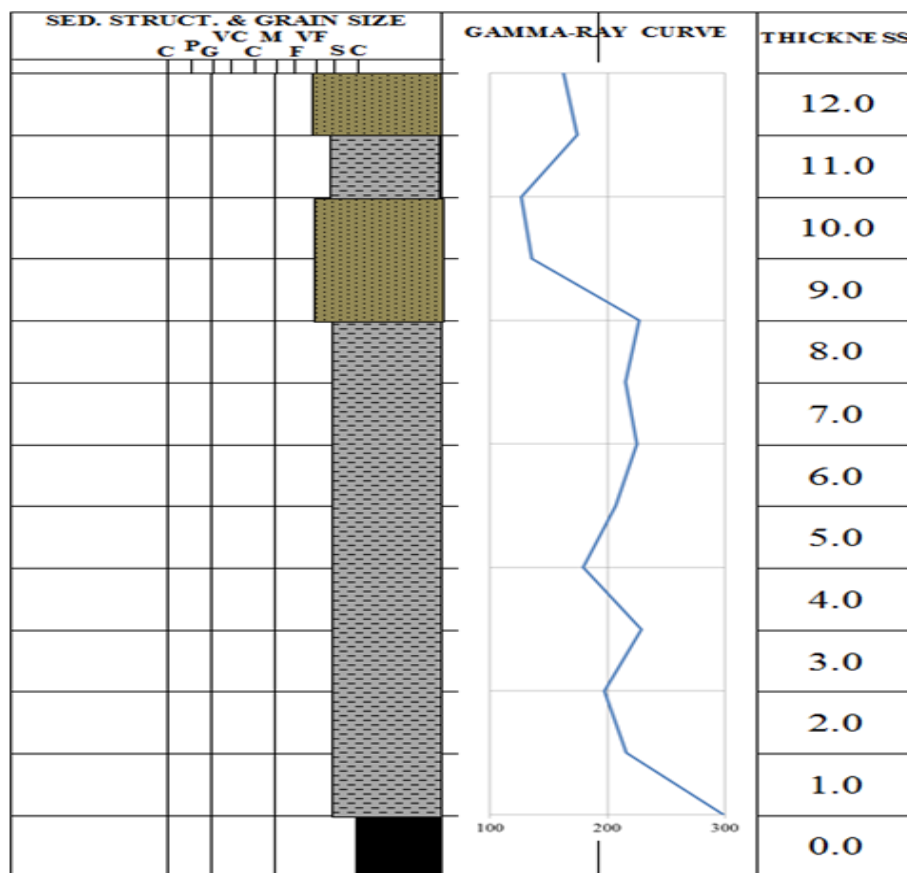


Figure 13-1: Gamma-ray curve for a measured section. Curve is based on average readings from Table 13-2.

Table 13-3: Scintillometer readings for each of the collected rock samples over a 66 second time period.

#	GW101-2013TK	GW102-2013TK	GW103-2013TK	GW104-2013TK	GW105-2013TK	GW106-2013TK	GW107-2013TK	GW108-2013TK
1	124	129	128	119	119	130	117	118
2	134	134	149	143	124	120	121	130
3	140	140	124	114	123	133	127	128
4	129	127	133	132	137	134	128	119
5	131	143	130	131	115	131	123	128
6	132	135	134	128	125	123	128	129
7	135	131	133	135	131	124	134	126
8	133	151	132	129	135	120	125	120
9	128	121	144	123	137	122	124	126
10	130	130	131	132	134	125	137	137
11	137	126	140	118	123	143	129	133
12	136	127	131	120	118	130	124	127
13	126	135	127	149	119	131	131	130
14	132	140	129	134	133	132	134	131
15	134	142	145	145	113	134	131	133
16	126	122	127	138	128	137	133	124
17	155	131	118	125	124	132	130	137
18	121	144	129	137	125	139	138	127
19	138	131	133	121	133	130	132	138
20	129	139	127	138	131	139	123	130
21	116	134	145	132	126	128	126	125
22	135	141	130	125	125	138	130	119
23	129	135	120	134	126	129	112	129
24	130	132	125	126	122	139	122	130
25	117	125	130	122	128	130	118	120
26	132	126	125	130	129	132	140	123
27	133	136	133	116	130	124	134	132
28	115	130	131	133	137	121	137	126
29	129	137	140	131	138	128	125	121
30	135	140	129	138	118	136	126	120
31	127	127	135	120	132	129	131	131
32	133	133	149	134	143	126	129	124
33	134	117	128	142	134	128	131	135
34	137	120	130	122	130	134	138	126
35	135	132	118	139	129	131	130	118
36	144	117	142	137	120	135	134	123

Table 13-3: Continued...

#	GW101-2013TK	GW102-2013TK	GW103-2013TK	GW104-2013TK	GW105-2013TK	GW106-2013TK	GW107-2013TK	GW108-2013TK
37	131	127	134	132	141	137	136	133
38	127	132	129	134	124	124	137	134
39	128	126	132	137	129	131	142	119
40	133	133	135	111	127	137	135	120
41	146	128	136	136	140	126	131	123
42	127	139	130	135	132	131	133	124
43	131	133	128	144	118	130	131	122
44	130	134	131	132	133	126	133	130
45	128	132	129	127	120	141	145	127
46	130	119	130	122	123	127	139	136
47	133	135	132	133	139	134	124	142
48	124	129	138	127	127	138	130	132
49	135	116	128	137	133	135	135	128
50	126	133	141	122	126	128	126	130
51	137	132	128	131	129	132	123	123
52	138	133	131	116	128	136	131	127
53	137	116	147	138	138	135	127	128
54	133	122	138	130	130	125	138	125
55	137	133	142	127	121	121	132	123
56	130	125	123	125	140	141	130	131
57	134	131	133	135	125	138	136	130
58	141	129	139	130	137	127	124	122
59	122	130	120	134	126	133	126	120
60	130	136	137	154	132	135	130	131
61	128	122	131	124	122	142	129	125
62	144	129	137	130	129	133	119	135
63	136	141	144	138	131	128	135	122
64	125	135	131	131	125	126	138	133
65	129	134	133	128	122	136	137	112
66	142	133	132	125	134	126	141	127
Max.	155	151	149	154	143	143	145	142
Min.	115	116	118	111	113	120	112	112
Avg.	132	131	133	131	128	131	130	127

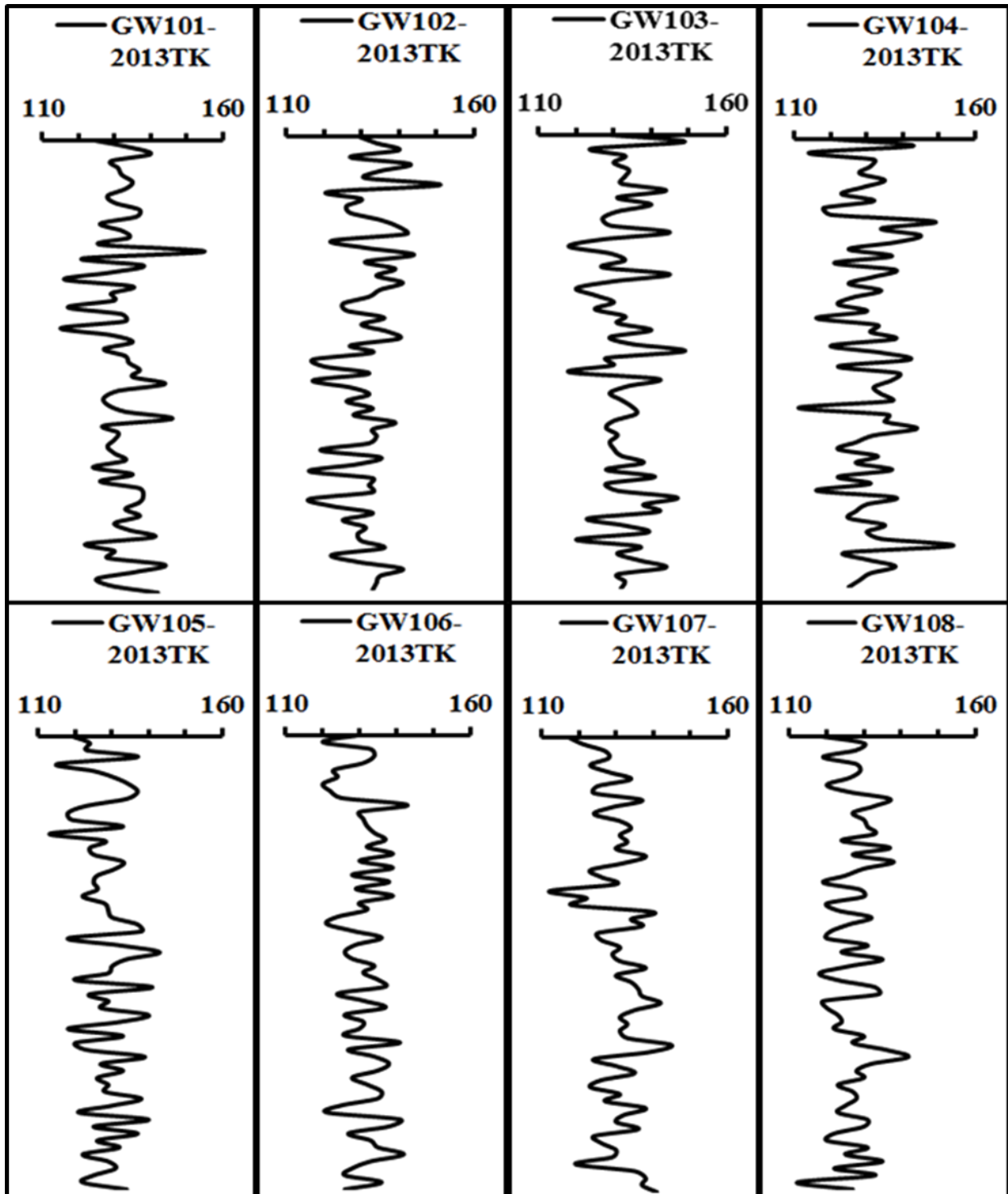


Figure 13-2: Scintillometer readings from each sample displayed as a trace for each of the eight samples collected.

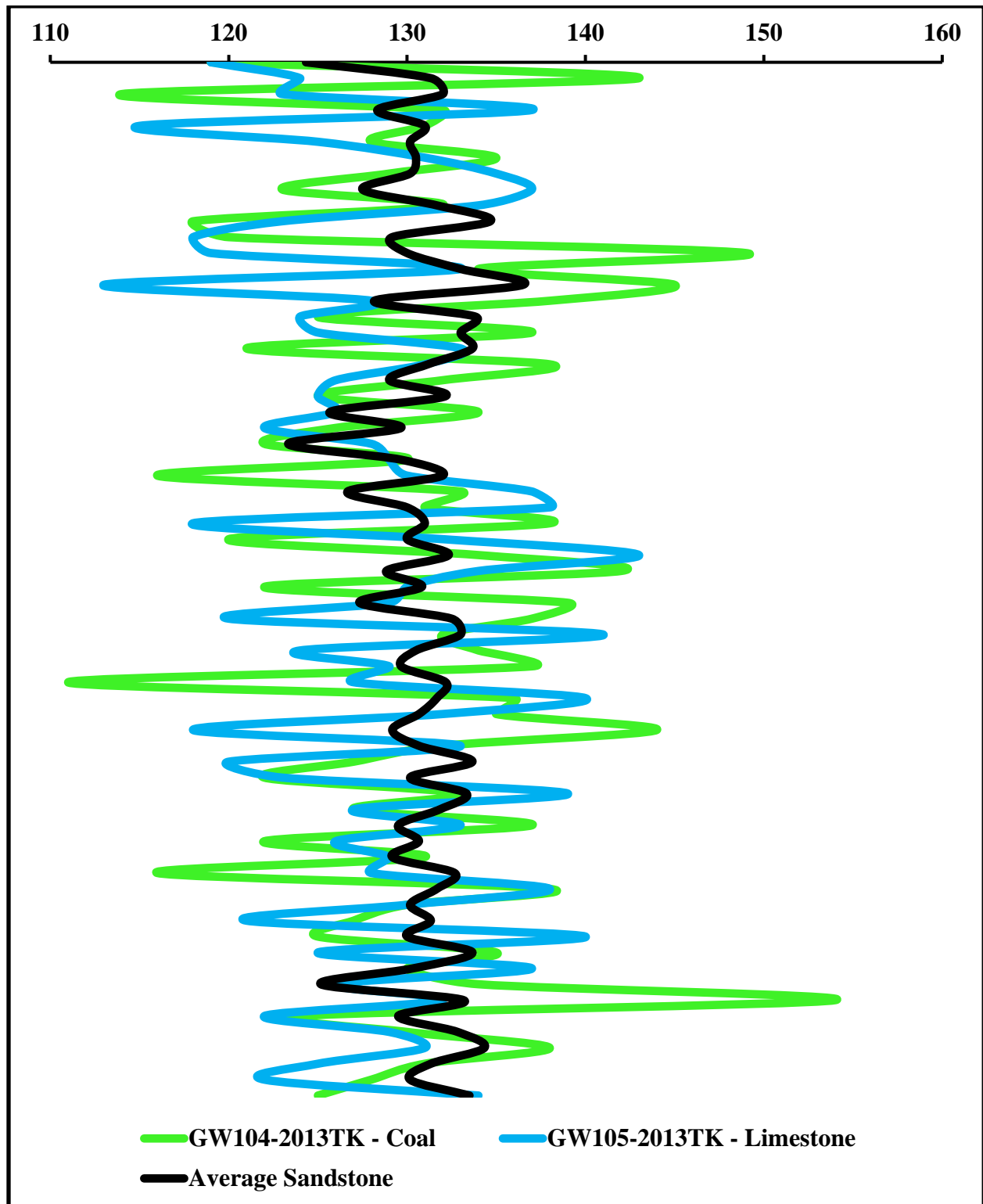


Figure 13-3: Scintillometer readings for the coal sample, limestone samples and the average of the six sandstones samples displayed together.

Table 13-4: Permeameter values collected on various fallen blocks.

Sample	Lithology	Reading	Perm. (mD)
1	sandstone	10.64	527
2	sandstone	11.38	66
3	sandstone	10.86	284
4	sandstone	10.75	387
5	sandstone	10.33	1,258
6	sandstone	10.44	924
7	sandstone	10.18	1,917
8	sandstone	10.88	269

Table 13-5: Permeameter measurements taken at the Strat. Class outcrop.

Sample	Description	Reading	Perm. (mD)
1	Fallen, blocky, silty-sandstone; horizontal	11.28	88
	Same as above; vertical	12.04	10
2	Fallen, grey, sandy-siltstone; vertical	11.99	12
	Same as above; horizontal	11.57	39
3	Large fossilized tree trunk, brown-red	12.17	7
4	Fine-grained massive sandstone; horizontal	11.61	35
	Same as above; vertical	11.68	28
5	Fine lower sandstone; vertical	11.23	101
	Same as above; horizontal	11.22	104
6	Very fine upper shale; vertical	11.86	17
7	Very fine upper shale	11.17	119
8	Coal bed on safe outcrop; horizontal	11.25	95
	Same as above; vertical	11.93	14
9	Large sandstone bedset; horizontal	10.88	269
	Same as above but with climbing ripple	10.73	410
10	Conglomerate; horizontal	10.97	209

LOCATION: Joggins – Fundy Coal Seam + Fundy Forest
 DATE: Thursday May 30th, 2013

PAGE: 1 of 3

GEOLOGIST: Grant Wach + Trevor Kelly

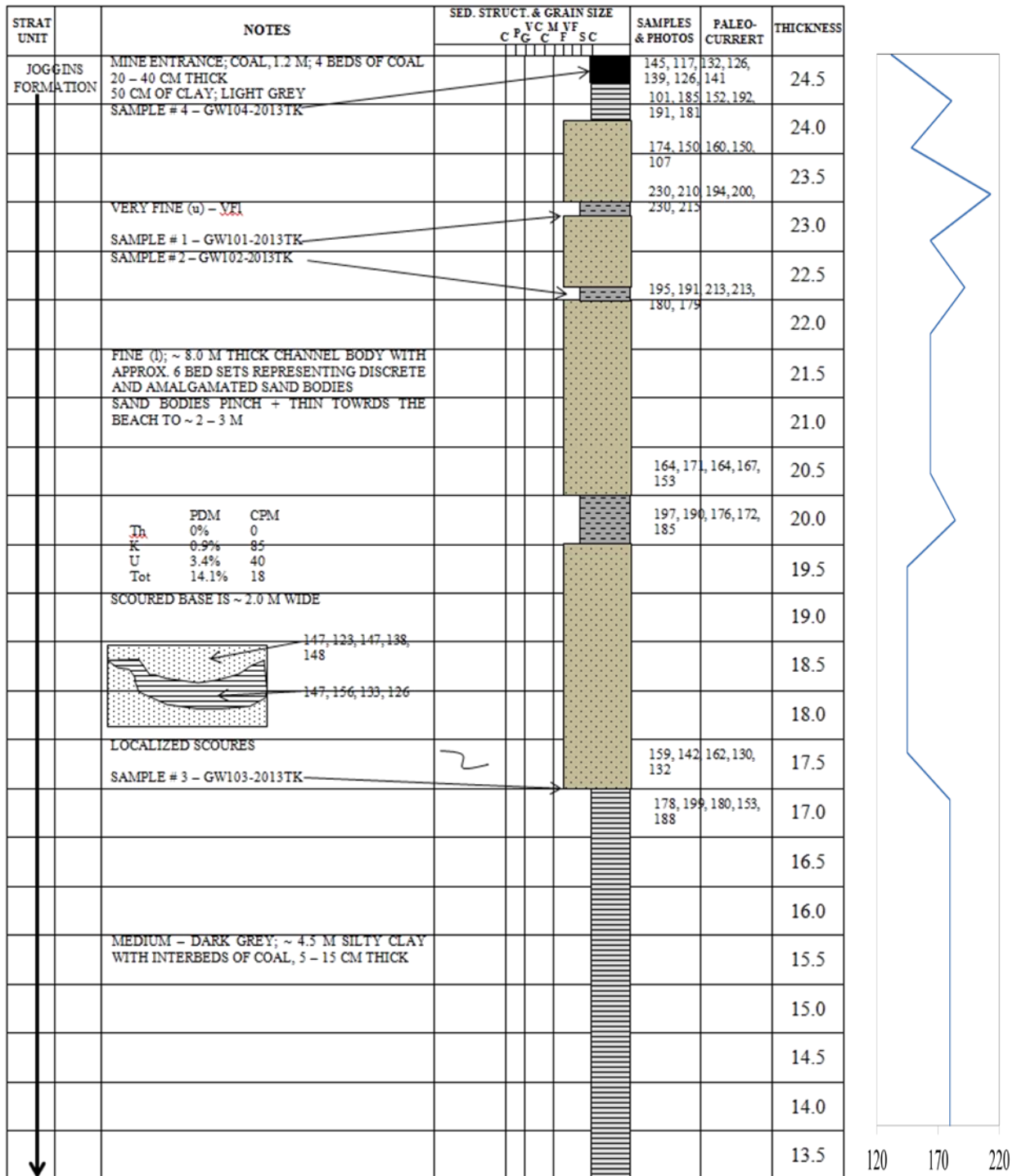


Figure 13-4: Measured section along the Fundy Coal Seam and Fundy Forest at Joggins. Gamma-ray readings were recorded at various points along this portion of the section and the corresponding plot is to the right of the section.

13-4: Continued....

LOCATION: Joggins – Fundy Coal Seam + Fundy Forest
 DATE: Thursday May 30th, 2013

PAGE: 3 of 3
 GEOLOGIST: Grant Wach + Trevor Kelly

STRAT UNIT	NOTES	SED. STRUCT. & GRAIN SIZE							SAMPLES & PHOTOS	PALEO-CURRENT	THICKNESS
		C	P	G	V	M	F	SC			
↓	MEDIUM TO DARK GREY FISSILE CLAY + SILT WITH SILTSTONE NODULES (UP TO 10 CM SIZE) WITH ORGANIC DETRITUS	○									1.5
											1.0
											0.5
											0.0

LOCATION: Joggins – Hardscrabble Point/Coal Mine Point
 DATE: Friday May 31st, 2013

PAGE: 1 of 2
 GEOLOGIST: Grant Wach + Jillian Haynes

STRAT UNIT	NOTES	SED. STRUCT. & GRAIN SIZE						SAMPLES & PHOTOS	PALFO-CURRENT	THICKNESS
		C	P	G	C	F	S			
JOGGINS FORMATION										12.0
										11.5
										11.0
										10.5
	4 – 6 M THICK MASSIVE + BLOCKY									10.0
	M1 – Fu SANDSTONE; MULTI-STORY CHANNEL BODY – VAGUE BED BOUNDARIES; 1 – 2.5 M AT BASE; BECOMING 50 CM TO 30 CM AT UNIT TOP									9.5
										9.0
										8.5
	SAMPLE # 6 – GW106-2013TK							116, 120, 121, 118, 122, 113, 121, 112		8.0
										7.5
								176, 189, 182, 176, 166, 183		7.0
	SAMPLE # 5 – GW105-2013TK							144, 162, 137, 158, 153, 139, 155		7.0
								160, 153, 143, 148, 155, 153, 166		6.5
								149, 162, 155, 153, 166, 144, 163		6.0
	FLASSY INTERBEDDED SANDSTONE WITH THIN SAND/SILT; F-M-F1+VFu-VF1;									5.5
	SCoured CHANNELS DOWNCUTTING 1.5 M X 10 M WIDE – ABANDONED;									5.0
	INFILLED WITH THIN SILTSTONE AND V. FINE SANDSTONE + CLAYSTONE									4.5
										4.0
										3.5
	3.5 M OF DARK GREY FISSILE TO SMALL BLOCKY SILT + CLAY WITH THIN 10 – 15 CM VERY FINE SANDSTONE;									3.0
	LIGHT GREY WITH SOME IRON STAINING; SOME YELLOW STAINING									2.5
										2.0
										1.5
										1.0

Figure 13-5: Measured section at Hardscrabble Point/Coal Mine Point at Joggins.

Figure 13-5: Continued....

LOCATION: Joggins – Hardscrabble Point/Coal Mine Point
 DATE: Friday May 31st, 2013

PAGE: 2 of 2
 GEOLOGIST: Grant Wach + Jillian Haynes

STRAT UNIT	NOTES	SED. STRUCT. & GRAIN SIZE										SAMPLES & PHOTOS	PALEO-CURRENT	THICKNESS	
		V	C	M	F	S	C	C	C	C	C				
↓															0.5
↓	BASE/TOP OF SANDSTONE														0.0

14.0 Appendix D: Hand Sample Descriptions

Sample: GW101-2013TK

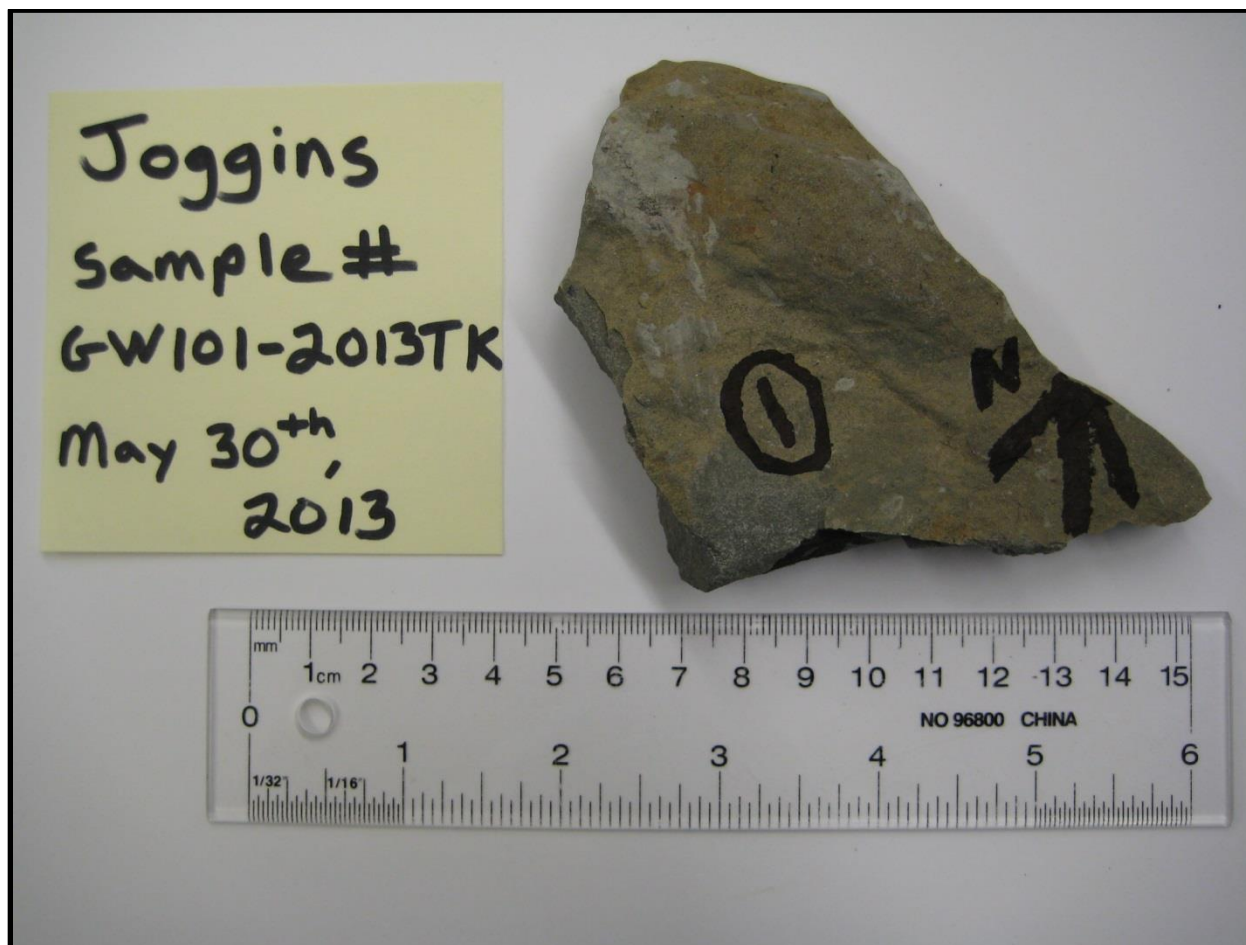


Figure 14-1: Photograph of hand sample GW101-2013TK.

Sample GW101-2013TK is a light grey to medium grey sandstone, most likely a quartzite variety. It appears to be medium-grained, clastic and equigranular. The sample reacts vigorously with 9 % HCl, suggesting cementation by a carbonate mineral; most likely calcite. The sample is hard and has gritty feel. The sample displays brittle, conchoidal-looking fractures. There are dark grey to black mineral occurrences in the sample that have random sizes and orientations that are ellipsoidal to thin, needle-like shapes. They may be fragments of rock or perhaps a mineral.

Sample: GW102-2013TK

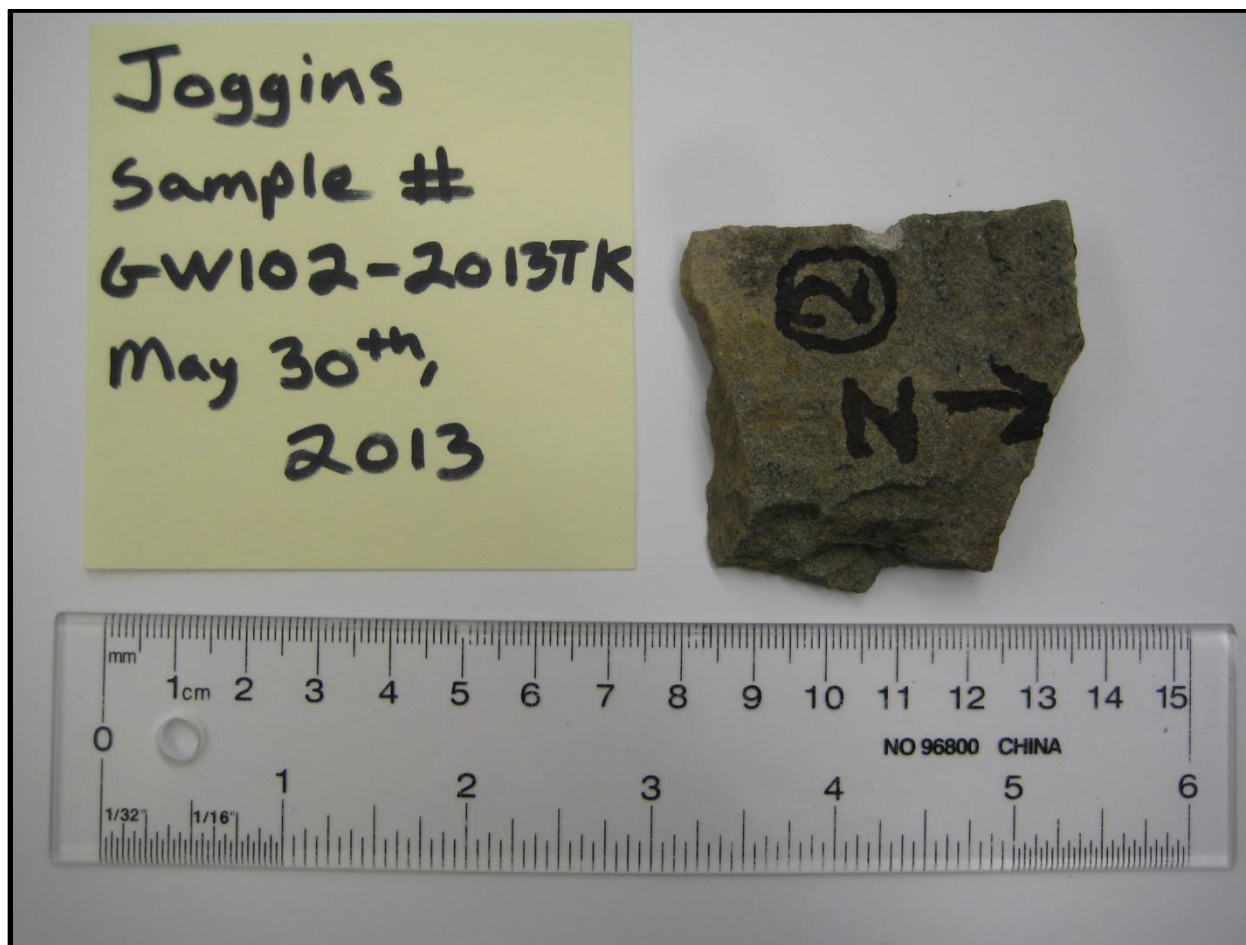


Figure 14-2: Photograph of hand sample GW102-2013TK.

Sample GW102-2013TK is a light grey sandstone that does not resemble the quartzite-looking appearance of GW010-2013TK. Viewing a fresh cut surface through a hand lens reveals the equigranular, clastic and medium-grained texture. The sample reacts weakly with 9 % HCl, suggesting the presence of calcite cement, but perhaps only as a minor constituent of the matrix cement. The sample lacks the hardness of sample GW101-2013TK. GW102-2013TK has a gritty feel along with brittle, conchoidal-looking fractures. The sample is most likely a quartz arenite.

Sample: GW103-2013TK

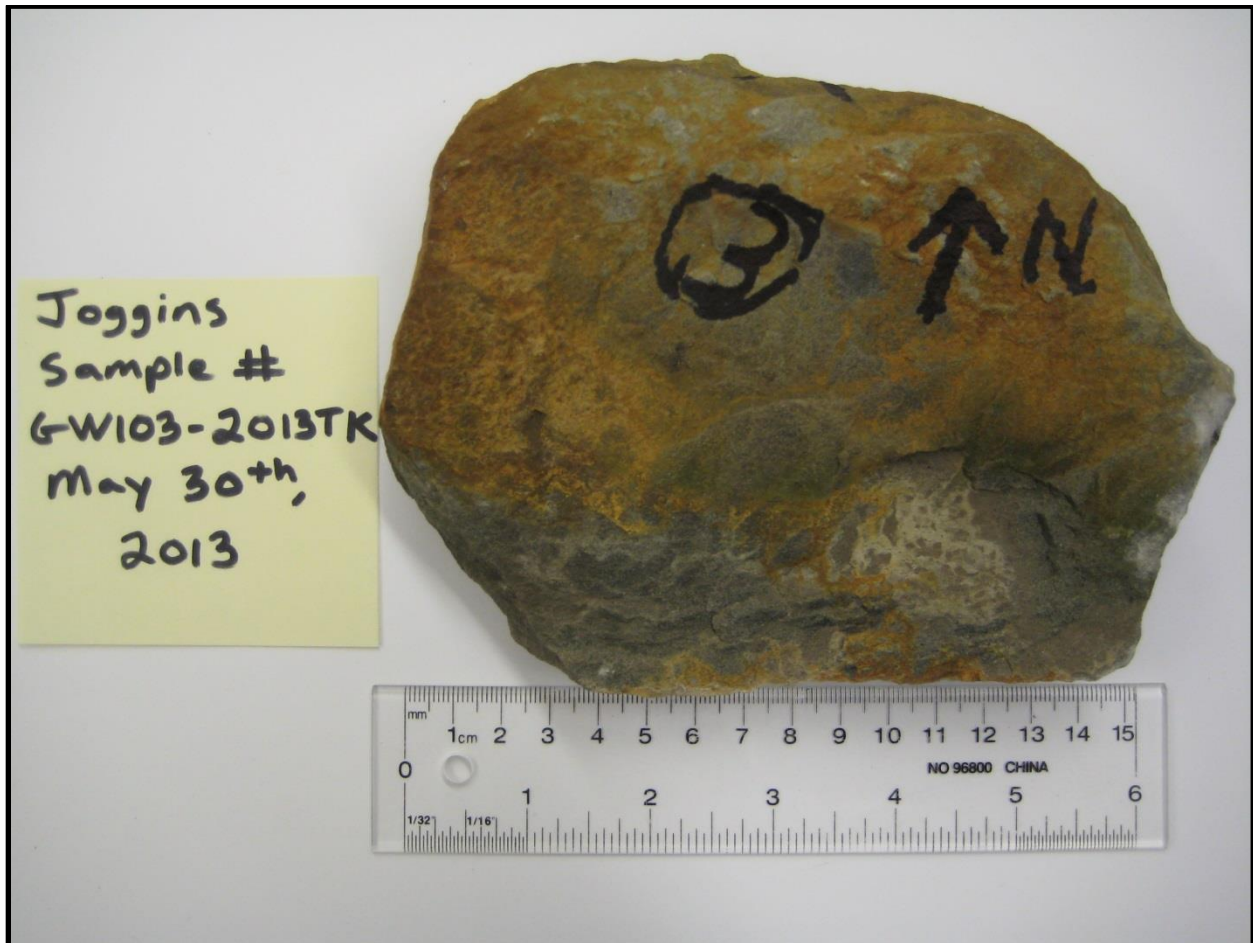


Figure 14-3: Photograph of hand sample GW103-2013TK.

Sample GW103-2013TK is a light grey, fine to medium grained, clastic and equigranular sandstone that is both massive and homogenous. The sample reacts weakly with 9 % HCl, suggesting that calcite cement is present, but perhaps only as a minor constituent of the cement. The hardness resembles that of Sample GW101-2013TK. The sample has a much smoother feel to it and is not as gritty as the previous samples had been. The sample is most likely a quartzite.

Sample: GW104-2013TK



Figure 14-4: Photograph of hand sample GW104-2013TK.

Sample GW104-2013TK is a very light, sub-vitreous, non-clastic, massive and homogenous carbonaceous shale or coal. The variety of the coal is probably that of anthracite due to its shiny appearance, massive and homogenous structure and the fact that it breaks conchoidally. The sample has a low hardness and is composed primarily of carbon. The sample displays an oily, rainbow sheen look with blues, purples and yellows visible at many locations within the hand sample. Calcite occurs as thin veinlets throughout and would have formed during secondary mineralization sometime after the coal fractured. It is likely that hydrothermal fluids are responsible for the calcite precipitation seen within the coal sample.

Sample: GW105-2013TK

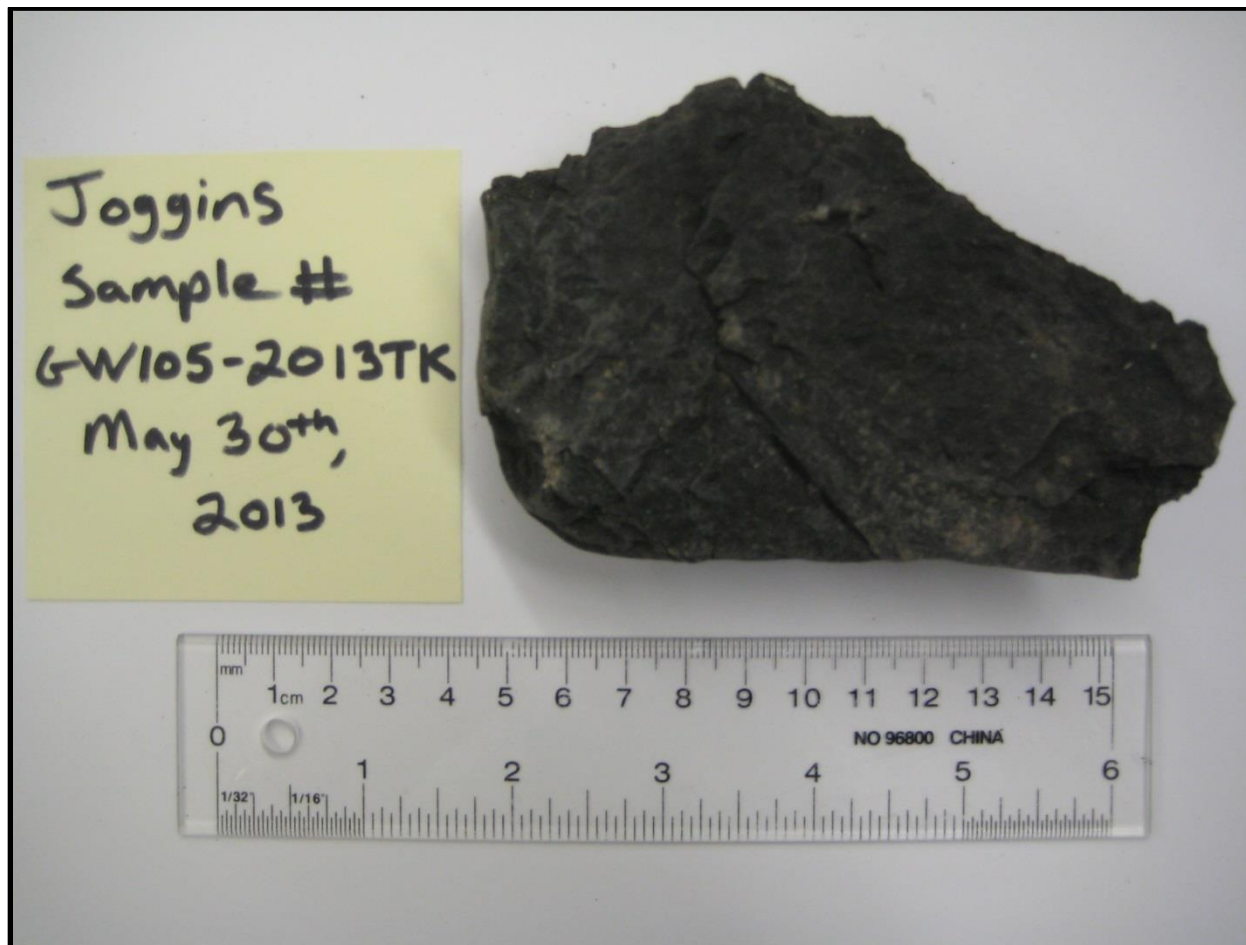


Figure 14-5: Photograph of hand sample GW105-2013TK.

Sample GW105-2013TK is a medium to dark grey, dense, equigranular and fine-grained clastic limestone. It has a hardness of between 3 – 4. The sample breaks conchoidally. There are abundant ellipsoidally shaped features, possibly representing fossils or fossil fragments occurring throughout the sample. The hand sample reacts vigorously with acid. According to Folks classification, this rock would likely be classified as a biomicrite. According to the Dunham classification of carbonate rocks, this sample would most likely represent a wackestone.

Sample: GW106-2013TK

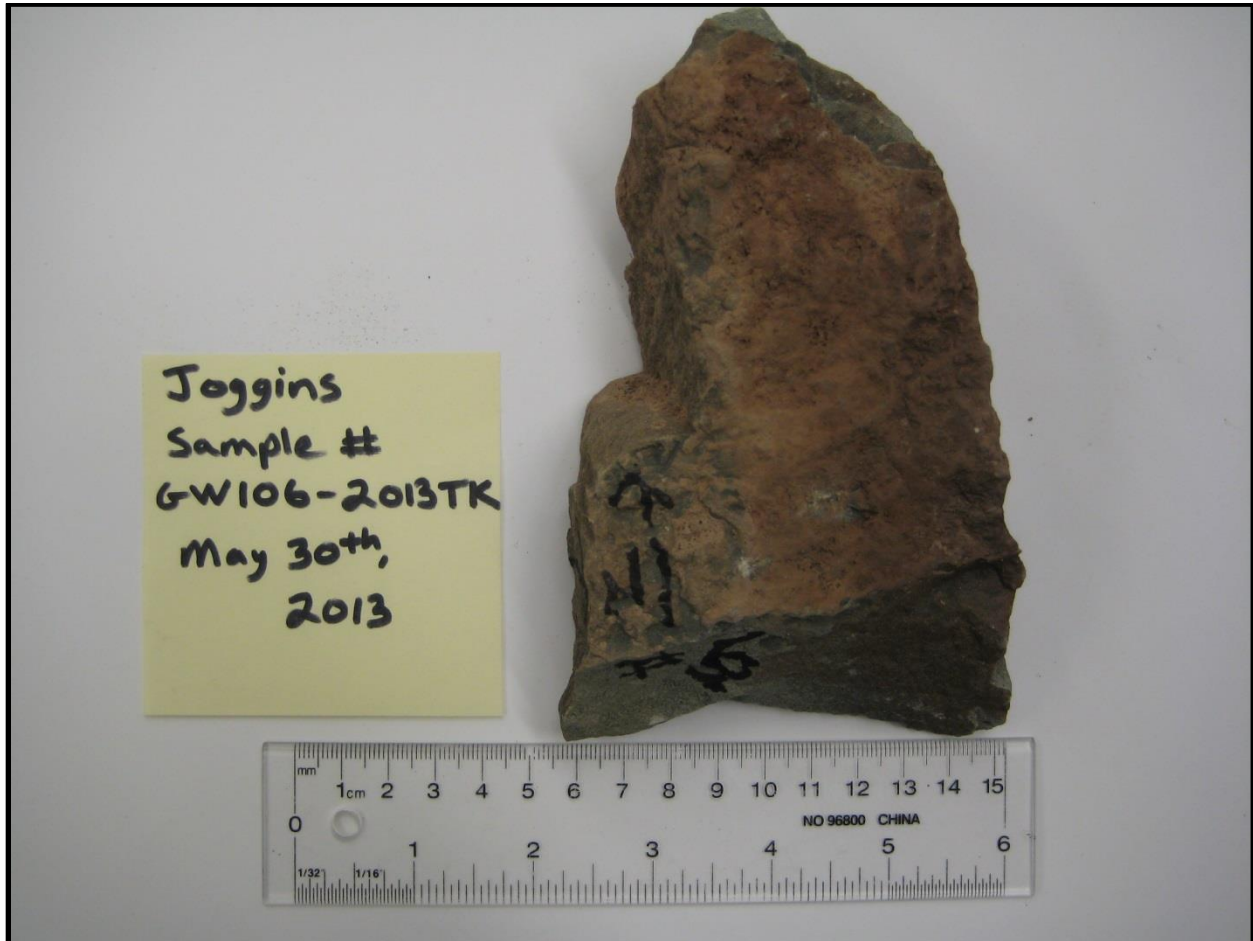


Figure 14-6: Photograph of hand sample GW106-2013TK.

Sample GW106-2013TK is a light grey, equigranular, medium-grained, clastic sandstone with some calcite cement as evidenced by a weak effervescence in the presence of 9 % HCl. The sample is homogenous, massive and hard, similar to that of GW101-2013TK. The sample has a gritty feel and displays conchoidal-looking fractures. The rock is most likely a quartz arenite or quartzite.

Sample: GW107-2013TK

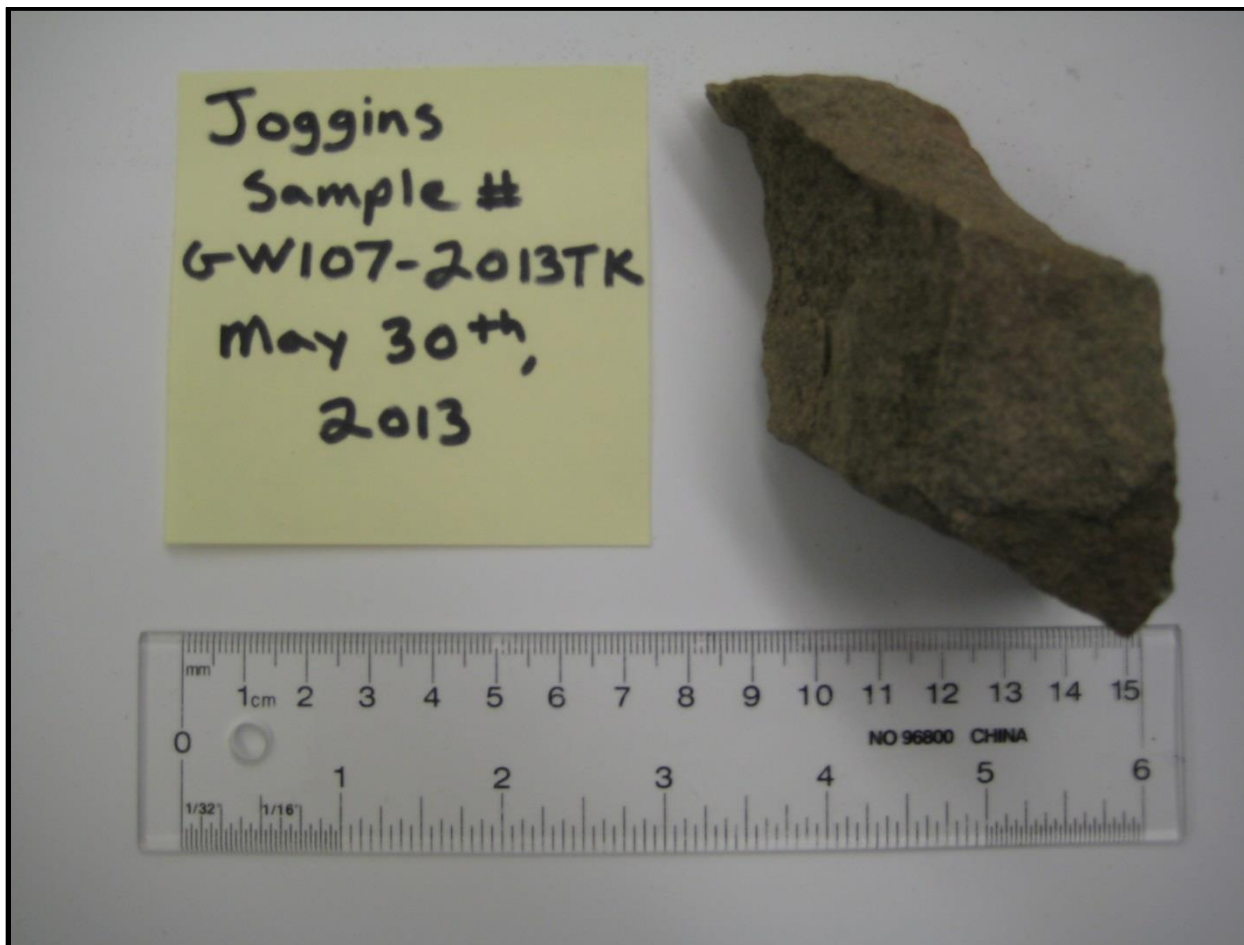


Figure 14-7: Photograph of hand sample GW107-2013TK.

Sample GW107-2013TK is a light grey, equigranular, medium-grained, clastic sandstone. It is highly reactive with 9 % HCl, indicating an abundance of calcite is present. Through a hand lens, the sample has a mottled-looking colour with white, black, brown and grey coloured grains. The sample is hard and has conchoidal fracture.

Sample: GW108-2013TK

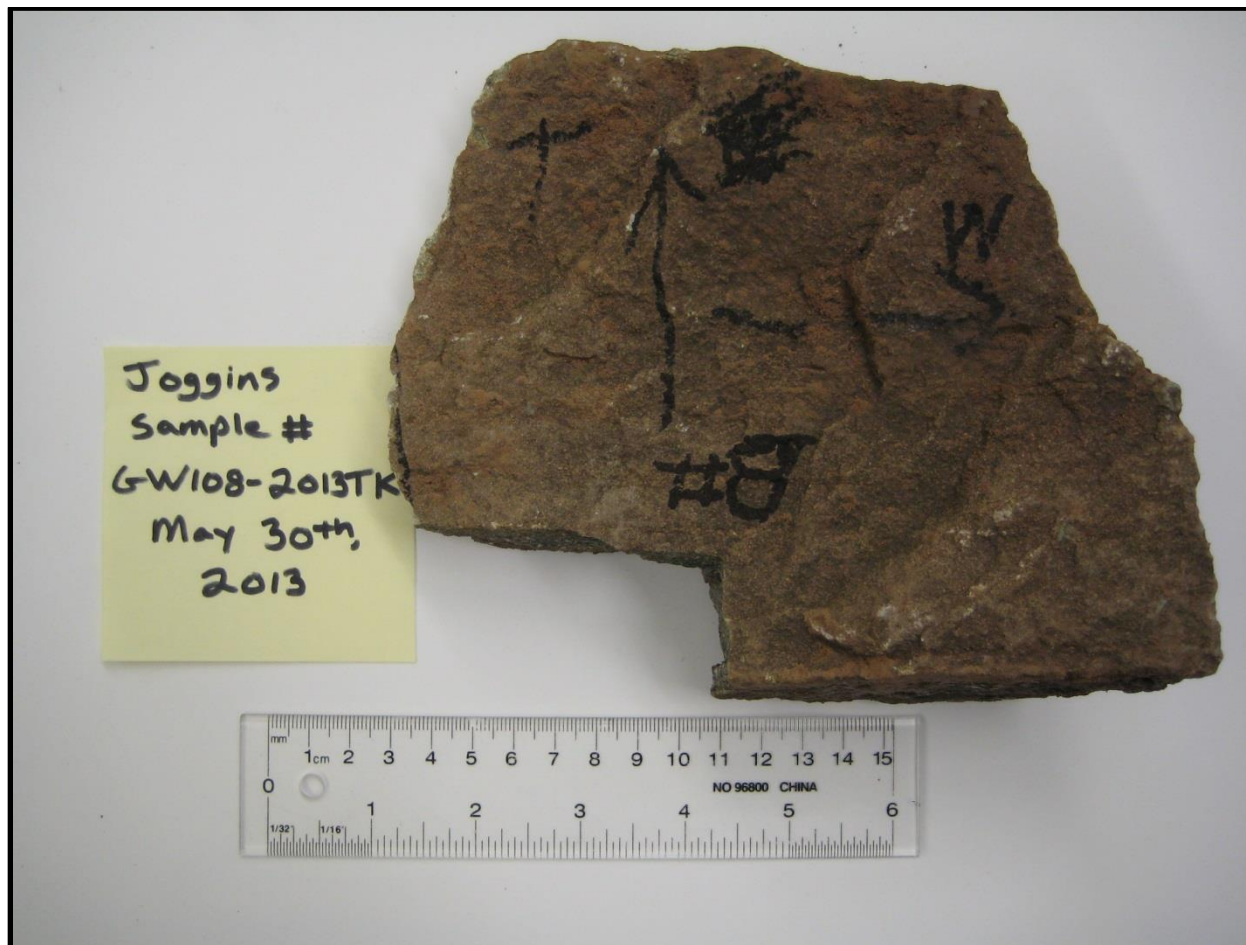


Figure 14-8: Photograph of hand sample GW108-2013TK.

Sample GW108-2013TK is a light grey, medium grained, equigranular sandstone that displays conchoidal fractures. The sample is also hard and brittle with a gritty feel. The hand sample reacts moderately with acid, indicating the presence of calcite. There is an alignment of minerals or grains that appear as dark brown in colour. There is also a lithic fragment that occurs in the sample. It appears to be chert and is 10 mm long by 5 mm high and has a dark brown rim, yellow center and is ellipsoidal in shape.

15.0 Appendix E: Thin Section Descriptions (Mineralogy)

Sample: GW101-2013TK

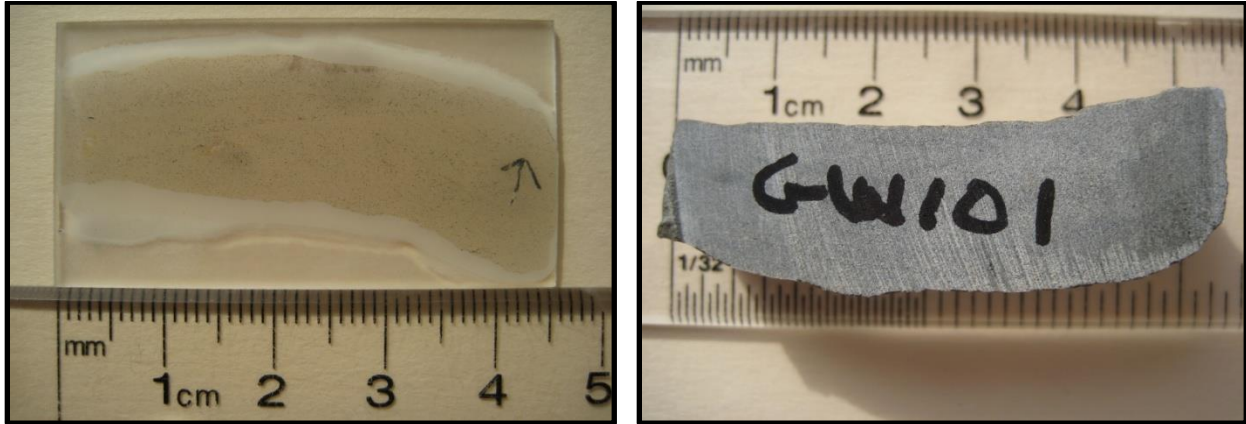


Figure 15-1: Left; photograph of thin section from hand sample GW101-2013TK. Right; corresponding photograph of rock sample that thin section was made from.

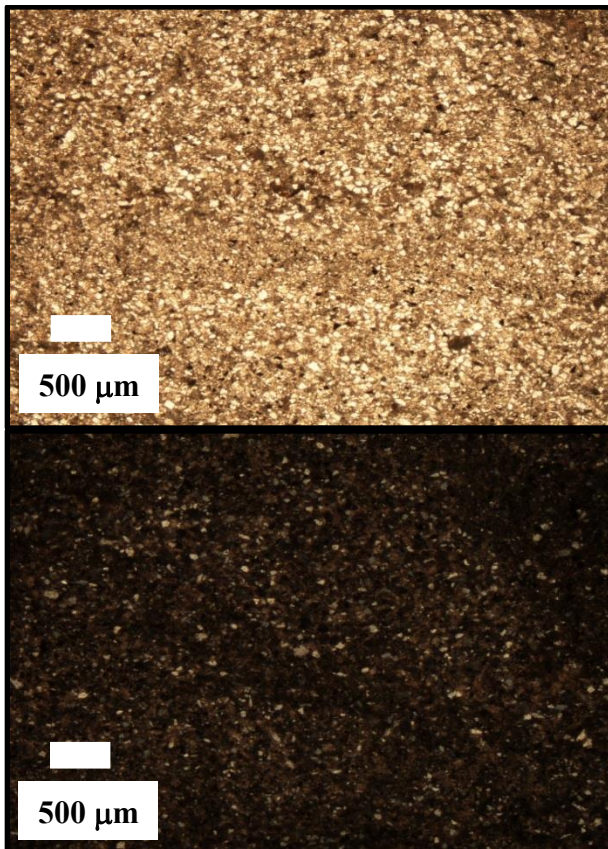


Figure 15-2: Top; sample GW101-2013TK in ordinary light at 2X magnification. Bottom; sample in plane polarized light at 2X magnification.

Sample: GW101-2013TK Continued...

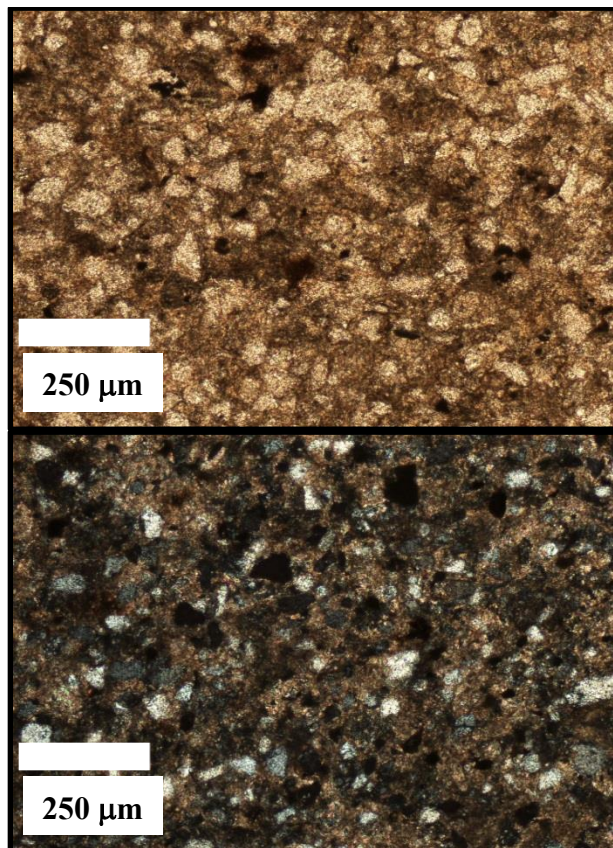


Figure 15-3: Top; sample GW101-2013TK in ordinary light at 10X magnification. Bottom; sample in plane polarized light at 10X magnification.

Description:

In thin section, the sample appears fine-grained and mainly equigranular. The dominant minerals are quartz and calcite. The quartz crystals are rounded to angular and randomly shaped with no preferred orientation. Less than 1% accessory hornblende is present. There is an opaque mineral, probably siderite, that occurs in the sample and makes up approximately 2 % of the sample. Calcite/ankerite occurs as a fine-grained greyish-brown coloured mineral, probably as a result of secondary mineralization. In plane polarized, there does appear to be a discrete layering texture which is exhibited by what appears to be a greater concentration of calcite occurring as bands as well as the apparent concentration of the black/dark brown opaque mineral along these bands.

Sample: GW102-2013TK

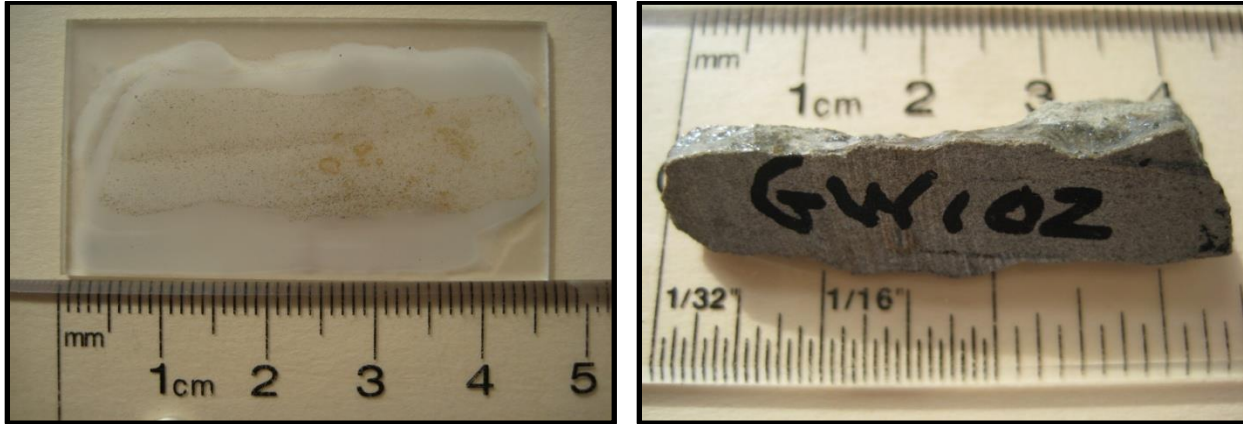


Figure 15-4: Left; photograph of thin section from hand sample GW101-2013TK. Right; corresponding photograph of rock sample that thin section was made from.

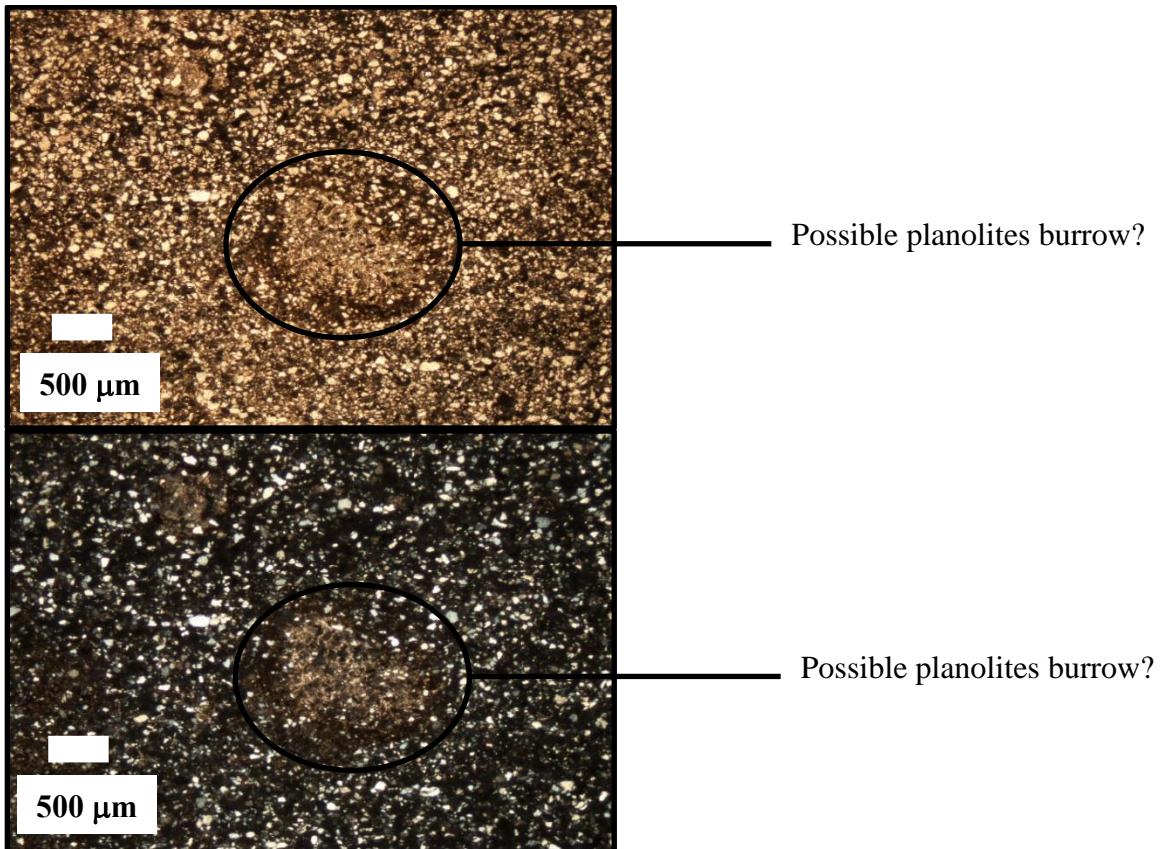


Figure 15-5: Top; sample GW102-2013TK in ordinary light at 2X magnification. Bottom; sample in plane polarized light at 2X magnification.

Sample: GW102-2013TK Continued...

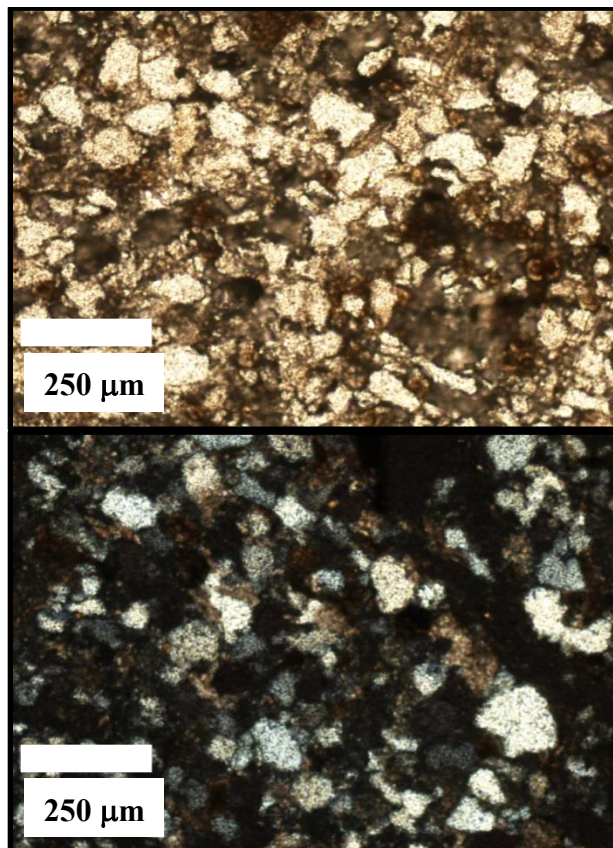


Figure 15-6: Top; sample GW102-2013TK in ordinary light at 10X magnification. Bottom; sample in plane polarized light at 10X magnification.

Description:

In thin section, the sample is mainly equigranular and fine-grained. Quartz and calcite are the dominant minerals with the quartz crystals being rounded to angular in shape and randomly oriented. The grain size is similar to that of sample GW101-2013TK. Calcite/ankerite occurs in the sample as a matrix material. There are zones that are round in shape and contain abundant calcite as infill and are rimmed by a yellowish/brown mineral, possibly siderite. These features could be planolites burrows. There is also the occurrence of some accessory hornblende ($\ll 1\%$). The thin section can be divided into two approximately equal halves, with the halves separated by a gap/crack in the thin section; one side dark (more calcite/ankerite cement), one side light (less cement). The sample is composed of approximately 75 % quartz, 20 % calcite/ankerite and 5 % siderite.

Sample: GW103-2013TK

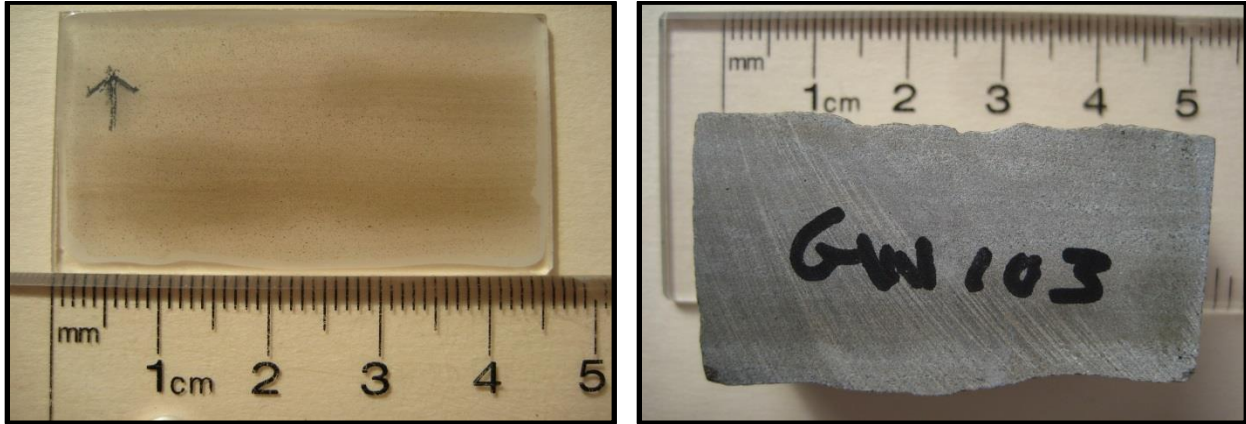


Figure 15-7: Left; photograph of thin section from hand sample GW103-2013TK. Right; corresponding photograph of rock sample that thin section was made from.

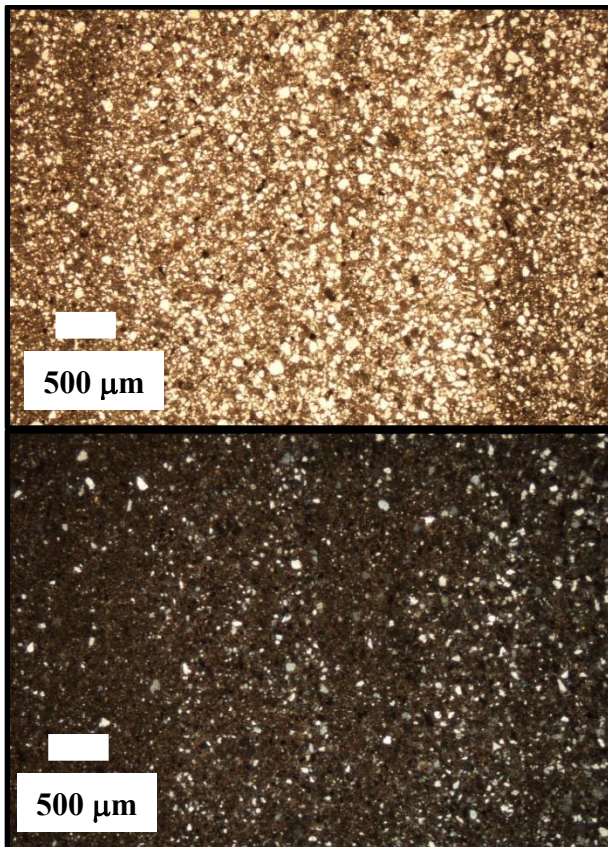


Figure 15-8: Top; sample GW103-2013TK in ordinary light at 2X magnification. Bottom; sample in plane polarized light at 2X magnification.

Sample: GW103-2013TK Continued...

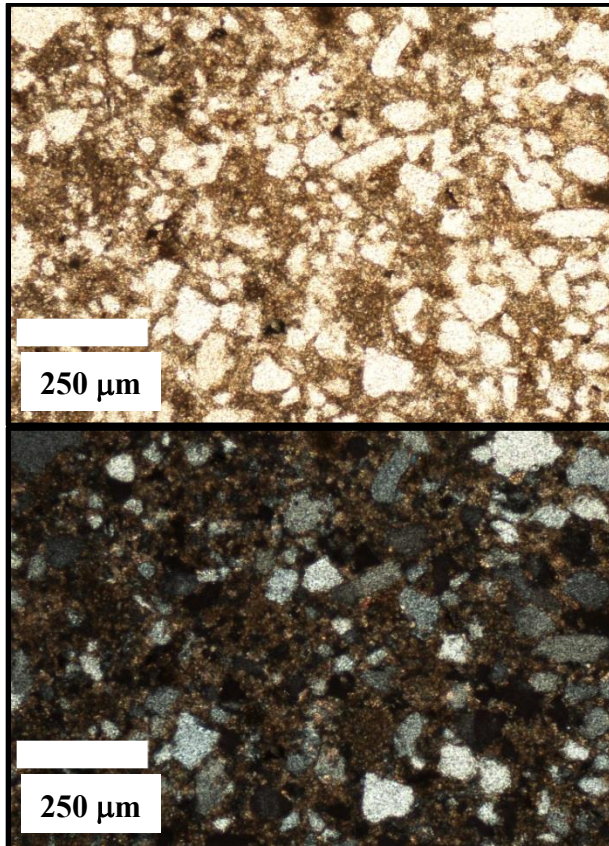


Figure 15-9: Top; sample GW103-2013TK in ordinary light at 10X magnification. Bottom; sample in plane polarized light at 10X magnification.

Description:

This thin section can be described as equigranular, fine-grained and angular crystals. The sample is layered with calcite-rich and quartz-rich layers occurring. The calcite-rich layers are brownish/grey in colour. The quartz-rich areas have much less calcite/ankerite cement and the quartz crystals are in greater contact with one another. The calcite/ankerite-rich areas contain minor quartz crystals that are surrounded with calcite/ankerite. Siderite occurs as a yellowish/brownish colour. Quartz is approximately 60 % of the sample, with calcite/ankerite the remaining 40 %.

Sample: GW104-2013TK

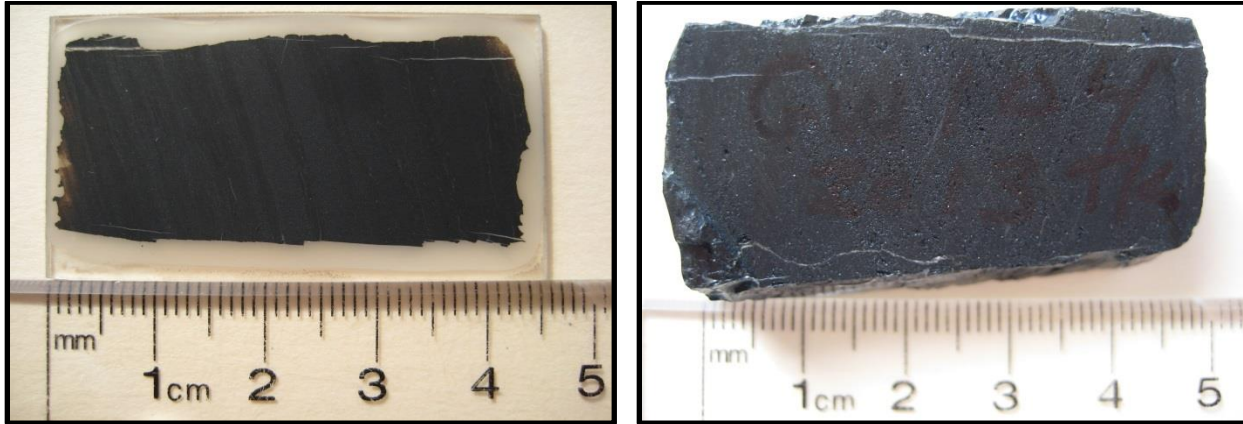


Figure 15-10: Left; photograph of thin section from hand sample GW104-2013TK. Right; corresponding photograph of rock sample that thin section was made from.

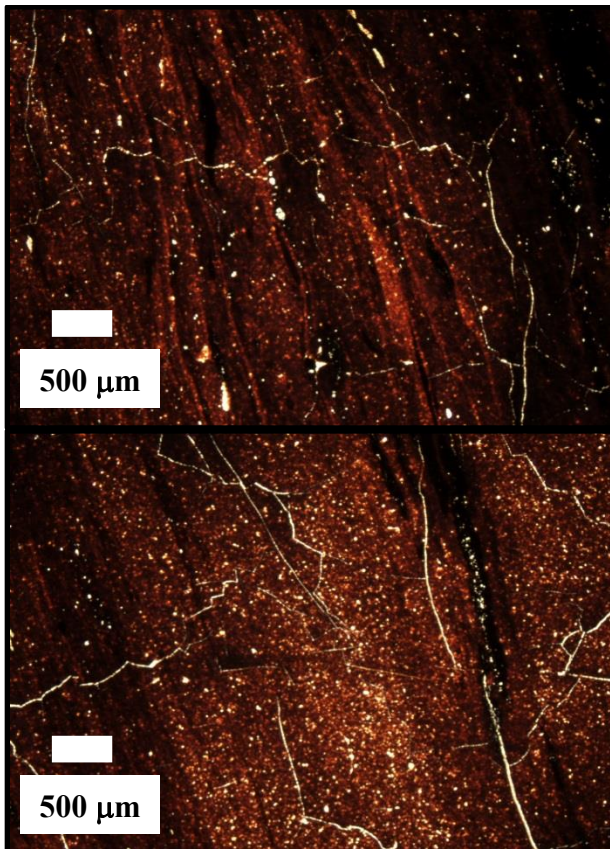


Figure 15-11: Top; sample GW104-2013TK in ordinary light at 2X magnification. Bottom; another image of the sample in ordinary light at 2X magnification.

Sample: GW104-2013TK Continued...

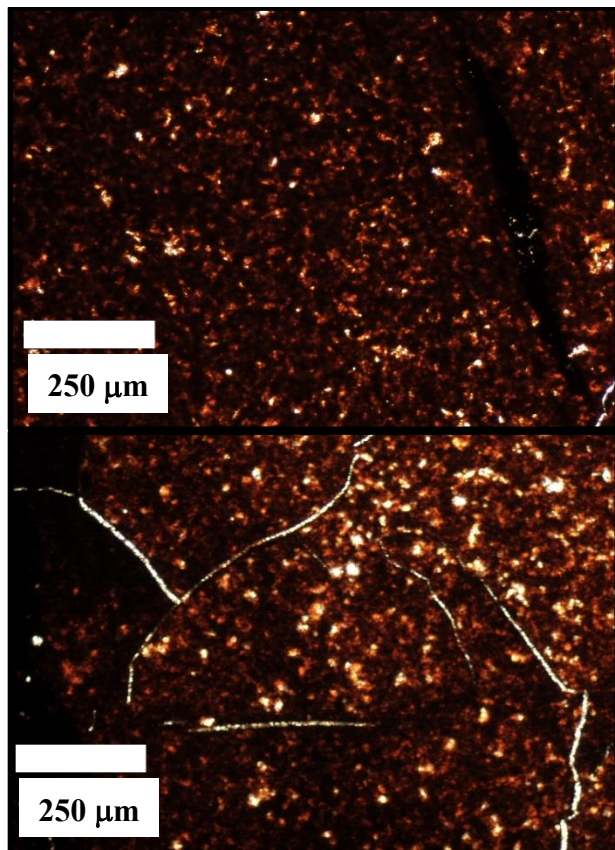


Figure 15-12: Top; sample GW104-2013TK in ordinary light at 10X magnification. Bottom; another image of the sample in ordinary light at 10X magnification.

Description:

This thin section represents coal. It is composed mainly of graphite/opaque mineral matter. The sample contains thin red shreds that are red in colour. They probably represent woody material that has been well preserved. The smaller yellow/orange coloured particles are likely spores or algal material.

Sample: GW105-2013TK



Figure 15-13: Left; photograph of thin section from hand sample GW105-2013TK. Right; corresponding photograph of rock sample that thin section was made from.

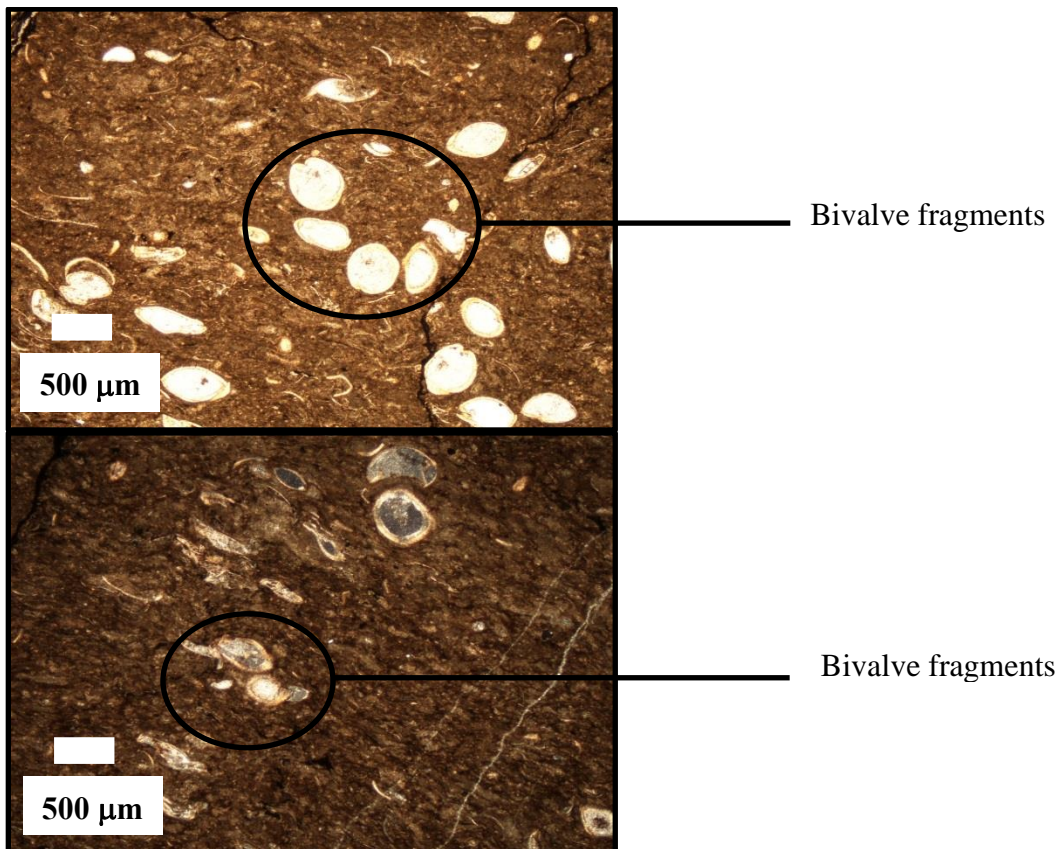


Figure 15-14: Top; sample GW105-2013TK in ordinary light at 2X magnification. Bottom; sample in plane polarized light at 2X magnification.

Sample: GW105-2013TK Continued...

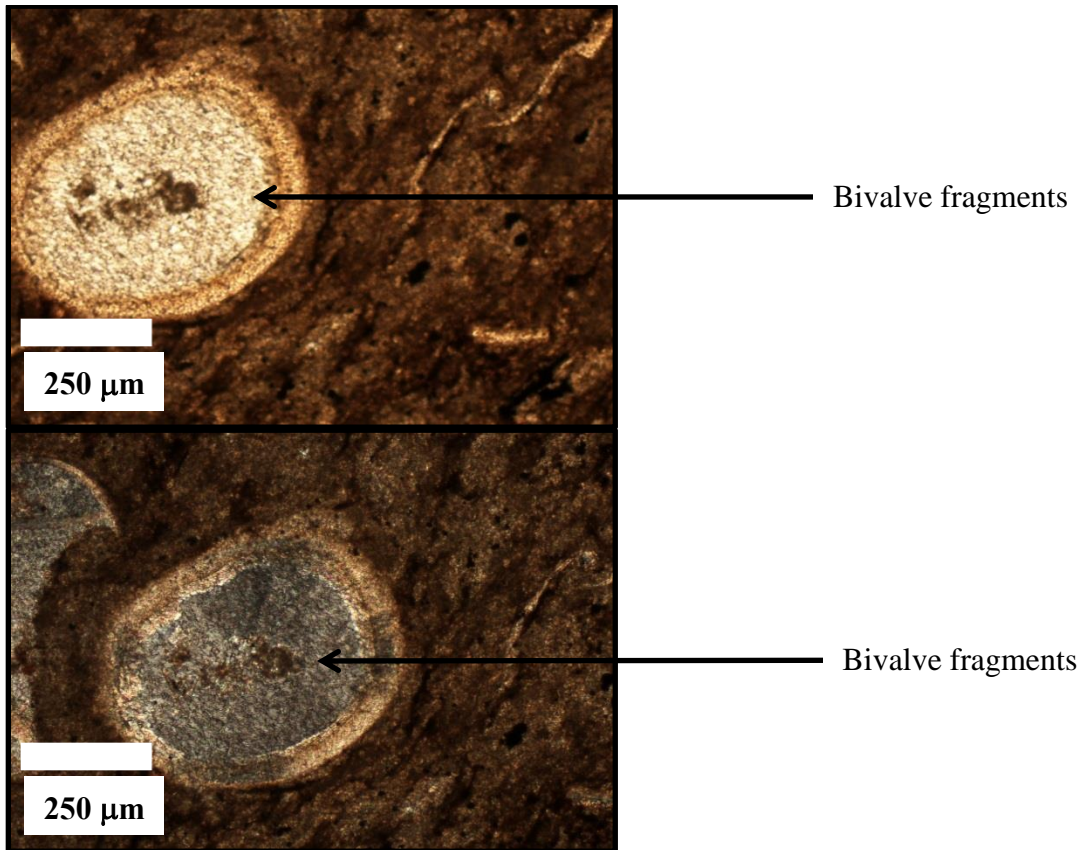


Figure 15-15: Top; sample GW105-2013TK in ordinary light at 10X magnification. Bottom; sample in plane polarized light at 10X magnification.

Description:

This thin section represents a fossiliferous limestone that is composed primarily of calcite with some residual siderite and opaque minerals. The sample contains abundant shell fragments that appear to represent bivalves. Calcite/ankerite combine to make up 95 % of the sample, while the black/opaque minerals combine for approximately 5 %. The black/opaque mineralization occurs as single crystals, groupings of crystals or as veinlets.

Sample: GW106-2013TK

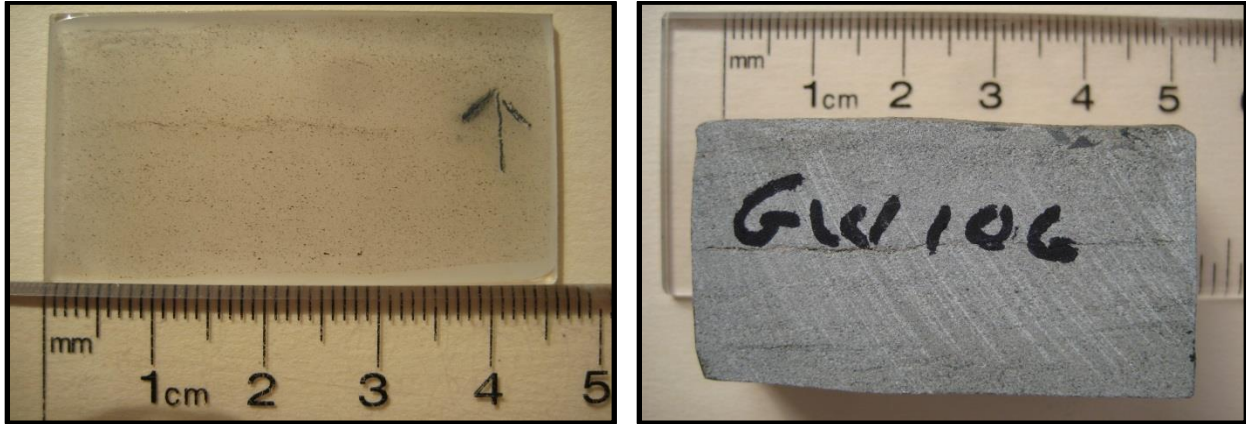


Figure 15-16: Left; photograph of thin section from hand sample GW106-2013TK. Right; corresponding photograph of rock sample that thin section was made from.

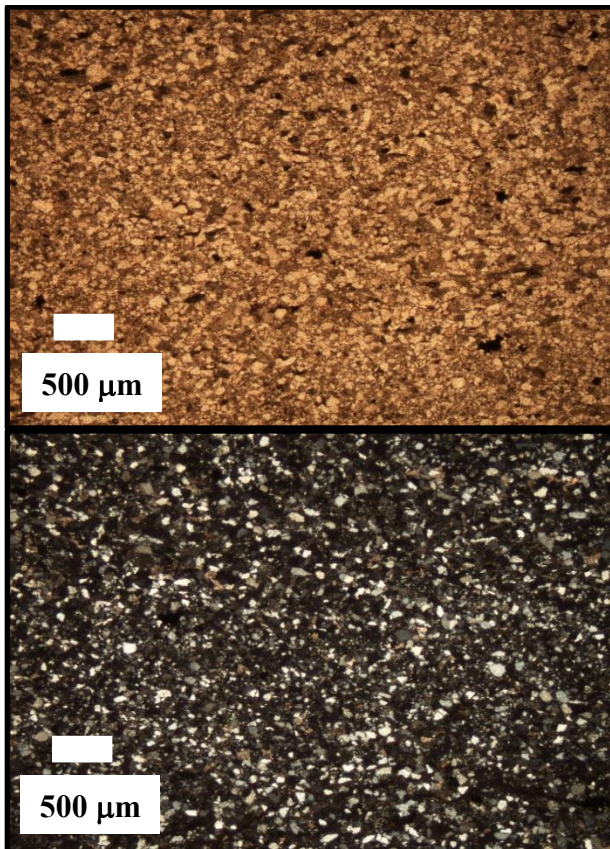


Figure 15-17: Top; sample GW106-2013TK in ordinary light at 2X magnification. Bottom; sample in plane polarized light at 2X magnification.

Sample: GW106-2013TK Continued...

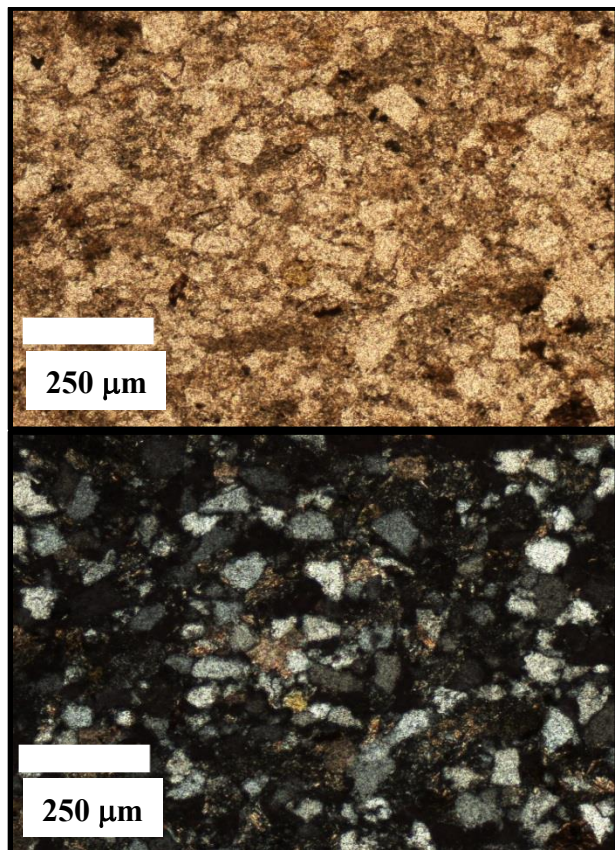


Figure 15-18: Top; sample GW106-2013TK in ordinary light at 10X magnification. Bottom; sample in plane polarized light at 10X magnification.

Description:

This thin section represents a sandstone that is equigranular, angular and fine-grained. The sample contains mainly quartz and calcite/ankerite with an accessory opaque mineral. Quartz composes of approximately 75 % of the sample, with calcite/ankerite being the remaining 25 %.

Sample: GW107-2013TK

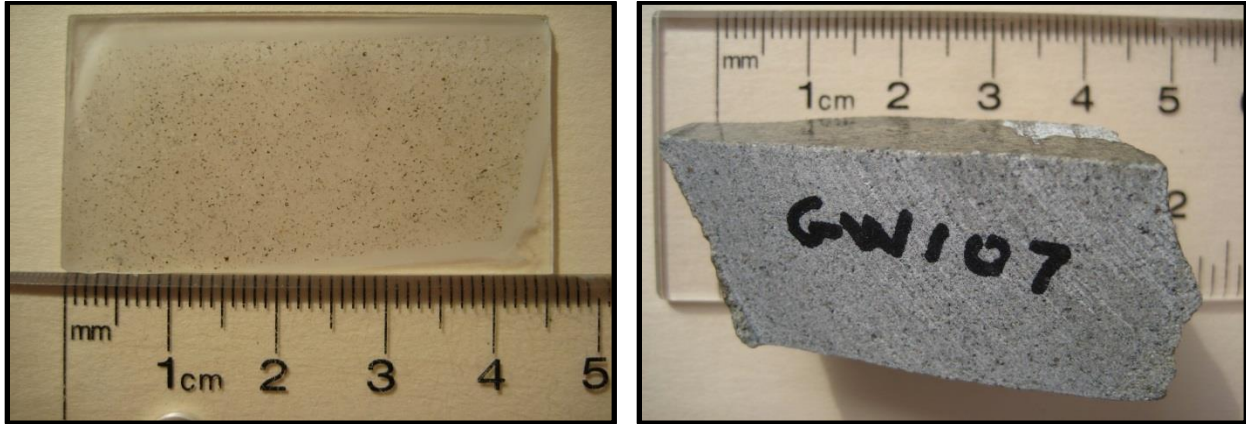


Figure 15-19: Left; photograph of thin section from hand sample GW107-2013TK. Right; corresponding photograph of rock sample that thin section was made from.

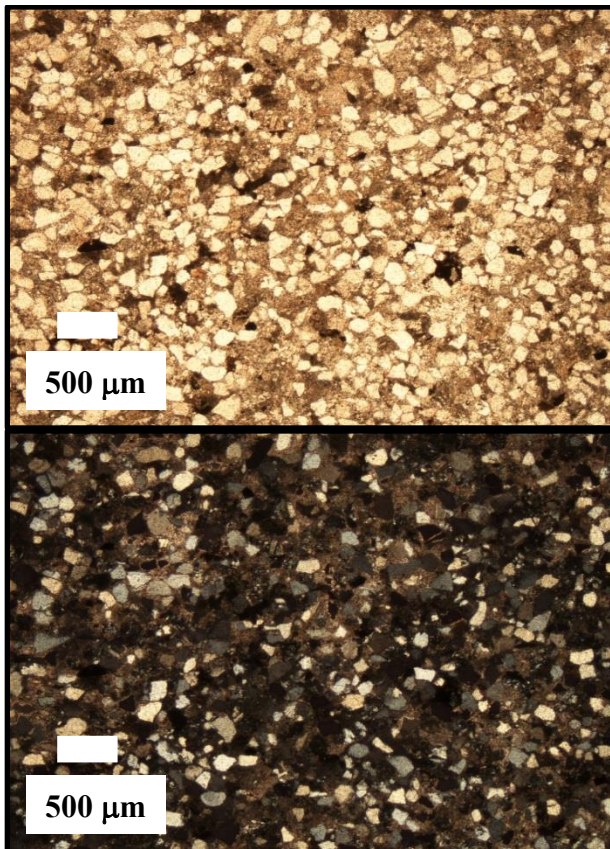


Figure 15-20: Top; sample GW107-2013TK in ordinary light at 2X magnification. Bottom; sample in plane polarized light at 2X magnification.

Sample: GW107-2013TK Continued...

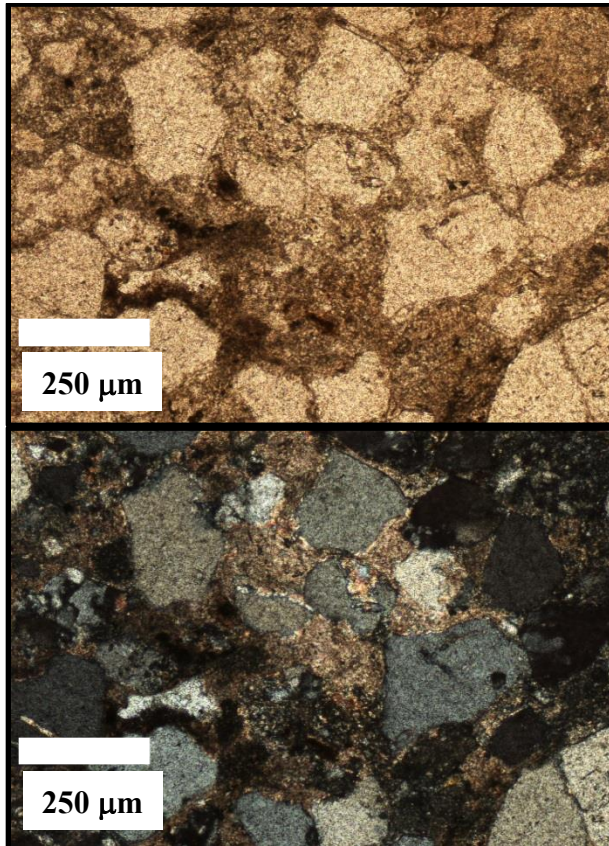


Figure 15-21: Top; sample GW107-2013TK in ordinary light at 10X magnification. Bottom; sample in plane polarized light at 10X magnification.

Description:

This thin section represents a sandstone that is equigranular, angular and fine-grained. The sample contains mainly quartz and calcite with an accessory opaque mineral. Quartz composes of approximately 65 % of the sample, with calcite/ankerite being the remaining 35 %.

Sample: GW108-2013TK

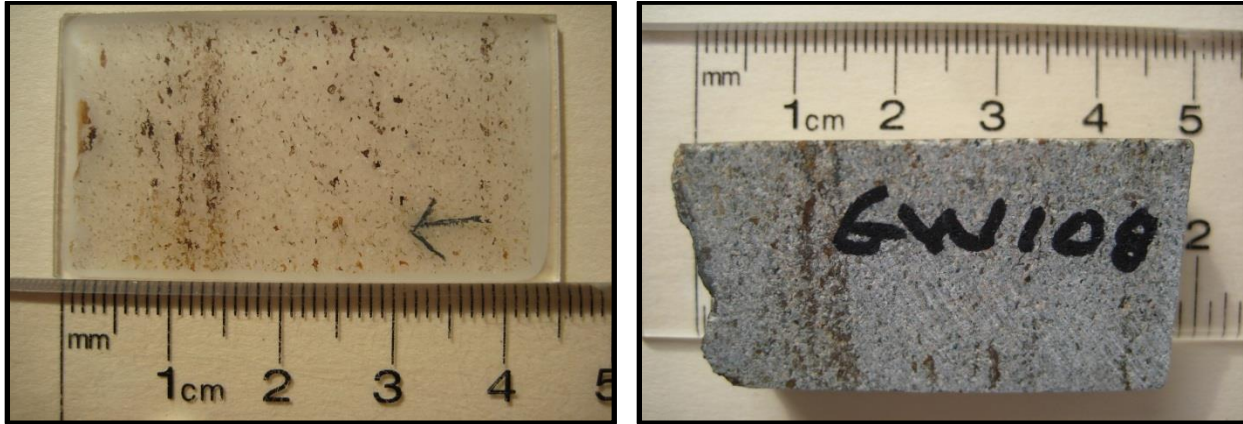


Figure 15-22: Left; photograph of thin section from hand sample GW108-2013TK. Right; corresponding photograph of rock sample that thin section was made from.

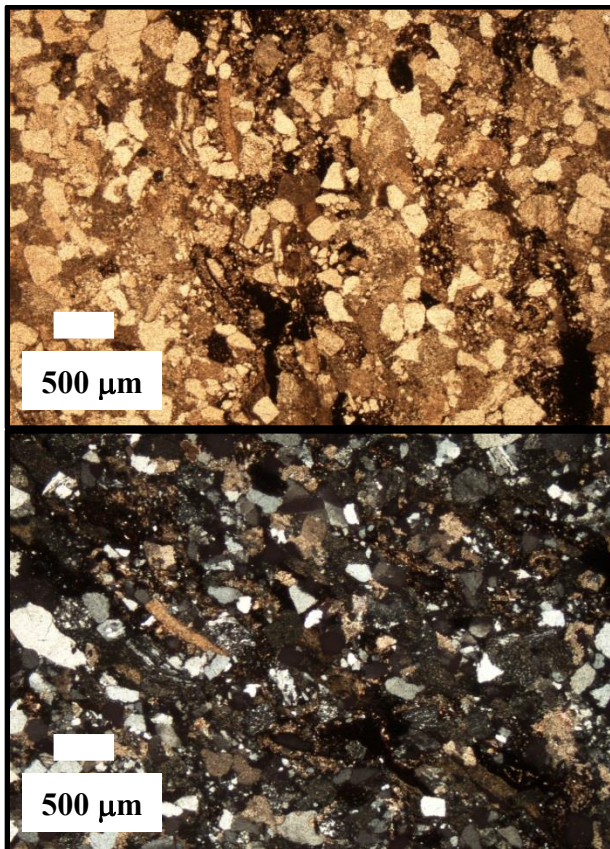


Figure 15-23: Top; sample GW108-2013TK in ordinary light at 2X magnification. Bottom; sample in plane polarized light at 2X magnification.

Sample: GW108-2013TK Continued...

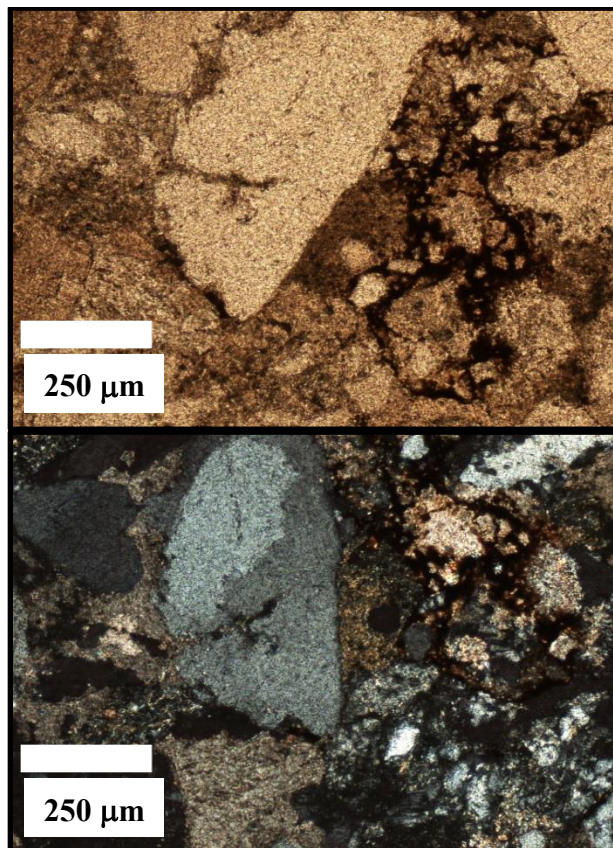


Figure 15-24: Top; sample GW108-2013TK in ordinary light at 10X magnification. Bottom; sample in plane polarized light at 10X magnification.

Description:

This thin section is an in-equigranular, angular, coarse-grained sandstone. Approximately 80 % of the sample is quartz and calcite/ankerite represents the remaining 20 %. Siderite occurs but at a low percentage. There is some banding/layering as a result of the siderite occurring in concentrated form as bands.

16.0 Appendix F: Thin Section Descriptions (Porosity)

Sample: GW101-2013TK

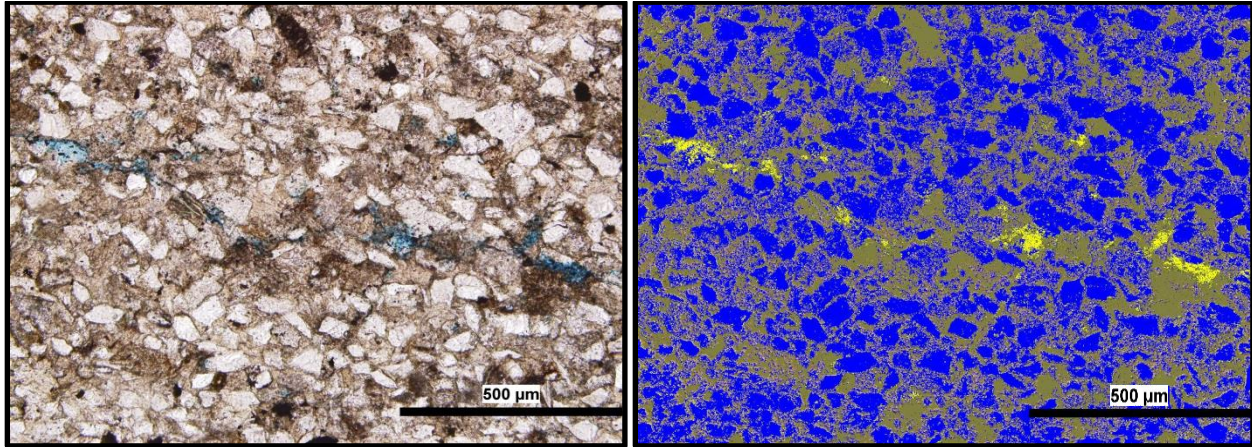


Figure 16-1: Left; thin section image GW101-2013TK-1 (@ 10X) in normal light with porosity shown in blue (dye). Right; same image, but with porosity shown in yellow, grains as blue and cement as brown.

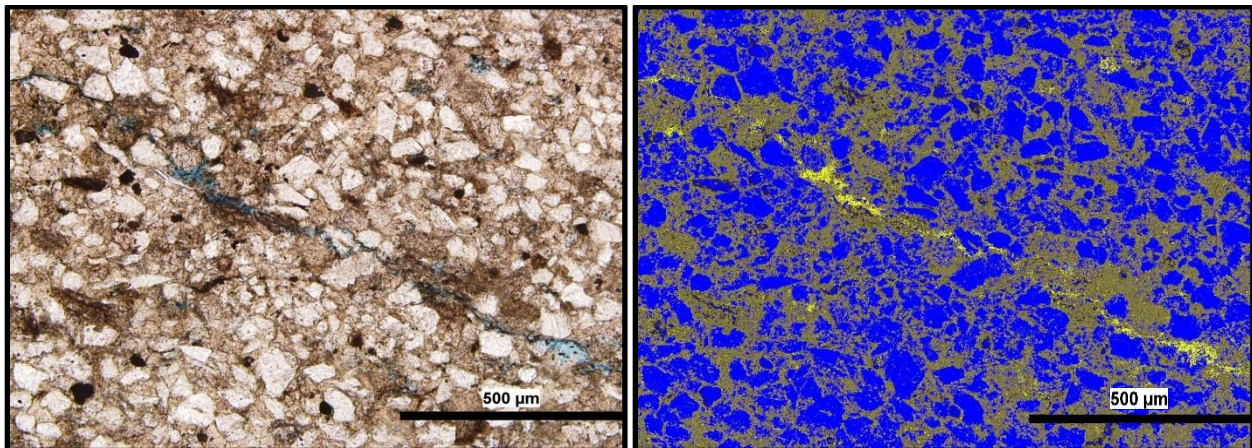


Figure 16-2: Left; thin section image GW101-2013TK-2 (@ 10X) in normal light with porosity shown in blue (dye). Right; same image, but with porosity shown in yellow, grains as blue and cement as brown.

Sample: GW101-2013TK Continued...

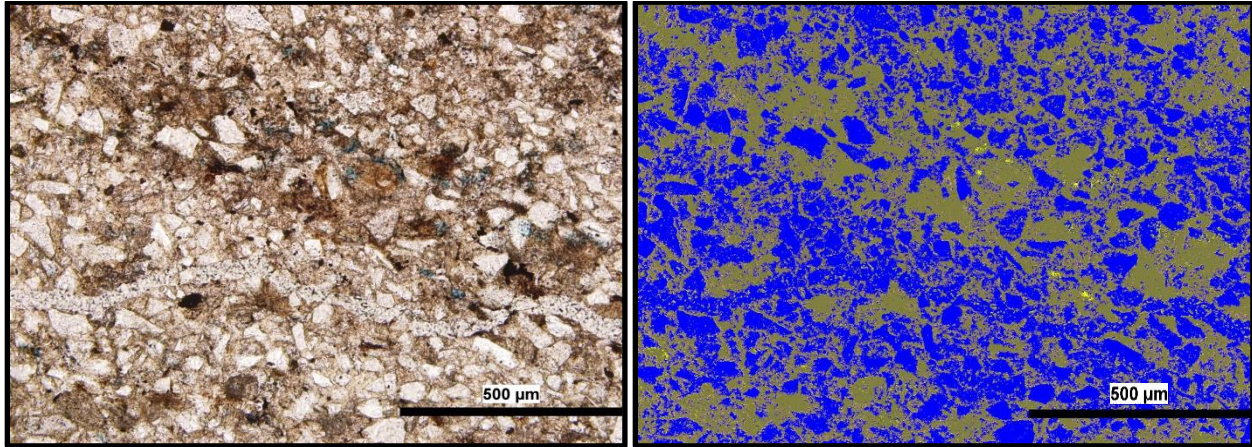


Figure 16-3: Left; thin section image GW101-2013TK-3 (@ 10X) in normal light with porosity shown in blue (dye). Right; same image, but with porosity shown in yellow, grains as blue and cement as brown.

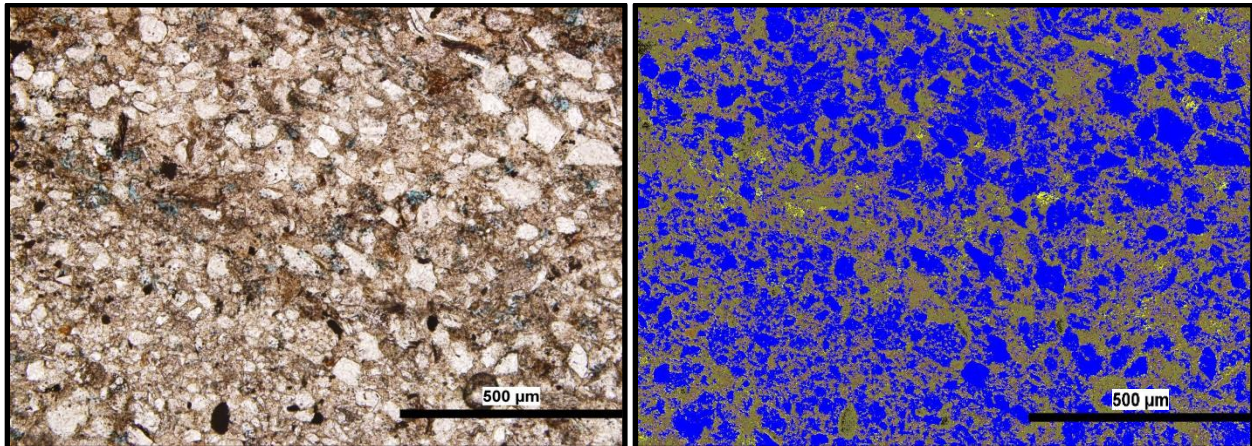


Figure 16-4: Left; thin section image GW101-2013TK-4 (@ 10X) in normal light with porosity shown in blue (dye). Right; same image, but with porosity shown in yellow, grains as blue and cement as brown.

Sample: GW101-2013TK Continued...

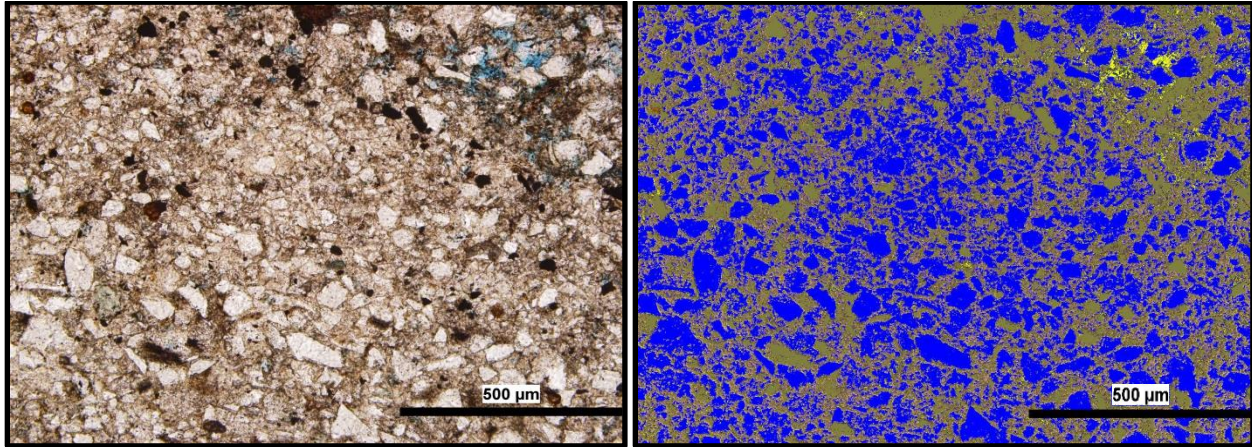


Figure 16-5: Left; thin section image GW101-2013TK-5 (@ 10X) in normal light with porosity shown in blue (dye). Right; same image, but with porosity shown in yellow, grains as blue and cement as brown.

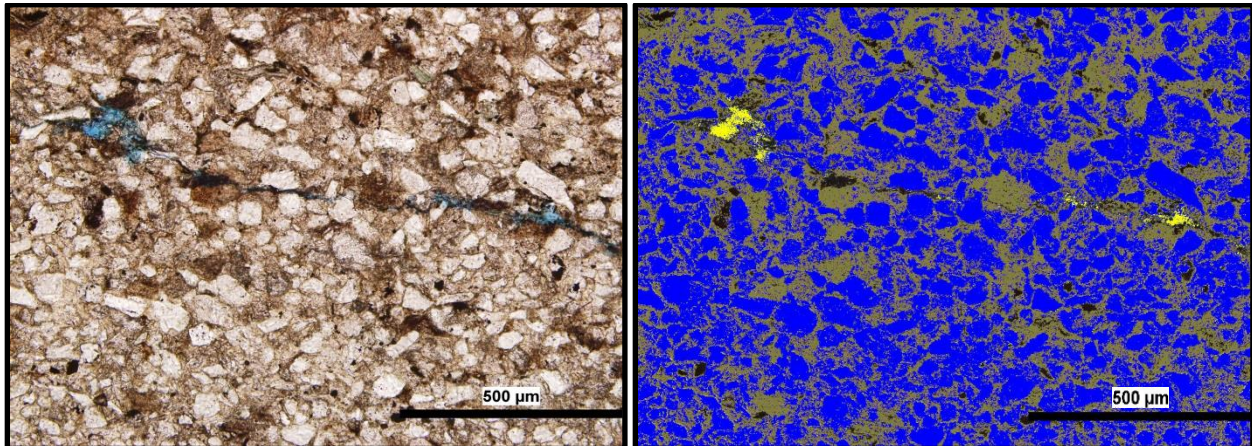


Figure 16-6: Left; thin section image GW101-2013TK-6 (@ 10X) in normal light with porosity shown in blue (dye). Right; same image, but with porosity shown in yellow, grains as blue and cement as brown.

Sample: GW101-2013TK Continued...

Table 16-1: Summary table for sample GW101-2013TK listing the area percentage for voids, grains and cement in each image captured of the thin section. The average area for each of the three parameters is also calculated.

Image Number	Area Type	Area %
GW101-2013TK-1	Voids	2.6
	Grains	72.8
	Cement	24.6
GW101-2013TK-2	Voids	2.5
	Grains	65.5
	Cement	32.0
GW101-2013TK-3	Voids	0.6
	Grains	58.8
	Cement	40.7
GW101-2013TK-4	Voids	2.0
	Grains	75.8
	Cement	22.2
GW101-2013TK-5	Voids	2.0
	Grains	72.2
	Cement	25.8
GW101-2013TK-6	Voids	0.7
	Grains	69.6
	Cement	29.7
Average	Voids	1.7
	Grains	69.1
	Cement	29.2

Sample: GW102-2013TK

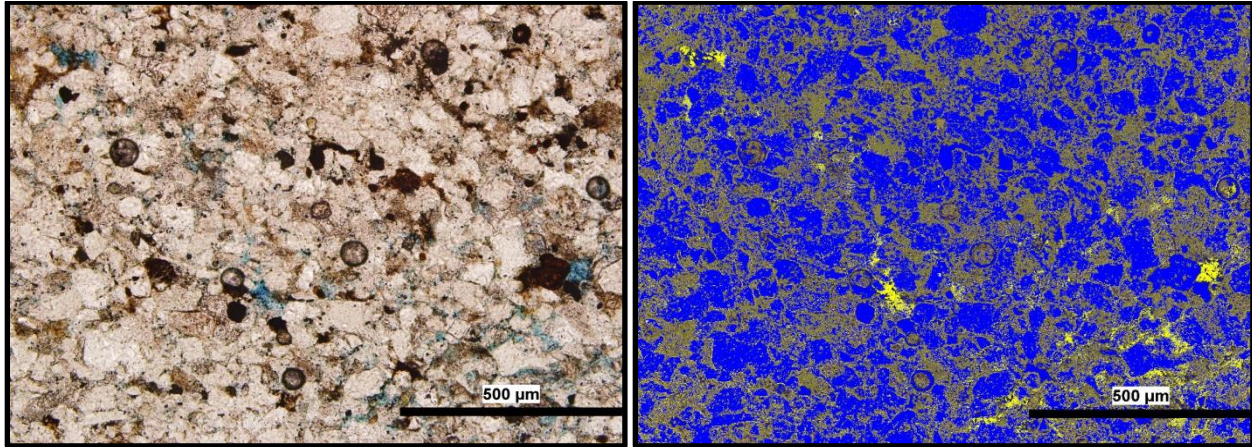


Figure 16-7: Left; thin section image GW102-2013TK-1 (@ 10X) in normal light with porosity shown in blue (dye). Right; same image, but with porosity shown in yellow, grains as blue and cement as brown.

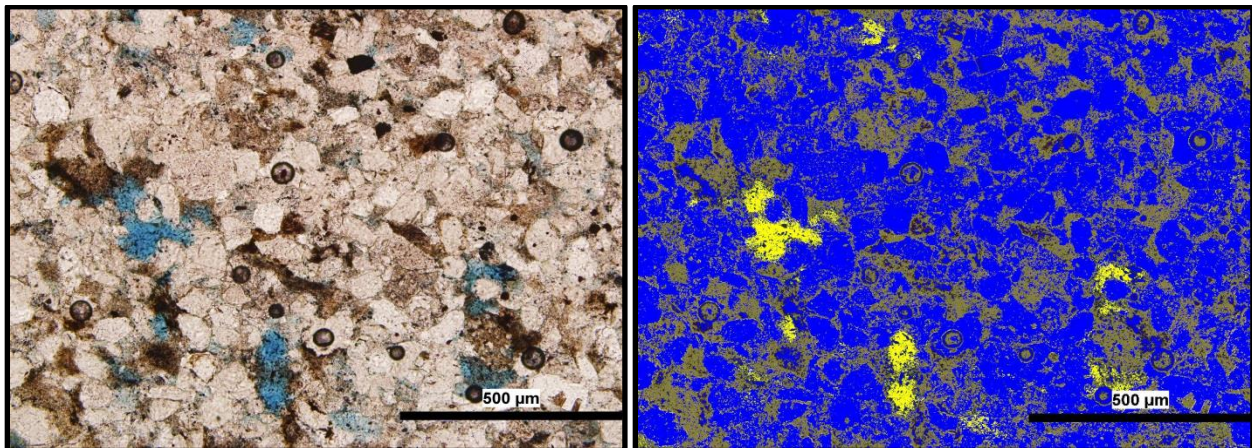


Figure 16-8: Left; thin section image GW102-2013TK-2 (@ 10X) in normal light with porosity shown in blue (dye). Right; same image, but with porosity shown in yellow, grains as blue and cement as brown.

Sample: GW102-2013TK Continued...

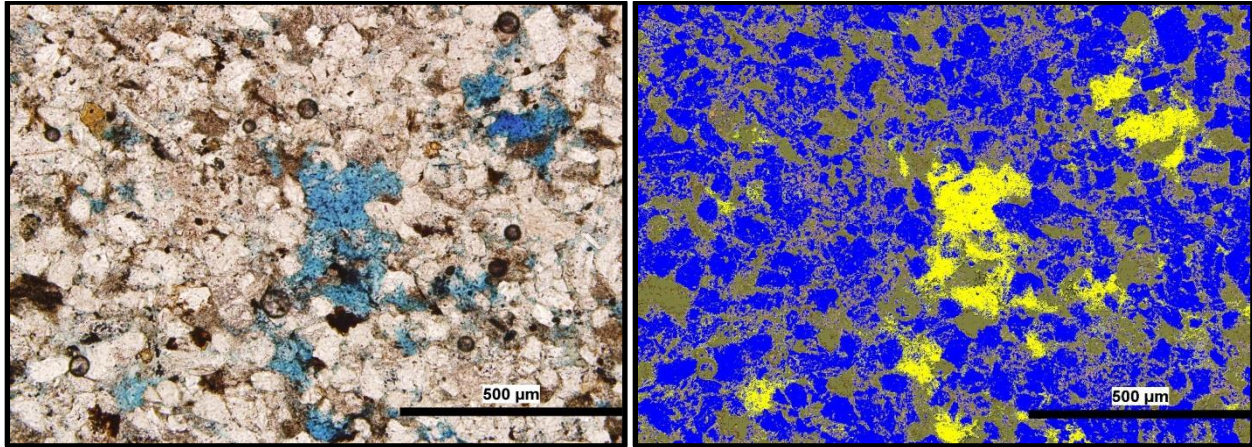


Figure 16-9: Left; thin section image GW102-2013TK-3 (@ 10X) in normal light with porosity shown in blue (dye). Right; same image, but with porosity shown in yellow, grains as blue and cement as brown.

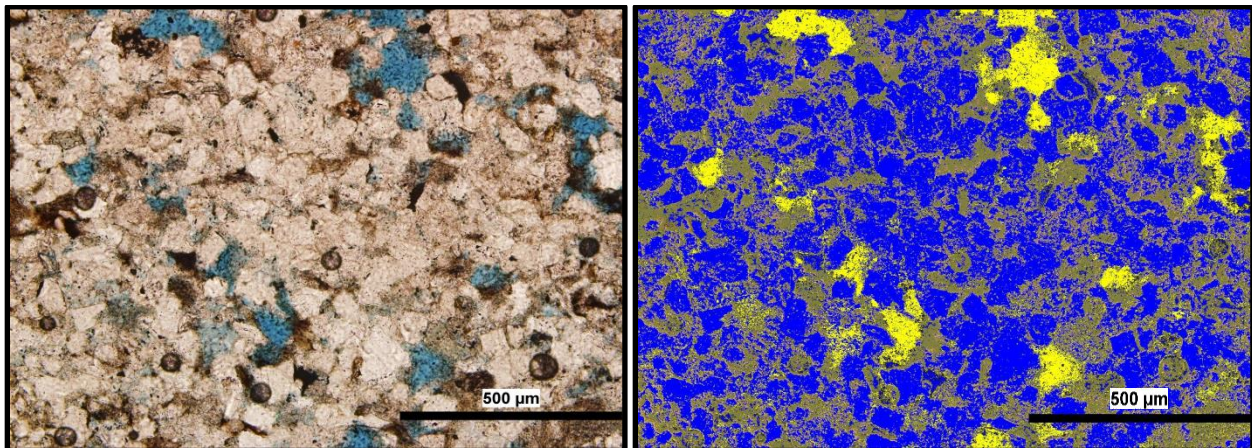


Figure 16-10: Left; thin section image GW102-2013TK-4 (@ 10X) in normal light with porosity shown in blue (dye). Right; same image, but with porosity shown in yellow, grains as blue and cement as brown.

Sample: GW102-2013TK Continued...

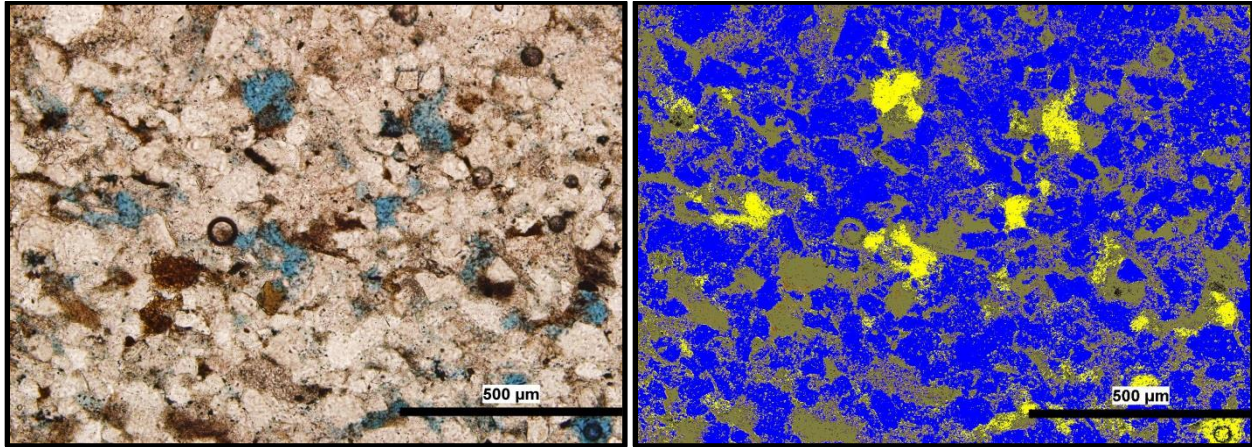


Figure 16-11: Left; thin section image GW102-2013TK-5 (@ 10X) in normal light with porosity shown in blue (dye). Right; same image, but with porosity shown in yellow, grains as blue and cement as brown.

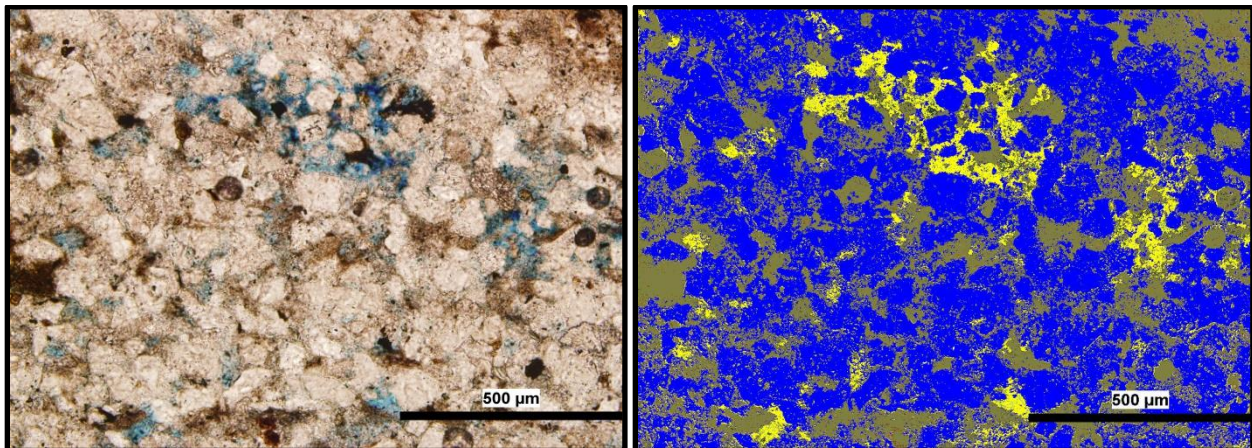


Figure 16-12: Left; thin section image GW102-2013TK-6 (@ 10X) in normal light with porosity shown in blue (dye). Right; same image, but with porosity shown in yellow, grains as blue and cement as brown.

Sample: GW102-2013TK Continued...

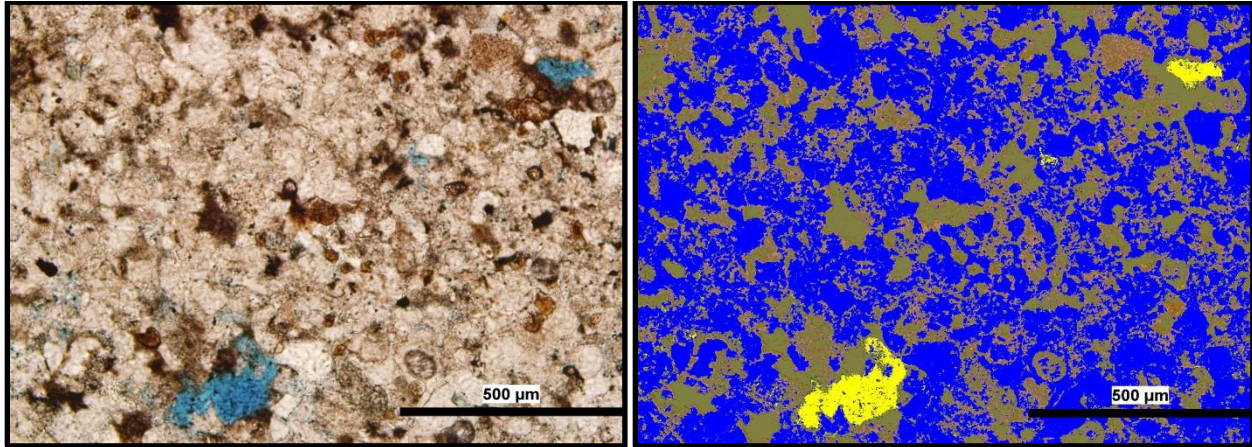


Figure 16-13: Left; thin section image GW102-2013TK-7 (@ 10X) in normal light with porosity shown in blue (dye). Right; same image, but with porosity shown in yellow, grains as blue and cement as brown.

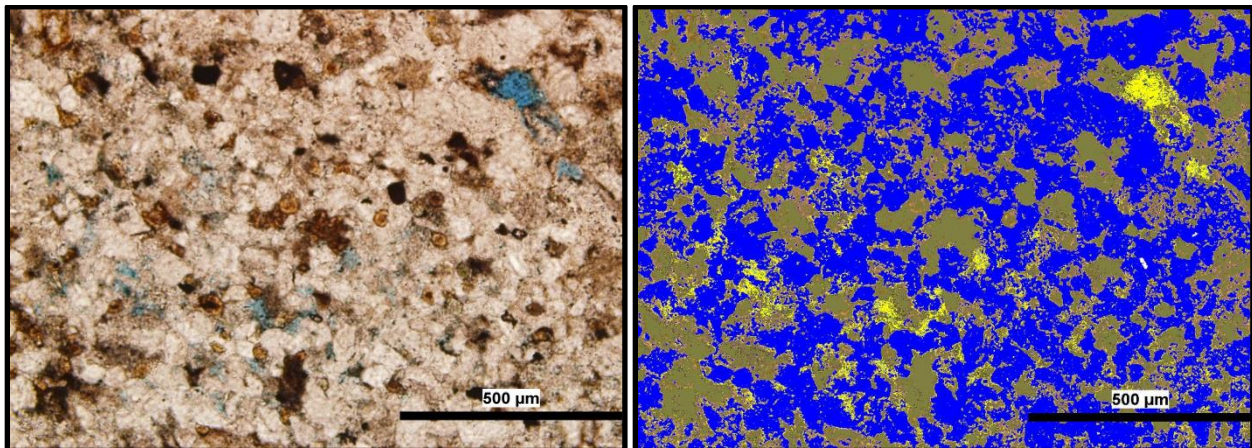


Figure 16-14: Left; thin section image GW102-2013TK-8 (@ 10X) in normal light with porosity shown in blue (dye). Right; same image, but with porosity shown in yellow, grains as blue and cement as brown.

Sample: GW102-2013TK Continued...

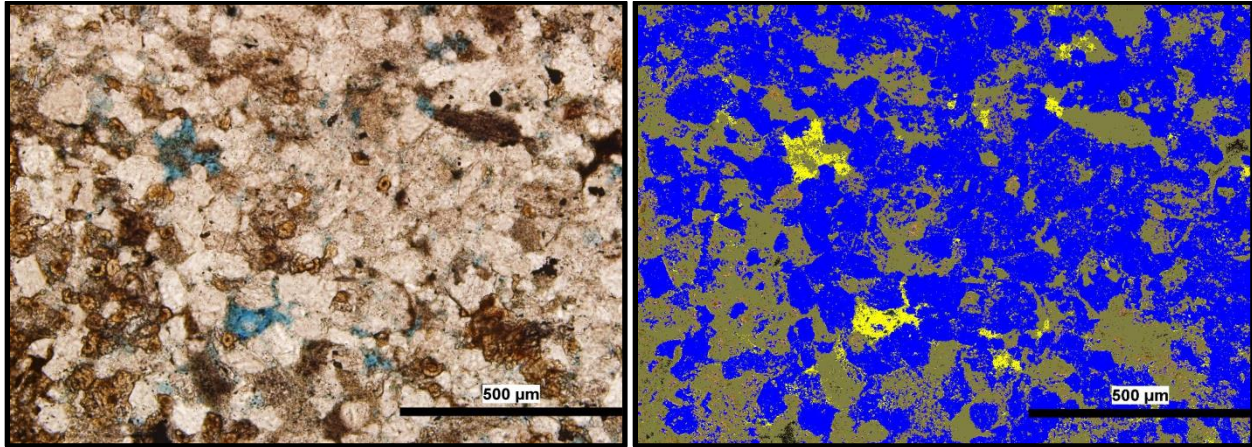


Figure 16-15: Left; thin section image GW102-2013TK-9 (@ 10X) in normal light with porosity shown in blue (dye). Right; same image, but with porosity shown in yellow, grains as blue and cement as brown.

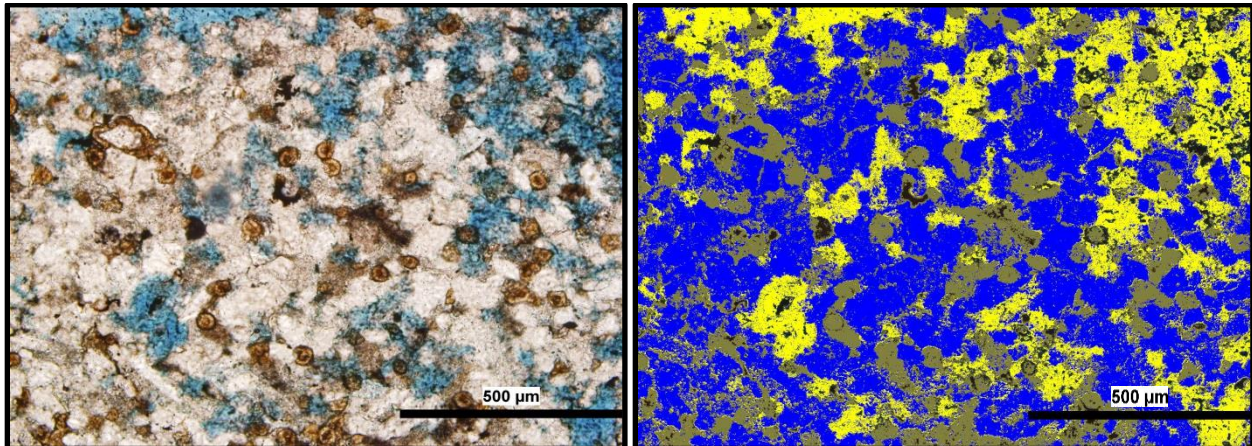


Figure 16-16: Left; thin section image GW102-2013TK-10 (@ 10X) in normal light with porosity shown in blue (dye). Right; same image, but with porosity shown in yellow, grains as blue and cement as brown.

Sample: GW102-2013TK Continued...

Table 16-2: Summary table for sample GW102-2013TK listing the area percentage for voids, grains and cement in each image captured of the thin section. The average area for each of the three parameters is also calculated.

Image Number	Area Type	Area %
GW102-2013TK-1	Voids	3.0
	Grains	60.2
	Cement	36.9
GW102-2013TK-2	Voids	7.6
	Grains	79.9
	Cement	12.5
GW102-2013TK-3	Voids	9.4
	Grains	64.2
	Cement	26.4
GW102-2013TK-4	Voids	8.5
	Grains	66.3
	Cement	25.2
GW102-2013TK-5	Voids	6.2
	Grains	76.1
	Cement	17.7
GW102-2013TK-6	Voids	7.0
	Grains	69.4
	Cement	23.7
GW102-2013TK-7	Voids	2.3
	Grains	80.3
	Cement	17.4
GW102-2013TK-8	Voids	5.7
	Grains	75.0
	Cement	19.3
GW102-2013TK-9	Voids	2.4
	Grains	68.3
	Cement	29.3
GW102-2013TK-10	Voids	22.3
	Grains	55.2
	Cement	22.5
Average	Voids	7.4
	Grains	69.5
	Cement	23.1

Sample: GW103-2013TK

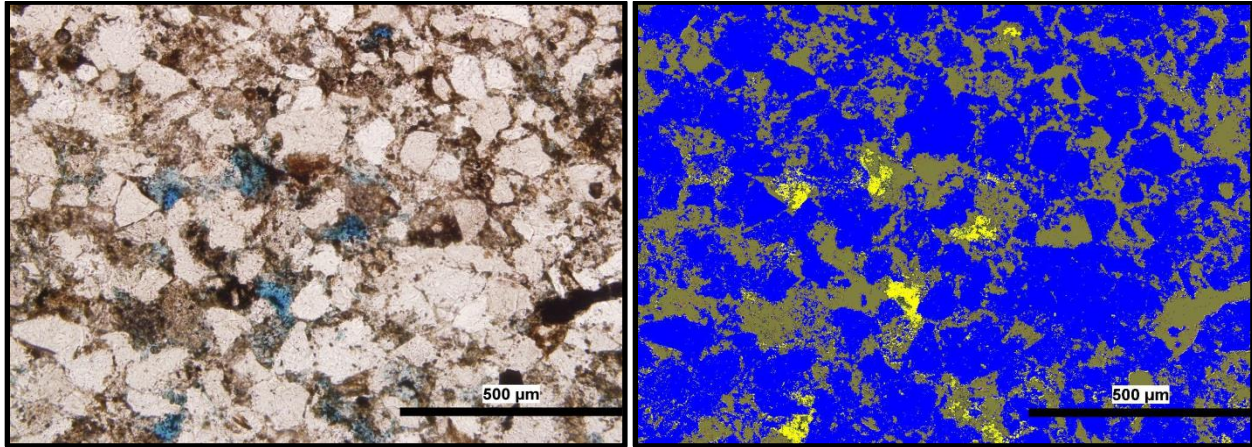


Figure 16-17: Left; thin section image GW103-2013TK-1 (@ 10X) in normal light with porosity shown in blue (dye). Right; same image, but with porosity shown in yellow, grains as blue and cement as brown.

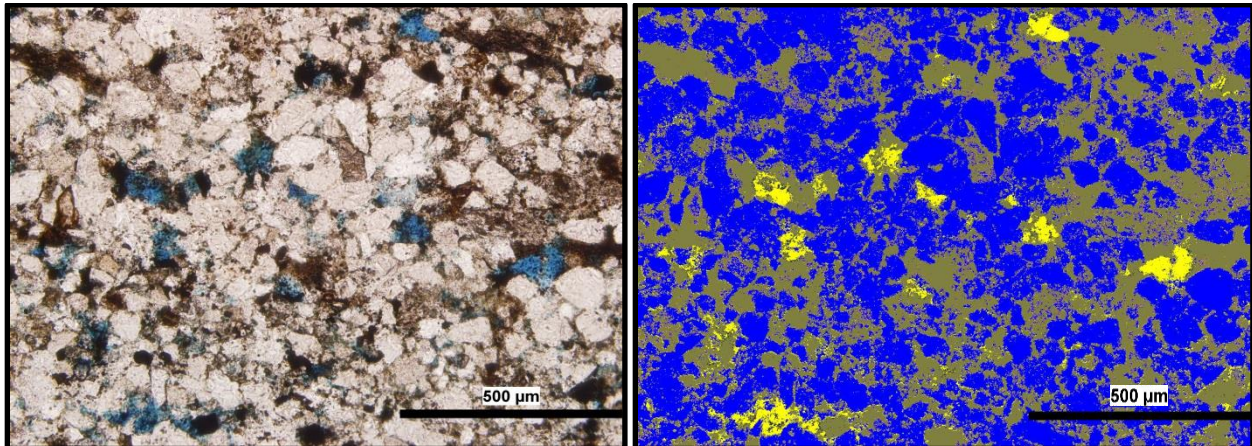


Figure 16-18: Left; thin section image GW103-2013TK-2 (@ 10X) in normal light with porosity shown in blue (dye). Right; same image, but with porosity shown in yellow, grains as blue and cement as brown.

Sample: GW103-2013TK Continued...

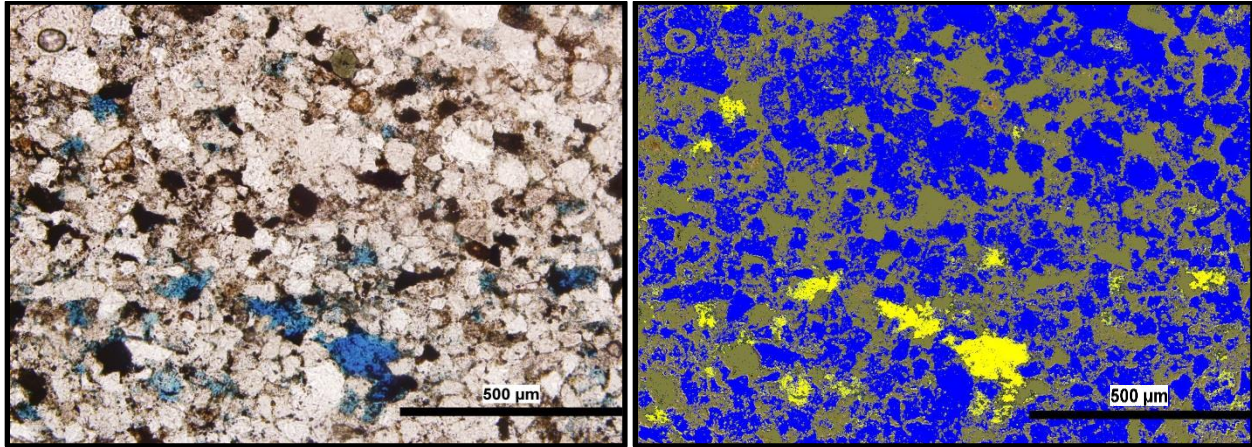


Figure 16-19: Left; thin section image GW103-2013TK-3 (@ 10X) in normal light with porosity shown in blue (dye). Right; same image, but with porosity shown in yellow, grains as blue and cement as brown.

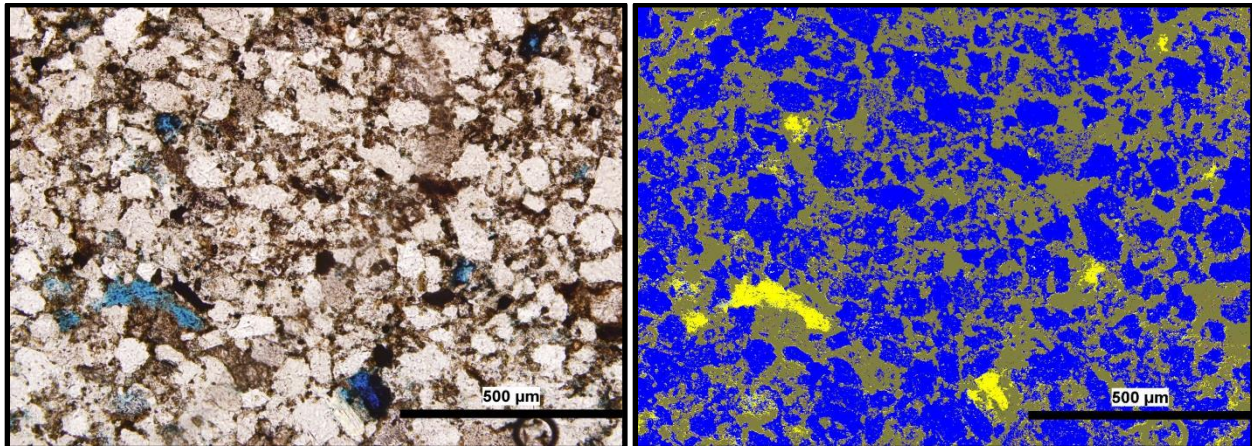


Figure 16-20: Left; thin section image GW103-2013TK-4 (@ 10X) in normal light with porosity shown in blue (dye). Right; same image, but with porosity shown in yellow, grains as blue and cement as brown.

Sample: GW103-2013TK Continued...

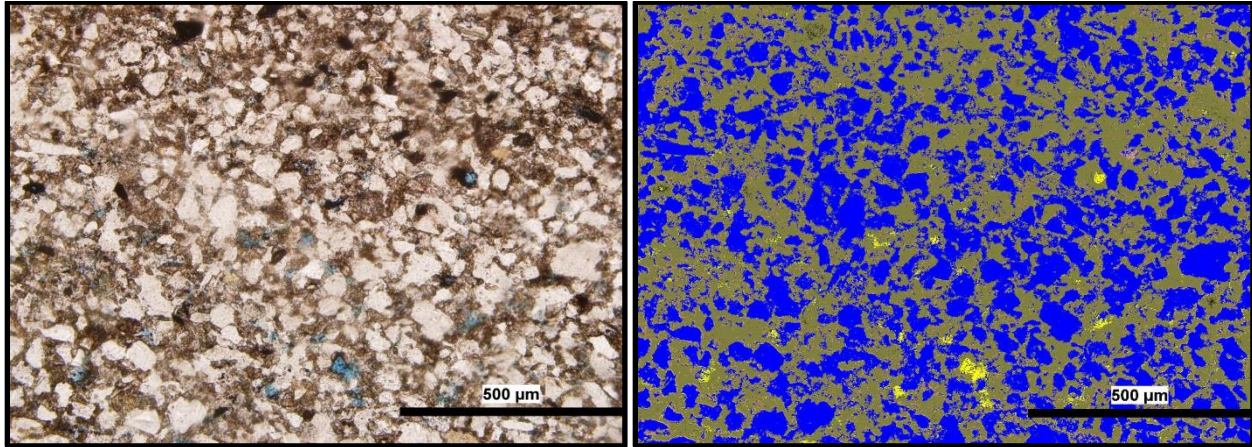


Figure 16-21: Left; thin section image GW103-2013TK-5 (@ 10X) in normal light with porosity shown in blue (dye). Right; same image, but with porosity shown in yellow, grains as blue and cement as brown.

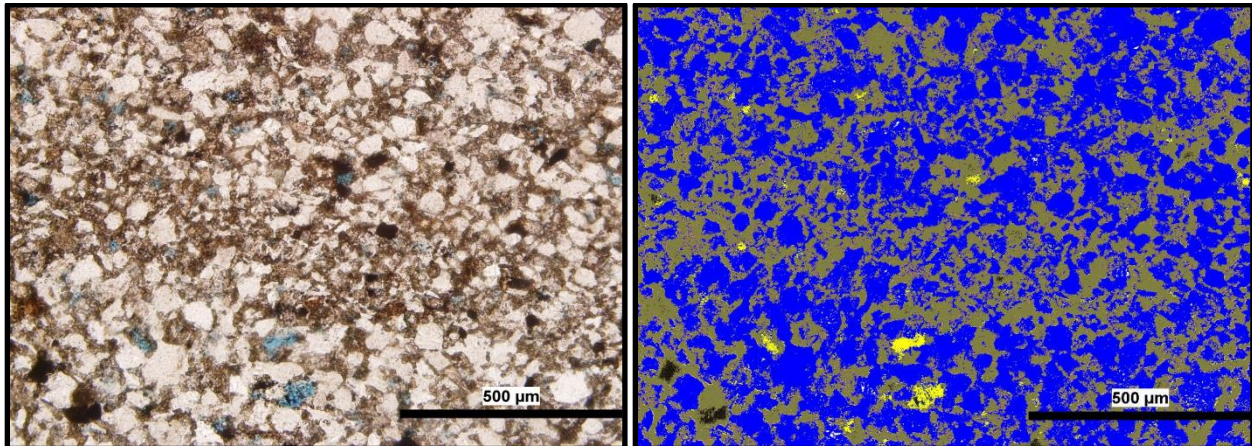


Figure 16-22: Left; thin section image GW103-2013TK-6 (@ 10X) in normal light with porosity shown in blue (dye). Right; same image, but with porosity shown in yellow, grains as blue and cement as brown.

Sample: GW103-2013TK Continued...

Table 16-3: Summary table for sample GW103-2013TK listing the area percentage for voids, grains and cement in each image captured of the thin section. The average area for each of the three parameters is also calculated.

Image Number	Area Type	Area %
GW103-2013TK-1	Voids	2.2
	Grains	73.4
	Cement	24.4
GW103-2013TK-2	Voids	4.0
	Grains	67.5
	Cement	28.6
GW103-2013TK-3	Voids	4.6
	Grains	51.7
	Cement	43.6
GW103-2013TK-4	Voids	3.6
	Grains	56.3
	Cement	40.1
GW103-2013TK-5	Voids	1.0
	Grains	39.5
	Cement	59.5
GW103-2013TK-6	Voids	1.3
	Grains	68.3
	Cement	30.4
Average	Voids	2.8
	Grains	59.5
	Cement	37.8

Sample: GW106-2013TK

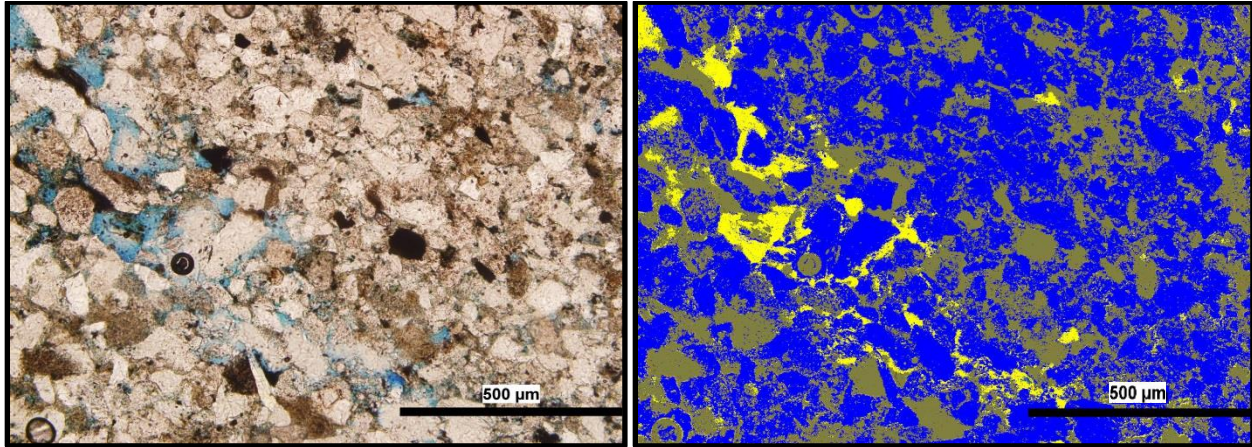


Figure 16-23: Left; thin section image GW106-2013TK-1 (@ 10X) in normal light with porosity shown in blue (dye). Right; same image, but with porosity shown in yellow, grains as blue and cement as brown.

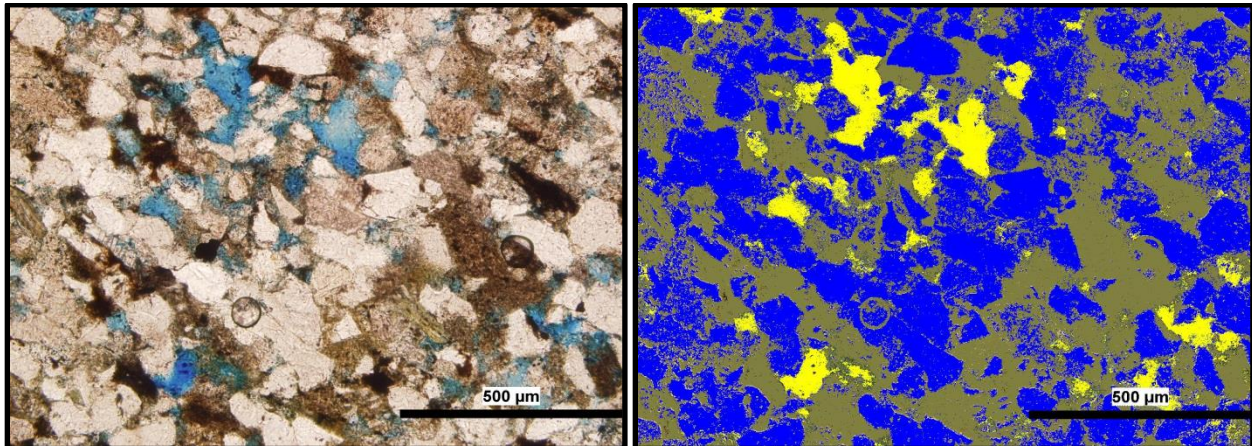


Figure 16-24: Left; thin section image GW106-2013TK-2 (@ 10X) in normal light with porosity shown in blue (dye). Right; same image, but with porosity shown in yellow, grains as blue and cement as brown.

Sample: GW106-2013TK Continued...

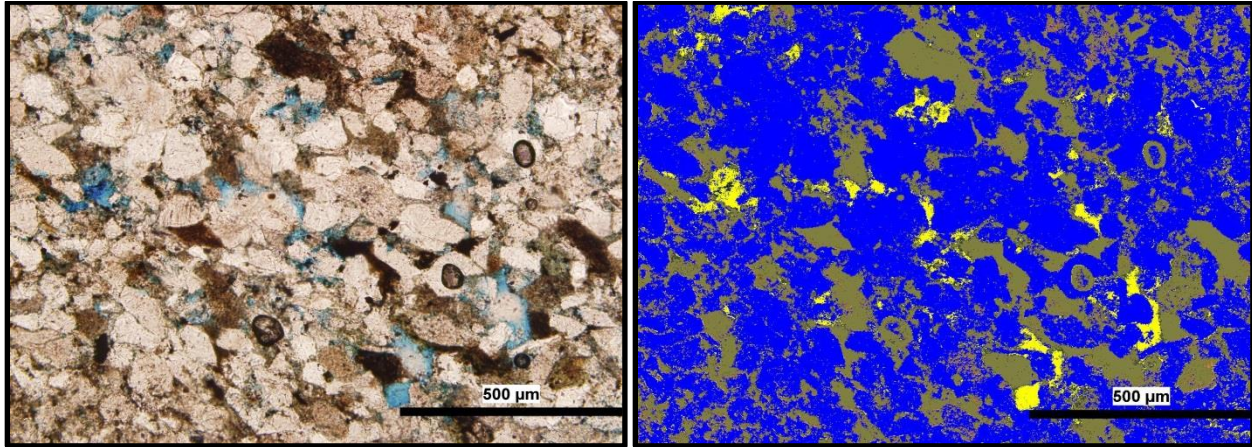


Figure 16-25: Left; thin section image GW106-2013TK-3 (@ 10X) in normal light with porosity shown in blue (dye). Right; same image, but with porosity shown in yellow, grains as blue and cement as brown.

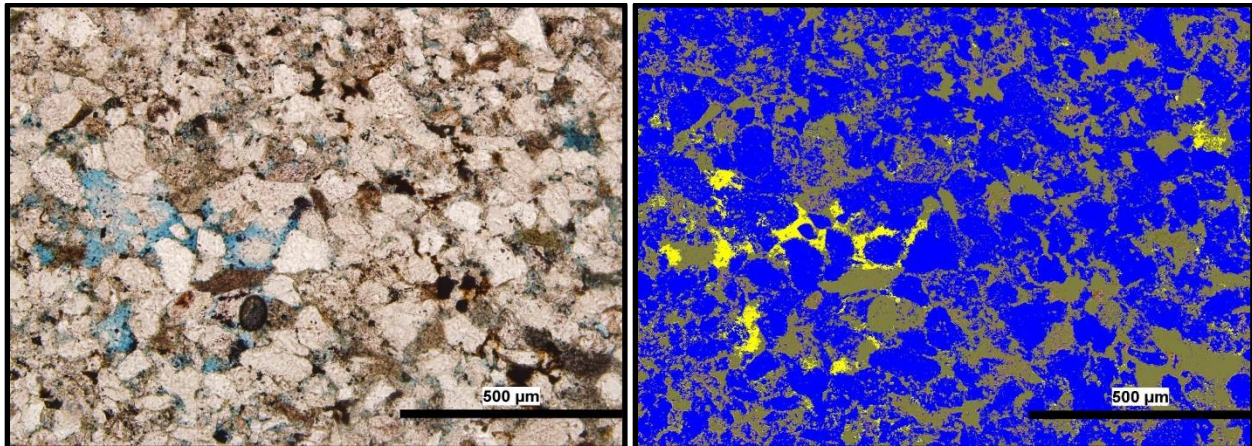


Figure 16-26: Left; thin section image GW106-2013TK-4 (@ 10X) in normal light with porosity shown in blue (dye). Right; same image, but with porosity shown in yellow, grains as blue and cement as brown.

Sample: GW106-2013TK Continued...

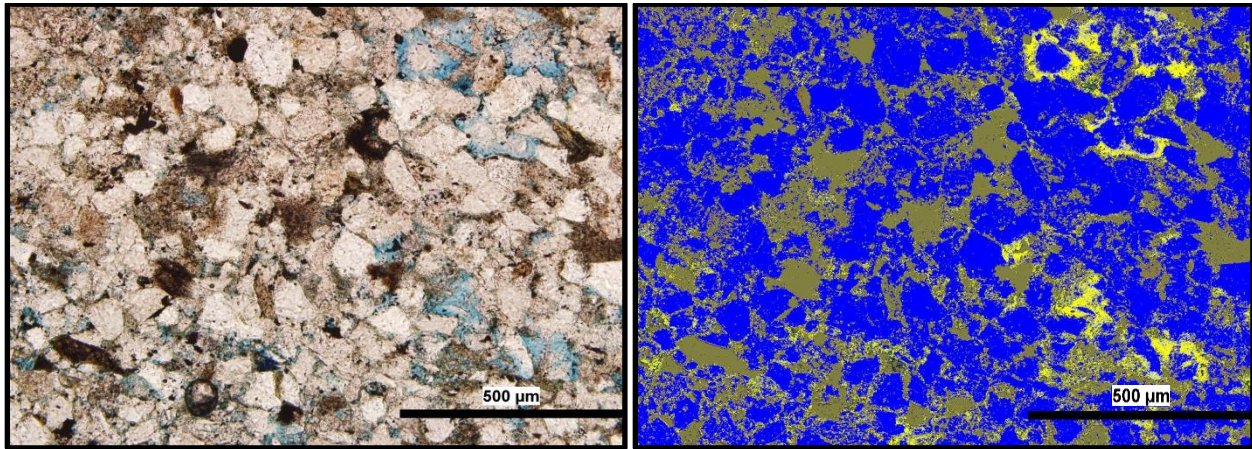


Figure 16-27: Left; thin section image GW106-2013TK-5 (@ 10X) in normal light with porosity shown in blue (dye). Right; same image, but with porosity shown in yellow, grains as blue and cement as brown.

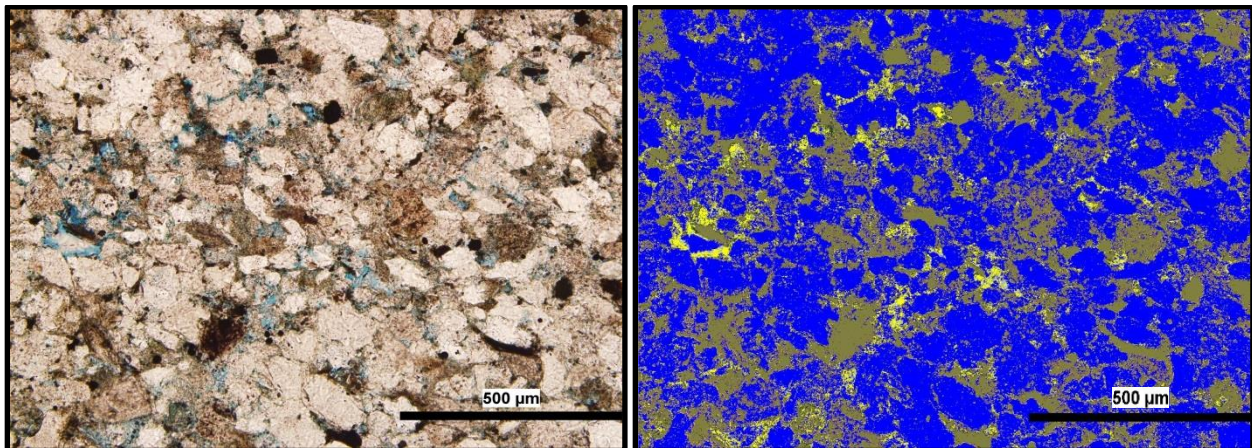


Figure 16-28: Left; thin section image GW106-2013TK-6 (@ 10X) in normal light with porosity shown in blue (dye). Right; same image, but with porosity shown in yellow, grains as blue and cement as brown.

Sample: GW106-2013TK Continued...

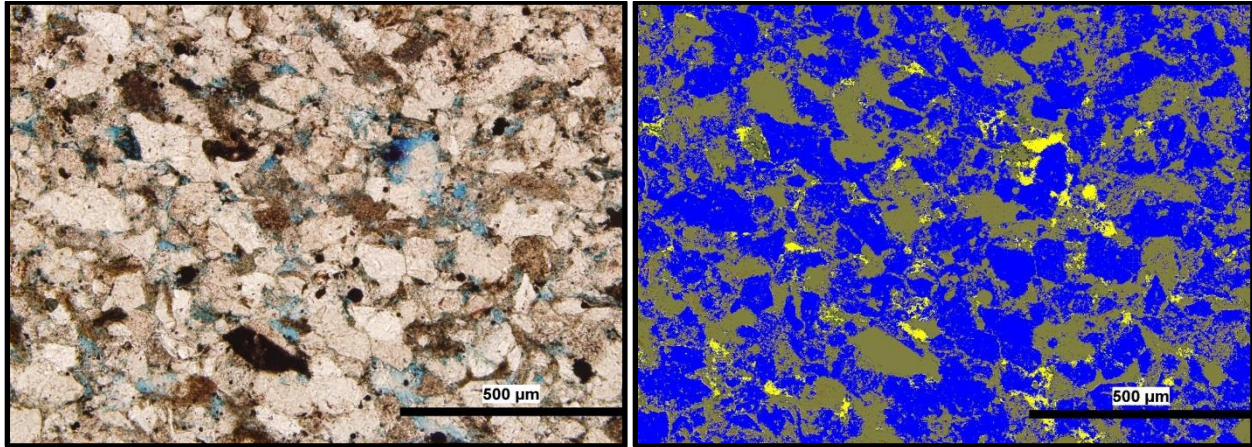


Figure 16-29: Left; thin section image GW106-2013TK-7 (@ 10X) in normal light with porosity shown in blue (dye). Right; same image, but with porosity shown in yellow, grains as blue and cement as brown.

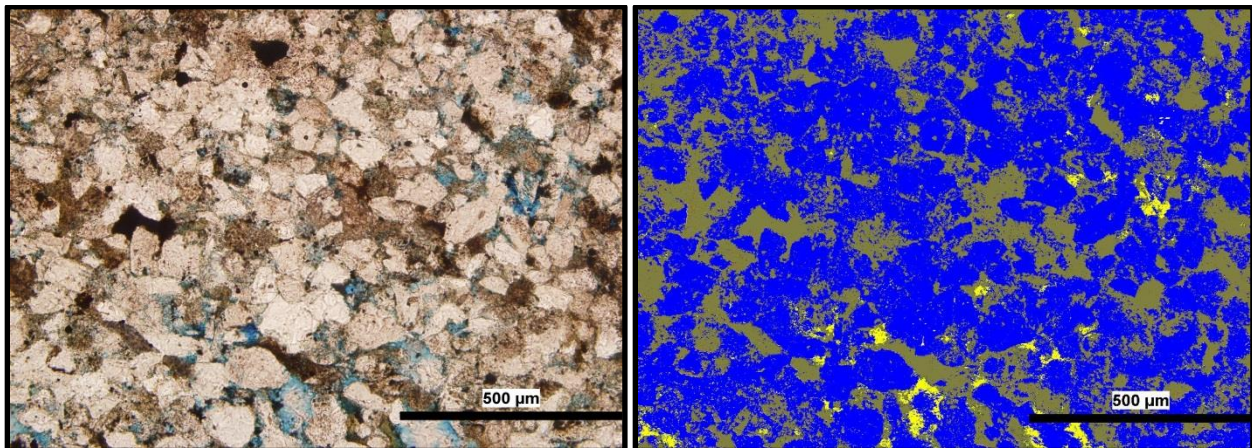


Figure 16-30: Left; thin section image GW106-2013TK-8 (@ 10X) in normal light with porosity shown in blue (dye). Right; same image, but with porosity shown in yellow, grains as blue and cement as brown.

Sample: GW106-2013TK Continued...

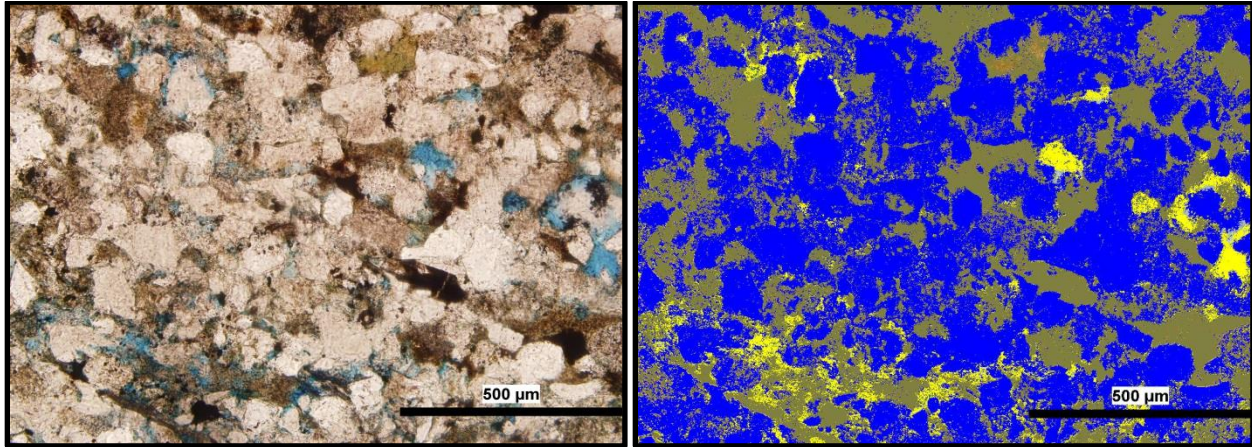


Figure 16-31: Left; thin section image GW106-2013TK-9 (@ 10X) in normal light with porosity shown in blue (dye). Right; same image, but with porosity shown in yellow, grains as blue and cement as brown.

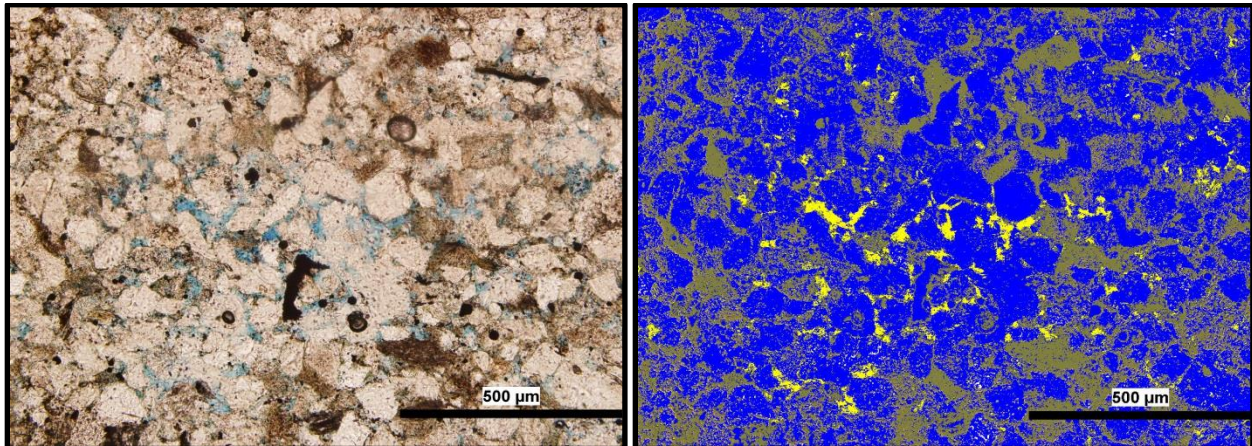


Figure 16-32: Left; thin section image GW106-2013TK-10 (@ 10X) in normal light with porosity shown in blue (dye). Right; same image, but with porosity shown in yellow, grains as blue and cement as brown.

Sample: GW106-2013TK Continued...

Table 16-4: Summary table for sample GW106-2013TK listing the area percentage for voids, grains and cement in each image captured of the thin section. The average area for each of the three parameters is also calculated.

Image Number	Area Type	Area %
GW106-2013TK-1	Voids	5.3
	Grains	67.6
	Cement	27.1
GW106-2013TK-2	Voids	7.2
	Grains	51.0
	Cement	41.8
GW106-2013TK-3	Voids	3.8
	Grains	77.5
	Cement	18.7
GW106-2013TK-4	Voids	2.8
	Grains	78.7
	Cement	18.5
GW106-2013TK-5	Voids	5.7
	Grains	72.8
	Cement	21.6
GW106-2013TK-6	Voids	3.4
	Grains	80.3
	Cement	16.3
GW106-2013TK-7	Voids	3.0
	Grains	65.1
	Cement	31.8
GW106-2013TK-8	Voids	1.5
	Grains	72.4
	Cement	26.2
GW106-2013TK-9	Voids	5.1
	Grains	64.0
	Cement	30.8
GW106-2013TK-10	Voids	3.6
	Grains	74.2
	Cement	22.3
Average	Voids	4.1
	Grains	70.4
	Cement	25.5

Sample: GW107-2013TK

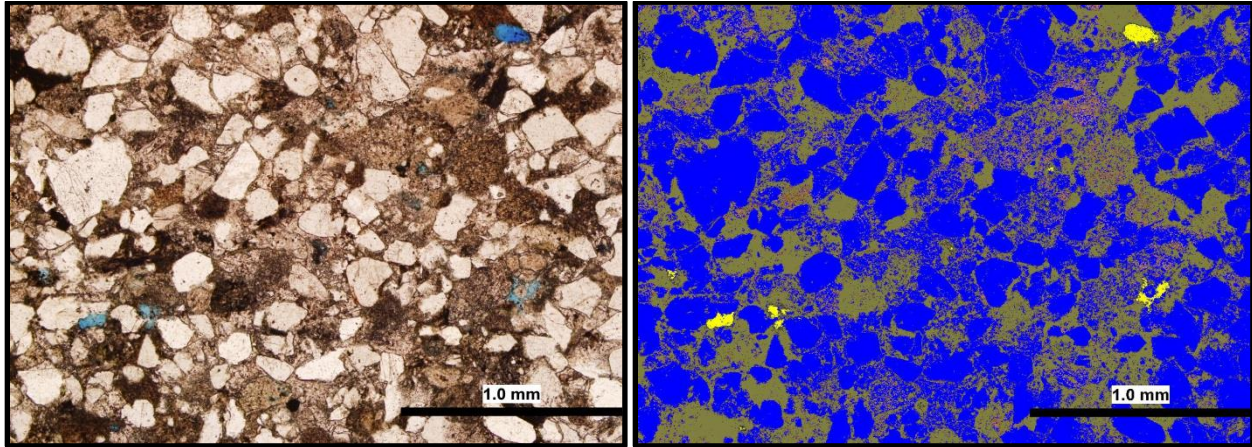


Figure 16-33: Left; thin section image GW107-2013TK-1 (@ 5X) in normal light with porosity shown in blue (dye). Right; same image, but with porosity shown in yellow, grains as blue and cement as brown.

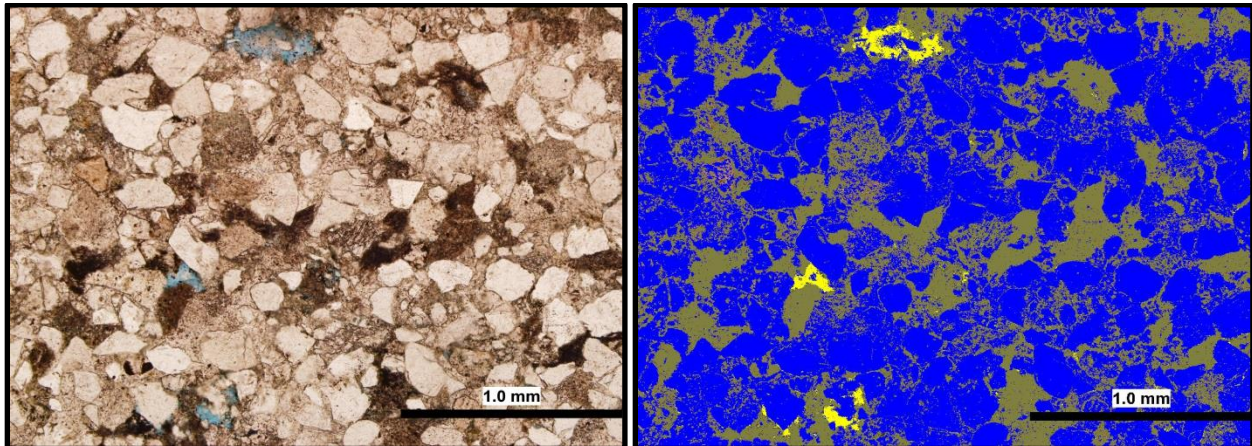


Figure 16-34: Left; thin section image GW107-2013TK-2 (@ 5X) in normal light with porosity shown in blue (dye). Right; same image, but with porosity shown in yellow, grains as blue and cement as brown.

Sample: GW107-2013TK Continued...

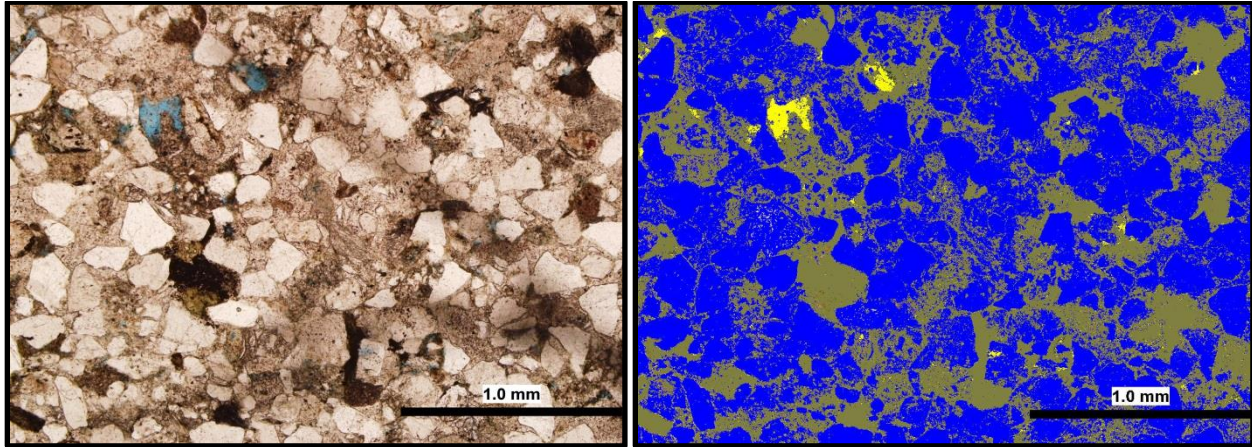


Figure 16-35: Left; thin section image GW107-2013TK-3 (@ 5X) in normal light with porosity shown in blue (dye). Right; same image, but with porosity shown in yellow, grains as blue and cement as brown.

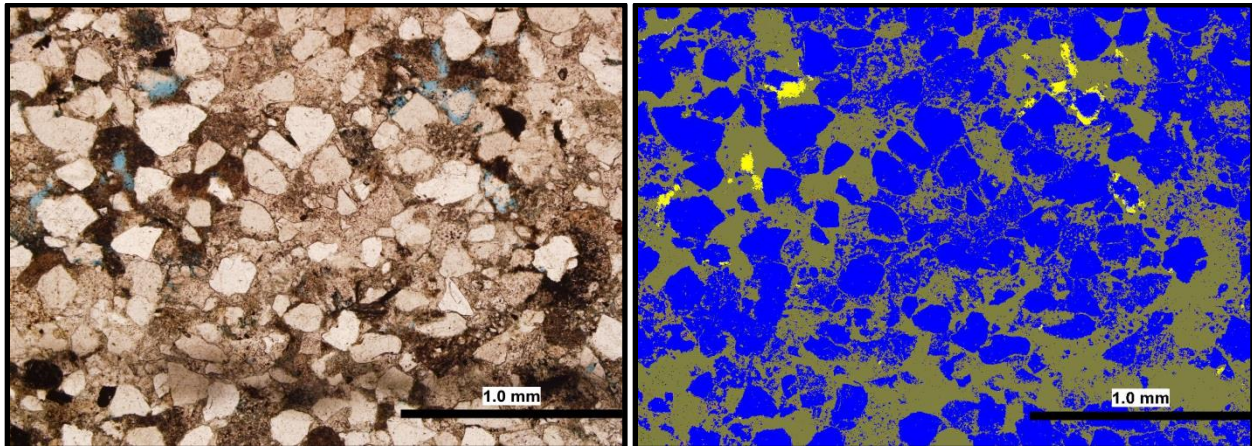


Figure 16-36: Left; thin section image GW107-2013TK-4 (@ 5X) in normal light with porosity shown in blue (dye). Right; same image, but with porosity shown in yellow, grains as blue and cement as brown.

Sample: GW107-2013TK Continued...

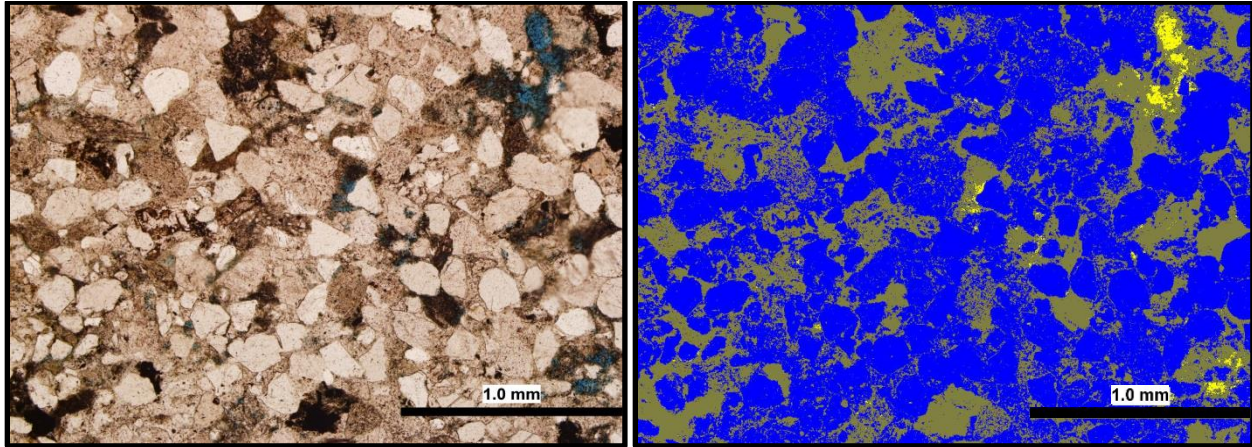


Figure 16-37: Left; thin section image GW107-2013TK-5 (@ 5X) in normal light with porosity shown in blue (dye). Right; same image, but with porosity shown in yellow, grains as blue and cement as brown.

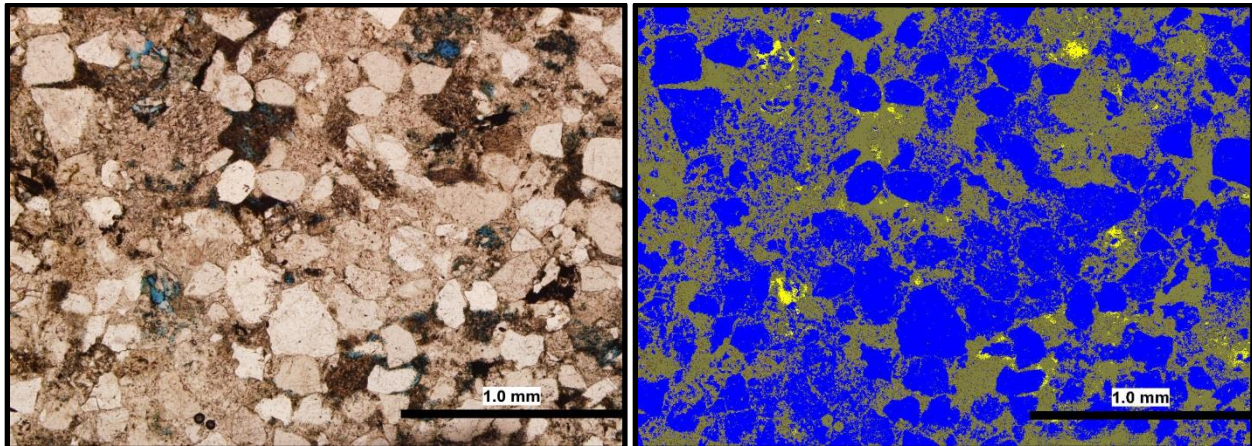


Figure 16-38: Left; thin section image GW107-2013TK-6 (@ 5X) in normal light with porosity shown in blue (dye). Right; same image, but with porosity shown in yellow, grains as blue and cement as brown.

Sample: GW107-2013TK Continued...

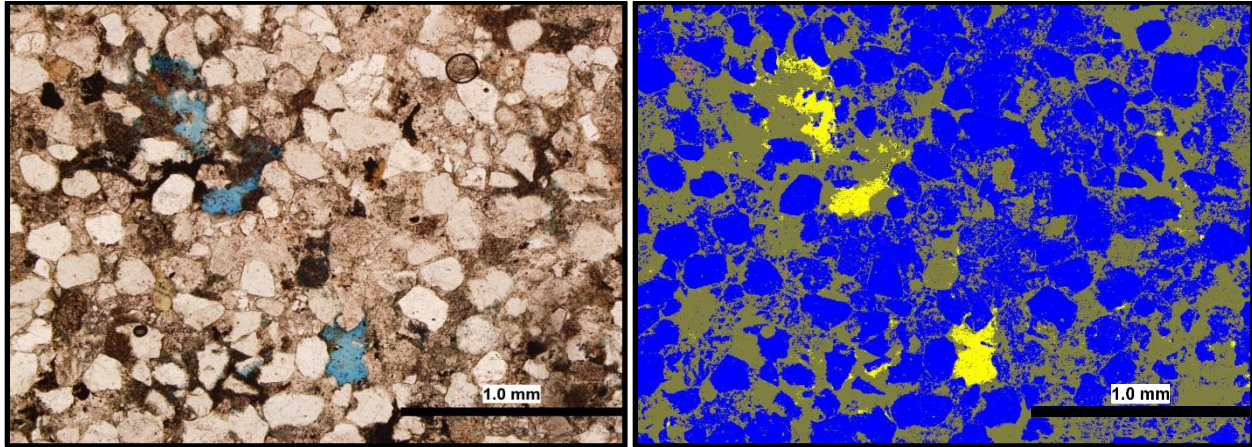


Figure 16-39: Left; thin section image GW107-2013TK-7 (@ 5X) in normal light with porosity shown in blue (dye). Right; same image, but with porosity shown in yellow, grains as blue and cement as brown.

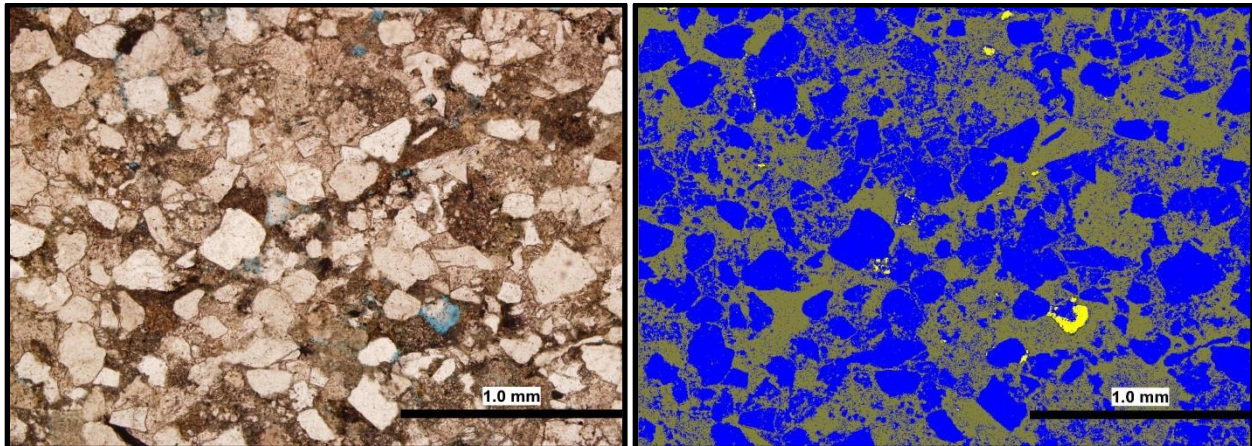


Figure 16-40: Left; thin section image GW107-2013TK-8 (@ 5X) in normal light with porosity shown in blue (dye). Right; same image, but with porosity shown in yellow, grains as blue and cement as brown.

Sample: GW107-2013TK Continued...

Table 16-5: Summary table for sample GW107-2013TK listing the area percentage for voids, grains and cement in each image captured of the thin section. The average area for each of the three parameters is also calculated.

Image Number	Area Type	Area %
GW107-2013TK-1	Voids	0.5
	Grains	69.4
	Cement	30.1
GW107-2013TK-2	Voids	1.0
	Grains	70.9
	Cement	28.1
GW107-2013TK-3	Voids	0.9
	Grains	66.4
	Cement	32.6
GW107-2013TK-4	Voids	0.7
	Grains	55.4
	Cement	43.9
GW107-2013TK-5	Voids	0.6
	Grains	67.4
	Cement	31.9
GW107-2013TK-6	Voids	0.7
	Grains	52.9
	Cement	46.3
GW107-2013TK-7	Voids	2.1
	Grains	53.6
	Cement	44.3
GW107-2013TK-8	Voids	0.3
	Grains	40.5
	Cement	59.2
Average	Voids	0.9
	Grains	59.6
	Cement	39.6

Sample: GW108-2013TK

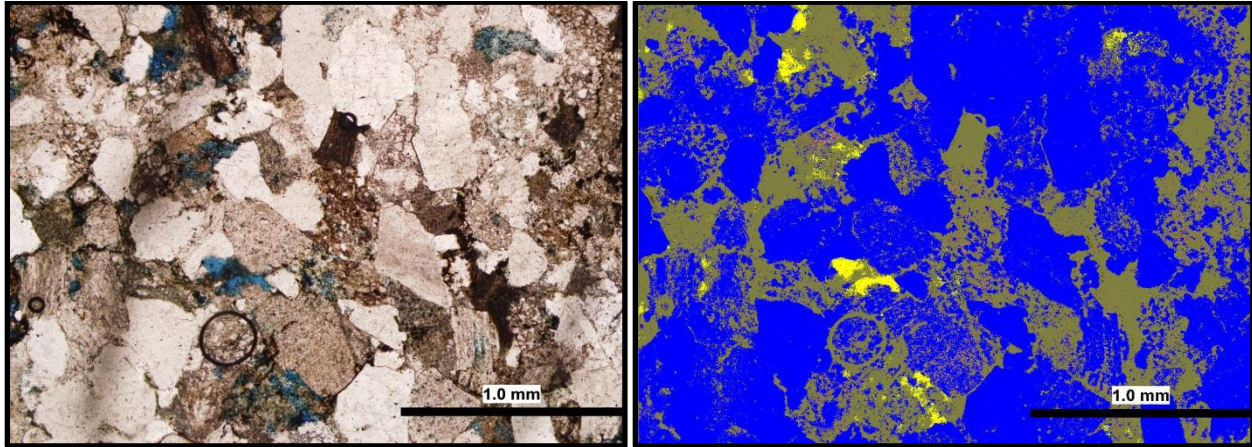


Figure 16-41: Left; thin section image GW108-2013TK-1 (@ 5X) in normal light with porosity shown in blue (dye). Right; same image, but with porosity shown in yellow, grains as blue and cement as brown.

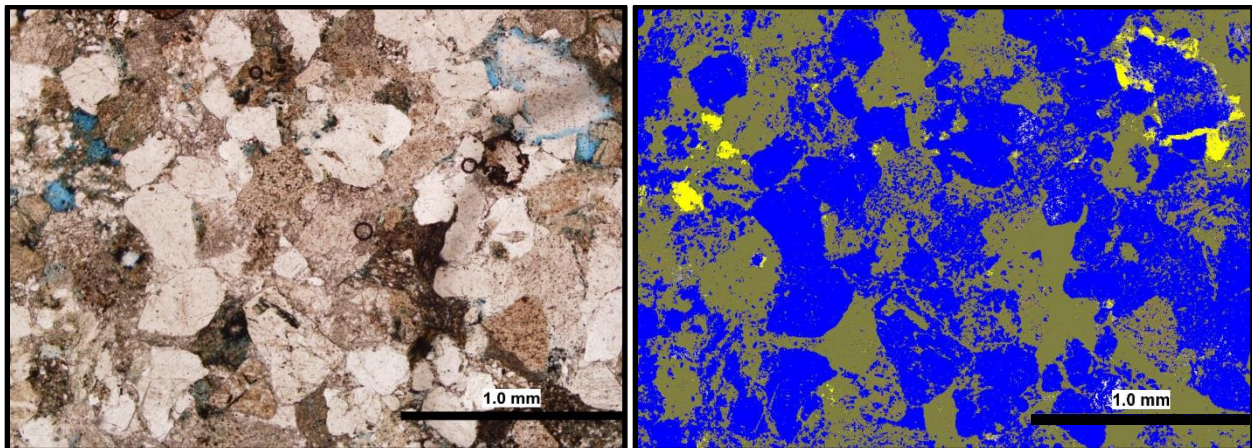


Figure 16-42: Left; thin section image GW108-2013TK-2 (@ 5X) in normal light with porosity shown in blue (dye). Right; same image, but with porosity shown in yellow, grains as blue and cement as brown.

Sample: GW108-2013TK Continued...

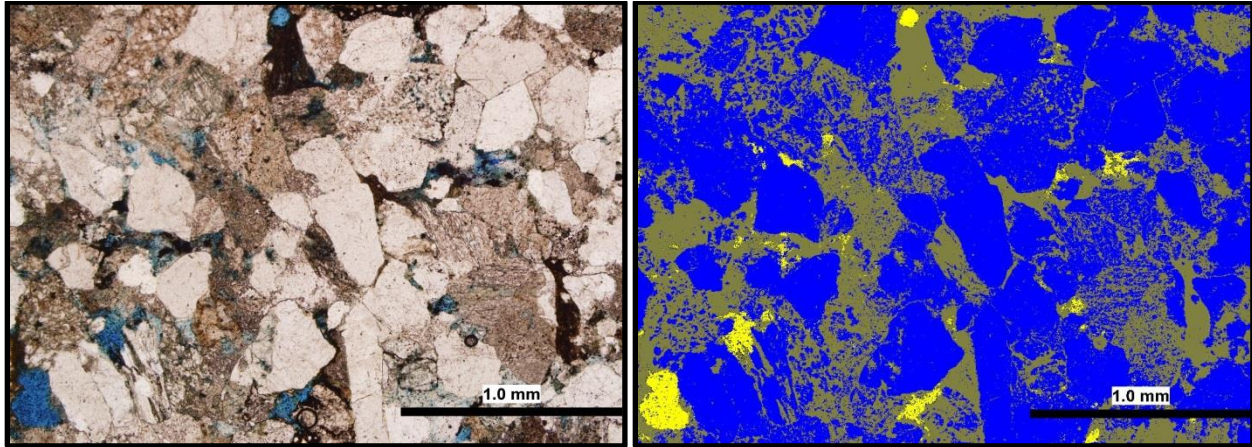


Figure 16-43: Left; thin section image GW108-2013TK-3 (@ 5X) in normal light with porosity shown in blue (dye). Right; same image, but with porosity shown in yellow, grains as blue and cement as brown.

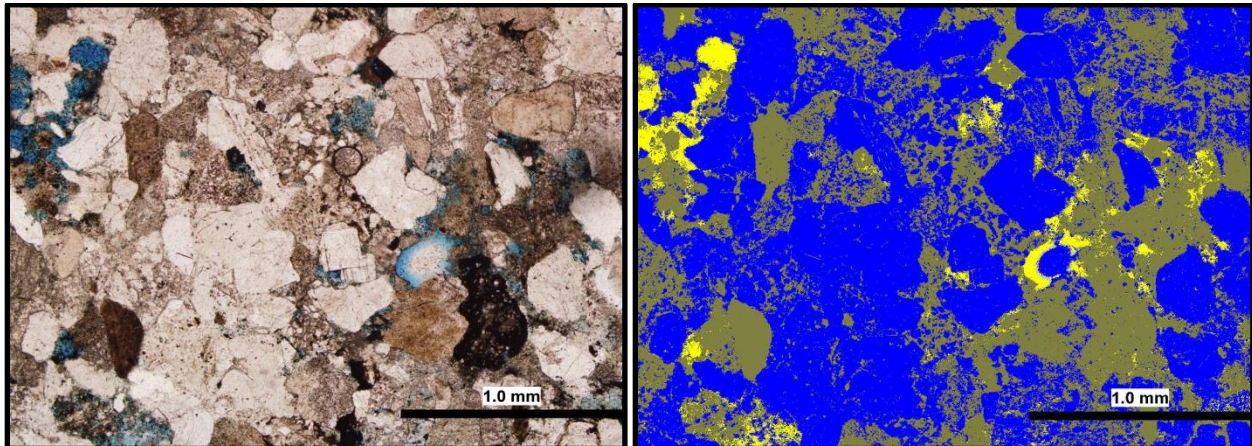


Figure 16-44: Left; thin section image GW108-2013TK-4 (@ 5X) in normal light with porosity shown in blue (dye). Right; same image, but with porosity shown in yellow, grains as blue and cement as brown.

Sample: GW108-2013TK Continued...

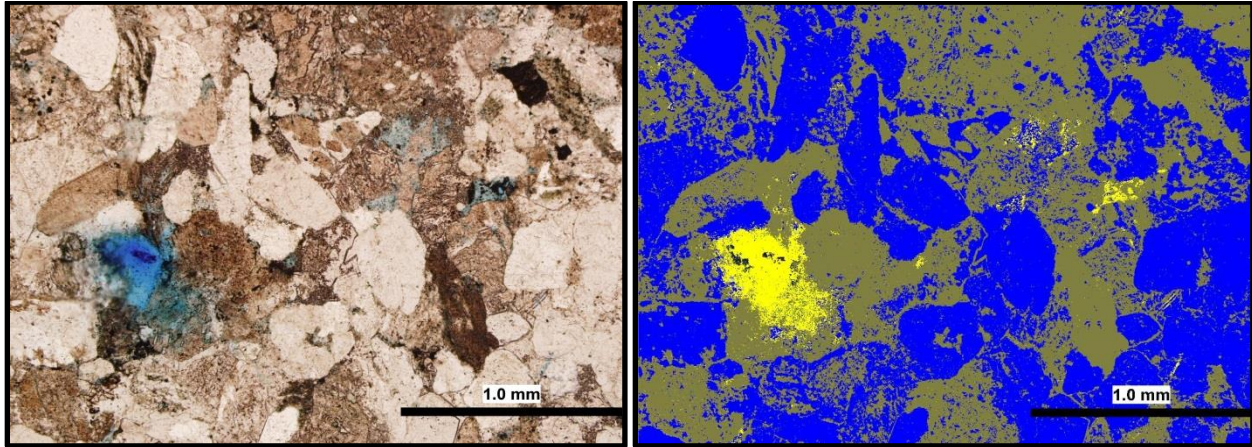


Figure 16-45: Left; thin section image GW108-2013TK-5 (@ 5X) in normal light with porosity shown in blue (dye). Right; same image, but with porosity shown in yellow, grains as blue and cement as brown.

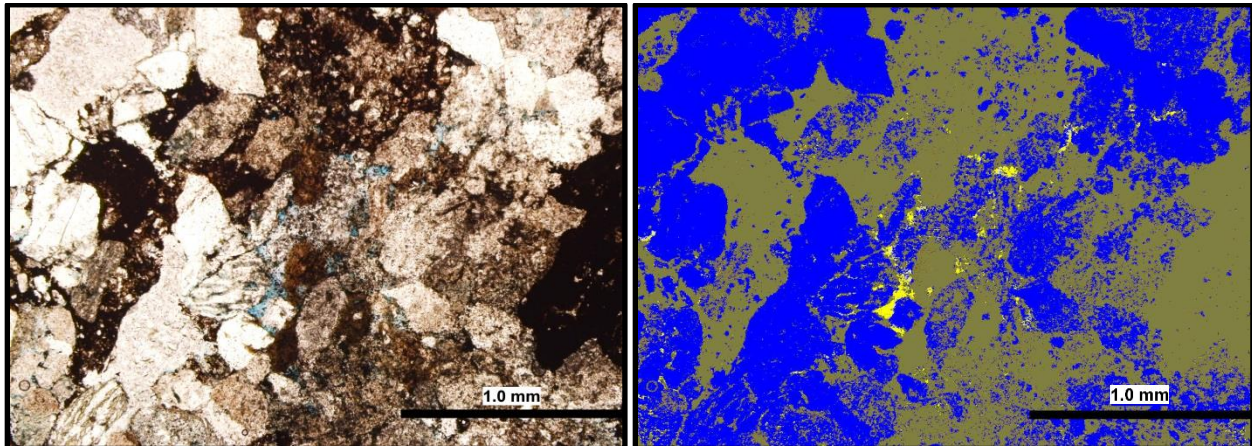


Figure 16-46: Left; thin section image GW108-2013TK-6 (@ 5X) in normal light with porosity shown in blue (dye). Right; same image, but with porosity shown in yellow, grains as blue and cement as brown.

Sample: GW108-2013TK Continued...

Table 16-6: Summary table for sample GW108-2013TK listing the area percentage for voids, grains and cement in each image captured of the thin section. The average area for each of the three parameters is also calculated.

Image Number	Area Type	Area %
GW108-2013TK-1	Voids	1.3
	Grains	69.9
	Cement	28.8
GW108-2013TK-2	Voids	1.3
	Grains	54.7
	Cement	44.0
GW108-2013TK-3	Voids	1.9
	Grains	59.0
	Cement	39.2
GW108-2013TK-4	Voids	3.5
	Grains	58.0
	Cement	38.5
GW108-2013TK-5	Voids	3.1
	Grains	47.5
	Cement	49.4
GW108-2013TK-6	Voids	0.9
	Grains	49.4
	Cement	49.7
Average	Voids	2.0
	Grains	56.4
	Cement	41.6